

Efimov Physics in an Ultracold Gas of Cesium Atoms: Universality and its Limitations

DISSERTATION

by

Bo Huang, MSc

submitted to the Faculty of Mathematics, Computer Science,
and Physics of the University of Innsbruck

in partial fulfillment of the requirements
for the degree of Doctor of Philosophy (PhD)

advisors:

Univ.-Prof. Dr. Rudolf Grimm,
Institute for Experimental Physics, University of Innsbruck
Institute for Quantum Optics and Quantum Information of the
Austrian Academy of Sciences

Univ.-Prof. Dr. Francesca Ferlaino,
Institute for Experimental Physics, University of Innsbruck
Institute for Quantum Optics and Quantum Information of the
Austrian Academy of Sciences

Innsbruck, May 2015

Summary

In the limit of ultra-low collision energies, the interactions between particles are dominated by s -wave scattering and higher partial waves are negligible. In this case, the two-body interaction can be characterized by a single parameter, the s -wave scattering length a , if the inter-particle potential is short-ranged. This simplification enables us to describe entirely different systems such as nuclei, molecules and neutral atoms universally. In this *universal* regime, quantum correlations between particles lead to exotic few-body phenomena, whose paradigm is the Efimov's prediction of a series of three-boson states. In the last decade, ultracold atomic gases have opened up the possibility to explore Efimov's scenario experimentally and to test further predictions of universal theory.

This thesis reports on a series of studies on Efimov physics performed with ultracold cesium gases. We first present a thorough study of the scattering properties of cesium atoms over a wide range of magnetic fields, where many magnetically induced Feshbach resonances enable us to tune the scattering length by varying the magnetic field. We then present a work in which three new triatomic Efimov resonances are observed at three broad Feshbach resonances. By comparing the four observed Efimov states in cesium, we find the value of the three-body parameter (3BP), which fixes the Efimov spectrum, to be approximately constant. This work has triggered the discovery of the 'van der Waals universality', which attributes the constancy of the 3BP to the van der Waals interaction between neutral atoms. On the other hand, we also measure the atom-dimer recombination resonance caused by an Efimov state and observe a substantial deviation from the universal relation. But these non-universal results can still be explained by a coupled-channel model in which the van der Waals interaction is considered. Furthermore, we observe a resonance due to a universal five-body state associated to an Efimov state. This is an important step towards understanding the general nature of N -body cluster states and their implications for many-body physics.

One distinguishing feature of the Efimov states is the discrete scaling symmetry, which predicts that the positions of Efimov resonances caused by successive Efimov states are connected by a universal factor of 22.7 in scattering length in the case of identical bosons. We observe an excited-state Efimov resonance and compare it with the ground-state one, extracting a value of 21.0(1.3) for the scaling factor. The small difference between the measured value and the ideal one suggests non-universal effects caused by the finite interaction range, which may particularly influence the position of the ground-state Efimov resonance.

In our analysis of the excited-state Efimov resonance, finite-temperature effects are considered by a universal zero-range model. We extend this model to consider distinguishable atoms and use it to analyze the excited-state Efimov resonance of ${}^6\text{Li}$ in a previous work. A precise value of the 3BP is obtained and compared with the one from cesium. The deviation between the ${}^6\text{Li}$ and cesium data shows that the van der Waals universality is only approximately fulfilled. Moreover, we perform finite-temperature measurements over a large temperature range on the ground-state Efimov resonance to test the universal zero-range theory directly. The prediction and observation are found to be generally consistent, while a small deviation between them is characterized by an empirical function and attributed to the finite-range of the van der Waals potential.

Contents

Summary	i
1 Introduction	1
1.1 Efimov physics in ultracold atomic gases	1
1.2 Structure of the thesis	3
2 Theoretical Background	5
2.1 Threshold scattering in ultracold atomic gases	5
2.1.1 The concept of universality	5
2.1.2 Scattering near the threshold	6
2.1.3 Magnetic field induced Feshbach resonances	7
2.2 Theory of Efimov states	9
2.2.1 The discovery of Efimov states	9
2.2.2 Hyperspherical coordinates	10
2.2.3 The Faddeev equations for bound states	13
2.2.4 Adiabatic solutions with two-body boundary conditions	16
2.2.5 The discrete symmetry of Efimov states	20
2.3 The three-body recombination rate at zero temperature	21
2.3.1 Analytic calculations of the main observables	21
2.3.2 The Skorniyakov-Ter-Martirosyan equation	22
2.3.3 Three-body recombination	23
2.4 Frontiers of the universal few-body physics	24
2.4.1 Ultracold atomic gases and other systems	24
2.4.2 Universal N -body system	25
2.4.3 Binding energies of the Efimov trimers	25
2.4.4 ‘van der Waals universality’ of the three-body parameter	26
2.4.5 Finite-temperature effects	28
2.4.6 The Efimov period	29
2.4.7 Efimov states in a confining potential	30
3 Publication: Feshbach resonances, weakly bound molecular states and coupled-channel potentials for cesium at high magnetic fields	32
3.1 Introduction	33
3.2 Near-threshold states of cesium dimer	34
3.3 Feshbach spectroscopy at high magnetic field	39
3.3.1 Sample preparation	39
3.3.2 Trap-loss spectroscopy	42
3.3.3 Binding energy measurements	46

3.4	Theoretical model	49
3.4.1	Computational methods for bound states and scattering	49
3.4.2	Representation of the potential curves	51
3.4.3	Magnetic dipole interaction and second-order spin-orbit coupling	51
3.5	Least-squares fitting of potential parameters	52
3.5.1	Region between 800 G and 920 G	55
3.5.2	Region around 550 G	55
3.5.3	Low-field region	57
3.5.4	Independent tests of the M2012 model	59
3.5.5	Mapping between scattering length and magnetic field	60
3.6	Conclusion	61
3.7	Supplemental Material	63
4	Publication: Universality of the three-body parameter for Efimov states in ultra-cold cesium	70
4.1	Introduction	71
4.2	The experiment	72
4.3	Efimov resonances at different Feshbach resonances	73
4.4	Conclusion	76
5	Publication: Resonant atom-dimer collisions in cesium: testing universality at positive scattering lengths	78
5.1	Introduction	79
5.2	Experimental procedures	80
5.3	Measurements of atom-dimer decay	83
5.4	Comparison with previous results and theory	84
5.4.1	Effective field theory	86
5.4.2	Universal van der Waals theory	87
5.4.3	Discussion	88
5.5	Search for an atom-dimer avalanche effect	89
5.6	Conclusions	91
6	Publication: Resonant five-body recombination in an ultracold gas of bosonic atoms	93
6.1	Introduction	94
6.2	Theoretical approach	95
6.3	Experiment	98
6.4	Conclusion	100
6.5	Appendix	101
7	Publication: Observation of the second triatomic resonance in Efimov's scenario	105
7.1	Introduction	106
7.2	The observations	107
7.3	Conclusion	112
7.4	Supplemental material	113
8	Publication: The three-body parameter for Efimov states in lithium-6	118
8.1	Introduction	119

8.2	Three-body parameter	120
8.3	Efimov states in a three-component Fermi gas	122
8.3.1	Three-fermion system	122
8.3.2	Three-body recombination	123
8.3.3	Lithium-6	123
8.3.4	The effective range	123
8.4	Finite-temperature theoretical approach	124
8.5	Excited-state Efimov resonance	125
8.6	Ground-state Efimov resonances	128
8.7	Conclusion	131
9	Finite-temperature effects on a triatomic Efimov resonance in ultracold cesium	134
9.1	Introduction	135
9.2	Finite-temperature regimes	136
9.3	Experiments	137
9.3.1	Experimental procedures	138
9.3.2	Experimental results and fit analysis	139
9.3.3	Empirical characterization of the resonance shift	141
9.4	Discussion	141
9.4.1	Ground-state Efimov resonance of Cs in the low-field region	143
9.4.2	Excited-state Efimov resonance in ${}^6\text{Li}$	144
9.4.3	Efimov period in Cs revisited	145
9.4.4	Open questions	145
9.5	Conclusion	146
	Bibliography	147
	Acknowledgments	163

Introduction

1.1 Efimov physics in ultracold atomic gases

Few-body problems arise in various branches of physics from classical systems involving several celestial bodies to quantum clusters like small molecules and light nuclei. Studies on few-body problems aim at revealing the structure and dynamical behavior of these systems, and such knowledge also provides a microscopic perspective on many-body physics. However, while the two-body problem is generally considered ‘solvable’, already the three-body problem exhibits the notorious complexity of few-body systems [Nie01].

Nonetheless, extraordinarily simplifications to quantum few-body problems can be made in the so called ‘universal regime’ where systems with vastly different properties, like nuclei and atomic clusters, exhibit similar long-range behavior [And04, Bra06]. In this regime, conceptually, we are allowed to approximate various complicated two-body interactions by a very simple isotropic zero-range potential, which is fully characterized by the s -wave scattering length a . This simplification is very general and has applications in both few-body and many-body physics. In the real world, the universal regime can be realized in experiments at very low energies when the pair-wise interaction between particles is short-ranged and resonant, which happens when a two-body bound state is very close to the zero-energy threshold.

A landmark result of universal few-body physics was obtained in the 1970s by the Russian physicist Vitaly Efimov [Efi70]. He studied the three-body problem in the universal regime and predicted a series of ultra-shallow three-boson states. Particularly, if the two-body interaction is resonant, the spectrum of Efimov states forms an infinite geometric series. Although Efimov states were predicted in the context of nuclear physics, nuclear systems are not ideal for observing them [Jen04]. Above all, the control over interaction properties is limited in nuclear systems, which makes it very difficult to reach the universal regime. Another complication comes from the non-universal effects induced by the long-range Coulomb interaction between protons in a nucleus. Therefore an Efimov state in nuclear systems may consist of two neutrons and another nuclei which interacts strongly with the neutrons [Maz06, Yam08]. But after decades of investigations, such Efimov states have remained elusive.

Beyond nuclear systems, Efimov states may also appear as weakly bound molecules. The helium-4 trimer state predicted in 1977 is considered the prime candidate for molecular Efimov states [Lim77]. But previous experiments on molecular beams could not detect it because of the very small binding energy. About twenty years ago, the ground helium trimer state was observed [Sch94], but it is too tightly bound to qualify as an Efimov state. The observation of the excited trimer state, which is an Efimov state, has remained elusive [Heg00, Brü05] until very recent experiments reported this year [Kun15].

The advent of ultracold neutral atomic gases paved another path towards observations of Efimov states. Thanks to Feshbach resonances [Fes58, Fes62, Chi10], experimentalists have acquired the unique opportunity to tune the interaction between atoms by changing the magnetic field strength. Such a convenience led to the first observation of an Efimov state in an ultracold gas of cesium atoms [Kra06]. Since then Efimov states have been observed in various ultracold gases of bosonic atoms [Zac09, Pol09, Gro09, Gro10, Wil09, Roy13], fermionic mixtures [Ott08, Huc09, Wil09, Nak10] and hetero-nuclear atomic mixtures [Bar09, Blo13, Pir14, Tun14]. The Efimov scenario has also been extended to universal four- and five-body states, which have also been observed [Fer09, Zac09, Pol09, Zen13].

While the observation of Efimov states and other universal N -body states generally agree with the predictions of universal theories, questions naturally arise about the limitations of universality in the real world. The main motivation of the studies reported in the current thesis is to clarify these questions by conducting experiments on an ultracold gas of cesium atoms. Particularly we are interested in how far the properties of universal few-atom states do follow universal predictions and how they deviate from the ideal scenario. For example, all the observables in a universal few-body system are predicted to be connected by universal relations, and these predictions can be tested with observables obtained at positive and negative scattering lengths and with features for Efimov states and universal clusters states consisting of more particles.

One of the key results of universality is the geometric Efimov spectrum, of which the Efimov scaling factor can be obtained experimentally by observing an excited Efimov state and comparing it with the corresponding ground Efimov state. Nevertheless, in earlier experiments [Zac09, Pol09, Dyk13], this could not be accomplished mainly because the extremely large size of the excited Efimov state sets a stringent temperature limit, which should be low enough to guarantee the quantum coherence throughout the three-body system. An excited Efimov state was observed in a spin mixture of fermionic ${}^6\text{Li}$, but it was difficult to obtain the scaling factor because of the involvement of three different scattering lengths [Wil09]. Recently, successive Efimov states have been observed in a cesium gas [Hua14b] and in mixtures of lithium and cesium atoms [Pir14, Tun14], and the geometric scaling symmetry of Efimov states has finally been confirmed. The observed value of the Efimov scaling factor in cesium deviates only slightly from the ideal value and shows both the validity and the limitation of universal theories.

Non-universal effects in atomic systems mostly originate from the the small yet non-zero range of interaction. One important finite-range effect is that the infinite Efimov spectrum is truncated from below and the position of the lowest Efimov state is described by a three-body parameter (3BP). Entering as an external parameter in universal theories, the 3BP

depends on the short-range details of the interaction [Bra06]. It has been an open issue in theories whether the 3BP is invariant for Efimov states appearing near different Feshbach resonances and in different atomic species [D'I09, Pet04, Mas08, Wan11, Lee07, JL10, Nai11]. Experimentally, the answer became evident when plenty of observations accumulated and lead to the discovery of an approximately constant 3BP in atomic systems. This phenomenon has been understood later as a result of the van der Waals interaction [Wan12], which dominates at long distances.

Moreover, universality is limited also when the temperature is so high that the thermal wavelength of atoms is no longer large enough to maintain quantum coherence [Rem13]. In addition, particles colliding at higher energies are more likely to probe interaction potentials at short distances and enhance non-universal effects. In experiments, these non-universal effects can be observed as temperature dependence of the observables.

1.2 Structure of the thesis

The main part of this thesis reports a series of experiments on ultracold cesium atoms, in which the problems introduced in the preceding section about the properties of Efimov states and associated N -body states are studied. Before that, in the following chapter, we first prepare the background knowledge of universal-few body theories. Particularly, Sec. 2.1 briefly summarizes the theory of universal two-body scattering in the context of ultracold atomic gases and Feshbach resonances. Then theories on Efimov states and related observables will be introduced in Sec. 2.2 and Sec. 2.3. After that in Sec. 2.4, we will discuss current research on universal few-body physics.

Then seven publications of the author are organized to present the experimental studies on the universal few-body physics in ultracold cesium gases. The author also contributed to one review paper [Fer11] that is not included in this thesis.

In the work of chapter 3, the positions and widths of Feshbach resonances and the binding energies of weakly bound molecular states are measured for cesium atoms at high magnetic fields. The high-field data, together with the data obtained earlier in the low-field region, are fitted by a coupled-channel model and an accurate mapping between the magnetic field and the s -wave scattering length is obtained for a large range of magnetic fields. This work provides a solid ground for further studies on universal few-body physics, which relies on the fine tuning of the scattering length.

In the work of chapter 4, we observe three Efimov resonances at three different broad Feshbach resonances at high magnetic field. Together with the Efimov resonance observed at low magnetic field, we find the positions of Efimov resonances are almost the same and suggest a nearly constant three-body parameter independent of the details of the Feshbach resonances. This constancy of the 3BP is later explained as the ‘van der Waals universality’.

In the work of chapter 5, we study the atom-dimer resonance at high magnetic field and find that the resonance position significantly deviates from the universal zero-range theory and

the value observed at low field. The experimental results are explained by a coupled-channel calculation in which the van der Waals interaction is considered.

In the work of chapter 6, an universal five-body state is observed as a resonance peak of the effective three-body recombination rate. Theoretical discussions on the five-body recombination rate are also involved.

In the work of chapter 7, the second Efimov resonance, corresponding to the first excited Efimov state, is observed in cesium gases and can be compared with the ground-state Efimov resonance to find the Efimov period as $21.0(1.3)$. We also observe the associated four-body and study the finite temperature effects on the second Efimov resonance.

In the work of chapter 8, the data of the Efimov resonances observed in ultracold ${}^6\text{Li}$ gases are reanalyzed with the finite-temperature model based on S -matrix formalism and STM equations (see subsection 2.3.2). Since the second Efimov resonance is less sensitive to the short-range details of the interactions, the position of the second Efimov resonance in fermionic ${}^6\text{Li}$ and the one in Cs are compared and serve as another test for the validity of the ‘van der Waals universality’.

In the work of chapter 9, the temperature effects on the Efimov resonance are observed over a large range of temperatures from tens of nano-Kelvin up to a few micro-Kelvin and analyzed with the universal zero-range finite-temperature model. We apply a phenomenological model to quantify the temperature dependence of the three-body parameter and attribute the temperature effects to the finite range of the two-body interaction.

Theoretical Background

2.1 Threshold scattering in ultracold atomic gases

2.1.1 The concept of universality

Low-energy particles interacting with symmetric short-range potentials exhibit *universal* properties that are independent of the short-distance details of the interaction and the particles' structure. With the s -wave scattering length a and a few basic parameters like the masses of particles and physical constants, we are able to obtain all the low-energy observables for totally different systems [And04, Bra06, Fer11]. In theories, the actual interactions can be replaced by proper boundary conditions or zero-range potentials (e.g. Wigner-Bethe-Peierls model [Wig33, Bet35a, Bet35b], delta potential [Cav99], contact pseudo-potential [Lee57] and Tan contact [Tan08]) to give universal and simple pictures for various situations in nuclei, ultracold atomic gases and condensed matter. These universal models should be irrelevant to temperature T at the zero- T limit, and for some observables, like scattering cross sections, their T -dependences are well known for finite yet small T values.

In experiments, low collisional energy, resonantly large scattering length a and short-ranged two-body potentials are the three criteria to reach the universal regime. For ultracold gases of alkali atoms, magnetically induced Feshbach resonances offer the opportunity to tune the scattering length and open the gate to the universal regime [Tim99, Chi10, Pet13, Ber11a]. Particularly, cesium atoms in the lowest internal level are stable against two-body decays and have a large family of Feshbach resonances with different widths. The rich and accurate knowledge of the magnetic field dependent scattering properties of cesium atoms makes cesium the prime candidate for investigations of universal few-body physics. In this section, we will discuss some essential properties of universal scattering physics in the context of ultracold alkali atoms and Feshbach resonances. Our work on the investigation of scattering properties of cesium atoms at high magnetic field is included in Chap. 3.

2.1.2 Scattering near the threshold

In the present work we are working on particles colliding in the low-temperature or *threshold* regime, whose meaning has several aspects. First, we imply that the two-body interaction is short-ranged, i.e. the potential decays faster than $1/r^2$, where r is the inter-particle distance. This implies that it is much weaker than the centrifugal potential when r is larger than a typical range R_e of the interaction. Usually R_e is defined as the distance at which the potential energy is comparable with the unit of the centrifugal potential $\hbar^2/2\mu r^2$, where μ is the reduced mass. For ultracold alkali atomic gases, the van der Waals interaction prevails and R_e is the van der Waals length

$$R_{\text{vdW}} = \frac{1}{2} \left(\frac{2\mu C_6}{\hbar^2} \right)^{1/4}, \quad (2.1)$$

where C_6 is the coefficient for the van der Waals interaction $-C_6/r^6$. The values of R_{vdW} are about tens of the Bohr radius a_0 for alkali atoms. The threshold regime also requires that the thermal wave length of the particles is much larger than R_e . In this case, we can approximate the wave function with the free-wave solution of the Schrödinger equation when r is much larger than R_e , and ignore the small total energy when r is smaller than R_e . The upper limit of temperature T can be identified by considering $1/k \gg R_{\text{vdW}}$ where $k = \sqrt{2\pi m k_B T}/\hbar$ is the wave number of the atom wave function. In the case of cesium atoms, the limit T is on the order of one milli-Kelvin.

When the two-body interaction, e.g. van der Waals interaction, is also isotropic, we can work in the orthogonal basis of partial waves with corresponding angular momentum l . When the collision is elastic for each partial wave, the scattering conserves flux and its effect can be characterized by the phase shift δ_l between the outgoing and incoming wave functions. According to the Wigner threshold law [Wig48, Chi10], $\tan \delta_l \propto k^{2l+1}$ when k approaches zero. More strictly, for a specific channel of angular momentum l , the asymptotic free-wave approximation is only valid when the interaction potential decays faster than r^{-2l-3} (see §130 in Ref. [Lan65]). Considering the van der Waals interaction, the above threshold law is valid for l equals 0 and 1, while being only qualitatively correct beyond that. Therefore the s -wave scattering ($l = 0$) dominates for distinguishable particles or identical bosons while the p -wave ($l = 1$) scattering is the strongest for identical fermions when kR_e is much smaller than 1.

Now, we can consider the energy dependence of the phase shift $\delta_0(k)$ of the s -wave scattering near the threshold by expanding it in powers of k . In most cases the system has a time-reversal symmetry, so the scattering wave function is invariant under $k \rightarrow -k$ as

$$A(k)e^{ikr} - B(k)e^{-ikr} = A(-k)e^{-ikr} - B(-k)e^{ikr}. \quad (2.2)$$

Then we have $\exp[2i\delta(k)] \equiv A(k)/B(k) = B(-k)/A(-k) \equiv \exp[-2i\delta(-k)]$. Consequently, the low-energy expansion of $k \cot[\delta(k)]$ contains only even orders of k :

$$k \cot(\delta_0) = -\frac{1}{a} + \frac{1}{2}r_0k^2 - O(k^4), \quad (2.3)$$

where a is the scattering length and r_0 is the effective range, and both parameters are given by the details of the interaction potential. Usually, a and r_0 should have the same magnitude

as the interaction range R_e . However, when there is a bound (or quasi-bound) state near the threshold, a can be much larger than R_e . Under the condition $r_0 \sim R_e \ll |a| \ll 1/k$, we ignore all the terms involving k on the right side of Eq. (2.3) and reach the *universal* regime, where the effects of scattering are fixed by a . Typically, for alkali atoms in a range of a values between 10^2 and $10^4 a_0$ at tens of nano-Kelvin, the second term on the right side of Eq. (2.3) is on the order of 10^{-2} of the leading term.

The concept of *universality* comes from the approximation of replacing the real potential with a two-body boundary condition at zero distance, or a zero-range pseudo potential, that leaves a and the result low energy observables unchanged. Since this approximation is valid for various systems, e.g. nuclei and ultracold atoms, as long as particles are colliding in the threshold regime with short-ranged symmetrical potentials at zero angular momentum, the corresponding formalism and results are *universal* for all these systems.

When two bosons are colliding in the universal regime, the elastic cross section is given by $\sigma_0 = (8\pi/k^2) \sin^2 \delta_l$. By taking only the leading term in Eq. (2.3), we have

$$\sigma_0(k) = 8\pi a^2 / (1 + a^2 k^2). \quad (2.4)$$

At the low temperature limit $ka \rightarrow 0$, the cross section is $8\pi a^2$. When $|a|$ increases, the cross section becomes larger and approaches a maximum value of $8\pi/k^2$ when $k|a| \gg 1$. This limitation of cross section is usually called the *unitary limit* [Lan65], which can also be extended to inelastic collisions.

The condition $r_0 \sim R_{\text{vdW}} \ll |a| \ll 1/k$ is valid in most of the experimental situations presented in this work. At large values of scattering length, the unitary limit is the most significant effect from temperature. We will see later in Chap. 7 and 9 that a model considering zero-range two-body interactions and finite temperature effects in the context of the unitary limit can already reproduce nicely most of the measured results of the three-body inelastic collisions.

2.1.3 Magnetic field induced Feshbach resonances

One significant advantage of ultracold atomic gases in comparison with other particle systems is the tunability of the two-body interactions between atoms via Feshbach resonances [Fes58, Fes62, Fan61, Tim99, Chi10]. When two atoms are colliding at low temperature, the nuclei are moving in a certain adiabatic Born-Oppenheimer(BO) molecular potential formed by electrons in a corresponding configuration (channel) of spin and orbital angular momentum. The couplings between different BO potentials are provided by relatively weak and short-ranged effects like the hyperfine interactions caused by the magnetic moments of nuclei and electrons. See Chap. 3 for the details of cesium Feshbach resonances.

Typically in our experiment, we prepare the atoms in the lowest channel. In the asymptotic region ($r \rightarrow \infty$), the kinetic energy of the atoms is much smaller than the energy gaps to the upper channels given by the hyperfine splitting. Consequently, the atoms approach and exit always in the lowest channel (open channel) while all the upper channels (close channels) are

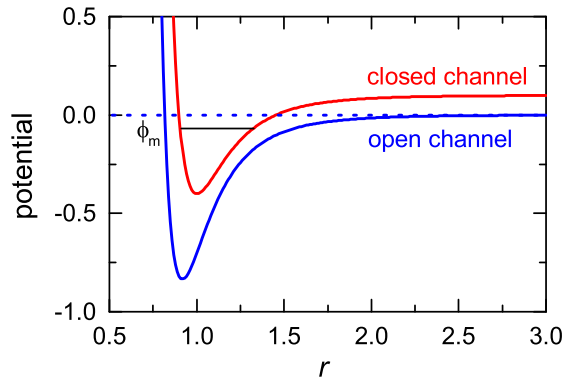


Figure 2.1: A simplified picture of the Feshbach resonance. The open (solid blue curve) and closed (solid red curve) channel have different magnetic moments, so the energy offset between them can be tuned by changing the strength of the magnetic field. When the dressed molecular state (ϕ_m , solid black line) approaches the threshold (dashed blue line) at a specific magnetic field B_0 , the incoming atoms from the threshold are coupled resonantly to the molecular state, resulting in very large scattering lengths. The potential and r are in arbitrary units.

forbidden by energy at $r \rightarrow \infty$. In the short-range region ($r \lesssim R_{\text{vdW}}$), the coupling between channels is strong and part of the wave function can propagate into the closed channels. For simplicity, we now consider only the lowest two channels (Fig. 2.1). If the two channels have different magnetic moments, we can change the relative energy between these channels by tuning the magnetic field B , and the scattering length a diverges when a molecule state reaches the threshold. In the vicinity of the resonance position B_0 , the value of a is given by the function

$$a = a_{bg} \left(1 - \frac{\Delta}{B - B_0} \right), \quad (2.5)$$

where a_{bg} is the background scattering length for the open channel without the influence of the close channel, $\Delta \equiv \gamma/a_{bg}\delta\mu$ is the width of the Feshbach resonance that is related to the strength of the coupling γ and the difference of magnetic moment $\delta\mu$ between the closed and the open channels. B_0 is the B field where the dressed molecule state, which is a superposition that mainly consists of the shallowest discrete states in the closed and open channel and the open channel continuum state, crosses the threshold. Near the Feshbach resonance, this shallow dimer state is bounded with a binding energy of $E = \hbar^2/2\mu a^2$, where μ is the reduced mass of the atom pair, when $a > 0$.

The B dependence of a in Eq. (2.5) can be understood as a general result for coupled systems [Fes58, Fes62, Tim99]. For simplicity, we consider the Schrödinger equation for a continuum (channel 1) coupled to a discrete state in channel 2 as

$$\begin{pmatrix} H_{11} & H_{12} \\ H_{21} & H_{22} \end{pmatrix} \begin{pmatrix} \Psi_1 \\ \Psi_2 \end{pmatrix} = E \begin{pmatrix} \Psi_1 \\ \Psi_2 \end{pmatrix}, \quad (2.6)$$

where Ψ_1 and Ψ_2 are the projected components of the full wave function in the corresponding channel, and $(H_{22} - E)\phi = 0$ has only one discrete solution ϕ_m with E_m . Considering no initial wave in the second channel, we express Ψ_2 using the second row of Eq. (2.6) as $|\Psi_2\rangle = (E - H_{22})^{-1}H_{21}|\Psi_1\rangle$. Taking this result into the first row of Eq. (2.6), we arrive at

the effective single channel Schrödinger equation for channel 1

$$\left(H_{11} + H_{12} \frac{1}{E - H_{22}} H_{21} - E \right) |\Psi_1\rangle = 0. \quad (2.7)$$

We treat H_{11} as the bare Hamiltonian and denote its outgoing solution of $(E - H_{11})\Psi_0^+ = 0$ with initial state $|k_0\rangle$ as Ψ_0^+ . Then the outgoing solution of the Schrödinger equation is

$$|\Psi\rangle = |\Psi_0^+\rangle + \frac{1}{E + i0^+ - H_{11}} \frac{|H_{12}\phi_m\rangle\langle\phi_m H_{21}|\Psi_0^+\rangle}{E - E_m - \langle\phi_m H_{21}|\frac{1}{E + i0^+ - H_{11}}|H_{12}\phi_m\rangle}, \quad (2.8)$$

where we simplify $H_{12}(E - H_{22})^{-1}H_{21}$ to $(E - E_m)^{-1}|H_{12}\phi_m\rangle\langle\phi_m H_{21}|$ since there is only one discrete state. The full transition matrix T then gives the amplitude for a transition from the initial state $|k_0\rangle$ to $|k\rangle$

$$\langle k|T|k_0\rangle = \langle k|T_1|k_0\rangle + \frac{\langle k|H_{12}\phi_m\rangle\langle\phi_m H_{21}|\Psi_0^+\rangle}{E - E_m - \langle\phi_m H_{21}|\frac{1}{E + i0^+ - H_{11}}|H_{12}\phi_m\rangle}, \quad (2.9)$$

where T_1 is the T -matrix considering only channel 1. At the zero energy limit we have $a = \langle k|T|k_0\rangle$, and Eq. (2.9) is identical to Eq. (2.5).

Another important quantity of a Feshbach resonance is its strength s_{res} , which is defined as

$$s_{\text{res}} = \frac{a_{bg} \delta\mu\Delta}{\bar{a} \bar{E}}, \quad (2.10)$$

where the mean scattering length $\bar{a} \approx 0.956R_{\text{vdW}}$ [Gr93] is an equivalent length scale of R_{vdW} and the corresponding energy scale is $\bar{E} = \hbar^2/2\mu\bar{a}^2$ [Chi10]. When $s_{\text{res}} \gg 1$, a_{bg} is large and the coupling is strong. So the shallow bound state in the open channel is ‘shifted up’ a little and merges with the continuum before obtaining a significant component from the close-channel states, and we call this resonance *open channel dominated*. Such a system can be further simplified as a single channel problem. Moreover, the width Δ is large while the effective range r_0 remains small, so the system is in the universal regime over a large region of B field and we call this kind of resonances *broad*. On the other limit, when $s_{\text{res}} \ll 1$, the dressed bound state has a dominating fraction from the closed channel and couples weakly to the continuum. For such a *closed channel dominated* resonance, the width Δ is small while the effective range r_0 can be much larger than R_{vdW} . Therefore this resonance is *narrow* and may no longer stay in the universal regime. As a result, the very broad Feshbach resonances with wide and precise tunability of a and relatively small r_0 are generally preferred in our experiments exploring universal few-body physics. Moderately broad and narrow Feshbach resonances, however, are useful for a fast and efficient association of Feshbach molecules.

2.2 Theory of Efimov states

2.2.1 The discovery of Efimov states

Famous examples of few-body systems include the prominent sun-moon-earth system, small molecules, light nuclei, heavy quarks, quantum dots and colliding atoms. Similar to its

classical counterpart that has been proven to be difficult, quantum few-body systems are intrinsically complicated [Fad60, Zei78, Mar91]. In the work on the structure of H^3 nucleus in 1937 [Tho35], Thomas found that the three-body ground state's binding energy diverges if the range of the two-body interaction approaches zero while keeping the scattering length finite, and this gives a lower limit on the range of the nuclear force. However, the attempts to solve the three-body problem by a simple analogy to the two-body case, e.g. using Lippmann-Schwinger equation, encountered persistent difficulties. Around 1960s, Skornyakov and Ter-Martirosyan (STM) gave the equation for three particles by replacing the two-body interaction with boundary conditions at zero distances [Sko57]. Later, Danilov [Dan61] pointed out the Hamiltonian in the STM model is not self-adjoint and the results have a non-uniqueness problem. Minlos and Faddeev [Min61] then used a contact boundary condition for the configuration that three particles are contacting to fix the solution. Even though the zero-range model leads to a geometric spectrum that is unbounded from below and is related to the phenomena found by Thomas, and the model of a particle falling into the center of a $1/r^2$ potential (§35 in Ref. [Lan65]). The breakthrough of Efimov [Efi70] came in the 1970's when he gave the physical meaning of these states and studied their structure in the configuration space and the exotic discrete symmetry in the system. Hence the states are named after him.

In the following part of this section, we will introduce the widely used hyperspherical coordinates and its application in the three identical boson system, and Efimov states emerge naturally when the two-body interaction is simplified as s -wave scattering in the resonance limit.

2.2.2 Hyperspherical coordinates

The general idea of Hyperspherical coordinates is to transform the independent coordinates of several particles into a coordinate system considering the few-body system as a whole. In the low energy limit, a system of identical particles can even be reduced to a one dimensional problem like a single particle moving in an effective potential. Here we briefly illustrate how to simplify the three-body problem in the limit of zero-range interaction. See Ref. [Fad60, Nie01, Sun02, Bra06] for details.

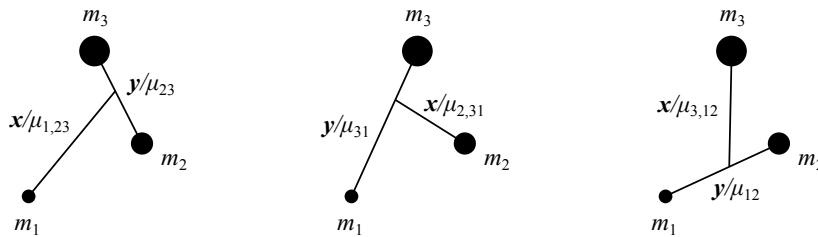


Figure 2.2: Three sets of Jacobi coordinates, corresponding to three sets of hyperspherical coordinates.

For three particles (see Fig. 2.2) in the center of mass (COM) frame, there are 6 degrees of freedom remaining. The overall size of the three-body system is characterized by the hyperradius R , which is the root-mean-square of the distance between atoms and defined

as

$$R^2 = \frac{m_1 m_2 \mathbf{r}_{12}^2 + m_2 m_3 \mathbf{r}_{23}^2 + m_3 m_1 \mathbf{r}_{31}^2}{m(m_1 + m_2 + m_3)} = \frac{1}{2} (\mathbf{x}_{k,ij}^2 + \mathbf{y}_{ij}^2). \quad (2.11)$$

Here we used the three sets of Jacobi coordinates defined as:

$$\mathbf{x}_i = \mu_{i,jk} \left(\mathbf{r}_i - \frac{m_j \mathbf{r}_j + m_k \mathbf{r}_k}{m_j + m_k} \right), \quad \mu_{i,jk} = \sqrt{\frac{2m_i(m_j + m_k)}{m(m_i + m_j + m_k)}}, \quad (2.12)$$

$$\mathbf{y}_i = \mu_{ijk} (\mathbf{r}_j - \mathbf{r}_k), \quad \mu_{ijk} = \sqrt{\frac{2m_j m_k}{m(m_j + m_k)}}, \quad (2.13)$$

where (i, j, k) is a permutation of $(1, 2, 3)$ and m is a normalization mass. To describe the relative position of the particles in the system, we define the hyperangles α_i as

$$\alpha_i = \arctan\left(\frac{y_i}{x_i}\right), \quad (2.14)$$

so that we have the simple expressions $x_i = \sqrt{2}R \cos \alpha_i$ and $y_i = \sqrt{2}R \sin \alpha_i$. The dimensionless parameters $(\alpha_i, \hat{\mathbf{x}}_i, \hat{\mathbf{y}}_i)$ with 5 degrees of freedom are called hyperangular variables and denoted collectively by Ω . For the 4 degrees of freedom in $(\hat{\mathbf{x}}_i, \hat{\mathbf{y}}_i)$, we can also choose three of them as the Euler angles γ for the whole system while the remaining one denoted by ϕ_i is an equivalence of another hyperangle (e.g. α_j) related to the angle between $\hat{\mathbf{x}}_i$ and $\hat{\mathbf{y}}_i$. Then Ω can be denoted also as $(\alpha_i, \phi_i, \gamma)$.

In the case of three identical particles, the static three-body wave function in the Cartesian coordinates is denoted as $\Psi(\mathbf{r}_1, \mathbf{r}_2, \mathbf{r}_3)$ and the Schrödinger equation is

$$\left(-\frac{\hbar^2}{2m} \sum_{i=1}^3 \nabla_i^2 + V(\mathbf{r}_1, \mathbf{r}_2, \mathbf{r}_3) \right) \Psi = E\Psi. \quad (2.15)$$

Assuming that V is independent of the COM movement, we rewrite Eq. (2.15) in the COM system with (R, Ω) as

$$\left(T_R + T_{\alpha_i} + \frac{\Lambda_{i,jk}^2}{2mR^2} + V(R, \Omega) \right) \Psi = E\Psi, \quad (2.16)$$

where

$$T_R = \frac{\hbar^2}{2m} R^{-5/2} \left[-\frac{\partial^2}{\partial R^2} + \frac{15}{4R^2} \right] R^{5/2} \quad (2.17)$$

is the hyperradial kinetic energy operator,

$$T_{\alpha_i} = \frac{\hbar^2}{2mR^2} \frac{1}{\sin(2\alpha_i)} \left[-\frac{\partial^2}{\partial \alpha_i^2} - 4 \right] \sin(2\alpha_i) \quad (2.18)$$

is the kinetic energy operator related to α_i , and $\Lambda_{i,jk}^2$ is a generalized angular momentum operator containing the normal angular momentum operators for $\hat{\mathbf{x}}_i$ and $\hat{\mathbf{y}}_i$ [Bra06]. If we switch to the variables $(\alpha_i, \phi_i, \gamma)$ for Ω , the Λ^2 term contains one part associated with the conventional angular momentum for γ and another part T_{ϕ_i} connected to ϕ_i [Sun02]. The potential term $V(R, \Omega)$ is usually independent of the orientation of the system and depends only on (R, α_i, ϕ_i) .

To solve Eq. (2.16), we expand $\Psi(R, \Omega)$ at each R with a complete set of hyperangular functions $\{\Phi_n(R, \Omega)\}$:

$$\Psi(R, \Omega) = R^{-5/2} \sum_n f_n(R) \Phi_n(R, \Omega). \quad (2.19)$$

Taking this expansion into the Schrödinger equation (2.16), we separate the variables to have two sets of coupled equations. For a chosen i , the hyperangular part is

$$\left[T_{\alpha_i} + \frac{\Lambda_{i,jk}^2}{2mR^2} + V(R, \Omega) \right] \Phi_n(R, \Omega) = V_n(R) \Phi_n(R, \Omega), \quad (2.20)$$

where R is treated as a parameter and $V_n(R)$ are the corresponding eigenvalues at a certain R . With proper orthogonality and normalization such that $\langle \Phi_n(R, \Omega) | \Phi_m(R, \Omega) \rangle = \delta_{nm}$,¹ we can project Eq. (2.16) onto Φ_n and get the hyperradial part for f_n as

$$\left[-\frac{\hbar^2}{2m} \frac{\partial^2}{\partial R^2} + \left(\frac{\hbar^2}{2m} \frac{15}{4R^2} + V_n(R) \right) \right] f_n(R) + \sum_m W_{nm} f_m(R) = E f_n(R), \quad (2.21)$$

where W_{nm} contains terms proportional to $\langle \Phi_n | \partial / \partial R | \Phi_m \rangle \partial / \partial R$ and $\langle \Phi_n | \partial^2 / \partial R^2 | \Phi_m \rangle$. With Eq. (2.21), we can define the hyperradial potential $U_n(R) \equiv (\hbar^2/2m)15/4R^2 + V_n(R) + W_{nn}$ for channel n and the coupling between channels $U_{nm} \equiv W_{nm}$ for $n \neq m$.

If we plug in the interaction $V(R, \Omega)$ between particles, Eq. (2.20) and (2.21) are enough to solve the three-body problem numerically. At low collisional energies, terms with non-zero angular momentum are suppressed similarly to the threshold law in the two-body case, and any dependence on the Euler angles γ vanishes. Eq. (2.20) and (2.21) are then simplified to

$$[T_{\alpha_i} + T_{\phi_i} + V(R, \alpha_i, \phi_i)] \Phi_n(R, \alpha_i, \phi_i) = V_n(R) \Phi_n(R, \alpha_i, \phi_i) \quad (2.22)$$

$$\left[-\frac{\hbar^2}{2m} \frac{\partial^2}{\partial R^2} + U_n(R) \right] f_n(R) + \sum_{m \neq n} U_{nm} f_m(R) = E f_n(R). \quad (2.23)$$

Under certain conditions, e.g. when $R_{\text{vdW}} \ll R \ll |a|$ for ultracold neutral atoms [Bra06], it is possible to ignore the off diagonal terms U_{nm} or even the diagonal terms W_{nn} in U_n , and the three-body system is reduced to an equivalent particle moving in one of the effective one-dimensional potentials. This approximation is called the adiabatic hyperspherical approximation [Mac68]. The separation of hyperangular and hyperradial parts of the wave function is similar to the Born-Oppenheimer approximation in molecular physics, while the validity of the approximation is more restricted in our case.

In Ref. [Wan12], the above formalism is applied to different two-body model potentials with a van der Waals tail, e.g. the Lennard-Jones potential, at the resonance limit $a \rightarrow \infty$ to calculate the hyperradial potentials U_n and associated three-body bound states f_n for ultracold alkali atoms. The result shows significant contributions from the W_{nn} terms only when $R \sim R_{\text{vdW}}$ and a robust repulsive potential appears near $R \approx 1.6R_{\text{vdW}}$ and it fixes the binding energies of the three-body bound states.² We observed this effect experimentally before Ref. [Wan12], see Chap. 4 for the experiment and subsection 2.4.4 in this chapter for detailed discussions.

¹ Here the bracket notation means the integration is carried out over only Ω .

² They have a different definition of R , which is $\sqrt{2}$ times our R .

2.2.3 The Faddeev equations for bound states

Although the three-body Schrödinger equation can be solved numerically, alternative approximative methods like the Skornyakov-Ter-Martirosyan (STM) equation [Sko57], the Faddeev set of Equations [Fad60, Zei78, Fed93, Nie01] and the effective field theory [Bed99, Bed00, Bra06] present simpler and physically more transparent solutions. Here we introduce the homogeneous Faddeev equations in a heuristic manner and follow mainly the procedure of Ref. [Fed93] and [Bra06] to obtain the energies and wave functions of Efimov states.

The first approximation we made is decomposing the interaction into pair-wise terms, so the Schrödinger equation becomes

$$(H_0 + v_{23} + v_{31} + v_{12} - E)\Psi = 0, \quad (2.24)$$

where H_0 is the operator for kinetic energy and v_{ij} refers to the interaction between particle i and j . v_{ij} depends only on the displacement $\mathbf{r}_{ij} = \mathbf{r}_i - \mathbf{r}_j$ between the particles and vanishes as $r_{ij} \rightarrow \infty$. To obtain the bound states and take advantage of the simple form of H_0 , we modify Eq. (2.24) in order to get a homogeneous Lippmann-Schwinger equation as³

$$\Psi = -\frac{1}{H_0 - z}(v_{23} + v_{31} + v_{12})\Psi, \quad (2.25)$$

where the real valued energy E is replaced by a complex variable z . If we treat $-1/(H_0 - z)(v_{23} + v_{31} + v_{12})$ as a transform from the Hilbert space spanned by the possible Ψ to itself, it is convenient to decompose it into smaller parts containing only one term of interaction v_{jk} . The wave function is then split correspondingly as $\Psi = \Psi_1 + \Psi_2 + \Psi_3$, where the Faddeev components are $\Psi_i = -[1/(H_0 - z)]v_{jk}\Psi$ and (i, j, k) are permutations of $(1, 2, 3)$. The set of equations for the Faddeev components can be presented in matrix form as

$$\begin{pmatrix} \Psi_1 \\ \Psi_2 \\ \Psi_3 \end{pmatrix} = -\frac{1}{H_0 - z} \begin{pmatrix} v_{23} & v_{23} & v_{23} \\ v_{31} & v_{31} & v_{31} \\ v_{12} & v_{12} & v_{12} \end{pmatrix} \begin{pmatrix} \Psi_1 \\ \Psi_2 \\ \Psi_3 \end{pmatrix}, \quad (2.26)$$

and we can simplify its notation as $\bar{\Psi} = \hat{A}_v \bar{\Psi}$, where $\bar{\Psi}$ is the column vector formed by the Faddeev components Ψ_i and \hat{A}_v is the transformation applied on $\bar{\Psi}$ on the right side of Eq. (2.26).

From the perspective of perturbation expansion or field theory, Eq. (2.26) means the particles are scattered multiple times by the interactions and Ψ_i is the component of wave function where the last scattering process is caused by v_{jk} . Another way of understanding this formalism is by studying the asymptotic behavior of the components when the hyperradius R is at infinity. Limited by the conservation of energy, there are four non-vanishing situations in the asymptotic regime: either one dimer ψ_{jk} is infinitely far away from the third particle i ($i=1, 2$, or 3) and the total wave function is denoted as $\Psi_{i,jk}$. Or, only possible when $E > 0$, all three particles are free and far separated. When $E < 0$, because v_{jk} is non-zero only for the component of Ψ that becomes $\Psi_{i,jk}$ in the asymptotic regime, we recognize Ψ_i as

³ The original Faddeev equations are derived for scattering and given with the inhomogeneous term, see [Fad60] and [Mar91] for details and proofs in mathematics.

the component of Ψ that has the asymptotic form of $\Psi_{i,jk}$. When $E > 0$, each Ψ_i has an additional contribution from the free-atom state.

As Ψ_i describes the system where particle j and k are highly correlated when $E < 0$, we prefer to use the i th set of hyperspherical coordinates $(R, \alpha_i, \hat{\mathbf{x}}_i, \hat{\mathbf{y}}_i)$ for it. Since we are interested in obtaining the bound states rather than solving the scattering problem, the Faddeev equations are commonly presented in a form slightly different from Eq. (2.26):

$$\begin{aligned} (H_{01} - E)\Psi_1 + v_{23}(\Psi_1 + \Psi_2 + \Psi_3) &= 0 \\ (H_{02} - E)\Psi_2 + v_{31}(\Psi_1 + \Psi_2 + \Psi_3) &= 0 \\ (H_{03} - E)\Psi_3 + v_{12}(\Psi_1 + \Psi_2 + \Psi_3) &= 0, \end{aligned} \quad (2.27)$$

where $H_{0i} = T_R + T_{\alpha_i} + \frac{\Lambda_{i,jk}^2}{2mR^2}$ is the kinetic energy operator in the COM frame and expressed with the i th set of hyperspherical coordinates. In comparison with the Schrödinger equation Eq. (2.16), the Faddeev equations have several advantages. In the first place, for each Faddeev component of the wave function, one of the corresponding coordinates directly describes the relative motion between the highly correlated pair of particles. Consequently, we can easily specify the interaction between the two strongly correlated particles by a boundary condition (or a zero-range potential) instead of the actual potential. In the second place, this choice of coordinates also requires much less angular momenta to describe the system [Nie01]. Finally, different angular momentum states in the Schrödinger equation are coupled by terms of first order in the potential, but the couplings between different angular momenta in each Faddeev component are of second order in the two-body short-range potentials [Nie01].

Now we proceed in a similar way as we did for the Schrödinger equation Eq. (2.16). At low energy, we can restrict our attention to the zero angular momentum case and $\Psi(R, \alpha_i, \hat{\mathbf{x}}_i, \hat{\mathbf{y}}_i)$ is simplified to $\Psi_i(R, \alpha_i)$ [Fed93, Nie01].⁴ The Faddeev equations in Eq. (2.27) then reduce to three similar equations different only by a permutation of the indices:

$$(T_R + T_{\alpha_i} - E)\Psi_i(R, \alpha_i) + v(\sqrt{2}R \sin \alpha_i) [\Psi_i(R, \alpha_i) + \Psi_j(R, \alpha_i) + \Psi_k(R, \alpha_i)] = 0 \quad (2.28)$$

Since we consider three identical bosons, $\Psi_i(R, \alpha_i)$ ($i=1,2$ and 3) have the same form $\Psi(R, \alpha_i)$. To solve Eq. (2.28) in the first coordinate system, $\Psi_j(R, \alpha_j)$ ($j=2$ and 3) are replaced by $\Psi(R, \alpha_j)$ with a transfer of the coordinates as⁵

$$\frac{2}{\sqrt{3}} \int_{|\pi/3-\alpha_1|}^{\pi/2-|\pi/6-\alpha_1|} \frac{\sin(2\alpha_j)}{\sin(2\alpha_1)} \Psi(R, \alpha_j) d\alpha_j. \quad (2.29)$$

For simplicity, we replace α_1 with α and the resulting equation for $\Psi(R, \alpha)$ is the low-energy Faddeev equation for identical particles:

$$(T_R + T_\alpha - E)\Psi(R, \alpha) + v(\sqrt{2}R \sin \alpha) \left[\Psi(R, \alpha) + \frac{4}{\sqrt{3}} \int_{|\pi/3-\alpha|}^{\pi/2-|\pi/6-\alpha|} \frac{\sin(2\alpha')}{\sin(2\alpha)} \Psi(R, \alpha') d\alpha' \right] = 0. \quad (2.30)$$

⁴ Different from the case of the Schrödinger equation where only body-frame angular momenta related to $\mathbf{x}_i \times \mathbf{y}_i$ is ignored, here we ignores also the angular momentum related to the angle between \mathbf{x}_i and \mathbf{y}_i since the Faddeev components considered already the basic correlations between particles.

⁵ Strictly speaking, Ψ_i is a subspace of the total Hilbert space, so the state is firstly transferred with the whole set of angular coordinates Ω , then projected onto the desired subspace Ψ_1 .

Similar to the procedures for adiabatic hyperspherical approximation, we expand the wave function Ψ in a complete set of hyperangular functions $\phi_n(R, \alpha)$:

$$\Psi(R, \alpha) = \frac{1}{R^{5/2} \sin(2\alpha)} \sum_n f_n(R) \phi_n(R, \alpha), \quad (2.31)$$

where $\phi_n(R, \alpha)$ is the eigenfunctions of the α -dependent part of Eq. (2.30)

$$\left[-\frac{\partial^2}{\partial \alpha^2} - \lambda_n(R) \right] \phi_n(R, \alpha) = -\frac{2mR^2}{\hbar^2} v(\sqrt{2}R \sin \alpha) \times \left[\phi_n(R, \alpha) + \frac{4}{\sqrt{3}} \int_{|\pi/3-\alpha|}^{\pi/2-|\pi/6-\alpha|} \phi_n(R, \alpha') d\alpha' \right]. \quad (2.32)$$

In Eq. (2.32), R is a parameter and the prefactor $1/\sin(2\alpha)$ in Eq. (2.31) imposes boundary conditions that $\phi_n(R, \alpha) = 0$ at the end points $\alpha = 0$ and $\pi/2$. Since the operator on the right side of Eq. (2.32) is not Hermitian, the set of ϕ_n is not necessarily an orthogonal basis. Take Eq. (2.31) into Eq. (2.30), the resulting R -dependent equation is

$$\left[\frac{\hbar^2}{2m} \left(-\frac{\partial^2}{\partial R^2} + \frac{\lambda(R) - 1/4}{R^2} \right) - E \right] f_n(R) + \frac{\hbar^2}{2m} \sum_m \left[2P_{nm}(R) \frac{\partial}{\partial R} + Q_{nm} \right] f_m(R) = 0, \quad (2.33)$$

where we define

$$G_{nm} = \int_0^{\pi/2} \phi_n^*(R, \alpha) \phi_m(R, \alpha) d\alpha = \langle \phi_n | \phi_m \rangle \quad (2.34)$$

$$P_{nm} = -\sum_k G_{nk}^{-1} \langle \phi_k | \partial / \partial R | \phi_m \rangle \quad (2.35)$$

$$Q_{nm} = -\sum_k G_{nk}^{-1} \langle \phi_k | \partial^2 / \partial R^2 | \phi_m \rangle, \quad (2.36)$$

We should point out that $G_{nm}(R)$ is a matrix while $G_{nm}^{-1}(R)$ is its inverse, and $G_{nm}(R)$ should be fixed by the normalization condition of the components of the angular part of the total wave function (2.31). In the zero angular momentum case

$$\begin{aligned} \delta_{nm} &= \int d\Omega \left(\sum_{i=1,2,3} \frac{\phi_n(R, \alpha_i)}{\sin(2\alpha_i)} \right)^* \left(\sum_{i=1,2,3} \frac{\phi_m(R, \alpha_i)}{\sin(2\alpha_i)} \right) \\ &= 6(4\pi)^2 \int d\alpha \phi_n^*(R, \alpha) \left(\phi_m(R, \alpha) + \int_{|\pi/3-\alpha|}^{\pi/2-|\pi/6-\alpha|} \phi_m(R, \alpha') d\alpha' \right) \\ &= 6(4\pi)^2 \langle \phi_n | 1 + \hat{S} | \phi_m \rangle \\ &= 6(4\pi)^2 \left[G_{nm} + \langle \phi_n | \hat{S} | \phi_m \rangle \right], \end{aligned} \quad (2.37)$$

where the operator \hat{S} is $\int_{|\pi/3-\alpha|}^{\pi/2-|\pi/6-\alpha|} d\alpha'$ and the bracket symbol here means integral over α . We recognize $(1 + \hat{S})/\langle \phi_n | 1 + \hat{S} | \phi_n \rangle$ as the unit operator in the basis of ϕ_n . By inserting the unit operator into Eq. (2.35) and (2.36), we eliminate the summation over different channels

and arrive at

$$P_{nm}(R) = -\frac{\langle \phi_n | (1 + \hat{S}) \partial / \partial R | \phi_m \rangle}{\langle \phi_n | 1 + \hat{S} | \phi_n \rangle} \quad (2.38)$$

$$Q_{nm}(R) = -\frac{\langle \phi_n | (1 + \hat{S}) \partial^2 / \partial R^2 | \phi_m \rangle}{\langle \phi_n | 1 + \hat{S} | \phi_n \rangle}. \quad (2.39)$$

Since $1 + \hat{S}$ is symmetric and $\phi_n(R, \alpha)$ vanishes at the end points 0 and $\pi/2$, we find $P_{nn} = 0$ and $Q_{nm} \geq 0$ after integrating by parts.

The set of radial equations (2.33) look similar to Eq. (2.23) obtained from the Schrödinger equation. The difference is that the angular equations (2.32) generating the adiabatic potential containing $\lambda_n(R)$ have only one variable. The simplification originates from the proper choice of coordinates and ignoring of angular momenta in each subsystem.

2.2.4 Adiabatic solutions with two-body boundary conditions

We apply the hyperspherical adiabatic approximation [Mac68] to ignore terms containing P_{nm} and Q_{nm} in Eq. (2.33) and arrive at

$$\left[\frac{\hbar^2}{2m} \left(-\frac{\partial^2}{\partial R^2} + \frac{\lambda_n(R) - 1/4}{R^2} \right) - E \right] f_n(R) = 0. \quad (2.40)$$

What we need now is to solve the angular equation (2.32) and obtain the parameter $\lambda_n(R)$ for the radial equation (2.40).

If the two-body interaction $v(r)$ decays faster than $1/r^2$, the problem is greatly simplified and we can replace the actual two-body potential with a short-distance two-body boundary condition to fix the solution. To show this, let's consider an interaction $v(r) = R_e^{n-2}/r^n$, where n is larger than 2 and R_e is the typical interaction range and the coefficient R_e^{n-2} maintains the dimension of energy as $length^{-2}$ when $\hbar = m = 1$. Since the universal physics happens in the low energy regime, we are interested in the situation when $R \gg R_e$ and can find out two important regions for α .

In region I, $\alpha \gg (R_e/R)^{(n-2)/n}$ and consequently $R^2 v(R\alpha) \ll 1$. Since λ is on the order of 1, we can ignore the energy term of Eq. (2.32) and reach

$$\left[-\frac{\partial^2}{\partial \alpha^2} - \lambda_n(R) \right] \phi_n^I(R, \alpha) = 0. \quad (2.41)$$

The corresponding solution ϕ_n^I with the boundary condition $\phi^I(\pi/2) = 0$ is

$$\phi^I(\alpha) = \sin \left[\sqrt{\lambda_n} (\pi/2 - \alpha) \right]. \quad (2.42)$$

In region II, we have $R_e/R \ll \alpha \ll (R_e/R)^{(n-2)/n}$. On the contrary to the situation in region I, here we can ignore the λ term and get

$$\left[-\frac{\partial^2}{\partial \alpha^2} + \frac{2mR^2}{\hbar^2} v(\sqrt{2}R\alpha) \right] \phi_n^{II}(R, \alpha) = -\frac{2mR^2}{\hbar^2} v(\sqrt{2}R\alpha) \frac{8\alpha}{\sqrt{3}} \phi^I(R, \pi/3). \quad (2.43)$$

If the right side of Eq. (2.43) is zero, the equation reduces to the two-body Schrödinger equation at zero energy. Then the solution as a sum of the homogeneous two-body solution $\phi^{(2B)}(\sqrt{2}R\alpha)$ and a specific solution is

$$\begin{aligned}\phi_n^{II}(R, \alpha) &= A(R)\phi^{(2B)}(\sqrt{2}R\alpha) - \frac{8\alpha}{\sqrt{3}}\phi^I(R, \pi/3) \\ &= A(R)\phi^{(2B)}(\sqrt{2}R\alpha) - \frac{8\alpha}{\sqrt{3}}\sin\left[\sqrt{\lambda}(\pi/6)\right].\end{aligned}\quad (2.44)$$

where $A(R)$ will be determined by matching ϕ_n^I and ϕ_n^{II} at $\alpha = 0$.

Since the potential between region I and II is smooth and the range of region II is very small, the low-energy wave function hardly changes when it goes from region II to the lower limit of region I. As a result, the zero-distance boundary conditions for ϕ_n^{II} and ϕ_n^I are practically the same. With the universal two-body boundary condition $\phi_n^{(2B)}(\sqrt{2}R\alpha) = \sqrt{2}R\alpha - a$, we smoothly extrapolate Eq. (2.42) and Eq. (2.44) to $\alpha = 0$ and match their values and derivatives there. The result gives $A(R) = -\sin\left[\sqrt{\lambda_n(R)}(\pi/2)\right]/a$, where $\lambda_n(R)$ are solutions of the equation

$$\sqrt{\lambda_n}\cos\left[\sqrt{\lambda_n}\pi/2\right] - \frac{8}{\sqrt{3}}\sin\left[\sqrt{\lambda_n}\pi/6\right] = \sqrt{2}\sin\left[\sqrt{\lambda_n}\pi/2\right]\frac{R}{a}.\quad (2.45)$$

Because the corresponding solution $\phi_n(R, \alpha) = \phi_n^I(R, \alpha)$ is only valid for finite values of α ($R\alpha \gg R_e$), the boundary condition $\phi_n(R, \alpha = 0) = 0$ is not reflected in a solution with the form of Eq. (2.42).

One trivial solution of Eq. (2.45) is $\lambda(R) = 16$, which gives $\phi(R, \alpha) = \sin(4\alpha)$. But the corresponding Faddeev component becomes $\Psi(R, \alpha) = \frac{2\cos(2\alpha)}{R^{5/2}}f$, where f is a constant. Then the wave function containing three Faddeev components vanishes because

$$\cos(2\alpha) + \frac{4}{\sqrt{3}}\int_{|\pi/3-\alpha|}^{\pi/2-|\pi/6-\alpha|}\frac{\sin(2\alpha')}{\sin(2\alpha)}\phi_n(R, \alpha')d\alpha' = 0.\quad (2.46)$$

The physical solutions of Eq. (2.45) can be obtained numerically, and the results for the lowest two channels are plotted in Fig. 2.3. When $a < 0$ ($a > 0$), the lowest solution $\lambda_0^-(R)$ ($\lambda_0^+(R)$) has asymptotic values as

$$\lambda_0^-(R) \rightarrow -s_0^2 \quad \text{when } \frac{R}{a} \rightarrow 0^-, \quad (2.47)$$

$$\lambda_0^-(R) \rightarrow 4 \quad \text{when } \frac{R}{a} \rightarrow -\infty. \quad (2.48)$$

$$\lambda_0^+(R) \rightarrow -s_0^2 \quad \text{when } \frac{R}{a} \rightarrow 0^+, \quad (2.49)$$

$$\lambda_0^+(R) \rightarrow -\frac{2R^2}{a^2} \quad \text{when } \frac{R}{a} \rightarrow +\infty. \quad (2.50)$$

The constant $s_0 \approx 1.0062378$ gives the only negative solution $\lambda_0(0)$ of Eq. (2.45) at $R/|a| \rightarrow 0$. Since the three-body potential in Eq. (2.40) is proportional to $(\lambda - 1/4)/R^2$, only the lowest

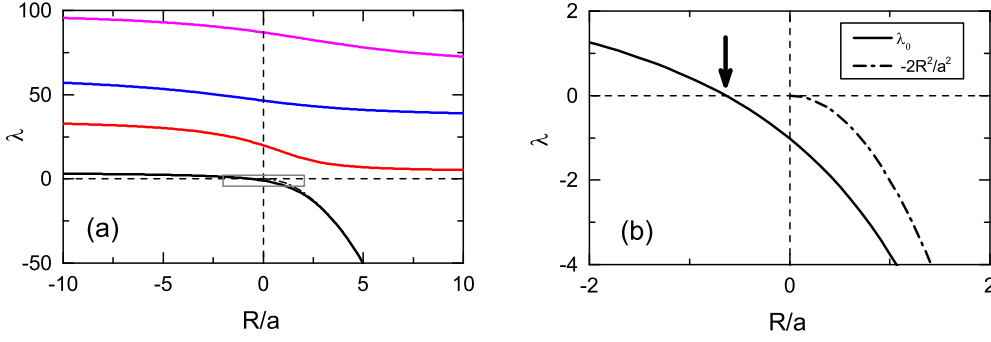


Figure 2.3: The four lowest $\lambda_n(R/a)$ (solid lines) obtained from Eq. (2.45). Plot (b) is a zoom-in of plot (a) near the zero region (gray box). The function $-2R^2/a^2$ is plotted as a dash-dot curve and it converges to λ_0 at large positive values of R/a , which indicates that the asymptotic state is an atom-dimer pair. In panel (b), λ_0 (solid black curve) becomes positive near -0.7 (black arrow). Considering that λ_0 approaches 4 when $R/a \rightarrow -\infty$, the ground channel three-body potential $(\lambda_0 - 1/4)/R^2$ has a ‘barrier’ near $R/a = -1$.

channel with $\lambda_0(R)$ is possible to induce an attractive three-body potential in a range of R/a . In the lowest channel, when $a < 0$, the attractive three-body potential vanishes near $R \approx |a|$. When $a > 0$, the asymptotic value of $\lambda_0(R)$ gives a constant shift $\frac{-\hbar^2}{ma^2}$ in energy, which is just the binding energy of the shallow dimer and the total wave function is the dimer plus a free single particle.

Take the obtained $\lambda_0(R)$ into the radial equation (2.40), we will find the bounded three-body states known as Efimov states. For simplicity, here we consider only the resonance limit when a diverges, so $\lambda_0(R/|a|)$ is treated as the constant $-s_0^2$ and analytic results are available. In this case, Eq. (2.40) is simply

$$\left[\frac{\hbar^2}{2m} \left(-\frac{\partial^2}{\partial R^2} - \frac{s_0^2 + 1/4}{R^2} \right) - E \right] f_n(R) = 0. \quad (2.51)$$

Its solution that decays to zero at $R \rightarrow \infty$ is

$$f_0(R) = \sqrt{R} K_{is_0}(\sqrt{2}\kappa R), \quad (2.52)$$

where K_{is_0} is the modified Bessel function of the second kind with a imaginary index is_0 and $E = -\hbar^2\kappa^2/m$ will be fixed by the boundary condition at $R = 0$. When $R \rightarrow 0$,

$$K_{is_0}(\sqrt{2}\kappa R) \approx - \left[\frac{\pi}{s_0 \sinh(\pi s_0)} \right]^{1/2} \sin [s_0 \ln(\kappa R) + \theta_{s_0}], \quad (2.53)$$

where

$$\theta_{s_0} = -\frac{1}{2}s_0 \ln 2 - \frac{1}{2} \arg \frac{\Gamma(1 + is_0)}{\Gamma(1 - is_0)}. \quad (2.54)$$

Similar to the case of threshold s -wave scattering with short range interactions, the boundary condition is insensitive to E when E is near zero. This approximation restricts the boundary position R_0 with the criteria $R_e \ll R_0 \ll \sqrt{\hbar^2/m|E|}$ in order to ignore both E in Eq. (2.51) and the short-range potential near R_0 . Consequently, this zero-energy approximation is only

possible when $|E| \ll \hbar^2/mR_e^2$ or $\kappa \ll R_e$. At R_0 , we fix Eq. (2.52) with the asymptotic form Eq. (2.53) to a dimensionless constant boundary condition

$$R_0 \frac{f'_0(R_0)}{f(R_0)} = \frac{1}{2} + s_0 \cot [s_0 \ln(\kappa R_0) + \theta_{s_0}]. \quad (2.55)$$

To have a more transparent physical meaning of the boundary condition, we can introduce an equivalent parameter Λ_0 by requiring

$$\frac{1}{2} + s_0 \cot [s_0 \ln(\Lambda_0 R_0)] = R_0 \frac{f'_0(R_0)}{f(R_0)}, \text{ and } 0 \leq \Lambda_0 < \pi. \quad (2.56)$$

Matching Eq. (2.55) and Eq. (2.56), we obtain the eigenvalues

$$\kappa^{(n)} = [\exp(-\pi/s_0)]^n \exp(-\theta_{s_0}/s_0) \Lambda_0, \quad (2.57)$$

where $n \in \mathbb{Z}$.

Since our solution is only valid when $\kappa \ll 1/R_e$, we can find the largest $\kappa^{(n_*)}$ and set n_* as the reference value of n . By taking the replacement $(n - n_*) \rightarrow n$, $n_* \rightarrow 0$ and $E_T^{(0)} = \hbar^2 \kappa^{(0)2}/m$, we obtain the famous spectrum of Efimov states at the limit $R_e \rightarrow 0$ and $a \rightarrow \infty$ as

$$E_T^{(n)} = [\exp(-\pi/s_0)]^{2n} E_T^{(0)}, \quad (2.58)$$

where $n \in \mathbb{N}$. The corresponding wave function for the first Faddeev part is

$$\Psi_1^{(n)}(R, \alpha) = \frac{K_{is_0}(\sqrt{2}\kappa^{(n)}R) \sinh [s_0(\pi/2 - \alpha)]}{R^2 \sin(2\alpha)}, \quad (2.59)$$

and the total wave function is a symmetric summation of the three Faddeev parts, and the typical size of the n th Efimov states is $1/\kappa^{(n)}$.

The Efimov scaling factor for κ is $\eta_E \equiv \exp(-\pi/s_0) = 22.6944\dots \approx 22.7$, and the binding energy values of Efimov states form a geometric sequence with common ratio Λ^2 at the limit $R_e \rightarrow 0$ and $a \rightarrow \infty$. When a is finite, Efimov states (Fig. 2.4) are obtained numerically from the adiabatic three-body potential or via other methods like finding singular poles in the STM equation or the effective field theory formalism. It is convenient to introduce the wave number variable

$$K = \text{sign}(E) \sqrt{m|E|/\hbar^2} \quad (2.60)$$

and plot $(1/a, K)$ instead of $(1/a, E)$ to have the same physical unit and scaling factor for both axes. Qualitatively, when $|a|$ decreases to a value comparable to $1/\kappa^{(n)}$, the assumption $a \rightarrow \infty$ breaks down for the n th Efimov state, and this Efimov state will disappear into the continuum of three particles (at $a_-^{(n)} < 0$) or continuum with one shallow dimer and a third free particle (at $a_*^{(n)} > 0$). The relation between these parameters is [Bra06]

$$\begin{aligned} a_-^{(n)} &\approx -1.508/\kappa^{(n)} \\ a_*^{(n)} &\approx 0.0707645/\kappa^{(n)}. \end{aligned} \quad (2.61)$$

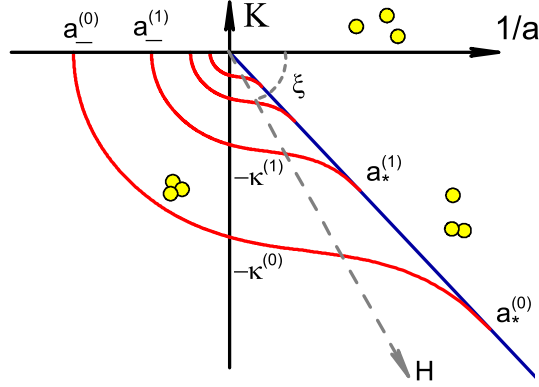


Figure 2.4: Schematic plot of the spectra of Efimov states (red curves), where K is defined in Eq. 2.60. The solid blue line is the universal atom-dimer threshold and the energy level at the x-axis is the three-atom threshold. $\hbar^2\kappa^2/m$ is the binding energy of the trimer state and a is the scattering length. When we turn to a polar coordinate system (dashed gray lines), the parameters are the angle ξ and the radius H .

We also have

$$\begin{aligned} a_-^{(n+1)} &= \eta_E a_-^{(n)} \\ a_*^{(n+1)} &= \eta_E a_*^{(n)}. \end{aligned} \quad (2.62)$$

Considering the requirement $R_e \ll R \ll |a|$, Efimov states exist only when a is resonantly large.

2.2.5 The discrete symmetry of Efimov states

At large but finite a , Eq. (2.45) shows the scale invariance of $\lambda_n(R)$. When we scale a by a factor of η , $\lambda_n(R)$ stays the same if R is also scaled by the same factor η . If we denote any relevant function $F(x)$ with a being a parameter as $F(a; x)$, the invariance of the angular functions under the scaling $a \rightarrow \eta a$ means

$$\lambda_n(\eta a; R) = \lambda_n(a; R/\eta) \quad (2.63)$$

$$\phi_n(\eta a; R) = \phi_n(a; R/\eta). \quad (2.64)$$

With the same scaling for the radial part, we have $f_n(\eta a; R) = f_n(a; R/\eta)$, which is also a solution of Equation (2.40) and the new energy $E(\eta a)$ equals $\eta^{-2}E(a)$.

Up to now, η can take any value and the scaling symmetry of the system is continuous. However, the boundary condition at short distance is fixed and breaks the continuous symmetry into a discrete symmetry and leads to Efimov states. To see this effect, we use a as the length scale for reference and introduce the dimensionless variable $\tilde{R} = R/a$ and parameter $\tilde{\kappa} = \kappa a$ to have a dimensionless version of Eq. (2.40) at finite a values as

$$\left[\frac{1}{2} \left(-\frac{\partial^2}{\partial \tilde{R}^2} + \frac{\lambda_n(\tilde{R}) - 1/4}{\tilde{R}^2} \right) + \tilde{\kappa}^2 \right] f_n(\tilde{R}) = 0, \quad (2.65)$$

where we set $\hbar = m = 1$. When $\tilde{R} \rightarrow 0$, the wave function is similar Eq. (2.52) but contains also the first kind Bessel function I_{is_0} and the limiting form becomes

$$f(\tilde{R}) = A \sin \left[s_0 \ln(\tilde{\kappa} \tilde{R}) + \theta_{s_0} + \Delta(\tilde{\kappa}) \right], \quad (2.66)$$

where A is the normalization constant and $\Delta(\tilde{\kappa})$ is fixed by the boundary condition at large \tilde{R} and depends on the only parameter $\tilde{\kappa}$. Since we should recover the result at infinite a , $\Delta(\tilde{\kappa})$ fulfills $\Delta(\infty) = 0$.

Then we apply the boundary condition Eq. (2.56) and get the equation for $\tilde{\kappa}$ as

$$\tilde{\kappa} = \tilde{\kappa}^{(0)} e^{\Delta(\tilde{\kappa})/s_0} \eta_E^{-n}, \quad (2.67)$$

where $n \in \mathbb{Z}$, $\tilde{\kappa}^{(0)} = a\kappa^{(0)} = a\Lambda_0 e^{-\theta_{s_0}/s_0}$ and $\eta_E = e^{\pi/s_0} \approx 22.7$. Since $\tilde{\kappa} = \kappa a$ is invariant under the scaling transform, we introduce $\xi = \arctan \tilde{\kappa}$ as a parameter and divide Eq. (2.67) by a to obtain a series of solutions:

$$\kappa_\xi^{(n)} = \kappa^{(0)} e^{\Delta(\xi)/s_0} \eta_E^{-n}. \quad (2.68)$$

For each $\kappa_\xi^{(n)}$, the corresponding $a_\xi^{(n)}$ equals $\tan \xi / \kappa^{(n)}$. When we describe the plot $1/a - \kappa$ (Fig. 2.4) with polar coordinates, ξ is the angular coordinate and a constant ξ defines a straight line (dashed straight grey line in Fig. 2.4) starting from the origin and at the angle ξ to the x -axis. The positions where the Efimov levels crosses this line are given by $\kappa_\xi^{(n)}$ and $a_\xi^{(n)}$ or equivalently by the radial position $H(\xi)^{(n)} = H(\xi)^{(0)} \eta_E^{-n}$, where $H(\xi)^{(0)} = \kappa_\xi^{(0)} / \cos \xi$. The *radial discrete scaling symmetry* of the series $H(\xi)^{(n)}$ shows that the binding energies of Efimov states are fixed by the universal function $\Delta(\xi)$, the Efimov scaling factor $\eta_E \approx 22.7$ and the short-range boundary condition Λ_0 . Since Λ_0 , $a_-^{(0)}$, $\kappa^{(0)}$ and some alternative parameters are equivalent in determining the Efimov spectra, it is free to pick one of them as the *three-body parameter* (3BP). In our work, we usually choose the observable $a_-^{(0)}$ as the three-body parameter.

2.3 The three-body recombination rate at zero temperature

2.3.1 Analytic calculations of the main observables

After decades of the prediction of Efimov states in the context of nuclear physics, the exotic phenomenon remained undetected in experiments until ultracold atomic gases provided an ideal platform to observe it. Up to now, the most important observables of the Efimov states in ultracold atom experiments have been the recombination rate coefficient of three free atoms and that of the atom-dimer collision. In the following subsections, we outline the calculation of the three-body recombination rates with the Skornyyakov-Ter-Martirosyan equation (STM) equation for free atoms at zero temperature where analytic solutions are available.

2.3.2 The Skornyakov-Ter-Martirosyan equation

In 1956, Skornyakov and Ter-Martirosyan obtained an equation for the scattering amplitude of three free particles via pair-wise two-body contact interactions [Sko57]. This equation also appears naturally from the inhomogeneous Faddeev equations when a zero-range force is assumed [Fad60], or can be derived in the effective field theory by expressing the effective vertex in an iterative form. Here we follow the procedures in Ref. [Pet13] to introduce the STM equation as a method to solve the free three-body Schrödinger equation with contact boundary conditions.

When the first set of Jacobi coordinates (subsection 2.2.2) is used for the three-body system, the original Schrödinger equation in the center-of-mass frame becomes a six-dimensional Schrödinger equation

$$\left[-\nabla_{\mathbf{x}_1}^2 - \nabla_{\mathbf{y}_1}^2 - E\right] \Psi(\mathbf{x}_1, \mathbf{y}_1) = V(\mathbf{x}_1, \mathbf{y}_1) \Psi(\mathbf{x}_1, \mathbf{y}_1). \quad (2.69)$$

The other two sets of Jacobi coordinates $\mathbf{r}_2 = (\mathbf{x}_2, \mathbf{y}_2)$ and $\mathbf{r}_3 = (\mathbf{x}_3, \mathbf{y}_3)$ can be expressed by a linear transformation from $\mathbf{r}_1 = (\mathbf{x}_1, \mathbf{y}_1)$.

Assuming the potential V is comprised of symmetric two-body contact potentials, we can replace $V\Psi$ with $\sum_{i=1}^3 f_i(\mathbf{x}_i)\delta(\mathbf{y}_i)$. Then the time-independent solution of the Eq. (2.69) caused by a plane wave has the form

$$\Psi(\mathbf{r}_1) = \Psi_0(\mathbf{r}_1) + \sum_{i=1,2,3} \int_{\mathbf{y}'_i=0} G_E(|\mathbf{r}_i - \mathbf{r}'_i|) f_i(\mathbf{x}'_i) d^3 \mathbf{x}'_i, \quad (2.70)$$

where $G_E(r)$ is the bare Green's function of Eq. (2.69) and $f_i(\mathbf{x}_i)$ behaves as auxiliary functions describing scattering amplitudes defined at the short-distance boundaries $\mathbf{y}_i = 0$ of two-body scattering. The total wave function has an extra plane wave term Ψ_0 as the initial state when we consider the scattering of three free particles, and the three integral terms in the summation of Eq. (2.70) correspond to the three pieces in Eq. (2.26).

The STM equation is obtained by fixing the wave function to the two-body boundary conditions. Near the boundary $\mathbf{y}_1 = 0$, the first term in the summation of Eq. (2.70) has a $1/y_1$ -singularity caused by the Green's function, and we can expand the wave function formally as

$$\lim_{y_1 \rightarrow 0} \Psi(\mathbf{r}_1) = C_{-1}(f, \mathbf{x}_1)/y + C_0(f, \mathbf{x}_1) + O(y), \quad (2.71)$$

where the expansion coefficients C_{-1} and C_0 depends on the form of $f_i(\mathbf{x}_i)$ and the position \mathbf{x}_1 . Compare this expansion with the two-body boundary condition $\mu_{23}/y_1 - 1/a$, we arrive at a formal equation for $f_i(\mathbf{x}_i)$ as $C_0 + C_{-1}/\mu_{23}a = 0$. Take the actual C_{-1} and C_0 from Eq. (2.70), the formal equation becomes the STM equation

$$\hat{L}_E f(x) + (\sqrt{-E} - 1/a)f(x) = 4\pi\Psi_0(x, 0), \quad (2.72)$$

where $x \equiv x_1$ and we already simplified the equation by considering three identical bosons with $\mu_{ij} = 1$ and $f_i(\mathbf{x}_i) = f(x_i)$, which is equivalent to assuming zero angular momentum.

The operator \hat{L} is defined as

$$\hat{L}_E f(x) = 4\pi \int \left\{ G_E(|x - x'|) [f(x) - f(x')] - G_E(\sqrt{x^2 + x'^2 + xx'}) f(x') \right\} d^3 x'. \quad (2.73)$$

Similar to the situation we have when solving the Faddeev equations, the discrete symmetry appears in the solution of the STM equation because Eq. (2.72) is scale invariant but the three-body boundary condition needed to fix $f(x)$ at small x is a constant. Moreover, negative E solutions for the homogeneous STM equation give the binding energies of Efimov states.

2.3.3 Three-body recombination

Generally, since the molecular potentials for two atoms support a lot of molecular states, three atoms can decay into an atom-dimer system and the released binding energy is usually large enough for the products to fly away from the trapping potential and get lost. The speed of such recombination processes can be characterized by the recombination rate coefficient L_3 , which gives the decay rate of the number density of atoms as

$$\frac{dn}{dt} = -L_3 n^3. \quad (2.74)$$

As a general result of resonant scattering, L_3 is influenced by the shallow Efimov states and reaches maximum values when an Efimov state merges into the three-body continuum. Since the first observation of the L_3 peak in ultracold cesium gases [Kra06], L_3 remains the most important observable for Efimov physics in different ultracold atomic gases.

In the zero-energy regime, L_3 can be calculated analytically from the solution of Eq. (2.72). The Green's function at zero energy has a simple form as $1/4\pi^3 r^4$, and Eq. (2.72) is further simplified by setting $E = 0$ to get $f(x)$. In the asymptotic region $x \rightarrow \infty$, a propagating form of $f(x)$ means the production of a shallow dimer and a free particle after the three-body combination (possible when $a > 0$). Since $f(x)$ is the scattered wave, it contains no incoming wave and the outgoing part should behave like $\xi \exp(ix)/x$ at $x \rightarrow \infty$ to describe the flux $|\xi|^2 \Phi_\infty$ of the products, where $\Phi_\infty = 3$ for symmetry reasons [Pet13]. Considering the number of three-atom systems in a unit volume is $n^3/3!$, a factor $\hbar a^4/m$ for the physical units, the normalized plane wave $\Psi_0 = \sqrt{6}V^{-3/2}$ and the volume factor $V^3 = 8/3\sqrt{3}$ between the Euclid coordinates and the Jacobi coordinates, the recombination rate coefficient is obtained from the flux as

$$L_{3s} = 128\pi^2 (4\pi - 3\sqrt{3}) \frac{\sin^2[s_0 \ln(a/a_{*0})] + \sinh^2 \eta_*}{\sinh^2(\pi s_0 + \eta_*) + \cos^2[s_0 \ln(a/a_{*0})]} \frac{\hbar a^4}{m}, \quad (2.75)$$

where η_* and a_{*0} is fixed by the boundary condition of $f(x)$ at $x \rightarrow 0$, so that the ratio between the outgoing and the incoming waves is $(A/A^*)e^{2i\theta}$, where A is a complex constant and $\theta = s_0 \ln(a/a_{*0}) + i\eta_*$.⁶

⁶ For a solution of the homogeneous STM equation, the number A is related to the ratio between the wave amplitude in the scale-invariant region and the one in the asymptotic region, see Eq. (3.94) in Ref. [Pet13] and the supplemental material of Ref. [Rem13]. For three identical bosons at zero energy, $\arg A = \delta_0 - \pi/2$, where the constant $\delta_0 \approx 1.588$ [Mac05].

Three atoms can also propagate into the short-range limit at $x \rightarrow 0$ and decay into deeply bound molecules. This process can be described phenomenologically by the imaginary part η_* of θ , and the contribution to the recombination rate coefficient is

$$L_{3d}(a > 0) = 128\pi^2(4\pi - 3\sqrt{3}) \frac{\coth(\pi s_0) \cosh \eta_* \sinh \eta_*}{\sinh^2(\pi s_0 + \eta_*) + \cos^2[s_0 \ln(a/a_{*0})]} \frac{\hbar a^4}{m}. \quad (2.76)$$

When $a < 0$, three atoms can only decay into deep dimers and the recombination rate coefficient can be obtained in a similar way as

$$L_{3d}(a < 0) = 128\pi^2(4\pi - 3\sqrt{3}) \frac{\coth(\pi s_0) \cosh \eta_* \sinh \eta_*}{\sinh^2(\eta_*) + \cos^2[s_0 \ln(|a|/a_{*0})]} \frac{\hbar a^4}{m}, \quad (2.77)$$

which is similar to Eq. (2.76), but gives a larger value at the same $|a|$. Since $L_{3d}(a < 0)$ is the main observable in experiments, we usually use the peak position $a_-^{(0)} = -a_{*0} \exp(\pi/2s_0)$ of $L_{3d}(a > 0)$ instead of a_{*0} in Eq. (2.77).

The above discussion can be extended to atom-dimer collisions, and we are interested in the atom-dimer recombination rate coefficient β defined as

$$\frac{dn_D}{dt} = \frac{dn_A}{dt} = -\beta n_D n_A, \quad (2.78)$$

where n_A (n_D) is the density of atoms (universal dimers). However, the above analytic method is only feasible at zero total energy and the atom-dimer scatterings can be solved only numerically. For broad Feshbach resonances, β is also modulated periodically by the scattering length a as [Bra06]

$$\beta(a) = \frac{20.3 \sinh(2\eta_*)}{\sin^2[s_0 \ln(a/a_*)] + \sinh^2 \eta_*} \frac{\hbar a}{m}, \quad (2.79)$$

where a_* is related to other observables via Eq. (2.61).

2.4 Frontiers of the universal few-body physics

2.4.1 Ultracold atomic gases and other systems

In this section, we will discuss some important achievements and undergoing tasks in universal few-body physics, especially from the perspective of experiments on ultracold atomic gases. Ultracold atoms have been the most popular and, until very recently, the only available systems for observing universal few-body states. Reference [Kun15] recently reported the observation of an Efimov state in a helium-4 molecular beam by means of Coulomb explosion imaging.

2.4.2 Universal N -body system

Shortly after the first observation of the Efimov resonance in three-body recombination, the theoretical work of Ref. [Ham07b] and [von09] predicted the existence of two universal four-body states associated to each Efimov state and the corresponding four-body resonances near each Efimov resonance. The results in Ref. [von09] were obtained from the four-body Schrödinger equation in the hyperspherical coordinates with different two- and three-body potentials, where the adiabatic hyperspherical approximation for the four-body potential is applied and the wave functions are expanded in a Gauss basis set. The results of Ref. [von09] is fixed by the universal three-body physics and need no more parameters like a four-body parameter. The calculated four-body resonances appear at $a_{4b1} \approx 0.43a_-$ and $a_{4b2} \approx 0.90a_-$, where $a_- < 0$ is the peak position of the related Efimov resonance. While the seminal observation in Ref. [Kra06] shows possible support to the theory, a refined observation in Ref. [Fer09] carefully distinguishes the three-body and four-body decay and agrees with the theory nicely. The four-body resonances are also reported in ^{39}K [Zac09] and ^7Li [Pol09].

A more general picture of universal N -body states and related recombination resonances are studied in [Meh09] in terms of general S -matrix elements. We observed the five-body resonance in an ultracold gas of cesium [Zen13], see Chap. 6 and references there for details.

2.4.3 Binding energies of the Efimov trimers

The binding energies of Efimov states have been calculated in various ways. In experiments of ultracold atomic gases, binding energies are usually observed by Radio-Frequency association and related recombination losses [Ber13]. This technique involves applying an oscillating electromagnetic field with frequency ν onto the atoms and inducing a frequency modulation of the wave functions. The resultant wave functions obtain side bands separated equally by ν in frequency, and their amplitudes are enveloped by a Bessel function. At low modulation intensity, the carrier and the first band dominates over high order side bands. When we tune $h\nu$ to the binding energy of the state, the first band of the continuum interacts resonantly with the carrier of the bound state, and vice versa, and induces a ‘first-order’ recombination peak. This technique has been used widely to measure the binding energies of shallow dimers and calibrate the scattering length near Feshbach resonances (see Chap. 3 for example).

Reference [Lom10b] and [Nak11] use a similar technique to measure the binding energy of the Efimov state in a mixture of fermionic ^6Li at different Zeemann levels near the atom-dimer threshold. The ‘first-order’ Efimov resonance appears as a smaller peak close to the shoulder of the ‘first-order’ Feshbach resonance. Their results indicate deviations from the universal theory. Technically, the system of distinguishable fermions offers more degrees of freedom for RF operations and the Pauli blocking makes them immune to three-body recombination during the preparing processes, which facilitates greatly the observations on the binding energies of the Efimov state.

2.4.4 ‘van der Waals universality’ of the three-body parameter

In theories assuming zero-range interactions (see subsection 2.3.3 and 2.2.5), the three-body parameter (3BP) is an external parameter to be fixed by the experiment. When observing L_3 , the real part of the 3BP θ fixes the peak positions $a_-^{(n)}$ of the Efimov resonances while the imaginary part η_* gives the width of the resonance. Theoretically, 3BP changes when different two-body potentials are involved, especially when non-additive three-body interactions are involved. However, in the work of Chap. 4, we observed almost constant values of $a_-^{(0)}$ at four different broad Feshbach resonances in cesium gases. Soon it is realized that the values of $a_-^{(0)}$ obtained in ultracold atomic gases near broad Feshbach resonances are always around $-9.1R_{\text{vdW}}$, independent of the specific Feshbach resonance and the atom species.

As mentioned in subsection 2.2.2, this ‘van der Waals universality’ emerges when the two-body potential has a van der Waals tail at large distances and is deep enough to support many bound dimer states. Then the three-body potential acquires a universal form with a repulsive wall near $1.6R_{\text{vdW}}$, which prevents atoms from probing further short-range details of the two-body potential or non-additive three-body interactions caused by chemical bonds and finally determines the 3BP. While Ref. [Wan12] numerically calculates the three-body potentials and related observables from the three-body Schrödinger equation, we can obtain the universal potential more transparently by solving the angular Faddeev equation (2.32) as Ref. [Nai14b] does. We consider a soft van der Waals potential

$$V(r) = -\frac{16}{r^6 + \sigma^6} \quad (2.80)$$

for two-body interaction, where $R_{\text{vdW}} = \hbar = m = 1$ and σ is tuned to have different number of bound states and scattering length a .

The panel (a) in Fig. 2.5 shows the total three-body potential $U_{0t}(R) = -(\lambda_0(R) + 1/4)/R^2 + Q_{00}(R)$ for the lowest three-body channel depending on the number n of two-body bound states (equivalent to the number of nodes in the radial two-body wave function) in the resonant limit where $a = \infty$. When n increases from 1 to 9 (solid blue curves) and finally reaches 10 (solid red curve), the three-body potentials shows a trend of converging to a *universal* form. This universality of the three-body potential is named as the *van der Waals universality* because it exists as long as the two-body potential has a van der Waals tail and supports several bound states [Wan12, Nai14b]. References [Wan12] and [Nai14b] also point out that this sharp barrier of the ‘van der Waals universal’ three-body potential is caused by the suppression of the wave function at short distances. Qualitatively, when the wave propagates from the asymptotic region to the origin, the positions of its first few anti-nodes are practically fixed if the scattering length a is large and there are many bound states below. As the two-body wave function is confined between the first node and R , a small R near the anti-node position increases the two-body kinetic energy that is related to the three-body potential and gives the repulsive potential. In Ref. [Nai14b] and [Nai14a], the two-body potential is finally replaced by a pseudopotential giving the proper two-body correlation to verify that the pair correlation is the reason of the three-body barrier and obtain the three-body observables. Generally, any form of short-range (decays faster than $1/r^2$) two-body potential corresponds to a specific correlation of the wave function in the threshold regime and determines a class of universality [Nai14a].

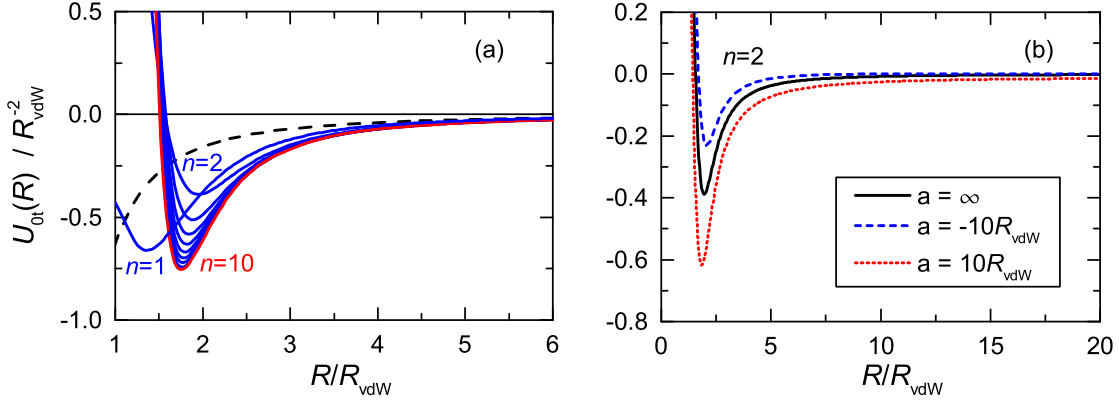


Figure 2.5: Numerically calculated three-body potential $U_{0t}(R)$ for the lowest three-body channel from soft van der Waals two-body potentials. The parameter σ in Eq. (2.80) is tuned to have n nodes in the radial two-body wave function and the wanted scattering length a . When $a = \infty$ and the number n of nodes are varied, the three-body potentials are plotted as solid blue curves for n between 1 and 9 and the potential of $n = 10$ is plotted as the solid red curve in panel (a). The ideal three-body potential $-(s_0^2 + 1/4)/2R^2$ is shown as a dashed black curve for comparison. It is clear that the three-body potential converges to a universal form when n increases. A figure similar to panel (a) with more results from various two-body potentials is in Ref. [Nai14b]. In panel (b), the three-body potentials of $a = \infty$ (solid black line), $a = -10R_{\text{vdW}}$ (dashed blue line) and $a = 10R_{\text{vdW}}$ (dotted red line) are shown for the case $n = 2$. The potential converges to the two-body binding energy at large R when $a > 0$, otherwise it converges to zero.

With the universal three-body potential, Ref. [Wan12] gives $a_-^{(0)} = -9.73(3)R_{\text{vdW}}$ and $\kappa^{(0)} = 0.226(2)/R_{\text{vdW}}$ while Ref. [Nai14b] has $a_-^{(0)} = -10.86(1)R_{\text{vdW}}$ and $\kappa^{(0)} = 0.187(1)R_{\text{vdW}}$. Both results fit fairly well with the observations and give values of $a_-^{(0)}\kappa^{(0)}$ near -2.1, which is larger than the ideal value of -1.508 in Eq. (2.61). Theoretical works also show that the excited-state Efimov resonance is less sensitive to the short range details than the ground-state Efimov resonance, and the value of 3BP obtained from the excited-state Efimov resonance is nearer to the value at the resonant limit. See Chap. 8 for details.

Concerning N -body universal states, the observations [Ber11b] and simulations [von09] support the three- and four-body observables are universally connected. In systems of ultracold alkali atoms, since all universal N -body states share the same high-energy cutoff determined by the two-body van der Waals potential tail, it is not surprising that the three-body parameter and all low-energy N -body observables are fixed and universally connected by the van der Waals length r_{vdW} . On the other hand, Ref. [Ham07b] suggests in the context of effective field theory that the correlations between universal N -body observables are general as long as short-range interactions are involved. Consequently no extra N -body parameter is needed beyond the three-body parameter [von10].

Up to now, the van der Waals universality is based on simulations with single channel potentials and only fits fairly well with the observations, while two-coupled-channel models are closer to the actual atomic systems involving Feshbach resonances and should be used to estimate the deviations from the ‘single channel’ van der Waals universality [Wan14]. This is especially interesting for the position a_* of the atom-dimer resonance, since a_* shows

significant deviation from the universal behavior in experiments (see Chap. 5).

2.4.5 Finite-temperature effects

When the s -wave scattering length a becomes resonantly large, the unitary limit constrains the cross section of elastic scattering by Eq. (2.4). The three-body recombination rate L_3 is also limited by the finite temperature. As an extension of the zero-energy case discussed in subsection 2.3.3, $L_3(E)$ can be obtained numerically from the STM equation for finite energy E and scattering length a . Then an average is performed over a thermalized ensemble to give $L_3(T)$ at a finite temperature T .

The S -matrix formalism is employed to simplify the calculation of $L_3(E)$ and gives an illustrative picture for the properties of $L_3(E)$. The hyperradius is divided into four regions according to the properties of $f(x)$ in the STM equation. In the scale invariant region where $R_e \ll R \ll R_{min} \equiv \min(a, 1/k)$, the STM equation is simply $\hat{L}f(x) = 0$ and the solution $f(x)$ is a superposition of the outgoing and incoming Efimov waves (marked as channel 1) with a ratio between the two waves being $\mathcal{A} = \Psi_1^{in}/\Psi_1^{out} = -(kR_0)^{-2is_0} e^{-2\eta_*}$, where incoming (outgoing) are defined with respect to the long-distance region.⁷ Ignoring higher angular momentum channels and in the asymptotic region where $x \rightarrow \infty$, $f(x)$ contains the free-atom component (channel 3) and, when $a > 0$, the atom-dimer wave (channel 2). The complicated long-distance region $R \approx |a|$ can be described by a unitary matrix s that connects the wave function between channel 1, 2 and 3. In the short-distance region where $R \approx R_e$, the physics is represented by the complex 3BP fixing the boundary condition of $f(x)$.

With the S -matrix formalism, we can explain the three-body recombination process by an analogy to the Fabry-Perot interferometer, where the short-range and long-range region being the two mirrors for the three-body wave function (Fig. 2.6). For example, in the simple case that the channel 2 does not exist ($a < 0$), a free three-atom wave approaches the long-range region and transmits partially into the ‘cavity’ in the scale invariant region. Then the wave is reflected between the short-range boundary and the long-range region for multiple times and interferes. The leakage flux into the short range region gives the three-body recombination rate $L_3(a < 0)$, which maximizes when the cavity is on resonance.

The elements of the matrix s can be calculated numerically using the STM equation. For example, the element s_{11} , describing the outgoing Efimov wave hitting the long-range region and being reflected back as incoming Efimov wave again, can be obtained from the homogeneous STM equation by fixing the incoming waves in the asymptotic region to zero.

⁷ When we consider the radial Faddeev equation instead of the STM equation, the total energy E term in Eq. (2.65) drops out in the scale invariant region because E is much smaller than the potential. As the equation is scale invariant, the resultant wave function is simply proportional to $\sqrt{R} \sin[s_0 \ln(\Lambda_0 R)]$ and the amplitude depends on the only parameter ka when the asymptotic ($R \rightarrow \infty$) wave function is given. Rewrite the scale invariant wave function as $\sqrt{R} \sin[s_0 \ln(kR) + s_0 \ln(\Lambda_0/k) + i\eta_*]$, the reflection coefficient \mathcal{A} is then $-(k/\Lambda_0)^{-2is_0} e^{-2\eta_*}$. We have introduced the real constant η_* for decaying into deep dimers. If we compare the reflection ratio here with the factor $(A/A^*)e^{2i\theta}$ in subsection 2.3.3, we get $\kappa_-^{(0)} a_-^{(0)} = \sqrt{2} e^{(\delta_0 - \pi/2 - \theta_{s_0})/s_0} \approx 1.508$ while the factor $\sqrt{2}$ comes from the factor between R and x in Eq. (2.11). In this subsection (and Chap. 8), we follow Ref. [Rem13] and uses a different convention of R that is by a factor of $\sqrt{2}$ larger than the one in Eq. (2.11).

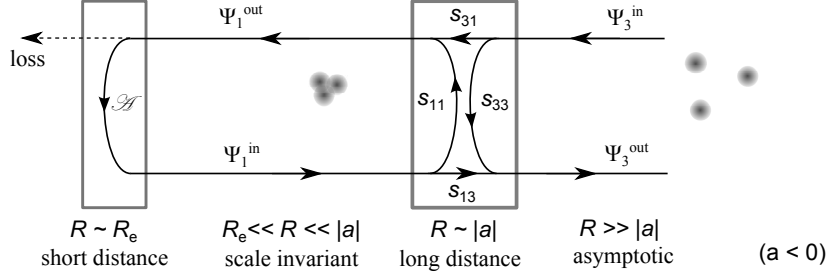


Figure 2.6: The Fabry-Perot analogy to the three-body potential at $a < 0$. The three atoms stay in the state of a hyperspherical wave (channel 1) in the scale invariant region and are free (channel 3) in the asymptotic region. Channel 1 and 3 are connected through the long-distance region, where effects from the barrier of the adiabatic potential and couplings to higher levels are described by a unitary scattering matrix s . The hyperspherical wave also goes to the short distance region, and the phase imposed by reflection is $\mathcal{A} = \Psi_1^{\text{in}}/\Psi_1^{\text{out}} = -(kR_0)^{-2i\eta_0} e^{-2\eta_*}$, where the parameter η_* describes the losses into the short distance region by forming deep molecules. For the matter wave, the short and long distance work like the two mirrors in a Fabry-Perot interferometer, while the coupling-in mirror's reflectivity and position can be tuned by a . When the cavity reaches the resonant condition, the transmission is maximized and the three-body recombination rate gives the Efimov resonance. Modified from the figure in Ref. [Rem13].

Especially, $|s_{11}|$ decreases to zero when $k|a| \gg 1$ ($E = \hbar^2 k^2/m$), so the quality of the cavity becomes low and the Efimov resonances disappear at this limit.

The finite temperature results of this S -matrix formalism agrees with our measurements of L_3 for the ground-state Efimov resonance in cesium gases nicely (Chap. 9). A possible small deviation at high T may originate from the finite size of the actual two-body interaction and resultant temperature dependence of the 3BP. The coupled-channel simulation in Ref. [Wan14] mentioned in subsection 2.4.4 also gives a finite- T results, and it is possible to explain such deviations.

2.4.6 The Efimov period

The discrete scaling symmetry is one of the key features of Efimov states. Despite several observations of the ground-state (first) Efimov resonances in different atomic species, the excited-state (second) Efimov resonance has been observed only in fermionic ${}^6\text{Li}$. But the Efimov series is complicated for ${}^6\text{Li}$, since three different scattering lengths are involved. The difficulties in observing the second Efimov resonance stems mainly from the extremely large a needed. L_3 is very large near the second Efimov resonance and vulnerable to the finite T effects. Moreover, a is tuned near the diverging point to reach necessary large values, which requires a very broad Feshbach resonance to keep the precision of a .

In the work of Chap. 7, we observe the second Efimov resonance directly in very dilute and cold cesium gases by using an extremely broad Feshbach resonance near 800 G to tune a , and the finite-temperature effects are considered by the theoretical model in subsection 2.4.5 and Chap. 9. Furthermore, our results also provide the evidence for the excited four-body resonance. The obtained scaling factor of 21.0(1.3) is very close to the ideal value of 22.7.

In the work of Chap. 8, we reanalyze the second Efimov resonance in ${}^6\text{Li}$ with the extended finite T model considering three different scattering lengths. The obtained 3BP expressed in $|a_-^{(1)}/22.7r_{\text{vdW}}|$ is smaller than the one from cesium, which gives a quantitative probing of the robustness of the ‘van der Waals universality’.

Another way to simplify the observation of consecutive Efimov resonances is by reducing the Efimov scaling factor by using a mass imbalanced mixture. In the case of two atoms with mass M interacting resonantly with the third one with mass m , the Efimov scaling factor decreases when m/M decreases. For instance, the system of Li-Cs-Cs has a predicted Efimov scaling factor of 4.9 [Bra06, D’I06], which is much smaller than the ideal value 22.7 for particles with identical mass. With such a small factor, the constraint imposed by temperature becomes less problematic, so the second Efimov resonances may no longer be heavily modified by the unitary limit. On the other hand, the involvement of two species and three scattering lengths technically complicates the preparing of the sample and the analysis of recombination rates. Recently, Refs. [Pir14, Tun14] report the observation of the excited-state Efimov resonances in the Li-Cs mixture with a scaling factor near 5.8.

2.4.7 Efimov states in a confining potential

Collisional properties of interacting particles can dramatically change when the dimensionality of the system is changed. Reference shows that Efimov states only exist when the dimension d is between 2.3 and 3.8 and cannot exist in two dimensions [Nie01]. One intuitive picture is that the $1/R^2$ three-body potential in the scale invariant region becomes weak or even repulsive when the dimension changes. Many open questions remain about the details of the crossover from three to two dimensions and about how the Efimov-related three-body recombination losses are affected. The original proposal of our undergoing experiment is to explore this dimension induced disappearing of Efimov resonance by applying a strong confining potential in one direction and changes the dimension of the system.

However, the real situation in the experiment is more complicated than a simple change of dimension. We use ultracold cesium atoms trapped tightly in a harmonic potential along one spatial direction z to realize the quasi-two-dimensional system, where the atoms stay in the ground state with a Gaussian shaped wave function in the z direction and the corresponding harmonic length l_{hz} is comparable to the scattering length $|a|$. Consequently, the modification to the three-body potential happens only significantly when R is similar or larger than $|a|$, which means that the scale invariant part ($R \ll |a|$) of the three-body potential is barely affected. The resultant three-body potential is roughly the original potential plus a harmonic trap at large R [Boh98]. When we consider the Fabry-Parot interferometer analogy, the finite ground state energy of a moderately strong harmonic trap shifts the entrance energy of three-body scattering and the Efimov resonance is affected in a way similar to the high T effects. If the harmonic trap is so strong that the three-body potential barrier around $R \approx |a|$ disappears, the Efimov resonance should also vanish. Strictly speaking, this is a quasi-two dimensional effect, rather than a normal change of dimension.

Recently, theoretical works [Lev14] calculated L_3 for the quasi-two dimensional system at

different T and a , and connected it to the broken scaling symmetry in the quasi-two dimensional system. In our latest observations, we obtained preliminary results in tracing a smooth modification of the Efimov resonance that may agree with the theoretical analysis.

Publication: Feshbach resonances, weakly bound molecular states and coupled-channel potentials for cesium at high magnetic fields[†]

Phys. Rev. A **87**, 032517 (2013)

Martin Berninger, Alessandro Zenesini, Bo Huang, Walter Harm, Hanns-Christoph Nägerl, Francesca Ferlaino, and Rudolf Grimm
*Institut für Experimentalphysik and Zentrum für Quantenphysik,
Universität Innsbruck, 6020 Innsbruck, Austria and
Institut für Quantenoptik und Quanteninformation,
Österreichische Akademie der Wissenschaften, 6020 Innsbruck, Austria*

Paul S. Julienne
*Joint Quantum Institute, NIST and the University of Maryland,
100 Bureau Drive Stop 8423, Gaithersburg, Maryland 20899-8423, USA*

Jeremy M. Hutson
*Joint Quantum Centre (JQC) Durham/Newcastle, Department of Chemistry,
Durham University, South Road, Durham, DH1 3LE, United Kingdom*

We explore the scattering properties of ultracold ground-state Cs atoms at magnetic fields between 450 G (45 mT) and 1000 G. We identify 17 new Feshbach resonances, including two very broad ones near 549 G and 787 G. We measure the binding energies of several different dimer states by magnetic field modulation spectroscopy. We use least-squares fitting

[†] The author of the present thesis contributed in upgrading the experimental setup to be capable of exploring a magnetic field strength of more than 1000 G. Especially, he set up the imaging system for detecting atoms at high magnetic fields. He also performed the measurements with M.B. and A.Z. P.S.J. and J.M.H. used their coupled-channels model to analyze our experimental data and obtained the scattering length as a function of the magnetic field.

to these experimental results, together with previous measurements at lower field, to determine a new 6-parameter model of the long-range interaction potential, designated M2012. Coupled-channels calculations using M2012 provide an accurate mapping between the s-wave scattering length and the magnetic field over the entire range of fields considered. This mapping is crucial for experiments that rely on precise tuning of the scattering length, such as those on Efimov physics.

3.1 Introduction

Cold cesium atoms have provided the foundation for many important experiments in basic science and also find application in precise atomic clocks. A thorough understanding of the collisions and interactions of two Cs atoms is crucial to interpret such experiments and optimize the applications. In particular, Cs has a complicated spectrum of magnetically tunable Feshbach resonances [Chi10], which allow precise control of the two-body interactions. These resonances are due to near-threshold bound states of the diatomic molecule Cs₂ that can be tuned to match the near-zero energy of the colliding atoms. The resonances also allow an atomic sample to be converted with high efficiency into diatomic molecules by tuning an applied magnetic field across a resonance [Her03]. We have previously shown that the weakly bound molecules formed in this way can be converted into deeply bound [Dan08] or even ground-state [Dan10] molecules by stimulated Raman adiabatic passage.

Early work with Cs atoms and its interactions was at low magnetic field, $B \lesssim 250$ G.¹ Results on low-field Feshbach resonances [Vul99, Chi00, Chi03, Chi04] made it possible to construct theoretical models of the near-threshold bound and scattering states of two cold Cs atoms [Leo00, Chi04]. These models used the full Hamiltonian of Cs₂, including the potential energy curves of the $^1\Sigma_g^+$ singlet and $^3\Sigma_u^+$ triplet states, the molecular spin-spin interaction, and the atomic hyperfine interactions. Fitting the data allowed four key parameters of the model to be adjusted so that the resonance structure could be reproduced accurately in the low-field region. These early models yielded an understanding of the large clock shifts in Cs atomic fountain clocks [Leo01], the anomalously large loss rates for collisions of doubly spin-polarized Cs atoms [Söd98], and the magnetic field regions of moderate positive scattering length where Bose-Einstein condensation (BEC) was possible [Web03a]. Subsequent measurements of the binding energies of weakly bound dimer states at fields up to 60 G [Mar07, Kno08] were mostly in good agreement with calculations based on the model of Ref. [Chi04], which we designate M2004.

Ultracold Cs is particularly important for the study of Efimov states [Efi70], which are high-lying bound states of triatomic molecules that appear when the two-body interaction has a bound state very close to threshold. Efimov states cause additional loss features close to 2-body Feshbach resonances. The first observation of an Efimov resonance in Cs [Kra06] was at a field near 8 G. We have recently extended this to observe Efimov features associated with three additional 2-body Feshbach resonances, at fields up to 900 G, and reached the remarkable conclusion that the Efimov features all occur at almost the same

¹ Units of gauss rather than Tesla, the accepted SI unit for the magnetic field, have been used in this paper to conform to the conventional usage in this field of physics.

2-body scattering length a , and thus all have almost the same binding energy at unitarity ($a = \infty$) [Ber11b]. This universality of Efimov states was quite unexpected, and contradicted previous theoretical indications [D'I09], although subsequent theoretical work is now starting to explain its origins [Wan12, Nai14b, Sch12, Chi11]. Efimov states in other ultracold systems are now also being found to show the same universal behavior [Pol09, Gro09, Ott08, Huc09, Wil12].

The new Efimov resonances used to demonstrate universality in Ref. [Ber11b] are in the vicinity of two open-channel-dominated s -wave Feshbach resonances that were theoretically predicted with pole positions around 550 G and 800 G [Chi10]. Model M2004 is quite accurate at fields below 100 G, but at higher fields its predictions are in error by up to ≈ 1 per cent, or 8 G for B on the order of 800 G. This is not accurate enough to describe the scattering physics to sufficient precision to interpret the Efimov resonances, so an improved theoretical model is essential.

The aim of the present paper is to describe the previously unexplored properties of ^{133}Cs in its absolute atomic ground state in the magnetic high-field region between 450 G and 1000 G. We present new measurements of both resonance positions and binding energies at fields up to 1000 G. We then use these results to develop a new optimized theoretical model, which we call M2012, that is accurate at both high and low magnetic fields. This model provides an accurate predictive tool to map the scattering length $a(B)$ as a function of magnetic field B (see Sec. 3.7), which it is difficult to measure directly. This mapping was key to interpreting the three new Efimov features reported in Ref. [Ber11b].

This paper is organized as follows. Section 3.2 describes the essential molecular physics of threshold Cs states and describes the notation we use. Section 3.3 describes our experimental methods and results in the high-field region. Section 3.4 describes our theoretical model. Section 3.5 describes our least-squares fits to the experimental results, and compares experiment with theory in the regions of high, middle, and low fields. Section 3.6 summarizes our conclusions.

3.2 Near-threshold states of cesium dimer

Two alkali-metal atoms in ^2S states interact at short range to form singlet ($X^1\Sigma^+$) and triplet ($a^3\Sigma^+$) states, with potential curves as shown in Figure 3.1. Levels that lie more than about 100 GHz below dissociation have fairly well-defined singlet or triplet character, so lie principally on one or the other of these curves. However, the levels of primary interest in the present work are very close to dissociation, and are bound by less than 1 GHz (and sometimes as little as 10 kHz). In this region the singlet and triplet states are strongly mixed by hyperfine interactions and it is more appropriate to describe the levels in terms of atomic quantum numbers.

The zero-field levels of the Cs atom are characterized by the nuclear spin $i = 7/2$, the electron spin $s = 1/2$ and their resultant $f = 3$ or 4, with the $f = 4$ level 9.19 GHz above $f = 3$. In a magnetic field B , each level splits into $2f+1$ sublevels labeled by m_f , with the ground state

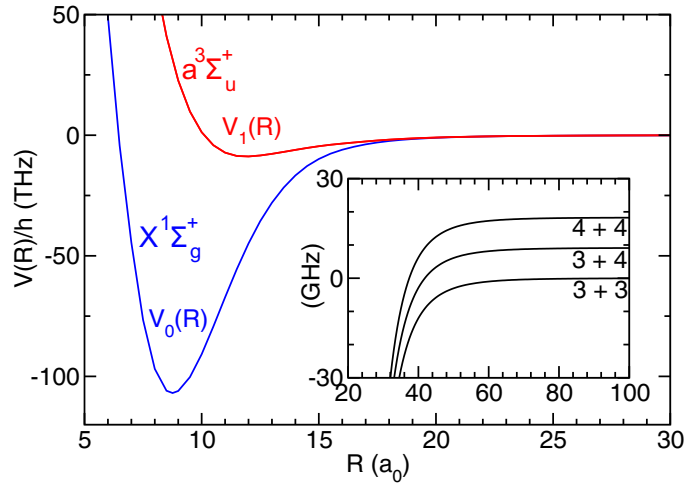


Figure 3.1: (Color online) Molecular potential energy curves $V_0(R)$ and $V_1(R)$ for the singlet and triplet states of Cs_2 . The inset shows an expanded view of the long-range potentials separating to the two different $f = 3$ and 4 hyperfine states of the atoms at magnetic field $B = 0$.

$(f, m_f) = (3, +3)$. In the present work we label the atomic states with letters a, b, c, \dots in increasing order of energy.

For Cs_2 there are 3 field-free atomic thresholds, labeled in increasing order of energy by $(f_1, f_2) = (3,3)$, $(3,4)$ and $(4,4)$, as shown in the inset of Fig. 3.1. In a magnetic field, each threshold splits into sublevels labeled by $(f_1, m_1) + (f_2, m_2)$. The near-threshold molecular states are to a good approximation described by quantum numbers (f_1, f_2, F, M_F) , where F is the resultant of f_1 and f_2 and $M_F = m_1 + m_2$ (though m_1 and m_2 are not individually conserved). M_F is a nearly good quantum number except near avoided crossings. For a homonuclear molecule such as Cs_2 , F is also nearly conserved in the region where the atomic Zeeman effect is near-linear. Additional quantum numbers are needed for the molecular vibration n and the partial-wave angular momentum L . For near-dissociation levels it is convenient to specify n with respect to dissociation, so that the topmost level is $n = -1$, the next is $n = -2$, etc. In the present work we describe near-threshold levels using a set of quantum numbers $n(f_1 f_2) FL(M_F)$, with $L = 0, 2, 4$, etc. indicated by the usual labels s, d, g , etc. This is sometimes abbreviated to $FL(M_F)$ to avoid repetition. Following Ref. [Chi10], we speak of bound levels with dominant s character in their wavefunction as s -wave levels; similarly for d - or g -wave levels with dominant $L = 2$ or 4 character in their wavefunctions.

Each molecular level lies within a “bin” below its associated threshold, with the boundaries of the bins determined by the long-range forces between the atoms. For Cs_2 , with $V(r) = -C_6 r^{-6}$ at long range and $C_6 \approx 6890 E_h a_0^6$ for both the singlet and triplet states, the $n = -1$ level lies between zero and -105 MHz, and the $n = -2$ level lies between -105 MHz and -725 MHz [Chi10]. Similarly, bin boundaries can be worked out for more deeply bound levels. For Cs_2 the background scattering length for each channel is large and positive, on the order of the scattering length of the triplet potential. Under these circumstances all the levels lie near the top of their respective bins, and their energies E are approximately given by those of the triplet Born-Oppenheimer potential. Numerically, E/h is -0.0046 GHz,

-0.11 GHz, -0.75 GHz, -2.4 GHz, -5.5 GHz, -10.6 GHz, and -18.1 GHz for $n = -1$ to -7 for the M2004 model [Chi04].

Feshbach resonances occur where a weakly bound state exists at the same energy as the colliding atoms. Zero-energy Feshbach resonances thus occur at magnetic fields where a bound state crosses an atomic threshold. Each resonance is labeled by the quantum numbers of the bound state that causes it. We will work here with the scattering and bound states associated with the aa entrance channel, with two atoms in state a with $(f_1, m_1) = (3, +3)$. The energy zero at any magnetic field strength B is set to the energy of two a -state atoms. In s -wave scattering, the projection of the total angular momentum onto the field, M_{tot} , is thus always $+6$ and is a rigorously conserved quantity. The left-hand panels of Figure 3.2 show the s -wave bound states with $M_{\text{tot}} = M_F = +6$ at magnetic fields up to 1000 G, together with the scattering length calculated using only s functions and thus including only resonances due to bound states with $L = 0$.

The $(f_1, f_2) = (3, 3)$ levels with $M_F = +6$ in Fig. 3.2 have the same magnetic moment as the separated aa atoms, and thus the energies of these bound states are parallel to the $E = 0$ axis. However, $M_F = +6$ levels arising from other (f_1, f_2) combinations, and $(3, 3)$ levels with $M_F \neq +6$, have different magnetic moments and can cross the aa threshold as the magnetic field is varied. The three strong s -wave resonances at fields below 1000 G are associated with ramping $n(f_1 f_2)FL(M_F)$ states of $-7(44)6s(6)$, $-6(34)7s(6)$ and $-6(34)6s(6)$ character. However, it should be noted that in each case the ramping s -wave state mixes strongly with the least-bound state $-1(33)6s(6)$, which has a binding energy near 50 kHz, and this mixed state crosses threshold (and causes a pole in the s -wave scattering length) at a magnetic field below the field where the unperturbed ramping s -wave state would cross threshold. Such shifts in pole position are discussed in Refs. [Jul04, Jul06, Chi10].

Figure 3.2 extends to negative magnetic field. This is to be interpreted as a reversal of axis, which is equivalent to changing the sign of all spin projection quantum numbers. Thus, the aa channel at $-|B|$ is equivalent to the gg channel at $+|B|$, where the gg channel has two g -state atoms $[(f_1, m_1) = (3, -3)]$. The bound states and scattering length are continuous across $B = 0$, and in particular the low-field behavior of the scattering length is largely due to the ramping $-7(44)6s(6)$ state, which actually produces a resonance around $B = -12$ G (i.e., in the gg channel), as shown in detail in Fig. 3.3.

Each s -wave bound state has a corresponding d -wave state, also with $M_F = +6$, that lies almost parallel to it but is shifted by the rotational energy of the vibrational state concerned; the rotational energy increases with binding energy and thus depends strongly on the vibrational quantum number n . However, levels with $L > 0$ and projection M_L such that $M_{\text{tot}} = M_F + M_L = +6$ will also cross the aa threshold and can contribute to s -wave threshold scattering [Hut08]. The lower-right panel of Fig. 3.2 shows the bound-state energies including the additional d -wave levels with $M_F \neq 6$. The upper-right panel shows the s -wave scattering length obtained with a basis set including both s and d functions (which we refer to as an sd basis set), showing the additional resonances that occur. Figure 3.3 shows an expanded view of the scattering length and near-threshold bound states calculated with an sd basis set in the low-field region between -60 and $+60$ G. Figure 3.4 shows the near-threshold g -wave bound states, as studied in Refs. [Chi04, Mar07, Hut08].

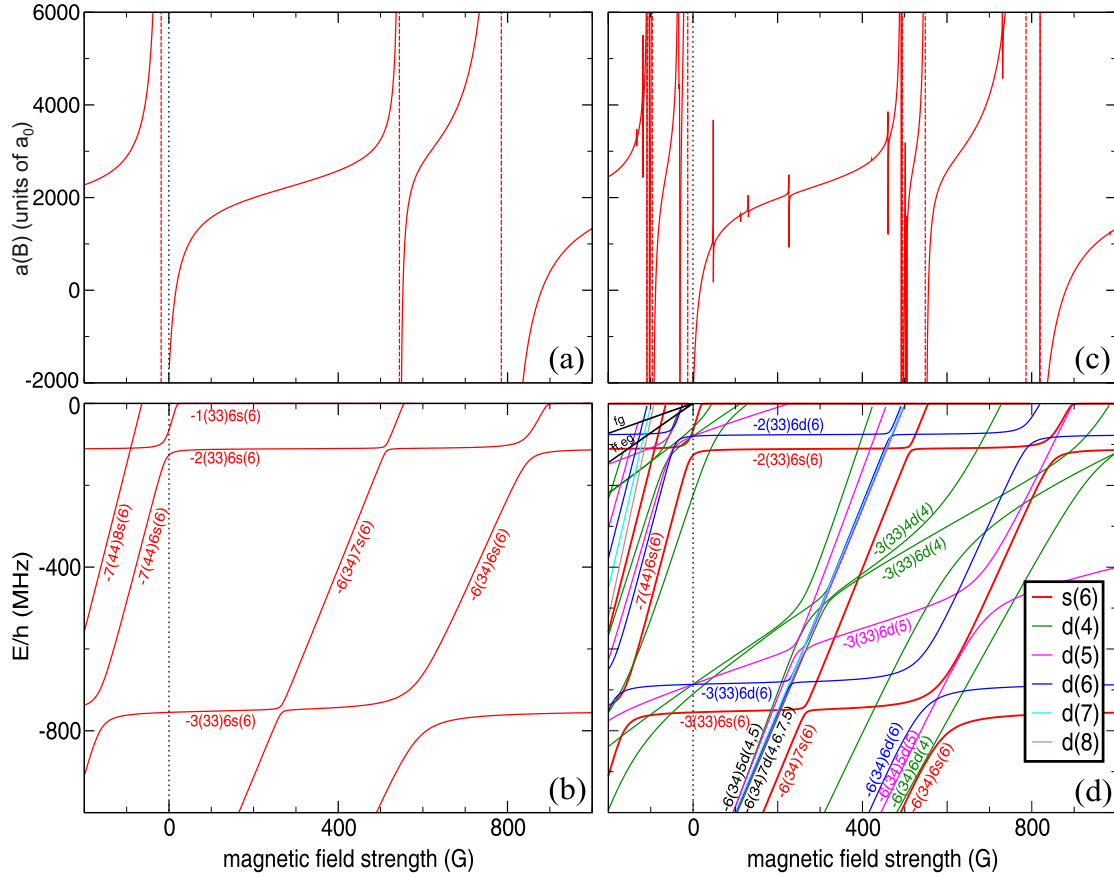


Figure 3.2: (Color online) Scattering length and energy levels versus magnetic field B for Cs collisions in the lowest energy aa spin channel. Panel (a): scattering length, calculated including only s basis functions. The vertical lines indicate the pole positions. Panel (b): Cs_2 s -wave bound-state energies below the aa threshold with $M_{\text{tot}} = +6$, $M_F = +6$ in the range $B = -200$ to 1000 G, calculated with s basis functions only. Panel (c): scattering length, calculated including s and d basis functions and including all matrix elements of the spin-dipolar coupling. Panel (d): Cs_2 s -wave and d -wave bound state energies below the aa threshold with $M_{\text{tot}} = +6$ and all allowed values of M_F in the range $B = -200$ to 1000 G. The legend shows the $L(M_F)$ labels. Levels with different L or M_F cross since small off-diagonal spin-dipolar matrix elements coupling them were not included in the calculation. Properties in the aa channel at negative values of B apply to the gg channel with reversed $M_{\text{tot}} = -6$ (see text). The lines in the upper left corner of Panel (d) show the energies of the fg , ff , and eg atomic channels.

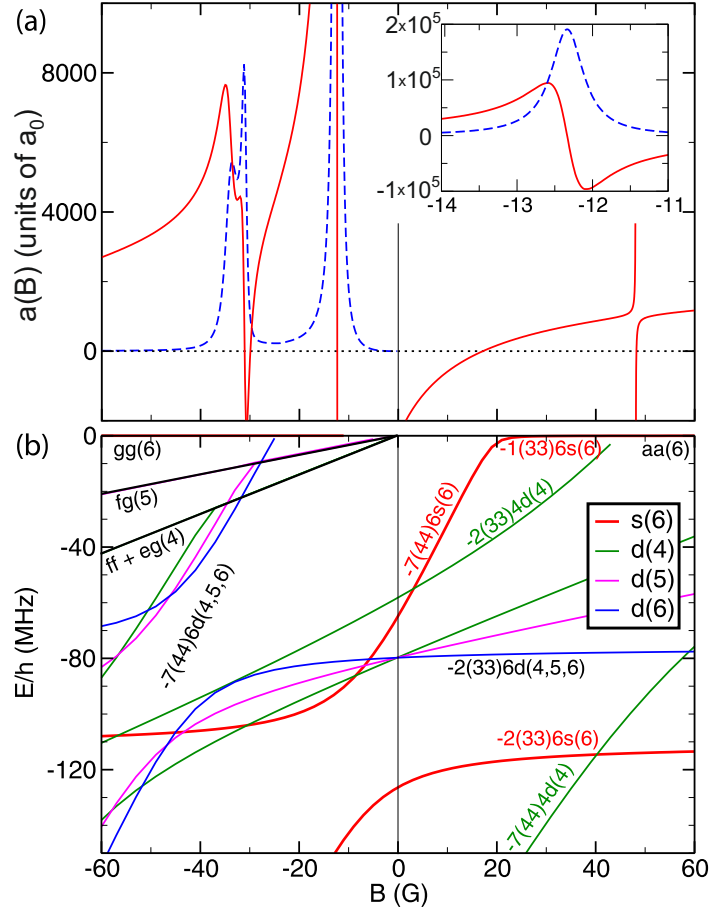


Figure 3.3: (Color online) Panel (a): the real (red, solid) and imaginary (blue, dashed) parts of the complex scattering length (see Section 3.4), calculated with an sd basis set. For $B < 0$, two-body relaxation is possible to channels fg , ff , or eg . The inset shows an expanded view of the pole region of the resonance near -12 G indicating a maximum variation in scattering length of $\approx \pm 10^5 a_0$ due to resonance decay. Panel (b) shows the bound states below threshold, calculated as in Fig. 3.2 so that levels of different L or M_F cross instead of showing avoided crossings. The M_F labels in the negative B regions are shown with reversed sign.

Previous work on ultracold Cs has focused on the low-field region. The first experimental studies of the collisional properties of Cs were performed at Paris [Söd98, GO98a, GO98b], Oxford [Hop00, Arl98] and Stanford [Vul99, Chi00, Chi03]. Chin *et al.* [Chi00] and Leo *et al.* [Leo00] studied over 30 resonances in several spin channels at fields below 130 G. Chin *et al.* [Chi04] observed over 60 resonances in 8 different spin channels (aa , gg , hh , an , ao , ap , hn and gf) for fields up to 250 G. In recent years, we have explored the energy spectrum of weakly bound Cs_2 Feshbach molecules by magnetic moment, microwave [Mar07] and magnetic field modulation spectroscopy [Lan09]. The zero crossing of the s -wave scattering length was also precisely determined, using an approach based on measuring the interaction-induced dephasing of Bloch oscillations [Gus08a, Gus08b].

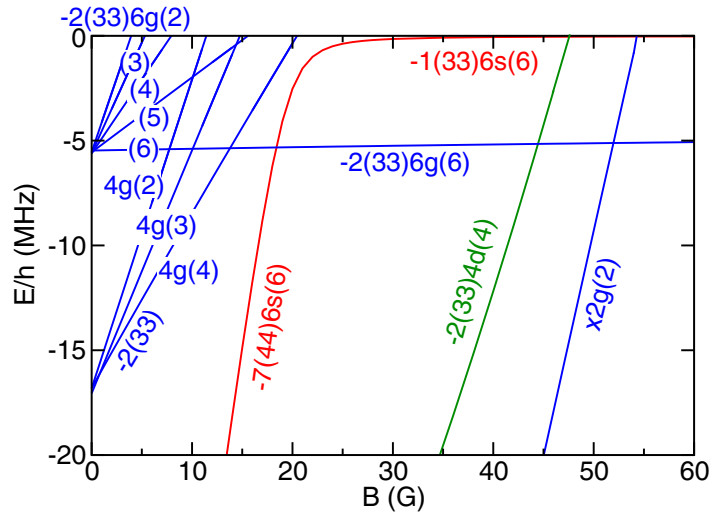


Figure 3.4: (Color online) Low-field near-threshold bound levels of s , d , and g symmetry. As for Figs. 3.2 and 3.3, the avoided crossings between states of different L or M_F are not calculated because spin-dipolar coupling is omitted in this calculation. The low-field g -wave levels are of $-2(33)$ character, whereas the level marked $x2g(2)$ is of mixed $n(f_1, f_2) = -2(33)$, $-6(34)$, and $-7(44)$ character.

3.3 Feshbach spectroscopy at high magnetic field

In the present work, we carry out a variety of different experiments on ultracold ^{133}Cs in its lowest internal state, $(f, m_f) = (3, 3)$, at magnetic fields in the range between 450 and 1000 G. We first discuss the main experimental procedures and conditions (Sec. 3.3.1). Next we report on trap-loss spectroscopy, which allows measurement of the positions of narrow Feshbach resonances (Sec. 3.3.2). Finally we present magnetic field modulation spectroscopy for the precise determination of molecular binding energies near broad Feshbach resonances (Sec. 3.3.3).

3.3.1 Sample preparation

To access the high-field region, we have implemented a new magnetic-field system in the experimental setup [Ber11a]. This system is able to reach maximum magnetic field strengths up to 1400 G in a steady-state condition with 10 mG long-term stability. The high magnetic bias fields are created by three separately controllable pairs of magnetic field coils, made of 4 mm and 6 mm square-profile copper tubes insulated by glass-fiber braided sleeveings. For each coil pair the electric currents, which are up to 400 A (4 mm tube) and 800 A (6 mm tube), respectively, are supplied by two 6 kW power supplies, connected in parallel. The temperature of the coil system is kept below 50°C by internal water cooling of the copper tubes using a 10-bar pump system. Magnetic field stability is governed by controlling the current in the coils by an active feedback system, which operates at a precision level of 10^{-5} . For this, the actual currents are measured by highly sensitive current transducers. We have checked that precise current control is sufficient for magnetic field control to the limit given

above. Other influences, such as thermal expansion of the copper coils, play a minor role. A detailed description of the magnetic-field coil system can be found in Ref. [Ber11a].

The procedure used to prepare an ultracold cesium sample in the absolute atomic ground is based on well established cooling and trapping techniques, which are similar to the ones described in Ref. [Kra04] down to the μK -regime. After Zeeman slowing and cooling in a magneto-optical trap, the atoms are loaded into a three-dimensional optical lattice created by four laser beams, where Raman-sideband cooling [Web03b, Ker00, Tre01] is performed for 3.5 ms. During this stage, where a small magnetic field of several hundred mG is applied, the atoms are cooled and spin-polarized into the absolute ground state. After Raman-sideband cooling the ensemble size amounts to 1.5×10^7 atoms at a temperature of about $1 \mu\text{K}$. Then, the atoms are transferred into a large-volume far-off-resonant dipole trap [Gri00] generated by two crossed 100 W CO_2 laser beams, featuring a waist of about $600 \mu\text{m}$ each. As the optical trap is not strong enough to hold the atoms against gravity, an additional magnetic levitation field of 31 G/cm is applied [Web03a].

We use two different schemes, which we refer to as *Scheme A* and *Scheme B*. *Scheme A* is based on evaporation and detection at low magnetic fields, similar to our previous work [Mar07]. This scheme could be implemented in a simple way, but ramping up to the high probe field and back down to the detection field involves crossing several Feshbach resonances, which causes additional losses and heating. In the course of performing the present experiments, we developed an improved approach (*Scheme B*) that allows imaging in the magnetic high-field region and optimization of evaporative cooling at higher fields. In the following, both schemes are described in detail. Figure 3.5 illustrates the generic timing sequence for both schemes.

In *Scheme A*, evaporation is performed for 2 s at constant depth of the CO_2 laser trap in the magnetic low-field region. This stage of plain evaporation results in $\approx 5 \times 10^6$ atoms at a temperature slightly below $1 \mu\text{K}$. Then, the CO_2 laser trap is spatially overlapped with a crossed dipole trap created by a 1064 nm fiber laser, with waists of $40 \mu\text{m}$ and $250 \mu\text{m}$. To continue evaporation, the tightly focussed $40 \mu\text{m}$ beam is ramped down from 60 mW to 3.5 mW within 6.5 s, while the intensity of the $250 \mu\text{m}$ beam is fixed at 400 mW. During this procedure, both CO_2 laser beams are switched off, finishing the sample transfer. The s -wave scattering length is large and positive during the evaporation sequence and is adjusted for the final evaporation step to $a \approx 200 a_0$, corresponding to a magnetic field strength of $B_{\text{evap}} \simeq 21 \text{ G}$. Efficient evaporation conditions are encountered at this field because of an Efimov-related three-body recombination loss minimum [Kra06]. In this way, we end up with 10^5 thermal atoms at a temperature of 70 nK in the magnetic low-field region.

When ramping over the broad Feshbach resonances, sizeable effects of three-body recombination are unavoidable, even when applying the fastest possible ramp speeds. This causes direct recombination losses and additional heating [Web03c], which can cause subsequent evaporation losses in the measurement process. To avoid the latter effect, we recompress the trap by increasing the intensity of the $40 \mu\text{m}$ beam by about a factor 10 before the magnetic field ramp is carried out. In the final step of the sample preparation, the levitation field is decreased to 8 G/cm. The mean trap frequency is about $\bar{\omega} = 2\pi \times 46(5) \text{ Hz}$, and the final sample contains 10^5 thermal atoms at a temperature of 120 nK in the magnetic low-field

region.

The measurements are performed by linearly ramping from B_{evap} within a ramp time $t_{\text{ramp},1} = 10$ ms to the probe fields B_{probe} in the magnetic high-field region. As described above, crossing of the broad s -wave Feshbach resonances leads to considerable heating of the sample and additional particle loss. We estimate the temperature at B_{probe} to be between 150 nK and 200 nK with *Scheme A*.

To determine the particle number, we linearly decrease the magnetic bias field to zero ($B_{\text{imag}} \simeq 0$) within $t_{\text{ramp},2} = 10$ ms and carry out resonant absorption imaging. The temperature is obtained in time-of-flight expansion measurements after release from the trap. The magnetic field strength is determined from measurements of the $(3,3) \rightarrow (4,4)$ microwave transition frequency by applying the Breit-Rabi formula [Bre31].

In *Scheme B*, after loading the atoms from the Raman lattice to the levitated CO₂ laser trap, the magnetic field is linearly ramped to the magnetic high-field region within 10 ms. For measurements performed below 800 G the ramp ends at 561 G ($a = 1090 a_0$), whereas for measurements above 800 G it ends at 970 G ($a = 1140 a_0$).

At this stage, the three-body recombination losses that are encountered while crossing the broad s -wave Feshbach resonances are limited because of the low density and the relatively high temperature ($T \simeq 1 \mu\text{K}$) of the sample. The temperature dependence of losses follows from the unitarity limitation of three-body recombination rates [D'I04]. To compensate for the small change in the magnetic moment that is encountered during the ramp as a consequence of the quadratic contribution to the Zeeman effect, the magnetic levitation field is adjusted simultaneously. Then, 2 s of plain evaporation result in $\approx 5 \times 10^6$ atoms at a temperature of about 1 μK (similar to *Scheme A*). Then, the CO₂ laser trap is spatially overlapped with the 1064 nm crossed dipole trap as described in *Scheme A*.

In the crossed dipole trap, we perform forced evaporation by decreasing the laser intensity of the 40 μm beam from 60 mW to 3.5 mW within 15 s. During this step, the intensity of the 250 μm beam is changed only slightly, from 400 mW to 300 mW. Both CO₂ lasers are switched off during the first 5 s of evaporation to achieve an efficient transfer to the 1064 nm trap. The magnetic bias field is adjusted during the evaporation sequence for optimized elastic scattering conditions. The last evaporation step of this sequence ends at $B_{\text{evap}} = 558.7$ G ($a \approx 700 a_0$) or $B_{\text{evap}} = 894$ G ($a \approx 300 a_0$), respectively. Note that close to 894 G an Efimov-related recombination minimum is present [Ber11b], which apparently facilitates efficient evaporation. After recompression and reshaping, leading to a mean trap frequency of $\bar{\omega} = 2\pi \times 26(3)$ Hz, we end up with a non-condensed sample of between 5×10^4 and 10^5 atoms at a temperature of about 50 nK.

For *Scheme B*, no broad s -wave Feshbach resonances are crossed in the final magnetic field ramps to reach B_{probe} , and therefore no noteworthy heating effects and particle losses are observed. The particle number is determined by high-field imaging in the vicinity of the zero crossing of the broad s -wave Feshbach resonances at $B_{\text{imag}} = 556.4$ G and $B_{\text{imag}} = 887.5$ G. The magnetic field ramps to and from B_{probe} involve linear changes of the magnetic field with $t_{\text{ramp},1} = t_{\text{ramp},2} = 10$ ms, as for *Scheme A*. The procedures for magnetic field calibration

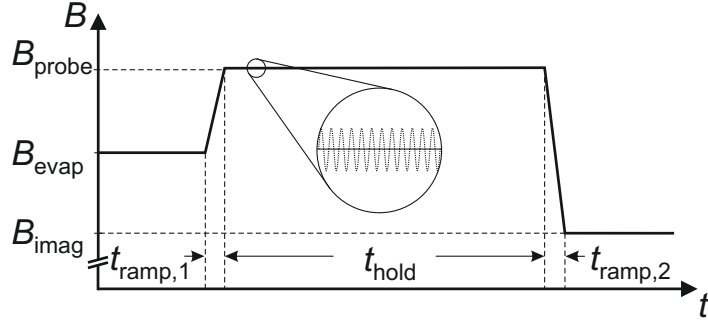


Figure 3.5: Timing sequence for the magnetic field ramps for trap-loss spectroscopy and binding energy measurements. The magnetic field strength B is linearly ramped from the final evaporation field B_{evap} within the ramping time $t_{\text{ramp},1}$ to the probe field B_{probe} . After an experimentally optimized hold time t_{hold} ranging between 0.2 and 1 s, the magnetic field strength is (linearly) ramped to the imaging field B_{imag} . For *Scheme A*, B_{evap} and B_{imag} are in the magnetic low-field region. The magnified segment visualizes B_{probe} , which is constant in time for trap-loss spectroscopy (solid line) and sinusoidally modulated for the determination of binding energies (dashed line).

and temperature determination are the same as the ones in *Scheme A*.

3.3.2 Trap-loss spectroscopy

Trap-loss spectroscopy is a well established method based on the enhancement of collisional losses in the vicinity of a Feshbach resonance [Chi10]. For atoms in the absolute atomic ground state, where inelastic binary collision are energetically forbidden, three-body recombination is the lowest-order loss process. In this process three colliding atoms recombine to a molecule and a free atom. Typically, the kinetic energy released far exceeds the trapping potential, leading to loss of the three particles involved. The general a^4 -scaling of three-body recombination rates [Fed96, Esr99, Nie99, Web03c] leads to a maximum in losses at the magnetic field position B_{max} , corresponding to the divergence of a at the Feshbach resonance pole, and a minimum at the position B_{min} , close to the zero crossing of the s -wave scattering length. This allows the observed losses to be directly related to the positions and widths of the Feshbach resonances.

In this Section, we will first report on experiments characterizing the scattering properties in the vicinity of the broad s -wave Feshbach resonances, as shown in Fig. 3.2(a), by performing a broad magnetic field scan with large step size. Then, we decrease the step size to perform detailed scans to identify and characterize narrow Feshbach resonances, which originate from states with higher rotational angular momentum ($L > 0$).

Trap-loss spectroscopy is performed by recording the remaining atom fraction after a hold time t_{hold} at the probe field B_{probe} . In general, we cannot exclude additional losses encountered within $t_{\text{ramp},1}$ and $t_{\text{ramp},2}$ during the magnetic field ramps $B_{\text{evap}} \rightarrow B_{\text{probe}}$ and $B_{\text{probe}} \rightarrow B_{\text{imag}}$. However, for the characterization of narrow Feshbach resonances only a small magnetic field region is investigated, where variations in the initial atom number are negligible. Furthermore, the measurements are performed with $t_{\text{hold}} \gg t_{\text{ramp},1}, t_{\text{ramp},2}$,

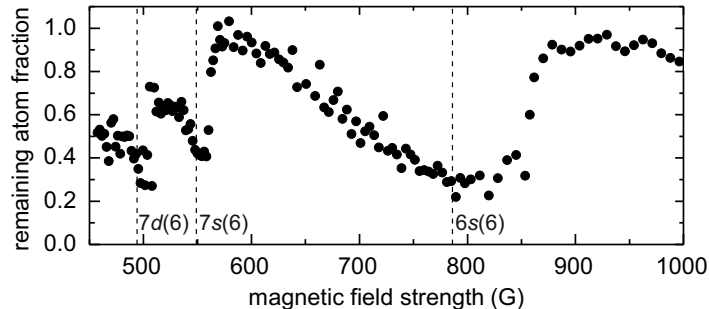


Figure 3.6: Results of trap-loss spectroscopy in the magnetic field region between 450 G and 1000 G, performed with *Scheme B*. The enhancements in losses result from broad Feshbach resonances centered at 494 G, 549 G and 787 G. The resonance positions, which are derived from our theoretical model (see Sec. 3.4), are indicated by dashed lines, labeled according to the quantum numbers $FL(M_F)$ of the molecular states that cause the resonances. The measurements are performed with a hold time of 500 ms. Narrow Feshbach resonances are not visible in this scan because of the large step size of about 2 G. A remaining atom fraction of 1.0 corresponds to 8×10^4 atoms.

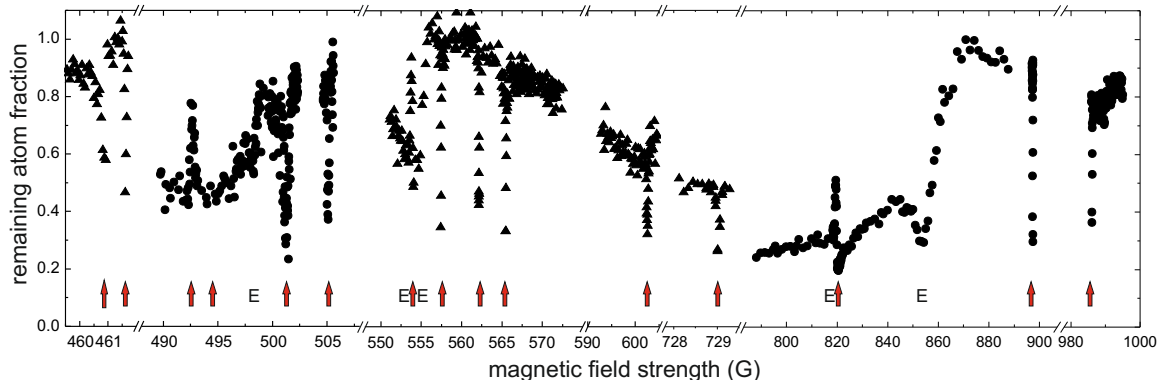


Figure 3.7: (Color online) Detailed results of trap-loss spectroscopy in the magnetic high-field region. We observe 15 Feshbach resonances, stemming from d -, g - and i -wave molecular states. Measurements indicated by (\blacktriangle)-symbols are obtained by *Scheme A*, whereas the (\bullet)-symbols refer to data points acquired with *Scheme B*. The poles of the Feshbach resonances, omitting the s -wave resonances, are marked with an arrow. The loss features at 498.1 G, 553.3 G, 554.7 G, 818.9 G and 853.1 G, which are indicated by “E”, are related to Efimov loss resonances as reported in Refs. [Ber11b, Fer11]. Note that the data in the intervals [728,729.5] G and [980,1000] G, which are measured for different t_{hold} , are multiplied by scaling factors of 0.5 and 0.9, respectively, to reproduce the overall behavior shown in Fig. 3.6. A remaining atom fraction of 1.0 corresponds to 8×10^4 atoms.

strongly limiting the effect of finite ramp times.

The broad scan of the magnetic high-field region covers a range from 450 to 1000 G, as shown in Fig. 3.6. This scan clearly shows two broad loss features around 550 G and 800 G, which can be assigned to the two high-field s -wave Feshbach resonances, as discussed in Sec. 3.2 (see upper panel Fig. 3.2). These measurements demonstrate the large width of the Feshbach resonance near 800 G. Because of the unitarity limitation of three-body recombination losses [D'I04], it is not possible to determine B_{\max} accurately for the s -wave resonances by trap-loss spectroscopy.

In the region around 500 G, no s -wave Feshbach resonance is expected, but the theoretical model predicts a series of closely adjoining d -wave Feshbach resonances, as shown in Fig. 3.2. One of these has a width of about 5 G, producing the broad loss signal around 495 G seen in Figs. 3.6 and 3.7.

We perform high-resolution scans by decreasing the step size of the magnetic field scans to a few mG. The results of these scans are displayed in Fig. 3.7. We observe 15 narrow loss features, which can be assigned according to the theoretical model given in Sec. 3.4 to Feshbach resonances originating from the coupling of the free atoms to molecular states with rotational angular momentum $L > 0$.

We observe three narrow resonances that cannot be attributed to s -, d - or g -wave molecular states in the present model. They are found at 461.62 G, 557.45 G and 562.17 G. Our model, however, predicts the existence of Feshbach resonances stemming from i -wave molecular states ($L = 6$) in the magnetic field regions where we observe these features. The calculations are not accurate enough to establish an unambiguous assignment, but the match between experiment and theory nevertheless provides strong evidence that this is the first experimental observation of i -wave Feshbach resonances. These resonances are discussed further in Sec. 3.4.

The positions of the poles of the d -, g - and i -wave Feshbach resonances obtained in these measurements are summarized in Table 3.1. The peak positions are determined by Gaussian fits to the loss peaks. For several of these resonances we also identify recombination loss minima, which also provide estimates for the corresponding resonance widths.

Figure 3.8 shows expanded views of two regions in Fig. 3.7, where interesting cases of overlapping FR scenarios occur. Figure 3.8(a) shows a g -wave resonance centered at 554.06(2) G sitting on the shoulder of the 549 G s -wave Feshbach resonance at a background scattering length of about $-1000 a_0$. The zero crossing of $a(B)$ leads to a loss minimum at 553.73(2) G. Even more intriguing is a d -wave Feshbach resonance situated at 820.4(2) G. There, the broad 787 G s -wave Feshbach resonance leads to an extremely large background scattering length of about $-4200 a_0$. Experimentally, this large background masks the loss maximum but clearly reveals the zero crossing at 819.41(2) G, as shown in Fig. 3.8(b). Both the g -wave and d -wave resonance have rather large widths, of 0.33(3) G and 0.96(22) G, respectively. Efimov-related three-body physics has been revealed in the vicinity of these resonances, as reported in Refs. [Ber11b, Fer11].

molecular state $n(f_1 f_2)FL(M_F)$	B_{\max} (G)	B_{\min} (G)
-6(34)5 <i>d</i> (5)	460.86(5)	
<i>i</i> -wave ¹⁾	461.62(5)	
-6(34)7 <i>d</i> (<i>x</i>) ²⁾	492.45(3)	492.63(3)
-6(34)7 <i>d</i> (<i>x</i>) ²⁾	494.4(9)	499.4(1)
-6(34)7 <i>d</i> (<i>x</i>) ²⁾	501.24(3)	
-6(34)7 <i>d</i> (<i>x</i>) ²⁾	505.07(3)	
<i>g</i> (3) ³⁾	554.06(2)	553.73(2)
<i>i</i> -wave ¹⁾	557.45(3)	
<i>i</i> -wave ¹⁾	562.17(3)	
<i>g</i> (4) ³⁾	565.48(3)	
-2(33)6 <i>g</i> (6) ⁴⁾	602.54(3)	
<i>g</i> (5) ³⁾	729.03(3)	
-6(34)6 <i>d</i> (6)	820.37(20)	819.41(2)
-6(34)5 <i>d</i> (5)	897.33(3)	
-6(34)6 <i>d</i> (4)	986.08(3)	

Table 3.1: Results of trap-loss spectroscopy in the magnetic high-field region. The table shows the magnetic field values for loss maxima (B_{\max}), resulting from the poles of the Feshbach resonances, and minima (B_{\min}), which are related to the zero crossings of the s -wave scattering length. The numbers in brackets are the experimental uncertainties, including statistical and systematic errors. The assignments of the Feshbach resonances identify the molecular states that cause the resonances. In the case of very narrow resonances, the zero crossings could not be determined experimentally.

¹⁾For the *i*-wave resonances only the L -quantum number of the molecular state is known.

²⁾These Feshbach resonances arise from d -wave molecular states with $M_F = 4, 5, 6$ and 7 , which are strongly mixed at the atomic threshold. Therefore, we cannot give simple M_F quantum numbers and use “ x ” to indicate the strong coupling.

³⁾For these states only the quantum numbers L and M_F are known.

⁴⁾This molecular state is strongly mixed with the state $-6(34)6g(6)$.

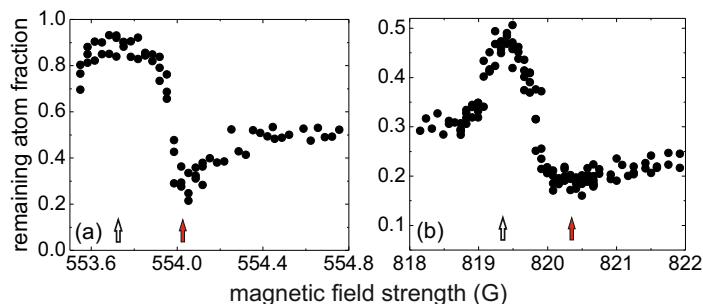


Figure 3.8: (Color online) Expanded view of Fig. 3.7, showing the Feshbach resonances arising from the $g(3)$ state (a) and the $-6(34)6d(6)$ state (b), which overlap with the broad s -wave resonances. The filled and empty arrows mark the poles and zero crossings of the scattering length, respectively. The remaining atom fraction at the zero crossing in (b) is limited due to losses during the magnetic field ramps.

3.3.3 Binding energy measurements

Binding energy measurements of weakly bound dimer states provide a powerful additional tool to extract information on the cesium interaction potentials and scattering properties. In particular, for the s -wave Feshbach resonances the exact positions of the poles are obscured by strong loss across a broad magnetic field range, but can be extracted accurately from binding energies. In the present work, we measure the binding energies by magnetic field modulation spectroscopy, a method which was introduced in Ref. [Tho05]. This method is based on a sinusoidal modulation of the magnetic bias field and allows the creation of dimers starting from an ultracold atom sample. This leads to an observable loss signal due to fast atom-dimer relaxation when the modulation frequency matches the binding energy of the dimers plus the small relative kinetic energy of the colliding atoms. Since the modulation of the magnetic field is parallel to the magnetic bias field, only transitions between states with the same projection quantum number of the total angular momentum are observed. This procedure has been successfully applied in several experiments [Tho05, Web08, Lan09, Tha09, Bea10, Pas10, Gro10] to determine atomic scattering properties.

The atom samples for the binding energy measurements are prepared according to *Scheme B*, as described in Sec. 3.3.1. At B_{probe} , a modulation signal is applied for a variable duration of $t_{\text{hold}} = 0.1$ to 1 s, in a frequency range of 50 to 1600 kHz and an amplitude between 0.5 and 3 G (see Fig. 3.5). The amplitude and the duration of the pulse are experimentally adjusted for each binding energy measurement to optimize the signal-to-noise ratio. The signal is generated by a programmable frequency generator and subsequently amplified by a commercial 25 W radio-frequency amplifier, which drives the current in a separate set of coils and thereby creates the modulation of the magnetic bias field.

The measurements are usually performed by varying the modulation frequency at a fixed B_{probe} . Another possibility, however, is to scan B_{probe} while the modulation frequency is kept constant. The advantage of the latter approach is that it is less sensitive to atom losses caused by technical imperfections, such as resonance phenomena in the electric circuit that drives the transitions. We checked that the two methods give consistent results in our measurements. Figure 3.9 shows sample loss signals derived in a frequency scan (a) and a magnetic field scan (b).

We studied the binding energies E_b of the high-field s -wave states and of several d -, g - and i -wave states, as shown in Fig. 3.10. For the s -wave states with $E_b/h < 200$ kHz, we observed asymmetric line shapes resulting from the finite temperature of the samples. We include this effect in our fitting routine using the line-shape model of Ref. [Nap94]. For s -wave states with $E_b/h > 200$ kHz and for dimer states with higher rotational angular momentum, the binding energy has a strong dependence on the magnetic field. In these cases, the magnetic field noise and the field gradient that is applied to levitate the atoms broaden and symmetrize the loss signals. For these symmetrized signals, the effect from the finite temperature plays a minor role, and we therefore obtain E_b by fitting a simple Gaussian distribution to the data.

In the binding energy measurements, we observe several avoided crossings between molecular states. Around 897 G and $E_b/h \approx 500$ kHz, the $-6(34)6s(6)$ state crosses the $-6(34)5d(5)$

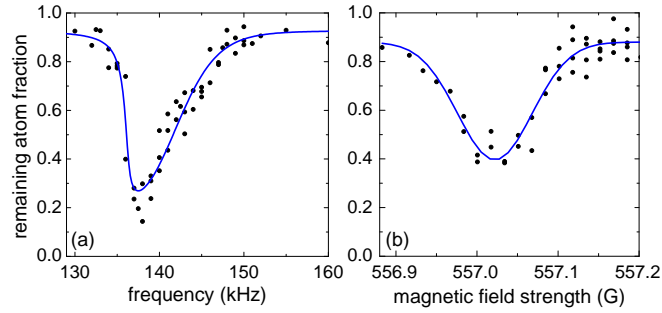


Figure 3.9: (Color online) Typical signals for magnetic field modulation spectroscopy. (a) Frequency scan at a fixed magnetic field strength of 911.69 G. The asymmetric shape of the signal is fitted by a model that takes the temperature of the sample into account [Nap94]. (b) Magnetic field scan at a constant modulation frequency of 425 kHz, revealing a loss resonance at 557.02 G. This resonance stems from the s -wave molecular state. The line represents a Gaussian fit. A remaining atom fraction of 1.0 corresponds to (a) 4.5×10^4 and (b) 2.5×10^4 atoms.

state. These two states are clearly resolved as separate loss features in each magnetic field scan performed at fixed frequency in the crossing region, as shown in the inset of Fig. 3.10(a). In addition, we observe an avoided crossing at about 557 G and $E_b/h \approx 350$ kHz between the $-6(34)7s(6)$ state and an i -wave state, which clearly shows up in the binding energy measurements presented in Fig. 3.10(b).

In view of the large difference in the partial-wave angular momentum $\Delta L = 6$, the crossing around 557 G appears to be surprisingly strongly avoided. To confirm this, we prepare molecular samples in the s -wave state by Feshbach ramps [Chi10] and perform magnetic moment spectroscopy for magnetic field strengths ranging from 556.5 G to 557.5 G using the Stern-Gerlach effect in the same way as described in Ref. [Mar07]. To do this, we release the dimers from the trap while the magnetic field gradient is switched on. After a fixed time of flight, the dimers are dissociated by ramping back over either the 557.45 G or the 565.48 G Feshbach resonance. Subsequently, the atoms are imaged and the molecular magnetic moment is extracted from the vertical position of the atom cloud. We observe a smooth change of the magnetic moment around 557.15 G over a magnetic field range of about 250 mG, indicating that the character of the molecular state also changes smoothly, from s -wave to i -wave character, over the width of the crossing. Because of large calibration uncertainties in these measurements, we cannot provide absolute values for the molecular magnetic moments. In another experiment, we start with weakly bound s -wave Feshbach molecules at a magnetic field of 560 G and attempt to jump the avoided crossing diabatically. As in the experiment previously outlined, we can simultaneously detect and distinguish s -wave and i -wave dimers by their magnetic moment. Applying a maximum ramp speed of 10 G/ms, the number of transferred dimers is below our detection limit. This sets a lower limit of 30 kHz to the strength of the avoided crossing according to the Landau-Zener formula [Lan32, Zen32].

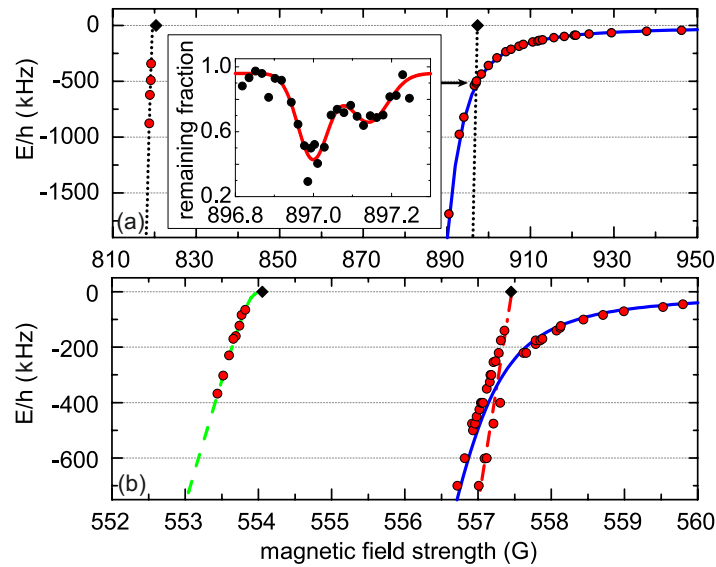


Figure 3.10: (Color online) Results of experimental binding energy measurements. (a) the $-6(34)6d(6)$ and $-6(34)5d(5)$ states (dashed lines) and the $-6(34)6s(6)$ state (solid line) between 820 G and 950 G. The lines are guides for the eye. The inset shows a binding energy measurement at the crossing of the $-6(34)6s(6)$ and $-6(34)5d(5)$ states at 509 kHz. At fields above 900 G the s -wave state takes on the character of the least-bound state $-1(33)6s(6)$, which has a binding energy around $h \times 50$ kHz away from avoided crossings. The strong variation of the magnetic moment follows from the avoided crossing with this threshold s -wave state. (b) the binding energies of the $g(3)$ state (dashed line), an i -wave state (dot-dash line) and the $-6(34)7s(6)$ state (solid line). The positions of the resonance poles are marked by a (\blacklozenge)-symbol, with values taken from Table 3.1.

3.4 Theoretical model

The Hamiltonian for the interaction of two Cs atoms may be written

$$\frac{\hbar^2}{2\mu} \left[-R^{-1} \frac{d^2}{dR^2} R + \frac{\hat{L}^2}{R^2} \right] + \hat{h}_1 + \hat{h}_2 + \hat{V}(R), \quad (3.1)$$

where μ is the reduced mass and \hat{L}^2 is the operator for the end-over-end angular momentum of the two atoms about one another. The monomer Hamiltonians including Zeeman terms are

$$\hat{h}_j = \zeta \hat{i}_j \cdot \hat{s}_j + g_e \mu_B B \hat{s}_{zj} + g_n \mu_B B \hat{i}_{zj}, \quad (3.2)$$

where ζ is the atomic hyperfine constant, \hat{s}_1 and \hat{s}_2 represent the electron spins of the two atoms and \hat{i}_1 and \hat{i}_2 represent nuclear spins. g_e and g_n are the electron and nuclear g -factors, μ_B is the Bohr magneton, and \hat{s}_z and \hat{i}_z represent the z -components of \hat{s} and \hat{i} along a space-fixed Z axis whose direction is defined by the external magnetic field B . The interaction between the two atoms $\hat{V}(R)$ is

$$\hat{V}(R) = \hat{V}^c(R) + \hat{V}^d(R). \quad (3.3)$$

Here $\hat{V}^c(R) = V_0(R) \hat{\mathcal{P}}^{(0)} + V_1(R) \hat{\mathcal{P}}^{(1)}$ is an isotropic potential operator that depends on the potential energy curves $V_0(R)$ and $V_1(R)$ for the respective $X^1\Sigma_g^+$ singlet and $a^3\Sigma_u^+$ triplet states of Cs_2 , as shown in Figure 3.1. The singlet and triplet projectors $\hat{\mathcal{P}}^{(0)}$ and $\hat{\mathcal{P}}^{(1)}$ project onto subspaces with total electron spin quantum numbers 0 and 1 respectively. The term $\hat{V}^d(R)$ represents small, anisotropic spin-dependent couplings that are responsible for the avoided crossings discussed in the present paper and are discussed further in Section 3.4.3 below.

3.4.1 Computational methods for bound states and scattering

The present work solves the Schrödinger equation for both scattering and Feshbach bound states of Cs_2 by coupled-channel methods, using a basis set for the electron and nuclear spins in a fully uncoupled representation,

$$|s_1 m_{s1}\rangle |i_1 m_{i1}\rangle |s_2 m_{s2}\rangle |i_2 m_{i2}\rangle |LM_L\rangle, \quad (3.4)$$

symmetrised to take account of exchange symmetry. The matrix elements of the different terms in the Hamiltonian in this basis set are given in the Appendix of Ref. [Hut08]. The only rigorously conserved quantities are the parity, $(-1)^L$, and the projection of the total angular momentum, $M_{\text{tot}} = m_{s1} + m_{i1} + m_{s2} + m_{i2} + M_L$. The calculations in this paper used basis sets with all possible values of m_s and m_i for both atoms that are consistent with the required M_{tot} and parity, truncated at $L_{\text{max}} = 4$ (an *sdg* basis set) unless otherwise indicated. All calculations in this paper are for s -wave incoming channels, so have even parity.

Both scattering and bound-state calculations use propagation methods and do not rely on basis sets in the interatomic distance coordinate R .

Scattering calculations are carried out using the MOLSCAT package [Hut94b], as modified to handle collisions in magnetic fields [GM07]. At each magnetic field B , the wavefunction log-derivative matrix at collision energy E is propagated from $R_{\min} = 6 a_0$ to $R_{\text{mid}} = 20 a_0$ using the propagator of Manolopoulos [Man86] with a fixed step size of $0.002 a_0$, and from R_{mid} to $R_{\max} = 4,000 a_0$ using the Airy propagator [Ale87] with a variable step size controlled by the parameter $\text{TOLHI}=10^{-5}$ [Ale84]. Scattering boundary conditions [Joh73] are applied at R_{\max} to obtain the scattering S-matrix. The energy-dependent s -wave scattering length $a(k)$ is then obtained from the diagonal S-matrix element in the incoming $L = 0$ channel using the identity [Hut07]

$$a(k) = \frac{1}{ik} \left(\frac{1 - S_{00}}{1 + S_{00}} \right), \quad (3.5)$$

where $k^2 = 2\mu E/\hbar^2$.

In the vicinity of a resonance at the lowest atomic threshold, the scattering length as a function of magnetic field (at small fixed k) follows the functional form

$$a(B) = a_{\text{bg}} [1 - \Delta/(B - B_{\text{res}})]. \quad (3.6)$$

The resonance pole position B_{res} may be associated with the 3-body loss maximum at a field B_{\max} . For a narrow resonance (where the background scattering length a_{bg} does not vary significantly across the resonance), the width Δ is conveniently obtained from the difference between the positions of the pole and zero in $a(B)$. Experimentally, this corresponds to the difference in field between the loss maximum at B_{\max} and the loss minimum at B_{\min} . We have extended MOLSCAT to provide an option to *converge* on poles and zeroes of $a(B)$, instead of extracting them from a fit to a grid of points.

Weakly bound levels for Feshbach molecules are obtained using a variant of the propagation method described in Ref. [Hut08]. The log-derivative matrix is propagated outwards from R_{\min} to R_{mid} with a fixed step size of $0.002 a_0$ and inwards from R_{\max} to R_{mid} with a variable step size, using the same propagators as for scattering calculations. $R_{\text{mid}} = 25 a_0$ and $R_{\max} = 4,000 a_0$ were used for most bound states, although $R_{\text{mid}} = 35 a_0$ and $R_{\max} = 8,000 a_0$ were needed for states within about 50 kHz of dissociation. In Ref. [Hut08], bound-state energies at a fixed value of the magnetic field B were located using the BOUND package [Hut93], which converges on energies where the smallest eigenvalue of the log-derivative matching determinant is zero [Hut94a]. However, for the purposes of the present work we used a new package, FIELD,² which instead works at fixed binding energy and converges in a similar manner on the magnetic fields at which bound states exist. BOUND and FIELD both implement a node-count algorithm [Hut94a] which makes it straightforward to ensure that *all* bound states that exist in a particular range of energy or field are located.

As described above, zero-energy Feshbach resonances can in principle be located as the fields at which the scattering length $a(B)$ passes through a pole. However, with this method it is necessary first to search for poles, and it is quite easy to miss narrow resonances. However, since resonances occur at fields where there is a bound state at zero energy, the FIELD package provides a much cleaner approach: simply running FIELD at zero energy provides a complete list of all fields at which zero-energy Feshbach resonances exist (see Sec. 3.7).

² J. M. Hutson, FIELD computer program, version 1.

In the present work we located resonances using FIELD and then obtained their widths by converging on the nearby zero in $a(B)$ using MOLSCAT.

3.4.2 Representation of the potential curves

At long range, the potentials are

$$V_S^{\text{LR}}(R) = - C_6 y_6(R)/R^6 - C_8 y_8(R)/R^8 - C_{10} y_{10}(R)/R^{10} \pm V_{\text{ex}}(R), \quad (3.7)$$

where $S = 0$ and 1 for singlet and triplet, respectively. The dispersion coefficients C_n are common to both potentials and the functions $y_n(R)$ account for retardation corrections [Mar94]. The exchange contribution is [Smi65]

$$V_{\text{ex}}(R) = A_{\text{ex}}(R/a_0)^\gamma \exp(-\beta_{\text{ex}}R/a_0), \quad (3.8)$$

and makes an attractive contribution for the singlet and a repulsive contribution for the triplet. The value of β_{ex} is usually obtained from the ionization energies of the atoms [Smi65], which for Cs gives $\beta_{\text{ex}} = 1.069946$, and γ is related to β by $\gamma = 7/\beta - 1$. In the present work we found that, to reproduce the experimental results, it was necessary to reduce β_{ex} slightly from its original value. We therefore introduce an additional factor ρ_{ex} so that $\beta_{\text{ex}} = 1.069946\rho_{\text{ex}}$, with γ adjusted accordingly.

The detailed shapes of the short-range singlet and triplet potentials are relatively unimportant for the ultracold scattering properties and near-threshold binding energies considered here, although it is crucial to be able to vary the *volume* of the potential wells to allow adjustment of the singlet and triplet scattering lengths. In the present work we retained the functional form used by Leo *et al.* [Leo00] and Chin *et al.* [Chi04]. Each short-range potential is represented by a set of 14 ab initio points between $R = 7$ and $20 a_0$ [Kra90]. The two sets of potential points are first multiplied by R^6 and the resulting (smoother) functions are interpolated using Akima splines [Aki91] to obtain their values at $R_{\text{LR}} = 17.6 a_0$. The value of A_{ex} is chosen to match V_{ex} to $(V_1 - V_0)/2$ at R_{LR} , and both sets of points are shifted to match $(V_1 + V_0)/2$ at R_{LR} . Finally, the analytic $V_S^{\text{LR}}(R)$ is used to generate new grid points between $17.6 a_0$ and $20 a_0$ and the resulting sets of points are reinterpolated as above between $R = 7$ and $20 a_0$. The analytic long-range form (3.7) is used outside $20 a_0$.

The flexibility needed to adjust the singlet and triplet scattering lengths is provided by simply adding a quadratic shift to each of the singlet and triplet potentials inside its minimum,

$$V_S^{\text{shift}}(R) = S_S(R - R_{eS})^2 \quad \text{for} \quad R < R_{eS}, \quad (3.9)$$

with $R_{e0} = 8.75 a_0$ and $R_{e1} = 11.8 a_0$.

3.4.3 Magnetic dipole interaction and second-order spin-orbit coupling

At long range, the coupling $\hat{V}^{\text{d}}(R)$ of Eq. (3.3) has a simple magnetic dipole-dipole form that varies as $1/R^3$ [Sto88, Moe95]. However, for atoms as heavy as Cs, second-order spin-orbit

coupling provides an additional contribution that has the same tensor form as the dipole-dipole term and dominates at short range [Mie96]. In the present work, $\hat{V}^d(R)$ is represented as

$$\hat{V}^d(R) = \lambda(R) (\hat{s}_1 \cdot \hat{s}_2 - 3(\hat{s}_1 \cdot \vec{e}_R)(\hat{s}_2 \cdot \vec{e}_R)) , \quad (3.10)$$

where \vec{e}_R is a unit vector along the internuclear axis and λ is an R -dependent coupling constant. The second-order term has been calculated by Kotochigova *et al.* [Kot00] and fitted to a biexponential form, so that the overall form of $\lambda(R)$ is

$$\lambda(R) = E_h \alpha^2 \left[\begin{array}{l} A_{2\text{SO}}^{\text{short}} \exp(-2\beta_{2\text{SO}}R) \\ + A_{2\text{SO}}^{\text{long}} \exp(-\beta_{2\text{SO}}R) + \frac{1}{(R/a_0)^3} \end{array} \right], \quad (3.11)$$

where $\alpha \approx 1/137$ is the fine-structure constant and the parameters obtained from fitting to the electronic structure calculations [Kot00] are $A_{2\text{SO}}^{\text{short}}/hc = 34.4 \text{ cm}^{-1}$, $A_{2\text{SO}}^{\text{long}}/hc = 0.25 \text{ cm}^{-1}$ and $\beta_{2\text{SO}} = -0.35 a_0^{-1}$. However, in fitting to the experimental results, this coupling function was found to be slightly too strong. We therefore retained the functional form (3.11) but introduced an additional scaling factor $S_{2\text{SO}}$ that multiplies both exponential terms and is allowed to vary in the least-squares fit to the experimental results.

3.5 Least-squares fitting of potential parameters

In the present work, our primary objective is to obtain potential parameters that give a reliable representation of $a(B)$ in the regions where Efimov resonances occur, namely near 8 G, 554 G and 853 G. Earlier potentials [Leo00, Chi04] focused on representing the positions of Feshbach resonances in the low-field region below about 60 G.

A key advantage of the propagator approach to locating bound states and resonances, implemented in the BOUND and FIELD programs, is that it is fast enough to be incorporated in a least-squares fitting program. We have therefore carried out direct least-squares refinement of the potential parameters. We experimented with fitting various combinations of parameters, and concluded that adequate flexibility is available in the 6-parameter space $S_0, S_1, C_6, C_8, S_{2\text{SO}}, \rho_{\text{ex}}$.

Table 3.2: Quality of fit between calculations using the M2012 model and the experimental results used in the fit.

	B_{obs} (G)	B_{calc} (G)	$B_{\text{obs}} - B_{\text{calc}}$ (G)	Unc. (G)	method	reference
$-7(44)6s(6)$ at 7.8 MHz	17.53	17.51	0.02	0.02	microwave spectr.	[Mar07]
$-7(44)6s(6)$ at 1.2 MHz	21.60	21.59	0.01	0.02	microwave spectr.	[Mar07]
$-7(44)6s(6)$ at 104 kHz	32.05	31.70	0.35	0.03	magnetic field mod.	[Lan09]
Zero crossing near 17 G	17.12	17.14	-0.02	0.01	Bloch oscillations	[Gus08a]
$-2(33)4d(4)$ at 174 kHz	48.01	48.01	0.00	0.06	magnetic field mod.	[Lan09]
$-2(33)4d(4)$ crossing strength 78-24 kHz	1.19	1.21	-0.02	0.02	magnetic field mod.	[Hut08]
Loss minimum (d) near 48 G	47.94	47.98	-0.04	0.04	inferred from magn. field mod.	[Lan09]
Loss maximum (d) near 48 G	47.78	47.79	-0.01	0.06	inferred from magn. field mod.	[Lan09]
Δ (d) near 48 G	0.16	0.18	-0.02	0.06	inferred from magn. field mod.	[Lan09]
$2g(2)$ at 17 kHz	53.42	53.76	-0.34	0.08	magnetic field mod.	[Lan09]
$-2(33)6g(6)$ at 18.6 G (MHz, not G)	-5.03	-4.99	-0.04	0.01	microwave spectr.	[Mar07]
Loss maximum $-6(34)7d(x)$	492.45	492.68	-0.23	0.06	trap loss spectr.	<i>this work</i>
Loss maximum $-6(34)7d(x)$	501.24	501.44	-0.20	0.06	trap loss spectr.	<i>this work</i>
Loss maximum $-6(34)7d(x)$	505.07	505.37	-0.30	0.06	trap loss spectr.	<i>this work</i>
$-6(34)7s(6)$ at 1.0 MHz	556.47	556.48	-0.01	0.02	magnetic field mod.	<i>this work</i>
$-6(34)7s(6)$ at 700 kHz	556.72	556.76	-0.04	0.02	magnetic field mod.	<i>this work</i>
$-6(34)7s(6)$ at 170 kHz	557.88	557.80	0.08	0.03	magnetic field mod.	<i>this work</i>
$-6(34)7s(6)$ at 100 kHz	558.44	558.36	0.08	0.03	magnetic field mod.	<i>this work</i>
Zero crossing near 556 G	556.26	556.19	0.07	0.03	collapse of BEC	[Zen12]
$-3(33)6g(3)$ at 368 kHz	553.44	553.44	-0.00	0.01	magnetic field mod.	<i>this work</i>
Loss minimum (g) near 554 G	553.73	553.75	-0.02	0.01	trap loss spectr.	<i>this work</i>
Loss maximum (g) near 554 G	554.06	554.07	-0.01	0.02	trap loss spectr.	<i>this work</i>
Δ (g) near 554 G	0.33	0.32	0.01	0.01	trap loss spectr.	<i>this work</i>
$-6(34)6s(6)$ at 1.7 MHz	890.52	890.61	-0.09	0.02	magnetic field mod.	<i>this work</i>
$-6(34)6s(6)$ at 356 kHz	899.93	900.19	-0.26	0.03	magnetic field mod.	<i>this work</i>
$-6(34)6s(6)$ at 110 kHz	915.66	915.54	0.12	0.03	magnetic field mod.	<i>this work</i>
Zero crossing near 881 G	880.90	880.66	0.24	0.03	collapse of BEC	[Zen12]
$-6(34)6d(6)$ at 342 kHz	819.17	819.20	-0.03	0.03	magnetic field mod.	<i>this work</i>
Loss minimum (d) near 820 G	819.41	819.37	0.04	0.03	trap loss spectr.	<i>this work</i>
Loss maximum (d) near 820 G	820.37	820.33	0.04	0.02	trap loss spectr.	<i>this work</i>
Δ (d) near 820 G	0.96	0.97	-0.01	0.05	trap loss spectr.	<i>this work</i>

The set of experimental results used for fitting is listed in Table 3.2. It consists of all the observed resonance positions (loss maxima) in the regions relevant to Efimov physics, together representative bound-state positions. It also includes zero crossings of the scattering lengths measured from loss minima, Bloch oscillations [Gus08a] and BEC collapse measurements [Zen12]. All the bound-state positions are expressed as the fields at which bound states exist at specific binding energies, except for the $-3(33)6g(6)$ state, which is almost parallel to the lowest threshold and is included in the fit as a binding energy at $B = 18.6$ G. The strength of the avoided crossing between the $-2(33)4d(4)$ and $-7(44)6s(6)$ states near 48 G is included as an explicit difference between fields where states exist at energies of 78 kHz and 24 kHz. The quantity optimized in the least-squares fits was the sum of squares of residuals $((\text{obs}-\text{calc})/\text{uncertainty})$, with the uncertainties listed in Table 3.2.³

Table 3.3: Parameters of the fitted potential.

	fitted value	confidence limit (95%)	sensitivity
$C_6 (E_h a_0^6)$	6890.4768	0.081	0.0003
$C_8 (E_h a_0^8)$	1009289.6	2900	0.1
$S_0 (E_h a_0^{-2})$	3.172749×10^{-4}	2.5×10^{-6}	2.7×10^{-10}
$S_1 (E_h a_0^{-2})$	1.343217×10^{-4}	2.5×10^{-6}	1.3×10^{-10}
$S_{2\text{SO}}$	1.36432	0.022	0.00065
ρ_{ex}	0.978845	0.0026	5.5×10^{-7}

Although the experimental data do allow all 6 of the potential parameters described above to be determined, the fit is very highly correlated. Under these circumstances, a fully automated approach to fitting is unreliable: individual least-squares steps often reach points in parameter space where the levels have moved too far to be identified reliably, particularly in the early stages of fitting. We therefore carried out the fitting using the I-NoLLS package [Law97] (Interactive Non-Linear Least-Squares), which gives the user interactive control over step lengths and assignments as the fit proceeds. This allowed us to converge on a minimum in the sum of weighted squares, with the parameters given in Table 3.3.

Table 3.4: Comparison between key quantities calculated from different potentials.

derived parameters	M2012	M2004
a_S (bohr)	286.5(1)	280.37(6)
a_T (bohr)	2858(19)	2440(24)
s pole near -10 (G)	$-12.38(8)$	
s pole near 550 (G)	548.78(9)	
s pole near 800 (G)	786.8(6)	

The parameter uncertainties are given in Table 3.3 as 95% confidence limits [LR98]. However, it should be emphasized that these are *statistical* uncertainties within the particular parameter set. They do not include any errors due to the choice of the potential functions.

³ In order to obtain the a good fit to the experimental results in the regions important for Efimov physics, the uncertainties used here differ from the experimental uncertainties in some cases.

Such model errors are far harder to estimate, except by performing a large number of fits with different potential models, which is not possible in the present case.

In a correlated fit, the statistical uncertainty in a fitted parameter depends on the degree of correlation. However, to reproduce the results from a set of parameters, it is often necessary to specify many more digits than implied by the uncertainty. A guide to the number of digits required is given by the *parameter sensitivity* [LR98], which essentially measures how fast the observables change when one parameter is varied with all others held fixed. This quantity is included in Table 3.3.

The singlet and triplet scattering lengths and the pole positions of the *s*-wave resonances are not directly observed quantities. Nevertheless, their values may be extracted from the final potential. In addition, the statistical uncertainties in derived parameters such as these may be obtained as described in Ref. [LR98]. The values and 95% uncertainties obtained in this way are given in Table 3.4.

3.5.1 Region between 800 G and 920 G

In the region between 800 and 920 G, the near-threshold molecular structure and the corresponding scattering properties are relatively straightforward. As seen in Fig. 3.2, the ramping $-6(34)6s(6)$ state has a strong avoided crossing with $-2(33)6s(6)$ near 850 G at a binding energy of about 110 MHz. This crossing is still incomplete when the mixed state crosses the least-bound state $-1(33)6s(6)$ around 100 kHz. It is the state resulting from this second crossing that is observed at binding energies of 0.1 to 1.7 MHz between 890 and 920 G. These points are very well reproduced by the fit, as seen in Figure 3.11. The $-3(34)6d(6)$ state that crosses the axis at 820.37 G is also well reproduced by the fit, as seen in Figure 3.12.

The position of the *s*-wave resonance pole in this region has not been observed because of large 3-body losses, but it is predicted by the fitted potential at 786.8(6) G. It is interesting to note that, because of the shift produced by the crossing with the least-bound state, the *s*-wave resonance occurs at a *lower* field than the corresponding *d*-wave resonance in this case, even though (as always) the unperturbed ramping *s*-wave state is lower in energy.

3.5.2 Region around 550 G

The region around 550 G is considerably more complicated. In this case the crossing between the ramping $-6(34)7s(6)$ state and $-2(33)6s(6)$ near 510 G is much narrower, so is almost complete by the time $-6(34)7s(6)$ crosses the least-bound state $-1(33)6s(6)$. This produces a zero crossing near 556 G. However, as described in the experimental section, there is also a ramping $-3(33)3g(3)$ state that crosses threshold just below this, producing an additional pole and zero crossing near 554 G. Because of the large background scattering length arising from its proximity to the *s*-wave resonance, the *g*-wave resonance is far wider than is usual.

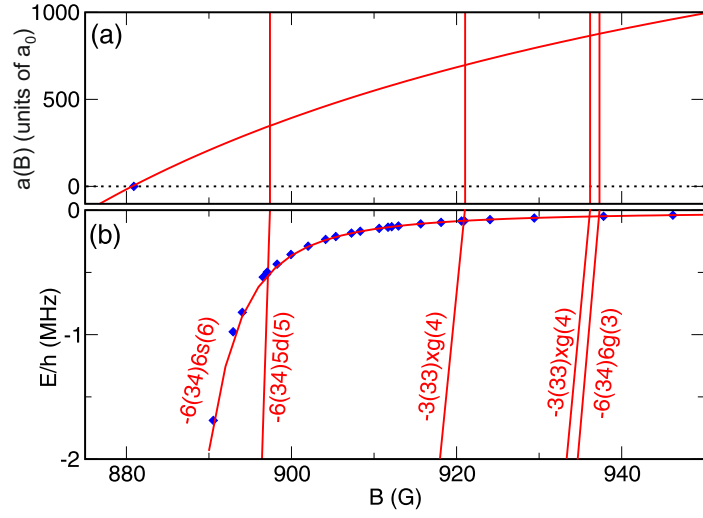


Figure 3.11: (Color online) (a) The scattering length in the region between 875 G and 950 G. The solid lines show results calculated for the M2012 potential with an *sdg* basis set. The diamond near 880 G indicates the position of the zero crossing. (b) The calculated bound-state energies with the same basis set. The diamonds show the measured energies in this region.

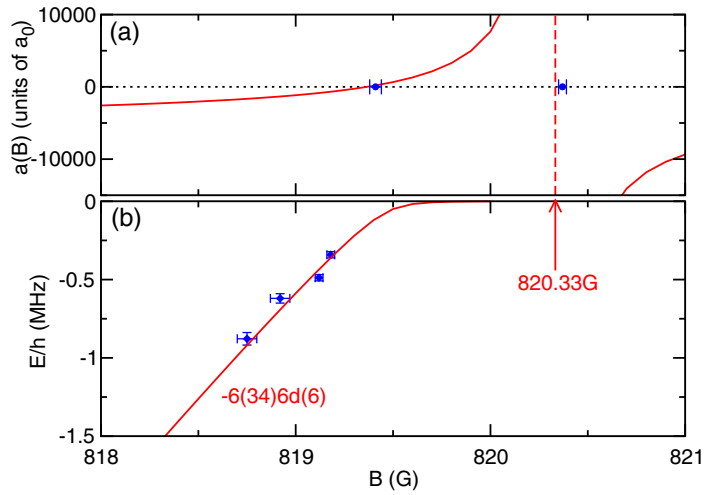


Figure 3.12: (Color online) The scattering length and bound-state energy in the pole region of the $-6(34)6d(6)$ resonance. The solid lines show results from model M2012, calculated with an *sdg* basis set. The points in panel (a) show the measured pole position and loss minimum. The points in panel (b) show the measured binding energies. The dashed line in (a) and the arrow in (b) shows the calculated pole position. Error bars refer to 1σ uncertainties.

The bound-state measurements near 557 G are further complicated by an additional state that crosses and appears to mix with the s -wave state in the top 1 MHz. This cannot be assigned as s -, d - or g -wave; it must be due to an i -wave state, and indeed the M2004 model predicts four i -wave levels to be in the range between around 530 G and 590 G, with two between 555 G and 565 G. However, these states are associated with hyperfine-excited thresholds, and their exact positions are very sensitive to details of the potential that do not significantly affect the other experimentally measured quantities considered here. We have been unable to decide unambiguously which one is responsible for the observed crossing. In addition, the i -wave states have very little influence on the s -wave scattering length that is the main object of interest in this region. We therefore decided to fit using a basis set with $L_{\max} = 4$, which excludes the i -wave states entirely, and also to exclude from the fit any binding energies affected by the crossing between the s - and i -wave states.

The general fit to the ramping s -wave bound state is shown in Fig. 3.13 and an expanded view of the fit to the g -wave state is shown in Fig. 3.14. It may be seen that the calculated s -wave state passes well through the experimental points either side of the crossing with the i -wave state, while the calculated g -wave state reproduces the bound-state energies as well as the zero crossing and pole in the scattering length.

The crossing between the i -wave state and the $-6(34)7s(6)$ state near 557 G is surprisingly strongly avoided. As described above, we were unable to ramp the magnetic field fast enough to transfer a detectable number of molecules between the two states, which sets a lower limit of 30 kHz to the strength of the avoided crossing. In a zeroth-order picture, the two states are separated by $\Delta L = 6$ and the only coupling off-diagonal in L is $\hat{V}^d(R)$, which can couple only $\Delta L = 2$ and is quite small. However, quantitative modeling of this effect requires a theoretical model that places the i -wave state in the correct place. This is likely to require simultaneous modeling of the present results and the spectroscopy of more deeply bound levels, and this remains a subject for future work.

3.5.3 Low-field region

The low-field region, below 60 G, is also quite complicated. The ramping s -wave state responsible for the Efimov resonances in this region is $-7(44)6s(6)$. However, there are also families of ramping $-2(33)6g$ states that cross threshold between 4 and 8 G and $-2(33)4g$ states that cross between 11 and 21 G. In addition, there is a $-2(33)4d(4)$ state that crosses near 48 G and a $2g(2)$ state that crosses near 54 G. The latter state does not carry a clear $n(f_1 f_2)$ signature, but it clearly has $2g(2)$ character.

The binding energies of many of these states have been measured by magnetic moment spectroscopy at binding energies up to about 10 MHz [Mar07], though these measurements have significant uncertainties associated with the integration over field. However, there are much more precise results for the $-7(44)6s(6)$ state as it crosses with the least-bound state, obtained from microwave spectroscopy [Mar07] and magnetic field modulation spectroscopy [Lan09]. Particularly important are measurements of the crossing between this mixed state and the $-2(33)4d(4)$ state near 48 G, since the strength of this crossing provides the most

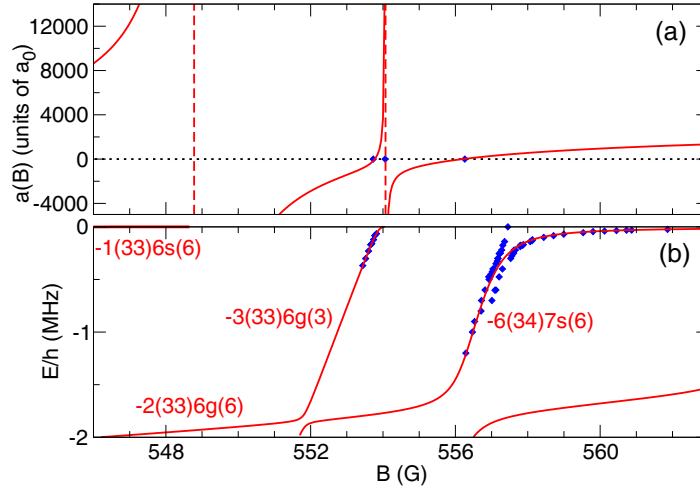


Figure 3.13: (Color online) (a) The scattering length between 546 G and 564 G. The solid lines show results calculated for the M2012 potential with an *sdg* basis set. The diamonds show the measured pole position and loss minimum near 554 G and the zero crossing near 556 G. The dashed line shows the calculated pole position. (b) The calculated binding energies with the same basis set as for Panel (a). The diamonds show the measured binding energies.

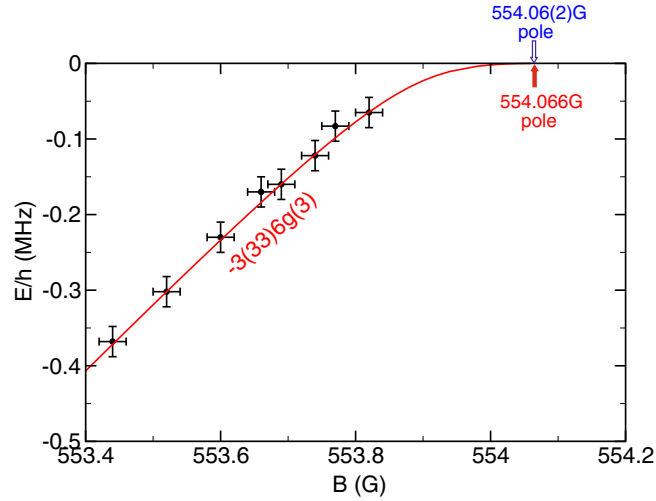


Figure 3.14: (Color online) Expanded view of the scattering length in the pole region of the $-3(33)6g(3)$ resonance. The solid line shows results calculated for the M2012 potential with an *sdg* basis set. The points show the measured bound-state energies. The calculated and measured pole positions are indicated by solid and open arrows, respectively. Error bars refer to 1σ uncertainties.

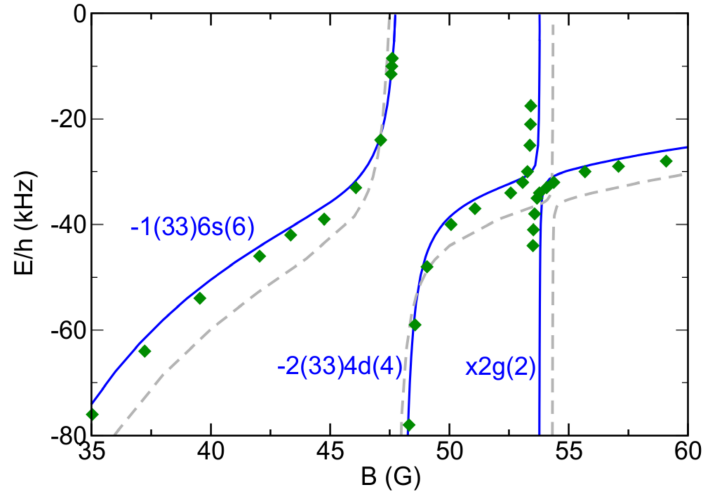


Figure 3.15: (Color online) The bound-state energies between 35 G and 60 G. The solid lines show results calculated for the M2012 potential with an *sdg* basis set, showing one side of the avoided crossings of the $-7(44)6s(6)$ bound state with the $-1(33)6s(6)$ least-bound state in the threshold entrance channel. The points show the previously measured bound-state energies [Mar07, Lan09]. The agreement is much better with the new M2012 model than with the old M2004 model, shown as light dashed lines.

direct experimental information available on the strength of the second-order spin-orbit coupling and thus on the potential parameter S_{2SO} .

Figures 3.15 and 3.16 show the overall fit to the bound states below 60 G for both the M2004 and M2012 potentials. The ramping *s*-wave state between 17 G and 60 G is of particular interest. This state switches from $-7(44)6s(6)$ to $-1(33)6s(6)$ character as B increases. All the experimental energies are well reproduced, including those near the two avoided crossings with the $4d(4)$ and $2g(2)$ states shown in Fig. 3.15. Even in this region, the M2012 model agrees with the experimental results significantly better than the M2004 model.

3.5.4 Independent tests of the M2012 model

The older potential models [Leo00, Chi04] satisfactorily reproduced the bound states for *s*-, *d*- and *g*-wave states at fields below 60 G. However, the measurements also revealed the existence of *l*-wave ($L = 8$) states [Mar07, Kno08], which do not lead to observable Feshbach resonances because of their very weak coupling to the *s*-wave threshold channel. The M2004 model failed for these *l*-wave states, with errors of up to 5 G in the positions at a given bound-state energy. The *l*-wave states were not included explicitly in our fits, but the comparison between the calculated levels and experiment is shown in Fig. 3.16 for both the current model M2012 and the older M2004 one. It is clear that M2012 gives a far more satisfactory reproduction of the experimental *l*-wave levels.

There is a particularly interesting region near 500 G, where a group of four strongly coupled $-6(34)7d(M_F)$ levels cross threshold. The underlying levels have M_F values of 4, 5, 6, and

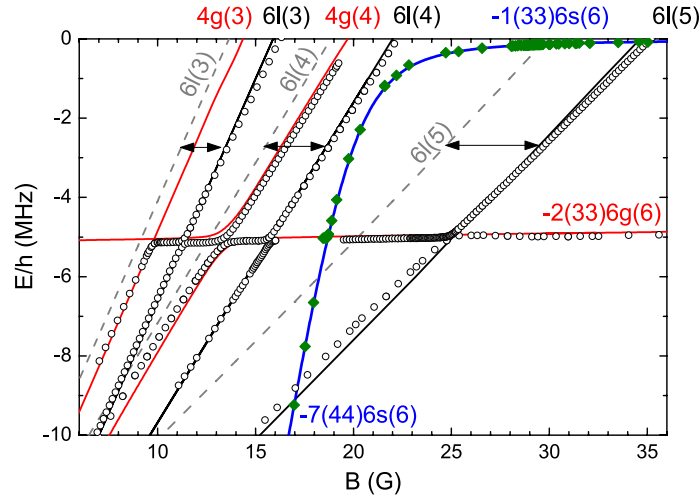


Figure 3.16: (Color online) Comparison between experimental results for s -wave levels (diamonds [Mar07, Lan09]) and g - and l -wave levels (open circles [Mar07, Kno08]) with the results of the M2012 model (solid lines). Only levels for which experimental results exist are shown. The s -wave and g -wave levels are calculated with the full sdg basis set. The l -wave levels are calculated with an l basis only. The light dashed lines show the l -wave levels calculated with the M2004 model. The arrows show the separation between equivalent levels in the M2004 and M2012 models. The additional quantum numbers $n(f_1 f_2)$ are $-2(33)$ for the two $4g$ levels and $-3(33)$ for the three $6l$ levels.

7, but are strongly mixed with one another so that M_F is not a good quantum number for the actual eigenstates. The bound states have not yet been measured in this region, but the calculated levels are shown in Fig. 3.17, together with the calculated scattering length and the positions of the measured loss maxima and minima. The loss maxima are well reproduced. The two loss minima at 499.6 G and 502.15 G are also well reproduced by the model, but the loss minimum at 492.8 G is not near a zero-crossing of the calculated scattering length. However, there are two strong overlapping and interfering resonances with poles in $a(B)$ at 492.7 G and 495.0 G, and it is not clear how to interpret the three-body loss in such a region. This complex region from 490 G to 510 G needs further investigation, especially since it may display rich Efimov physics [Fer11].

3.5.5 Mapping between scattering length and magnetic field

An important goal of this paper is to develop a theoretical model that is capable of giving an accurate mapping between the scattering length $a(B)$ and the magnetic field B , with particular focus on collisions between two Cs atoms in the lowest Zeeman level of the ground-state manifold. Our new M2012 model is based on realistic potentials and includes the full spin Hamiltonian for the Cs_2 molecule at long range. It has been calibrated against experimental binding energies and a large number of resonance positions at magnetic fields between 0 and 1000 G. We therefore expect it to provide an accurate representation of $a(B)$ across this entire range of fields. Figure 3.18 shows $a(B)$ on a grid with 0.1 G spacing over the new experimental range between 460 G and 1000 G. At this resolution, some narrow resonances are not fully resolved, and the narrowest ones are not visible at all.

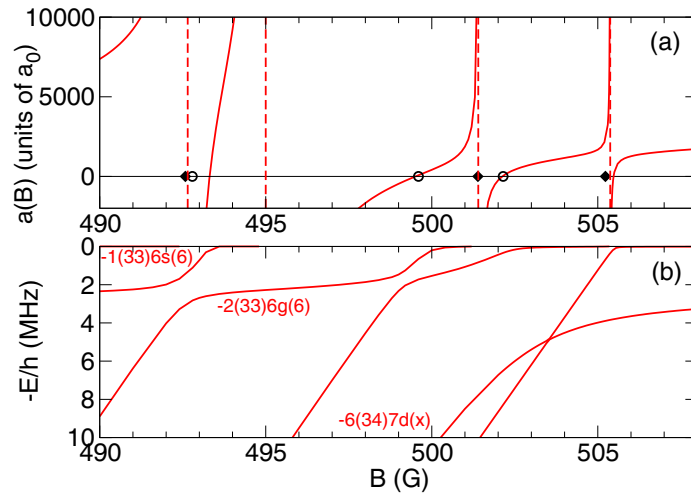


Figure 3.17: (Color online) The scattering length (a) and bound-state energies (b) between 490 G and 508 G, calculated for the M2012 potential with an *sdg* basis set. The solid diamonds in (a) show the positions of experimental loss maxima and the open circles show the positions of loss minima. The four ramping $-6(34)7d(x)$ levels, labeled collectively by x since their M_F components are mixed, undergo avoided crossings with the $-2(33)6g(6)$ level that passes through this region with $-E/h \approx 2$ MHz. The avoided crossings with the least-bound level $-1(33)6s(6)$ near $-E/h \approx 0.01$ MHz are too close to the $E = 0$ line to be seen on the figure.

The Supplemental Material ⁴ provides a tabulation of $a(B)$ against B over the full range of fields from 0 to 1200 G, for use in interpreting experiments. Additional tables lists all s -, d -, g -, i - and l -wave resonances up to 1000 G.

3.6 Conclusion

We have explored the scattering properties of ground-state Cs atoms and the binding energies of weakly bound Cs₂ molecules in the previously uncharted magnetic field range up to 1000 G, using a combination of experiment and theory. We have developed a new model of the interaction potential that reproduces the experiments accurately over the entire range of magnetic fields studied.

Experimentally, we have investigated Feshbach resonances and dimer binding energies in the magnetic field range between 450 G and 1000 G, utilizing an ultracold Cs sample in an optical dipole trap. Around 550 G and 800 G, we verified that the general scattering properties of atomic Cs are governed by two broad s -wave Feshbach resonances. Fifteen new Feshbach resonances stemming from molecular states with $L > 0$ were pinpointed by trap loss spectroscopy. We found the first evidence for the existence of i -wave Feshbach resonances, resulting from the coupling of molecular states with $L = 6$ to the atomic threshold. By performing magnetic field modulation spectroscopy, we determined the binding energies of

⁴ See Supplemental Material (Sec. 3.7) and the file at [URL will be inserted by publisher] for a tabulation of $a(B)$ against B from 0 to 1200 G and tables listing all s -, d -, g -, i - and l -wave Feshbach resonances up to 1000 G.

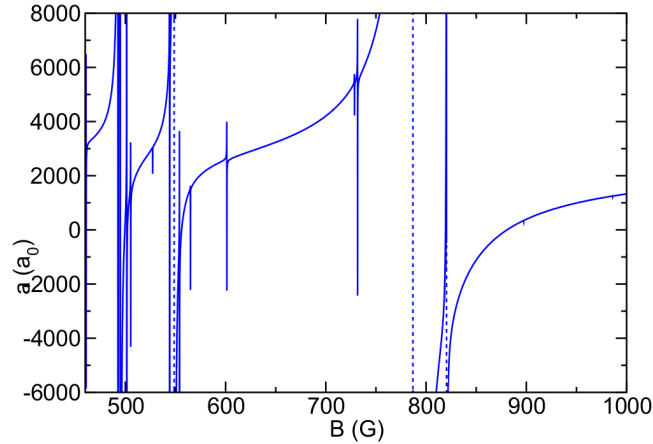


Figure 3.18: (Color online) The scattering length between 460 G and 1000 G, calculated for the M2012 potential with an *sdg* basis set. The dashed lines indicate the pole positions of the broad *s*-wave resonances near 549 G and 787 G and the *d*-wave one near 820 G. Note that some narrow resonances appear as spikes because of the limited grid spacing of 0.1 G, and some of the narrowest are not visible at all.

several dimer states, paying particular attention to the two *s*-wave states that are responsible for the general Cs scattering properties in the high-field region.

To calculate the scattering properties and bound-state energies, we solve the Schrödinger equation using coupled-channel methods. We carried out direct least-squares fitting to the combined experimental data of this article and Refs. [Mar07, Lan09, Zen12, Gus08a, Hut08] to obtain a new 6-parameter model of the long-range interaction potential, which we designate M2012.

The M2012 potential reproduces the experimental results much better than the earlier M2004 potential [Chi04], particularly at higher fields (above 250 G). It also predicts *i*-wave and *l*-wave states, which were not included in the least-squares fits. The calculated positions of *l*-wave bound states agree well with the experimental results reported in Ref. [Kno08], for which the M2004 potential failed; this demonstrates the predictive power of the new model. The pole positions of the two broad *s*-wave Feshbach resonances at high field are calculated to be 548.78 G and 786.80 G for the $-6(34)7s(6)$ and the $-6(34)6s(6)$ states, respectively.

The M2012 potential does have some remaining deficiencies. In particular, it is fitted only to results from ultracold collisions and the bound states that lies within 10 MHz of the atomic threshold. It does not include results from electronic spectroscopy on deeply bound levels of Cs₂, or the near-dissociation levels observed in 2-color photoassociation spectroscopy [Van04], which are bound by 5 to 80 GHz. It also does not satisfactorily reproduce the positions of *i*-wave states associated with excited hyperfine thresholds. Resolving these remaining issues will require a simultaneous fit to all the experiments together, and is a topic for future work.

Our new model allows us to make an accurate connection between the experimentally controllable magnetic field strength B and the s -wave scattering length a over a wide range of fields. The scattering length is the essential parameter in universal theories, and this connection was crucial in allowing us to interpret our measurements of three-body recombination in terms of universal Efimov physics in Ref. [Ber11b]. The present work is important not only for experiments on Cs, but also provides important information for ongoing and future experiments involving Cs mixtures, such as RbCs [Tak12], LiCs [Rep13, Tun13] and other interesting combinations.

Acknowledgments

We acknowledge support by the Austrian Science Fund FWF within project P23106. A. Z. was supported within the Marie Curie Intra-European Program of the European Commission (project LatTriCs). P. S. J. and J. M. H. acknowledge support from EPSRC, AFOSR MURI Grant FA9550-09-1-0617, and EOARD Grant FA8655-10-1-3033.

3.7 Supplemental Material

One goal of our work has been to provide an accurate theoretical model for mapping the the experimental magnetic field B to the two-body scattering length $a(B)$ for the collision of two Cs atoms in their lowest energy Zeeman sublevel. Therefore, we include here a table of $a(B)$ versus B calculated with the M2012 model described in the full paper. The calculations with an sdg basis set are tabulated in the Supplemental File [a_vs_B_sdg_M2012.txt](#) from 0.1 G to 1200 G with a grid spacing of 0.1 G. This choice of grid step is not sufficient to resolve the narrowest resonances, but is chosen since it should give a reasonably good representation for interpolating to fields used in experimental studies or for fitting isolated resonance to the form of Eq. (6) of the full paper.

Table I lists all s -, d -, or g -wave levels crossing threshold between 0 and 1000 G, calculated with an sdg basis. These represent the accurate predictions of the M2012 model. In addition, Tables II provides a list of all i -wave levels crossing threshold using only an i -wave basis. Table III provides an similar list of the l -wave levels. These i - and l -wave resonance positions are not expected to be as accurate as the s -, d -, or g -wave ones, since they have not been calibrated against data for such levels and the basis sets are limited in scope. They are listed in order to provide guidance as to the number and estimated locations of such resonances.

Figure 3.19 shows $a(B)$ over the full range calculated with an sdg basis and additionally the s , d , and g bound states between 0 and 1000 G. Figure 3.20 shows expanded views of the the scattering length in different regions between 0 and 940 G. There are no interesting resonances appearing between 940 G and 1200 G. Figure 3.21 shows an expanded view of the near-threshold s -, g -, and l -wave levels in the low field region up to 35 G.

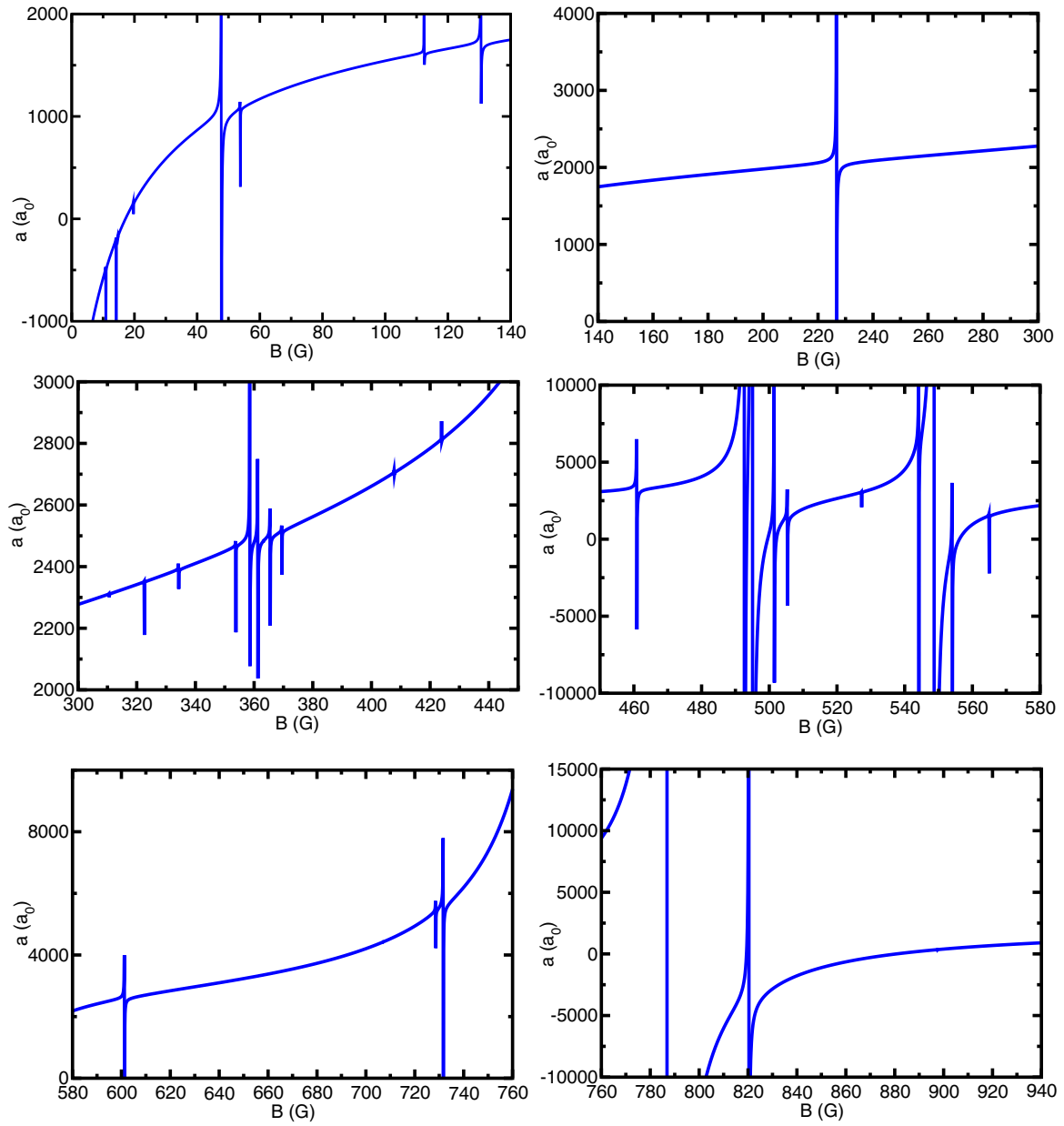


Figure 3.20: (Color online) The six different panels show expanded views of the M2012 scattering length a versus magnetic field B calculated with an sdg basis in different regions of B .

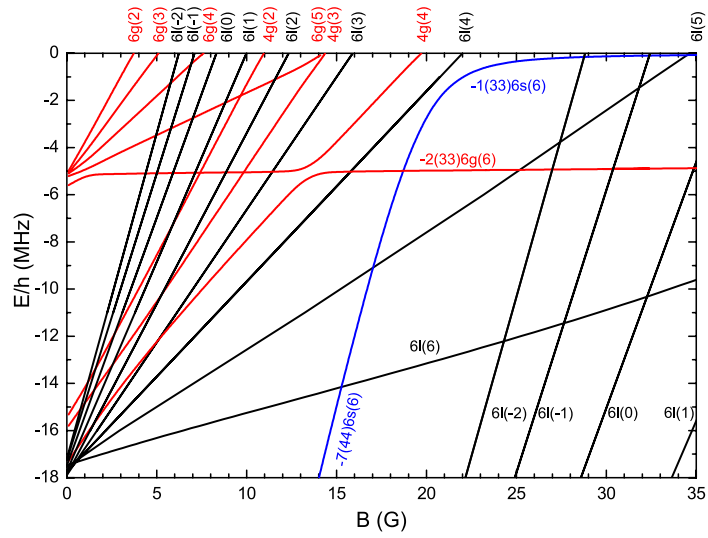


Figure 3.21: (Color online) Dimer levels in the magnetic low-field region up to $L = 8$ calculated with the M2012 potentials. The s - and g -levels were calculated with an sdg basis, but the l -levels were calculated with an l -basis alone.

$B_{\text{res}}(\text{G})$	Assignment	Measured(G)	$B_{\text{res}}(\text{G})$	Assignment	Measured(G)	$B_{\text{res}}(\text{G})$	Assignment	Measured(G)
3.70	-2(33)6g(2)		334.28	$g(5)$		544.18	$g(3)$	
5.04	-2(33)6g(3)		353.79	g		548.44	-6(34)7s(6)	broad
7.56	-2(33)6g(4)		358.54	g		554.06	$g(3)$	554.06(2)
10.90	-2(33)4g(2)	11.02(3) [1]	361.26	g		565.00	$g(4)$	565.48(3)
14.20	-2(33)4g(3)	14.37(3) [1]	363.29	g		601.28	-2(33)6g(6) ³⁾	602.54(3)
14.76	-2(33)6g(5)	15.06(3) [1]	365.48	g		707.03	$g(3)$	
19.69	-2(33)4g(4)	19.90(3) [1]	369.49	g		728.58	$g(5)$	729.03(3)
47.79	-2(33)4d(4)	47.97(3) [1]	407.75	g		731.68	-6(34)6d(4)	
53.79	$x2g(2)$	53.50(3) [1]	408.48	g		782.68	$g(4)$	
112.41	-2(33)6d(4)	112.78(3) [1]	417.67	g		782.97	-6(34)6s(6)	broad
130.52	-2(33)4d(4)	131.06(3) [1]	423.91	-6(34)5d(4)		793.86	$g(2)$	
226.73	-2(33)d(5)		460.87	-6(34)5d(5)	460.86(5)	820.26	-6(34)6d(6)	820.4(2)
247.01	$g(2)$ ¹⁾		492.55	-6(34)7d(x) ²⁾	492.45(3)	897.40	-6(34)5d(5)	897.33(3)
278.32	$g(3)$		494.83	-6(34)7d(x) ²⁾	494.4(9)	921.04	g ⁴⁾	
301.18	$g(2)$		501.43	-6(34)7d(x) ²⁾	501.24(3)	936.18	g ⁴⁾	
310.59	$g(4)$		505.37	-6(34)7d(x) ²⁾	505.07(3)	937.31	g ⁴⁾	
322.60	$g(3)$		527.30	$g(2)$		986.24	-6(34)6d(4)	986.08(3)

Table 3.5: Levels calculated with an sdg -basis.

¹⁾The g -wave states from 247 to 417 G involve a variety of crossing levels, some of which mix, making assignments difficult. We do not attempt to assign $n(f_1 f_2)$ quantum numbers to g -levels at higher fields.

²⁾ x = mixture of $M_F = 4, 5, 6, 7$.

³⁾Strongly mixed with -6(34)6g(6).

⁴⁾The g -wave states from 921 to 937 G are comprised of 2 $M_F = 2$.

[1] C. Chin, V. Vuletić, A. J. Kerman, S. Chu, E. Tiesinga, P. J. Leo, and C. J. Williams, Phys. Rev. A, **70**, 032701 (2004).

$B_{\text{res}}(\text{G})$	$B_{\text{res}}(\text{G})$	$B_{\text{res}}(\text{G})$	$B_{\text{res}}(\text{G})$
82.29	136.33	188.77	458.79 ¹⁾
96.98	139.18	196.32	476.18
98.75	141.09	227.87	534.73
106.73	143.36	232.28	555.39 ²⁾
110.48	144.79	286.83	559.18 ³⁾
116.72	148.57	295.85	583.25
122.19	156.31	299.97	679.49
124.23	158.88	306.43	682.68
127.57	163.71	332.62	861.80
128.09	174.54	429.80	880.75
129.21	180.68	431.75	922.78
129.87	185.09	431.89	943.96
135.65	187.55	441.01	971.33

Table 3.6: Levels calculated with an i -basis.

¹⁾Measured at 461.62(5) G.

²⁾Measured at 557.45(3) G.

³⁾Measured at 562.17(3) G.

$B_{\text{res}}(\text{G})$	Assignment	$B_{\text{res}}(\text{G})$	Assignment
6.22	-3(33)6l(-2)	146.25	6l(x) ⁴
7.13	-3(33)6l(-1)	146.88	6l(x) ⁴
8.36	-3(33)6l(0)	149.45	6l(x) ⁴
10.03	-3(33)6l(1)	151.14	6l(x) ⁴
12.40	-3(33)6l(2)	152.75	6l(x) ⁴
15.99	-3(33)6l(3)	155.95	6l(x) ⁴
22.12	-3(33)6l(4)	158.36	6l(x) ⁴
28.83	-3(33)2l(-2)	181.38	6l(5)
32.45	-3(33)2l(-1)	489.81	-4(33)xl(-2) ⁵
33.73	-3(33)0l(0) ¹⁾	503.09	-4(33)xl(-2) ⁵
34.75	-3(33)6l(4) ¹⁾	511.22	-4(33)xl(-2) ⁵
37.23	-3(33)2l(0)	565.14	-4(33)xl(-1) ⁶
43.80	-3(33)4l(1)	573.54	-4(33)xl(-1) ⁶
50.08	-3(33)6l(-2)	581.83	-4(33)xl(-1) ⁶
53.35	-3(33)4l(2)	653.49	-4(33)xl(0) ⁷
53.66	-3(33)6l(-1)	668.01	-4(33)xl(0) ⁷
58.16	-3(33)6l(0)	678.19	-4(33)xl(0) ⁷
62.01	-3(33)xl(6) ²⁾	699.20	-4(33)xl(0) ⁷
64.05	-3(33)6l(1)	797.84	-4(33)xl(1) ⁸
72.35	-3(33)6l(2)	825.71	-4(33)xl(1) ⁸
85.35	-3(33)6l(3)	843.90	-4(33)xl(1) ⁸
109.74	-3(33)xl(4) ³⁾		

Table 3.7: Levels calculated with an l -basis. For assignments including the place holder “ x ”, the states are mixed according to the footnotes given below.

¹⁾mixture of the -3(33)0l(0)- and the -3(33)6l(4)-state.

²⁾mixture of $F = 4$ and 6

³⁾mixture of $F = 4$ and 6

⁴⁾mixture of $M_F = -2, -1, 0, 1, 2, 3$ and 4

⁵⁾mixture of $F = 2, 4$ and 6

⁶⁾mixture of $F = 2, 4$ and 6

⁷⁾mixture of $F = 0, 2, 4$ and 6

⁸⁾mixture of $F = 2, 4$ and 6

Publication: Universality of the three-body parameter for Efimov states in ultracold cesium[†]

Phys. Rev. Lett. **107**, 120401 (2011)

Martin Berninger,^{1,2} Alessandro Zenesini,^{1,2} Bo Huang,^{1,2} Walter Harm,^{1,2}
Hanns-Christoph Nägerl,^{1,2} Francesca Ferlaino,^{1,2} Rudolf Grimm,^{1,2}
Paul S. Julienne,³ and Jeremy M. Hutson⁴

¹*Institut für Experimentalphysik and Zentrum für Quantenphysik,
Universität Innsbruck, 6020 Innsbruck, Austria*

²*Institut für Quantenoptik und Quanteninformation,
Österreichische Akademie der Wissenschaften, 6020 Innsbruck, Austria*

³*Joint Quantum Institute, NIST and the University of Maryland,
100 Bureau Drive Stop 8423, Gaithersburg, Maryland 20899-8423, USA*

⁴*Joint Quantum Centre (JQC) Durham/Newcastle, Department of Chemistry,
Durham University, South Road, Durham, DH1 3LE, United Kingdom*

We report on the observation of triatomic Efimov resonances in an ultracold gas of cesium atoms. Exploiting the wide tunability of interactions resulting from three broad Feshbach resonances in the same spin channel, we measure magnetic-field dependent three-body recombination loss. The positions of the loss resonances yield corresponding values for the three-body parameter, which in universal few-body physics is required to describe three-body phenomena and in particular to fix the spectrum of Efimov states. Our observations show a robust universal behavior with a three-body parameter that stays essentially constant.

[†] The author of the present thesis contributed to the upgrading of the experimental setup to be capable of working at high magnetic fields. He also took part in recording and analyzing the experimental data with M.B. and A.Z. Particularly, he performed the major part of the measurements near 550 G and recognized that there are two rather than one Efimov resonance there. P.S.J and J.M.H provided theoretical support.

4.1 Introduction

The concept of universality manifests itself in the fact that different physical systems can exhibit basically the same behavior, even if the relevant energy and length scales differ by many orders of magnitude [Bra06]. Universality thus allows us to understand in the same theoretical framework physical situations that at first glance seem completely different. In ultracold atomic collisions, the universal regime is realized when the s -wave scattering length a , characterizing the two-body interaction in the zero-energy limit, is much larger than the characteristic range of the interaction potential. Then the essential properties of the two-body system such as the binding energy of the most weakly bound dimer state and the dominating part of the two-body wave function can simply be described in terms of a , independent of any other system-dependent parameters. In the three-body sector, the description of a universal system requires an additional parameter, which incorporates all relevant short-range interactions not already included in a . In few-body physics, this important quantity is commonly referred to as the three-body parameter (3BP).

In Efimov's famous scenario [Efi70, Bra06], the infinite ladder of three-body bound states follows a discrete scaling invariance, which determines the relative energy spectrum of the states. The 3BP fixes the starting point of the ladder and thus the absolute energies of all states. The parameter enters the theoretical description as a short-range boundary condition for the three-body wave function in real space or as a high-frequency cut-off in momentum space. To determine the 3BP from theory would require precise knowledge of both the two-body interactions and the genuine three-body interactions at short range. In real systems, this is extremely difficult and the 3BP needs to be determined experimentally through the observation of few-body features such as Efimov resonances.

In the last few years, ultracold atomic systems have opened up the possibility to explore Efimov's scenario experimentally and to test further predictions of universal theory [Kra06, Kno09, Zac09, Pol09, Gro09, Huc09, Ott08, Wil09, Bar09, Gro10, Lom10a, Nak10]. The key ingredient of such experiments is the possibility to control a by an external magnetic field B via the Feshbach resonance phenomenon [Chi10]. This naturally leads to the important question whether the 3BP remains constant or whether it is affected by the magnetic tuning, in particular when different Feshbach resonances are involved.

The current status of theoretical and experimental research does not provide a conclusive picture on possible variations of the 3BP. A theoretical study [D'I09] points to strong possible variations when different two-body resonances are exploited in the same system, and even suggests a change of the 3BP on the two sides of a zero crossing of the scattering length. Other theoretical papers point to the importance of the particular character of the Feshbach resonance [Chi10]. While closed-channel dominated ("narrow") resonances involve an additional length scale that may fix the 3BP [Pet04, Mas08, Wan11], the case of entrance-channel dominated ("broad") resonances leaves the 3BP in principle open. However, predictions based on two-body scattering properties exist that apparently fix the 3BP for broad resonances as well [Lee07, JL10, Nai11]. The available experimental observations provide only fragmentary information. The first observation of Efimov physics in an ultracold Cs gas [Kra06] is consistent with the assumption of a constant 3BP on both sides of

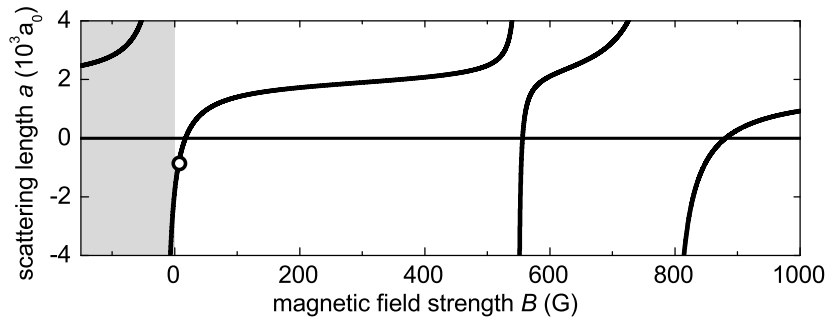


Figure 4.1: Illustration of the three broad s -wave Feshbach resonances for Cs in the absolute atomic ground state $|F=3, m_F=3\rangle$. The open circle corresponds to the previous observation of a triatomic Efimov resonance at 7.6 G [Kra06]. The many narrow Feshbach resonances resulting from d - and g -wave molecular states [Chi04] are not shown for the sake of clarity. The region with $B < 0$ corresponds to the state $|F=3, m_F=-3\rangle$, which is not stable against two-body decay. Scattering lengths are given in units of Bohr’s radius a_0 .

a zero crossing. A later observation on ^{39}K [Zac09] indicated different values of the 3BP on both sides of a Feshbach resonance. A similar conclusion was drawn from experiments on ^7Li [Pol09], but other experiments on ^7Li showed universal behavior with a constant 3BP for the whole tuning range of a single resonance [Gro09] and for another spin channel [Gro10]. Besides these observations on bosonic systems, experiments on fermionic gases of ^6Li [Ott08, Huc09, Wil09] can be interpreted based on a constant 3BP [Wen09]. A recent experiment on ^6Li , however, indicates small variations of the 3BP [Nak11].

4.2 The experiment

In the present work, we investigate universality in an ultracold gas of Cs atoms, which offers several broad Feshbach resonances in the same spin channel and thus offers unique possibilities to test for variations of the 3BP. In the lowest hyperfine and Zeeman sublevel $|F=3, m_F=3\rangle$, Cs features a variety of broad and narrow Feshbach resonances in combination with a large background scattering length [Chi04]. Of particular interest are three broad s -wave Feshbach resonances in the range up to 1000 G,¹ with poles near -10 G, 550 G, and 800 G [Chi04, Lee07, Chi10]. The character of these three resonances is strongly entrance-channel dominated, as highlighted by the large values of their resonance strength parameter s_{res} [Chi10] of 560, 170, and 1470, respectively. The resulting magnetic-field dependence $a(B)$ is illustrated in Fig. 4.1. In our previous work [Kra06, Kno09] we have focussed on the low-field region up to 150 G. After a major technical upgrade of our coil set-up, we are now in the position to apply magnetic fields B of up to 1.4 kG with precise control down to the 20 mG uncertainty level and thus to explore the resonance regions at 550 G and 800 G [Ber11a].

Our ultracold sample consists of about 2×10^4 optically trapped ^{133}Cs atoms, close to quan-

¹ Units of gauss instead of the SI unit tesla ($1\text{ G} = 10^{-4}\text{ T}$) are used to conform to conventional usage in this field.

tum degeneracy. The preparation is based on an all-optical cooling approach as presented in Refs. [Kra04, Mar07]. The final stage of evaporative cooling is performed in a crossed-beam dipole trap (laser wavelength 1064 nm) and stopped shortly before Bose-Einstein condensation is reached. Finally, the trap is adiabatically recompressed to twice the initial potential depth to suppress further evaporation loss. At this point, the mean trap frequency is about 10 Hz and the temperature is typically 15 nK.

Our experimental observable is the three-body loss coefficient L_3 , which in the framework of universal theory is conveniently expressed as $L_3 = 3C(a)\frac{\hbar a^4}{m}$ [Web03c], m denotes the atomic mass. The expression separates a log-periodic function $C(a)$ from the general a^4 -scaling of three-body loss. For $a < 0$, effective field theory [Bra06] provides the analytic expression

$$C(a) = 4590 \frac{\sinh(2\eta_-)}{\sin^2[s_0 \ln(a/a_-)] + \sinh^2 \eta_-}, \quad (4.1)$$

with $s_0 \approx 1.00624$ for identical bosons. The decay parameter η_- is a non-universal quantity that depends on the deeply-bound molecular spectrum [Wen09]. The scattering length a_- marks the situation where an Efimov state intersects the three-atom threshold and the resulting triatomic Efimov resonance leads to a giant three-body loss feature. In the following, the quantity a_- will serve us as the representation of the 3BP.

To measure L_3 we record the time evolution of the atom number after quickly (within 10 ms) ramping B from the evaporation to the target field strength. We determine the atom number N by absorption imaging. One-body decay, as caused by background collisions, is negligible under our experimental conditions. Furthermore, two-body decay is energetically suppressed in the atomic state used. We can therefore model the decay by $\dot{N}/N = -L_3 \langle n^2 \rangle$, where the brackets denote the spatial average weighted with the atomic density distribution n . Additional, weaker loss contributions caused by four-body recombination [Fer09] can be described in terms of an effective L_3 [von09]. For fitting the decay curves and extracting L_3 we use an analytic expression that takes into account the density decrease resulting from anti-evaporation heating [Web03c].

The experimental results are a function of B whereas theory expresses L_3 as a function of a . It is thus crucial to have a reliable conversion function $a(B)$. We have obtained $a(B)$ from full coupled-channel calculations on a Cs-Cs potential obtained by least-squares fitting to extensive new measurements of binding energies, obtained by magnetic-field modulation spectroscopy [Lan09], together with additional measurements of loss maxima and minima that occur at resonance poles and zero crossings. The new potential provides a much improved representation of the bound states and scattering across the whole range from low field to 1000 G. The experimental results and the procedures used to fit them will be described in a separate publication.

4.3 Efimov resonances at different Feshbach resonances

Figure 4.2 shows our experimental results on the magnetic-field dependent recombination loss near the two broad high-field Feshbach resonances (550 G and 800 G regions). For

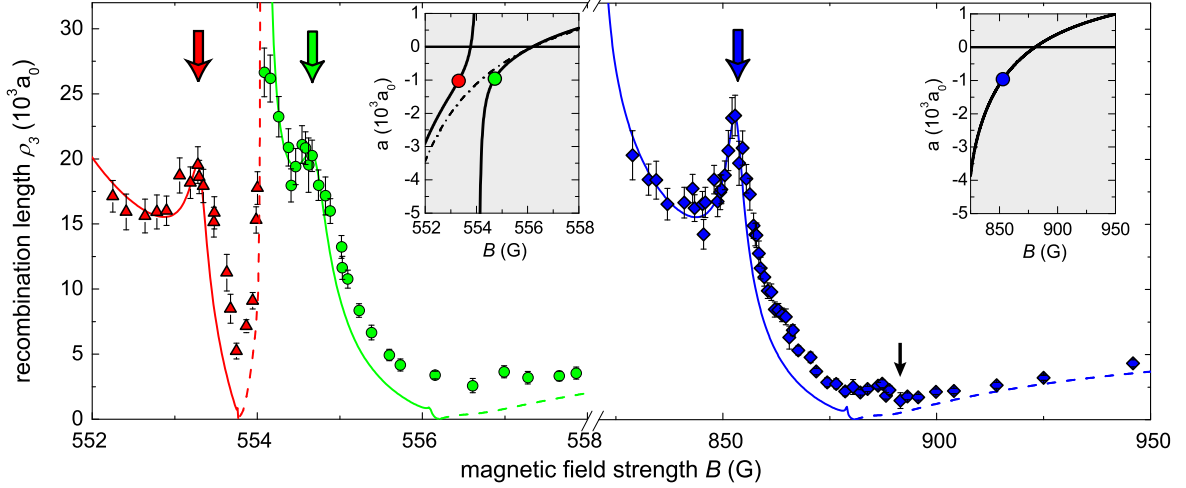


Figure 4.2: (color online) Recombination loss in the vicinity of the high-field Feshbach resonances. The measured recombination length ρ_3 is shown for three different regions (\blacktriangle , $552 \text{ G} < B < 554 \text{ G}$; \bullet , $554 \text{ G} < B < 558 \text{ G}$; \blacklozenge , $830 \text{ G} < B < 950 \text{ G}$), which are separated by the poles of different Feshbach resonances. The error bars indicate the statistical uncertainties. For all three regions, the solid lines represent independent fits to the data at negative a . The dashed lines show the predictions of effective field theory for $a > 0$ [Bra06], using the parameters obtained in the same region at $a < 0$. The insets show $a(B)$ (solid line, full calculation; dash-dot line, s -wave states only). The arrows in the main figure and the corresponding dots in the insets refer to the triatomic Efimov resonances. The small arrow indicates a recombination minimum.

convenience we plot our data in terms of the recombination length $\rho_3 = (2mL_3/(\sqrt{3}\hbar))^{1/4}$ [Esr99]. The three filled arrows indicate three observed loss resonances that do not coincide with the poles of two-body resonances. We interpret these three features as triatomic Efimov resonances.

In the 800 G region, a single loss resonance shows up at 853 G, which lies in the region of large negative values of a . We fit the L_3 data based on Eq. (4.1) and using the conversion function $a(B)$ described above.² The fit generally reproduces the experimental data well, apart from a small background loss that apparently does not result from three-body recombination.³ For the 3BP the fit yields the resonance position of $a_- = -955(28) a_0$, where the given error includes all statistical errors. For the decay parameter the fit gives $\eta_- = 0.08(1)$.

For the 550 G region, Fig. 4.1 suggests a qualitatively similar behavior as found in the 800 G region. The experimental data, however, reveal a more complicated structure with three loss maxima and a pronounced minimum. This behavior is explained by a g -wave resonance (not shown in Fig. 4.1) that overlaps with the broader s -wave resonance. We have thoroughly investigated this region by Feshbach spectroscopy. These studies clearly identify the central maximum (554.06 G) and the deep minimum (553.73 G) as the pole and zero crossing of the g -wave resonance (see inset). With $s_{\text{res}} = 0.9$, this resonance is an intermediate case between closed-channel and entrance-channel dominated.

² The fits include an additional free scaling factor λ to account for possible systematic errors in the number density. For the 800 G region, we obtain $\lambda = 0.89$. For the lower and upper 550 G region, we obtain $\lambda = 0.46$ and $\lambda = 1.06$, respectively.

³ The smallest values obtained for ρ_3 correspond to one-body lifetimes exceeding 100 s.

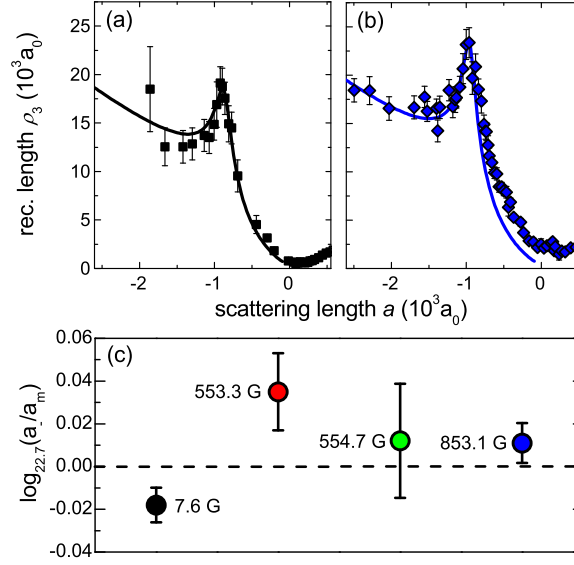


Figure 4.3: (color online) Efimov resonances and the 3BP. In (a) and (b), we compare the resonance previously observed [Kra06] at 7.6 G to the one found at 853 G. In (c), we plot the 3BPs obtained for all four resonances measured in Cs. The dashed line corresponds to a mean value of $a_m = -921 a_0$, calculated as a weighted average of the four different values. The logarithmic scale (to the basis of 22.7) covers one tenth of the Efimov period.

B_{res} (G)	a_-/a_0	δ_1/a_0	δ_2/a_0	δ_3/a_0	η_-
7.56(17)	-872(22)	21	3	6	0.10(3)
553.30(4)	-1029(58)	43	28	27	0.12(1)
554.71(6)	-957(80)	57	25	49	0.19(2)
853.07(56)	-955(28)	27	1	4	0.08(1)

Table 4.1: Parameters of the four triatomic Efimov resonances. The first and second column give the magnetic field values B_{res} at the resonance centers and the corresponding 3BPs together with their full statistical uncertainties. The individual error contributions δ_1 , δ_2 , and δ_3 refer to the statistical uncertainties from the fit to the L_3 data, from the determination of the magnetic field strength, and from the $a(B)$ -conversion, respectively.

The g -wave resonance causes a splitting that produces two Efimov resonances instead of one in this region. This explains the upper and the lower loss maxima, which are found at 553.30(4) G and 554.71(6) G (arrows in Fig. 4.2). To determine the parameters of these Efimov resonances, we independently fit the two relevant regions of negative scattering length using Eq. (4.1). This yields $a_- = -1029(58) a_0$ and $-957(80) a_0$ for the lower and the upper resonances, respectively.

We now compare all our observations on triatomic Efimov resonances in Cs. We also include the previous data of Ref. [Kra06] on the low-field resonance (7.6 G), which we have refitted using our improved $a(B)$ conversion. The relevant parameters for the four observed Efimov resonances are given in Table 4.1. Figure 4.3(a) and (b) show the recombination data for the low-field resonance and the 853 G resonance, using a convenient $\rho_3(a)$ representation. This comparison illustrates the striking similarity between both cases. For all four Efimov

resonances, Fig. 4.3(c) shows the 3BP on a logarithmic scale, which relates our results to the universal scaling factor 22.7. Note that the full scale is only one tenth of the Efimov period, i.e. a factor $22.7^{\frac{1}{10}} \approx 1.37$. The error bars indicate the corresponding uncertainties (one standard deviation), resulting from all statistical uncertainties.⁴ The data points somewhat scatter around an average value of about $-921 a_0$ (dashed line) with small deviations that stay within a few percent of the Efimov period. Taking the uncertainties into account, our data are consistent with a constant 3BP for all four resonances. However, between the values determined for the two broad resonances at 7.6 and 853 G we find a possible small aberration of about 2.5 standard deviations. This may be accidental but it may also hint at a small change in the 3BP.

Let us briefly discuss our findings on further few-body observables. For $a > 0$, three-body recombination minima are well known features related to Efimov physics [Bra06, Kra04, Zac09, Pol09]. In the 800 G region, we observe a minimum at $B = 893(1)$ G (small arrow in Fig. 4.2), corresponding to $a = +270(30) a_0$, which is very similar to the minimum previously observed in the low-field region [Kra04] and consistent with a universal connection to the $a < 0$ side. In general, however, these minima are difficult to access in Cs and dedicated experiments will be needed to provide stringent tests also for the $a > 0$ side. Also atom-dimer resonances [Kno09, Zac09, Pol09] have not yet been observed in the high-field region. Additional measurements in the 800 G region (not shown) reveal a pair of four-body resonances at 865.4(5) G and 855.0(2) G, corresponding to scattering lengths of $-444(8) a_0$ and $-862(9) a_0$. This excellently fits to universal relations [von09] and our previous observations at low magnetic fields [Fer09].

Our observations show that universality persists in a wide magnetic-field range across a series of Feshbach resonances in the same spin channel and that the 3BP shows only minor variations, if any. This rules out a scenario of large variations as suggested by the model calculations of Ref. [D'I09]. The apparent fact that the relevant short-range physics is not substantially affected by the magnetic field may be connected to the strongly entrance-channel dominated character [Chi10] of the broad resonances in Cs. However, even the case of overlapping s - and g -wave Feshbach resonances, where the latter one has intermediate character, is found to exhibit universal behavior consistent with an essentially constant 3BP. Our observation that universality is robust against passing through many poles and zero crossings of the scattering length also implies a strong argument in favor of a universal connection of both sides of a single Feshbach resonance. This supports conclusions from experiments on ${}^7\text{Li}$ as reported in Refs. [Gro09, Gro10], in contrast to Ref. [Pol09] and related work on ${}^{39}\text{K}$ [Zac09].

4.4 Conclusion

With the present experimental data there is growing experimental evidence that theories based on low-energy two-body scattering and the near-threshold dimer states [Lee07, JL10,

⁴ Systematic uncertainties are not included in our error budget. They may result from model-dependent errors in the determination of the scattering length from binding energy and scattering data and from finite-temperature shifts. All these errors, however, stay well below the statistical uncertainties.

[Nai11](#)] can provide reasonable predictions for the 3BP without invoking genuine short-range three-body forces, which are known to be substantial for all the alkali metal trimers [[Sol03](#)]. We also stress a remarkable similarity [[Gro09](#)] between the Cs data and experimental results on both Li isotopes. When the 3BP is normalized to the mean scattering length \bar{a} of the van der Waals potential [[Chi10](#)], our actual Cs value $a_-/\bar{a} = -9.5(4)$ is remarkably close to corresponding values for ^7Li [[Gro10](#), [Pol09](#)] and ^6Li [[Ott08](#), [Huc09](#), [Wil09](#), [Wen09](#)], which vary in the range between -8 and -10 .

Universality in tunable atomic quantum gases near Feshbach resonances appears to be rather robust, but the understanding of the particular reasons and conditions remains a challenge to few-body theories.

Acknowledgments

We thank M. Ueda, T. Mukaiyama, P. Naidon, and S. Jochim for discussions. We acknowledge support by the Austrian Science Fund FWF within project P23106. A.Z. is supported within the Marie Curie Intra-European Program of the European Commission. P.S.J. and J.M.H. acknowledge support from an AFOSR MURI grant.

Publication: Resonant atom-dimer collisions in cesium: testing universality at positive scattering lengths[†]

Phys. Rev. A **90**, 022704 (2014)

Alessandro Zenesini,^{1,2} Bo Huang,¹ Martin Berninger,¹ Hanns-Christoph Nägerl,¹ Francesca Ferlaino,¹ and Rudolf Grimm^{1,3}

¹*Institut für Experimentalphysik and Zentrum für Quantenphysik, Universität Innsbruck, 6020 Innsbruck, Austria*

²*Institute of Quantum Optics, Leibniz Universität Hannover, Welfengarten 1, 30167 Hannover, Germany*

³*Institut für Quantenoptik und Quanteninformation, Österreichische Akademie der Wissenschaften, 6020 Innsbruck, Austria*

We study the collisional properties of an ultracold mixture of cesium atoms and dimers close to a Feshbach resonance near 550 G in the regime of positive s -wave scattering lengths. We observe an atom-dimer loss resonance that is related to Efimov's scenario of trimer states. The resonance is found at a value of the scattering length that is different from a previous observation at low magnetic fields. This indicates non-universal behavior of the Efimov spectrum for positive scattering lengths. We compare our observations with predictions from effective field theory and with a recent model based on the van der Waals interaction. We present additional measurements on pure atomic samples in order to check for the presence of a resonant loss feature related to an avalanche effect as suggested by observations in other atomic species. We could not confirm the presence of such a feature.

[†] A.Z. and the author of the present thesis recorded and analyzed the experimental data together.

5.1 Introduction

Efimov’s solution to the problem of three resonantly interacting particles [Efi70] is widely considered to be the most prominent example of a *universal* few-body system, where the knowledge of the two-body scattering length a and an additional three-body parameter is sufficient to define the whole energy spectrum and to locate all the bound states. The details of the interparticle potential become irrelevant and different systems very far apart in energy and length scales can be described in the same way. The famous discrete scaling of the Efimov spectrum (scaling factor of 22.7) and the precise ratios that link its different parts have attracted large interest in the scientific community.

Universal behavior arises from the presence of resonant interactions leading to collisions on a length scale exceeding the typical size of the interparticle potential. In trimer systems, the contributions of the short-range details are commonly included in the “three-body parameter”. This parameter fixes the starting point of the spectrum and can be expressed in terms of the scattering length a_- at which the most deeply bound Efimov state crosses the zero-energy threshold [Bra06]. Within the ideal Efimov scenario, the positions of all the other features of the spectrum are uniquely determined, both at positive and negative values of a .

The validation of Efimov’s scenario had remained elusive for decades until experiments on ultracold atoms provided evidence for its existence [Kra06, Kno09, Zac09, Gro09, Gro10, Pol09, Wil12, Ber11b, Hua14b, Tun14, Pir14]. The appearance of trimer bound states has been shown by measuring inelastic collisional rates in atomic samples or atom-dimer mixtures by tuning the scattering length via magnetically controlled Feshbach resonances [Chi10]. The presence of trimer bound states leads to enhancement and suppression of losses [Esr99, Bra01, Pet04]. In particular the loss resonances represent a “smoking gun” for Efimov’s spectrum and occur where the trimer energy state crosses the atomic threshold (at a_- , in the region of negative a) or merges into the state of a dimer plus a free atom (at a_* , in the region of positive a).

In the region of negative scattering lengths, experimental observations have shown that the position a_- is essentially independent of the particular Feshbach resonance used for interaction tuning [Ber11b, Gro09, Roy13]. The comparison between experiments performed with different species [Zac09, Gro09, Gro10, Pol09, Wil12] shows that $a_- \approx -9.5 R_{\text{vdW}}$, where the van der Waals length R_{vdW} represents the length scale associated with the van der Waals interaction [Chi10]. This result suggested that the knowledge of R_{vdW} is sufficient to determine the three-body parameter. This idea is supported by theoretical results for the region of negative scattering lengths [Wan12, Sch12, Chi11, Nai14b, Nai14a], pointing to a new type of universality, named “van der Waals universality”, in atomic systems.

In the region of positive scattering lengths, the most suitable observables are atom-dimer resonances, as detected by enhanced losses in mixtures of atoms and dimers [Kno09, Blo13, Lom10a, Huc09, Nak10, Nak11]. They provide more direct and unambiguous evidence in contrast to related recombination minima and avalanches in atomic samples [Zac09, Gro09, Pol09]. The essential prerequisite for studying inelastic atom-dimer collisions is the existence

of efficient methods to convert atoms into dimers in a controlled manner. First measurements on atom-dimer mixtures were performed in samples consisting of Cs atoms and magneto-associated Cs dimers [Kno09]. Cesium represents an ideal candidate because of the rich Feshbach spectrum and the good atom-dimer conversion efficiency [Mar07]. These measurements, which were performed in the low magnetic field region, gave a first hint on large deviations from universal ratios [Kno09]. This result was unexpected as the experiments performed with atomic samples of Cs, in the same region of scattering lengths, have shown recombination minima at scattering length values consistent with universal behavior [Kra06]. Other experimental investigations have been performed with atom-dimer mixtures of different ^6Li hyperfine sublevels [Lom10a, Huc09, Nak10, Nak11] and in heteronuclear mixtures of fermionic $^{40}\text{K}^{87}\text{Rb}$ dimers and ^{87}Rb atoms [Blo13].

Theoretical models qualitatively explain the deviations in the relative positions of the atom-dimer features of the spectrum [Ham07a, Thø08b, D'I09, Pla09] by introducing finite-range effects. However, the predicted corrections are too small to explain the observed resonance positions. Recently, theoretical work [Wan14] has proposed a simple two-spin model to directly include the van der Waals (vdW) interaction into the Efimov problem for atomic systems. With this model, which we will refer to as “vdW model”, the predicted position of the atom-dimer resonance in Cs is in good agreement with the experimental observation made in the region of low magnetic field. The authors were also able to explain the deviation from the ideal scaling relation between positions of the triatomic and the atom-dimer loss resonances.

In this Article, we explore inelastic atom-dimer scattering in an ultracold mixture of Cs atoms and Cs_2 Feshbach molecules near a broad s -wave resonance located at about 550 G [Ber13]. Our measurements on the atom-dimer collisional rate coefficient β reveal a pronounced resonant feature similar to the one observed at low magnetic fields in our previous work [Kno09]. Our findings reveal a significant difference in the positions of the two atom-dimer resonances. This suggests that universality is much less robust for positive values of a as compared to the negative- a region. Nevertheless, we show that our observations can be quantitatively predicted in the framework of the universal vdW model according to Ref. [Wan14].

This Article is organized as follows. In Section 5.2 we describe the experimental procedure to create ultracold samples of atoms and molecules. In Section 5.3, we explain the measurement of the atom-dimer decay rates. Section 5.4 contains the comparison with previous results and available theoretical models. In Section 5.5 we discuss our experimental search for avalanche loss processes in samples of Cs atoms. In Section 5.6 we present our conclusions.

5.2 Experimental procedures

Our experiments are performed with an ultracold sample of Cs atoms in the ground-state sublevel $|F = 3, m_F = 3 \rangle$, where F is the hyperfine and m_F the magnetic quantum number. First we prepare the sample at high magnetic fields following the procedure described in Ref. [Ber13]. We then convert a fraction of the atoms into Feshbach molecules by magneto-association [Chi10, Her03]. More details on the near-threshold molecular structure, including

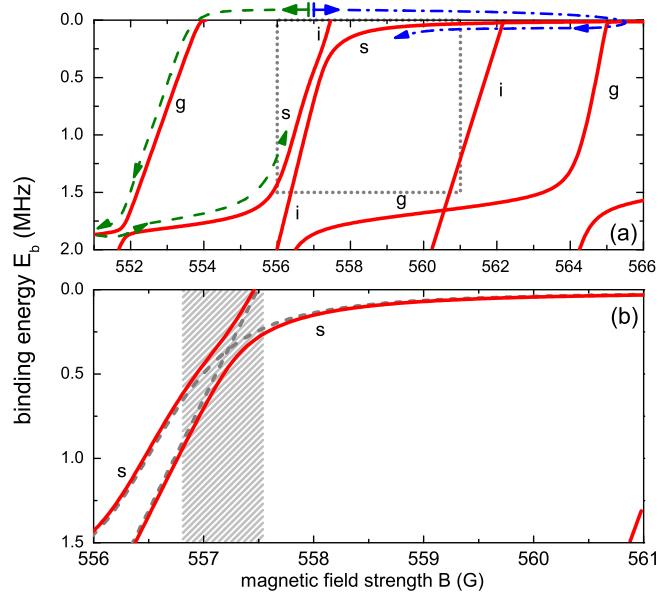


Figure 5.1: (color online) Near-threshold energy spectrum of Cs_2 in the magnetic-field region around 560 G. (a) The spectrum results from three g -, two i -, and two s -wave molecular states. The bent s -wave state is our target state for atom-dimer decay measurements and the g -wave states are used to prepare molecules in the s -wave state. The paths for molecule creation are indicated by the dashed and dash-dotted arrows. The dotted frame indicates the region of interest as magnified in panel (b). (b) The large i/s avoided crossing is highlighted by the difference between the uncoupled states (s , d , g basis set and i -wave state [Ber13]), shown as dashed lines, and the coupled states (solid lines); for details see text. The hatched region marks the range of B for which the s -wave character of the states is below 90%.

the relevant quantum numbers, can be found in Ref. [Ber13].

The atomic sample is evaporatively cooled in a crossed optical dipole trap generated by near-infrared single-frequency laser light at a wavelength of 1064.5 nm. As discussed in Ref. [Ber13] we take advantage of a broad open-channel dominated s -wave Feshbach resonance to control the elastic collisional rate during the evaporation stage. This resonance is centered at a magnetic field of $B = 548.78(9)$ G and has a width of $7.5(1)$ G.¹ Different from the experimental procedure described in Ref [Ber13], in the last part of the evaporation stage we set B to 556.9 G, corresponding to a scattering length a of about $280 a_0$, where a_0 is Bohr's radius.² We typically obtain 1.5×10^5 atoms at a temperature $T \approx 150$ nK. The final trap has a mean frequency of $\bar{\omega} = 2\pi \times 27.1(2)$ Hz. This non-condensed sample with a peak number density of $1.6 \times 10^{12} \text{ cm}^{-3}$ and a peak phase-space density of about 0.1 is our starting point for the creation of dimers.

Cesium exhibits a rich collection of Feshbach resonances [Ber13, Chi04]. These can be used

¹ For the present experiments, we have selected the 550-G Feshbach resonance instead of the even broader Feshbach resonance near 800 G, because the latter does not provide an efficient entrance gate to populate the weakly bound molecular state.

² The last stage of evaporation is performed at a smaller magnetic field as compared to Ref. [Ber13]. This is required to avoid entering the molecular state that causes the i -wave Feshbach resonance at 557.45 G when ramping down the magnetic field.

for magneto-association of atoms to molecules both in the low and in the high magnetic field regions. The near-threshold energy spectrum of the different molecular states in the magnetic-field region of interest is shown in Fig. 5.1. In absence of any coupling between the different energy states, the spectrum of the bare molecular states would show essentially straight lines: two states, an s - and a g -wave state, nearly parallel to the threshold ($E_b = 0$) with binding energies of about 25 kHz and 1.75 MHz,³ respectively, and five other states (one s -, two g -, and two i -wave states) with slopes of about 1 MHz/G relative to threshold. Various coupling mechanisms [Hut08] lead to a manifold of avoided crossings in the spectrum.

The bent s -wave state is the target state for our atom-dimer decay measurements. This state undergoes an avoided crossing with an i -wave state at $B = 557.25$ G and at a corresponding binding energy of 400 kHz. The coupling strength, *i.e.* half the energy splitting at the center of the crossing, is about 100 kHz. This is unusually strong for a crossing between states that differ by six units of angular momentum. The particular mechanism leading to this higher-order crossing is not understood in the framework of the available theory [Ber13]. The coupled-channel model presented in Ref. [Ber13] can accurately determine the positions and the coupling strengths of states with rotational quantum numbers up to $\ell = 4$ in a basis set of s , d , and g states. We have calculated the energies near the i/s -crossing as shown in Fig. 5.1 by fitting a simple two-level model to the experimental data [Ber13]. One level represents the bent molecular state in the s , d , g basis, and the other one is the bare i -wave state. In Fig. 5.1(b) we highlight with hatched shading the range of B in which the mixing reduces the s -wave character of the relevant state to below 90%. We can expect that the interaction physics of the dimers is open-channel dominated only outside of this region.

Because of the strong i/s avoided crossing we populate the s -wave state along two different paths similar to Ref. [Mar07]: To create s -wave molecules on the lower side of the avoided crossing we use the g -wave resonance at $B = 554.06(2)$ G; see dashed lines in Fig. 5.1. After the magneto-association the magnetic field B is slowly ramped down to 551 G to populate the g -wave state with binding energy of about 2 MHz by adiabatically following the g/g -wave avoided crossing near 552 G. A subsequent fast upward ramp for B allows diabatic transfer through the g/g -wave avoided crossing and then to easily access the lower region of the s -wave state by adiabatically following the s/g -wave crossing. The creation of molecules on the upper side of the i/s -wave crossing is achieved through the g -wave resonance at 565.48(2) G; see dash-dotted path in Fig 5.1. Here, the creation of s -wave molecules is facilitated by the relatively large coupling between the s -wave and the g -wave state at 565 G that allows us to switch from the g -wave to the s -wave state as we lower B . The coupling between the s -wave state and a second i -wave state at about 562 G is negligible and that crossing is always followed diabatically. In both cases, we convert about 8% of the initial atoms into molecules. The final samples contain about 10^5 atoms and 4×10^3 molecules in thermal equilibrium at a temperature $T \approx 175$ nK, atomic peak density of $9(1) \times 10^{11} \text{ cm}^{-3}$, and a molecular peak density of $9.8(2.1) \times 10^{10} \text{ cm}^{-3}$.

To determine the number of atoms and the number molecules we first release the mixture from the trap. We use the Stern-Gerlach technique by applying a strong magnetic field gradient for 3 ms to separate the molecules from the atoms. We then convert the molecules back to atoms by Feshbach dissociation ramps. Molecules above the s/i -crossing are dissociated

³ We give the values for the energies in frequency units.

by reversing the association path. For molecules below the s/i -crossing we ramp up the magnetic field to dissociate them to atoms via the i -wave state. We detect the atoms by standard absorption imaging.

5.3 Measurements of atom-dimer decay

Inelastic atom-dimer collisions are quantitatively described by the corresponding rate coefficient β . We measure this quantity by observing the decay of the number of molecules in the mixture. For this purpose, we record the time evolution of the atom number N_A and the molecule number N_D for different values of B , similarly to Ref. [Kno09]. We carry out additional measurements in pure dimer samples to determine the background losses caused by inelastic dimer-dimer collisions.

The decay of N_D in the trap can be modelled by the rate equation [Kno09]

$$\frac{\dot{N}_D}{N_D} = -\beta' \frac{N_A}{V} - \alpha \frac{N_D}{V}, \quad (5.1)$$

with an effective volume $V = [2\pi k_B T / (m\bar{\omega}^2)]^{3/2}$. Here, m is the Cs atomic mass. For the loss rate coefficient we use $\beta' = \sqrt{8/27} \times \beta$, where the factor $\sqrt{8/27}$ takes into account the overlap between the atomic and molecular clouds [Kno09]. The first term in Eq. (5.1) accounts for atom-dimer losses, while the second term models dimer-dimer background losses characterized by the rate coefficient α . In our samples, the number of atoms is typically 25 times larger than the number of molecules and thus N_A can be considered as approximately constant. Three-body losses take place on a timescale much larger than the timescale for atom-dimer losses and are negligible [Kra06, Kno09].

To determine the background contribution of dimer-dimer losses to the measured decay curves, we carry out measurements in pure molecular samples to extract the rate coefficient α . For such measurements, we remove the atoms with a pulse of resonant light [Mar07]. An example of a decay measurements on pure molecular samples is shown in Fig. 5.2 together with the data obtained with an atom-dimer mixture at the same value for B . The larger lifetime of the pure molecular sample is evident and clearly demonstrates that losses in our mixture are dominated by inelastic atom-dimer collisions.

Figure 5.3(a) shows the values of the loss rate coefficient α measured on the two sides of the avoided crossing. In the magnetic field region of interest the coefficient α shows a strong enhancement close to the avoided crossing. We attribute this to the strong closed-channel contribution in this region. Above the crossing, we observe a behavior resembling previous observations for dimer-dimer collisions in the low-field region [Fer08], showing an increase of α for higher magnetic fields where the scattering length a becomes larger. We note that we have also observed two narrow loss features in dimer-dimer collisions at about 556.65(5) G and 556.94(5) G similar to observations reported in Refs. [Chi05, Fer10b]. We attribute these features to Feshbach-like resonances, most likely resulting from the coupling of two colliding dimers to a tetramer state.

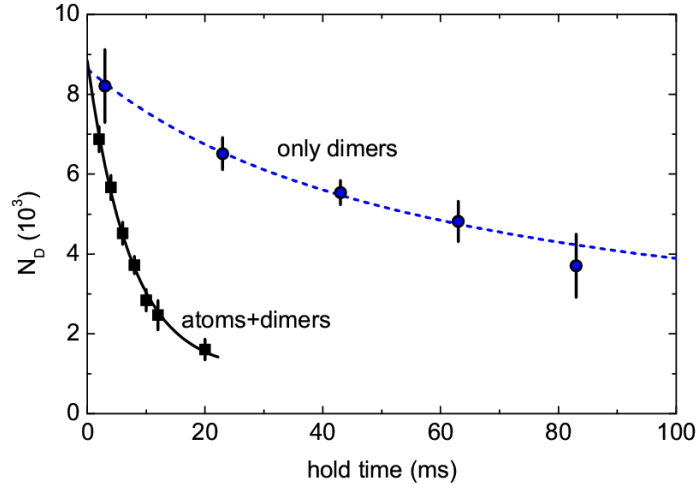


Figure 5.2: (color online) Atom-dimer versus dimer-dimer loss. The number N_D of remaining dimers after a variable hold time for $B = 557.7$ G ($a \approx 400 a_0$) for a pure molecular sample (circles) and for an atom-dimer mixture (squares). The dashed line is the result of the fit according to a two-body decay rate equation $\dot{N}_D = -\alpha N_D^2/V$ giving $\alpha = 2.4(3) \times 10^{-10} \text{ cm}^3/\text{s}$. The solid line is a fit according to Eq. (5.2). The error bars represent the standard deviation for N_D given 5 to 10 experimental runs. Note that, in this particular set of measurements, the initial number of dimers is twice higher than under usual experimental conditions, which enhances dimer-dimer losses.

The atom-dimer relaxation rate coefficient β' can now be determined by fitting the molecule number with the solution of Eq. (5.1) for constant N_A ,

$$N_D(t) = \frac{\beta' N_A N_{D,0}}{(\beta' N_A + \alpha N_{D,0}) e^{\beta' N_A t/V} - \alpha N_{D,0}}, \quad (5.2)$$

where the free parameters are the initial number of molecules $N_{D,0}$ and the rate coefficient β' , whereas α , N_A and V are separately measured quantities. The values obtained for the rate coefficient β are displayed in Fig.5.3(b) as a function of B . It shows a distinct maximum near $B = 558.5$ G in a range of B where the s -wave character is dominant and where dimer-dimer losses are very weak. We interpret this feature as an atom-dimer resonance caused by the coupling to an Efimov-like three-body state, in analogy with our previous low-field observation [Kno09].

5.4 Comparison with previous results and theory

The observation of an atom-dimer resonance in the region of high magnetic fields as reported here can be compared to the previous observation of an atom-dimer resonance at low magnetic fields [Kno09]. This comparison provides a test of the universality of the three-body system for $a > 0$ and thus complements our previous work on triatomic Efimov resonances for $a < 0$ [Ber11b].

Figure 5.4 presents the atom-dimer loss rate coefficient β as a function of the scattering length a . Panel (a) shows the new data and panel (b) shows the data from Ref. [Kno09].

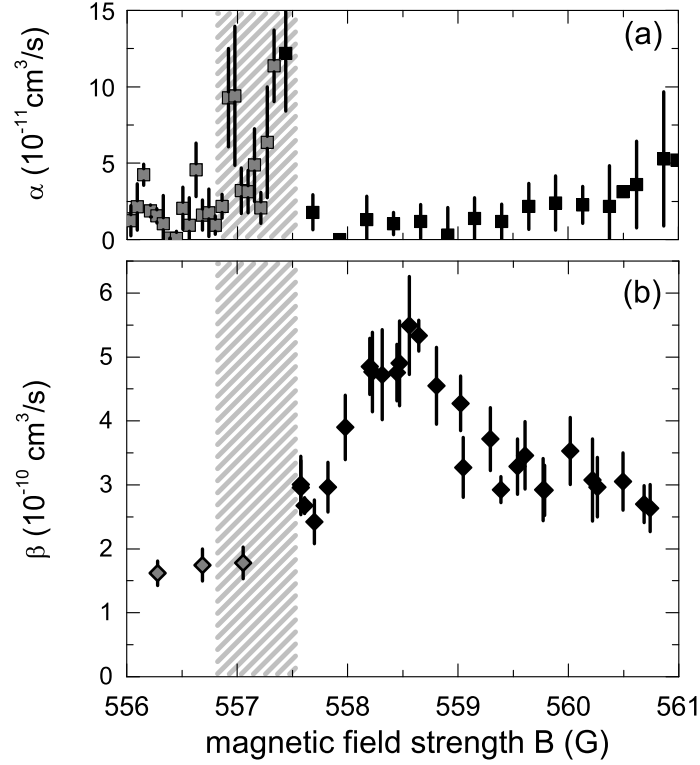


Figure 5.3: Measured dimer-dimer and atom-dimer loss rate coefficients. (a) The dimer-dimer loss rate coefficient α and (b) the atom-dimer loss rate coefficient β are plotted as a function of B . They are determined from measurements as shown in Fig. 5.2. The data in (a) is obtained for hold times of up to 10 ms at the lower side of the avoided crossing (gray squares) and up to 20 ms at the upper side (filled squares). In (b), gray diamonds are data obtained on the lower side of the avoided crossing and filled diamonds are data on the upper side. The error bars contain the statistical uncertainties on the number of atoms and dimers, trap frequencies, and temperature. As in Fig. 5.1, the hatched region indicates the range of B in which the s -wave character of the states is below 90%.

For the $a(B)$ conversion in both data sets, we have used the most recent and very accurate model M2012 [Ber13]. The different positions of the two resonant features are evident, with the one observed at high magnetic fields centered at $a \approx 600 a_0$ and the one at low fields centered at about $400 a_0$. This difference stands in contrast to the recent observations on triatomic Efimov resonances at negative a [Ber11b], where the resonance positions appear at essentially the same values of a .

In Sec. 5.4.1, we first present a fit of our experimental data based on effective field theory (EFT), which allows us to extract the parameters describing the atom-dimer resonances. In Sec. 5.4.2, we then compare our observations with a recently developed model [Wan14] that takes the vdW interaction into account. Finally, in Sec. 5.4.3 we, discuss our findings in view of the universality of three-body physics in real atomic systems.

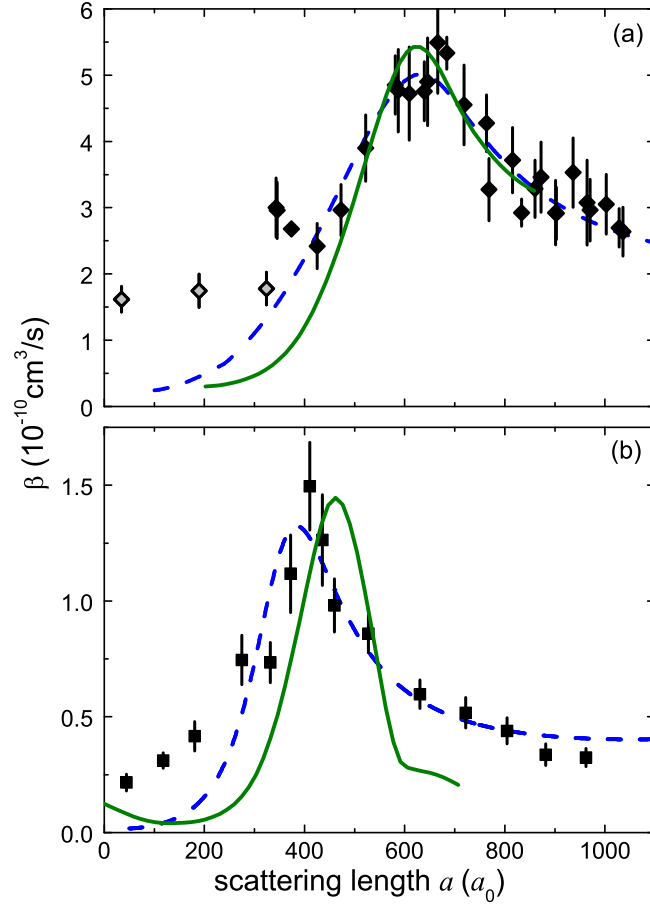


Figure 5.4: (color online) Atom-dimer loss rate coefficient β for Cs as a function of the scattering length a in the high (a) and low (b) magnetic field regions. In panel (a) the filled (gray) diamonds result from the measurements performed on the upper (lower) side of the avoided crossing at 175 nK, as in Fig. 5.3(b). In panel (b) the filled squares are data from Ref [Kno09] acquired at 170 nK. In both panels, the dashed and the solid lines represent the EFT fit and the prediction of vdW model scaled by the factors D and D' (see text), respectively. Error bars include statistical uncertainties on temperature, trap frequencies, and atom numbers and the fitting uncertainties.

5.4.1 Effective field theory

We analyze our measurements of the loss rate coefficient β by using the results of EFT [Bra07, Bra09a]. EFT provides a general description of the functional dependence $\beta(a)$, without being able to predict the resonance position and its width. The theory thus contains two free parameters, a_* and η_* , which are determined by fits to the experimental data. Our fit also includes an additional amplitude scaling factor D to account for systematic errors in the number density and other possible factors influencing the magnitude of β [Kno09, Ber11b].

The dashed lines in Fig. 5.4 show the results of the EFT fits for the two resonances. For the high-field data in panel (a), we exclude from the fit the five data points with $a < 400 a_0$, corresponding to the points below 557.6 G in Fig. 5.3(b). These points lie in the region where we suspect a strong influence by the i/s -wave crossing. Alternatively, we also include

B_{res}	s_{res}	a_{bg}/a_0	k_0/a_0	a_-/a_0 [Ber11b]
-12.3 G	560	≈ 1700	180(20)	-872(22)
548.8 G	170	≈ 2500	210(20)	-957(80)

continuation of the table (rows):

EFT fit					vdW	$a_*/ a_- $		
a_*/a_0	δ_1/a_0	δ_2/a_0	η_*	D	D'	Exp	Efim.	vdW
+419(10)	8	6	0.06(2)	0.64(23)	0.48(7)	0.48(2)	1.06	0.54
+653(25)	12	22	0.07(2)	2.8(9)	5.6(3)	0.68(6)	1.06	0.65

Table 5.1: Parameters for the two Feshbach resonances and the associated atom-dimer resonances. The first column gives the magnetic field value B_{res} for the center of the s -wave Feshbach resonance. The quantities s_{res} , a_{bg} , and k_0 are the resonance strength, the background scattering length, and the effective range, respectively [Chi10]. The effective range k_0 at the atom-dimer resonance position has been calculated by using the latest Cs potentials. The values for the triatomic resonance positions a_- are taken from Ref. [Ber11b] and the errors include all statistical uncertainties. For the values of a_* the number in parentheses gives the full statistical uncertainty, while δ_1/a_0 and δ_2/a_0 are the uncertainties resulting from the fit and from the conversion $a(B)$ [Ber13], respectively. The scaling factors D and D' result from the EFT fit [Bra01] and from the amplitude fit according to the results from the vdW model. The last three columns give the values for $a_*/|a_-|$ as determined by the experiment, as given by Efimov’s universal solution [Gog08], and as given by the vdW model. The error for $a_*/|a_-|$ includes all statistical uncertainties.

the lowest two data points in the fits (below the hatched region in Fig. 5.3(b)), finding that this has negligible effect on the resulting value of a_* . For the low-field data set in panel (b) [Kno09], the fit takes into account all data points.

Table 5.1 summarizes the fit parameters for the two atom-dimer resonances. The values a_* obtained for the resonance positions are $+653(25) a_0$ and $+419(10) a_0$ for the high and low field features, respectively. The uncertainties include the statistical contributions and the uncertainties for the $a(B)$ conversion [Ber13]. The difference in a_* is remarkable and much larger than the uncertainties, while the values obtained for the width parameter η_* are comparable within the error bars. The amplitude scaling factors resulting from the fit are $D = 2.8(9)$ (high-field case) and $0.64(23)$ (low-field case), showing considerable deviations from unity with an opposite trend.

5.4.2 Universal van der Waals theory

Recently, Wang and Julienne have introduced a new model [Wan14] that builds in the pairwise van der Waals (vdW) interaction and, based on a numerical solution of the three-body Schrödinger equation, predicts the collision rate constants without any adjustable parameters. To describe the Feshbach resonance, the background scattering length a_{bg} and the resonance strength parameter s_{res} [Chi10] are needed as the two input parameters. For both cases considered here, we are in the regime of $s_{\text{res}} \gg 1$ (entrance-channel dominated resonances) and of a large $a_{\text{bg}}/R_{\text{vdW}} \gg 1$. For Cs, R_{vdW} is equal to $101 a_0$ [Chi10].

The solid lines in Fig. 5.4 show the results of the universal vdW model.⁴ Although the theory, in principle, does not contain a free parameter, we introduce an additional amplitude scaling factor D' to obtain an optimum fit with the experimental data; this is analogous to the parameter D used in the EFT fit. The amplitude scaling factor takes into account possible amplitude variations between experiment and theory, which may result from various sources. On the experimental side, errors may result from the number density calibration and, on the theoretical side, the decay channels to deeply bound molecular states may not be properly taken into account because of the nonuniversal nature of these target states. Considerable amplitude deviations have been seen also in other experiments on atom-dimer resonances [Blo13, Lom10a, Nak10].

For the high-field resonance in Fig. 5.4(a), we find that the model describes its position and width very well, but an amplitude scaling factor of $D' = 5.6$ is needed to fit the data (see Table 5.1). The predicted value a_* for the loss maximum is $+625 a_0$, which is consistent with the observed value $+653(25) a_0$ within 1.1σ of its uncertainty. For the low-field resonance in (b), the maximum appears at $+460 a_0$, which is significantly (about 4σ) above the experimental value $a_* = +419(10) a_0$. This deviation corresponds to 3% of the Efimov period and may thus be considered as quite small. The required amplitude scaling factor $D' \approx 0.5$ is much smaller than in the high-field case.

5.4.3 Discussion

In the ideal Efimov scenario with its discrete scaling factor of 22.7, the positions of all observables follow fixed ratios [Bra06]. Those ratios, which are strictly valid only in the limit of very large a , provide benchmarks for testing the scenario in real atomic systems and for quantifying possible deviations. As such a benchmark, the position of the lowest atom-dimer resonance is ideally related to the one of the lowest triatomic resonance at a_- by the ratio $a_*/|a_-| = 1.06$. With the experimentally determined values for a_* , as presented in Sec. 5.4.1, and the values for a_- determined in our previous work [Ber11b], we obtain 0.68(6) for the high-field region and 0.48(2) for the low-field region. These two experimental determinations of $a_*/|a_-|$ both lie substantially below the ideal value. This general trend is qualitatively expected based on theoretical approaches beyond the universal Efimov limit [D'I09, Pla09, Tho08b].

The two results for $a_*/|a_-|$ obtained for different Feshbach resonances deviate from each other, which points to the importance of the character of the underlying Feshbach resonance. Finite-range corrections as described to first order in terms of the effective range k_0 [Chi10] are not likely to explain the deviations, as k_0 shows only minor differences for both cases. This raises the question whether higher-order finite-range corrections may be relevant.

The universal vdW model, discussed in Sec. 5.4.2, provides predictions remarkably close to the experimental observations and reproduces the central experimental findings that (i) the atom-dimer resonances are substantially down shifted as compared to the expectation from the universal Efimov limit, and that (ii) this down shift is smaller in the high-field region than

⁴ Y. Wang and P. S. Julienne, private communication (2014).

in the low-field case. Comparing the two Feshbach resonances, the question arises whether the different values for $a_*/|a_-|$ can be mainly attributed to the difference in s_{res} or in a_{bg} , or whether a combination of both is necessary to understand the situation.

An open issue concerns the amplitude of the observed atom-dimer resonances. In the high-field region the resonance amplitude is clearly larger than theoretically expected, which is quantified by the amplitude scaling parameters $D = 2.8(9)$ and $D' = 5.6(3)$ for the two fits applied. These values are too large to be explained by systematic experimental uncertainties, which we estimate to be below 50%. For the previously observed atom-dimer resonance in the low-field region, the amplitude scaling factors $D = 0.64(23)$ and $D' = 0.48(7)$ are smaller than one, which indicates a trend opposite to the high-field region, but consistent with the observations of Refs. [Blo13, Lom10a, Nak10]. We can only speculate about possible causes for this difference. The collisional decay leads to more tightly bound molecular states and therefore involves coupling at short ranges. The present models apparently get the order of magnitude right, but they do not permit to describe the amplitude of the resonant decay on a fully quantitative level.

5.5 Search for an atom-dimer avalanche effect

Three experimental groups have reported on the observation of atom-dimer resonances in measurements performed with purely atomic samples of ^{39}K [Zac09] and ^7Li [Gro09, Pol09]. These indirect observations have been attributed to an *avalanche* process, during which the dimers formed in three-body recombination events collide elastically with the trapped atoms before leaving the sample. The energy released in a single recombination event is sufficient to kick several atoms out of the trap, which leads to enhanced losses. These measurements are still debated [Mac12, Lan12, Lan13] as the atom-dimer peak position a_* can only be inferred employing a collisional model. In this Section, we present measurements obtained in pure atomic samples. We show that they are well described by EFT and the vdW model, without any significant avalanche effect.

We have measured the fraction of lost atoms after a fixed hold time in a magnetic field range corresponding to a between 400 and 1100 a_0 . The hold times have been chosen in order to have an observable loss fraction in the range between 10 and 50%. First we performed our measurements with the atomic sample as described in Sec. 5.2, having a temperature of 170 nK and an initial peak number density of $1.6 \times 10^{12} \text{ cm}^{-3}$. Figure 5.5(a) shows our results. As predicted, the loss fraction increases for larger values of a as expected from the a^4 scaling [Web03c]. However, within our experimental uncertainties, the losses do not show any significant enhancements, neither at the atom-dimer resonance position a_* nor at any other values of a . We have performed the loss measurements in samples with a higher peak density of $3.2 \times 10^{12} \text{ cm}^{-3}$, which are obtained in the course of a further evaporation step down to 40 nK. Also with these experimental conditions we have observed no significant loss enhancement, as can be seen from the data Fig. 5.5(b).

⁵ Y. Wang and P. S. Julienne, private communication (2014).

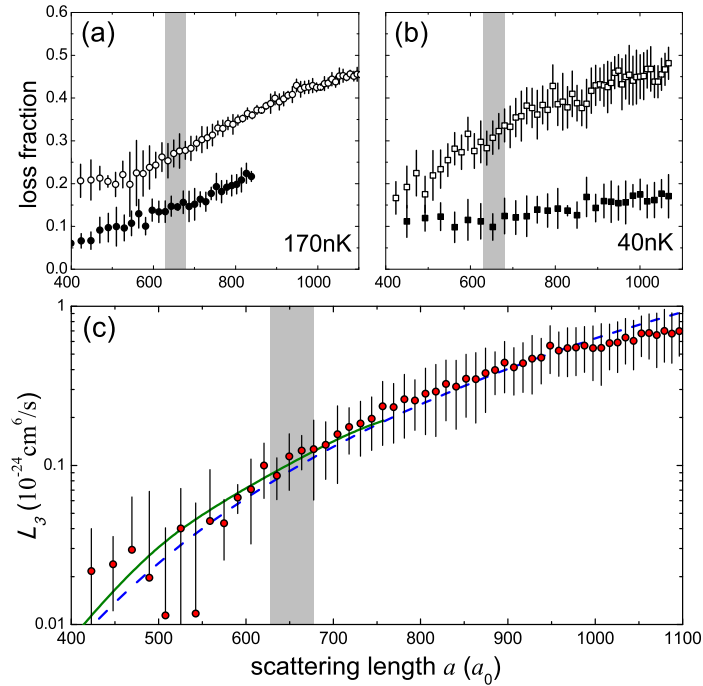


Figure 5.5: (color online) Loss measurements in pure atomic samples. The loss fraction is measured with samples of (a) 1.5×10^5 atoms at a temperature of about 170 nK and (b) 4×10^4 atoms at 40 nK. In (a), the hold time is 2 s for the open symbols and 400 ms for the filled ones. In (b), the hold time is 1 s for the open symbols and 50 ms for the filled ones. (c) The recombination rate coefficient L_3 is extracted from the data set with a hold time of 2 s from panel (a). The dashed line is the prediction from EFT [Bra01], while the solid one is derived within the vdW model.⁵ The error bars include the statistical uncertainties on the atom number. In all three panels, the grey region indicates the position of the loss resonance in atom-dimer mixtures; see Sec. 5.4. The width of this region reflects the uncertainty of the resonance’s center position.

From the loss fraction data obtained at 170 nK with a hold time of 2 s, see open symbols in Fig. 5.5(a), we extract the three-body recombination rate coefficient L_3 . This is possible under the assumption that three-body collisions are the dominant loss mechanism and that heating is caused by the anti-evaporation effect [Web03c]. For values of a below $500 a_0$, we observe additional background losses on a timescale exceeding tens of seconds. These background losses are subtracted in our data analysis. Figure 5.5(c) shows our results on $L_3(a)$ together with the predictions of EFT⁶ and the universal vdW model.

Our experimental data are consistent with the two loss models and this result suggests that losses in atomic samples of Cs under our experimental conditions can be predicted without including avalanche processes. Our results are consistent with earlier observations in the low magnetic field region that did not reveal any loss feature. Our observations are not consistent with predictions of a loss peak in Cs as discussed in [Mac12], but the model may not be appropriate for the specific situation of Cs.⁷ The model of Ref. [Lan12] predicts a very

⁶ Here we use $a_- = -957 a_0$ for the three-body parameter as determined in Ref. [Ber11b]. Assuming the relations of the ideal Efimov scenario [Fer11], this puts the three-body recombination minimum to about $+200 a_0$, which is well below the range displayed in Fig. 5.5(c).

⁷ L. Khaykovich, private communication (2013).

broad feature of moderately enhanced losses near a_* . As it is experimentally very difficult to discriminate such a feature from the background, we cannot draw any conclusion on its presence.

A recent preprint reports on a search for the avalanche effect in heteronuclear atomic mixtures of ^{40}K and ^{87}Rb [Hu14]. A narrow avalanche feature could not be observed, neither at values for a where an atom-dimer resonance has been observed previously [Zac09, Gro09, Pol09], nor at other values. These observations are consistent with our findings and the suggested avalanche mechanism [Zac09] remains an unresolved issue.

5.6 Conclusions

In conclusion, we have investigated inelastic atom-dimer collisions in mixtures of Cs atoms and Cs₂ dimers in the region of positive scattering lengths near the 550 G Feshbach resonance. Our measurements reveal a resonance that results from the coupling of an atom and a dimer to an Efimov trimer state. We fit the data by using effective field theory predictions and we determine the resonance position and width. The resonance position $a^* = +653(25)a_0$ significantly deviates from the previous result obtained in the low magnetic field region, $a^* = +419(10)a_0$. For both resonances, their positions relative to the corresponding triatomic loss resonances strongly deviate from the ratio predicted for an ideal realization of Efimov's scenario in the large- a limit. These observations demonstrate that universality is less robust in the positive- a region than previously observed in the negative- a region [Ber11b], much more depending on the particular properties of the underlying Feshbach resonances used for interaction tuning.

We have compared our results with recent predictions obtained within the universal vdW model of Ref. [Wan14], which only requires the Feshbach resonance parameters and the vdW length to locate the Efimov features. The positions and the widths of the observed loss resonances are in very good agreement with the vdW model. For both resonances, the observed amplitudes differ strongly from the theoretical predictions. Surprisingly, they deviate in opposite directions for the two Feshbach resonance scenarios. Our results are an important step towards a complete understanding of Efimov processes in atomic systems. The extension of similar theoretical and experimental investigations to other species and to heteronuclear mixtures can probably shed new light on the appearance of Efimov states in real atomic systems, the robustness of universality, and on the influence of the particular Feshbach resonances on the Efimov spectrum.

Additional loss measurements carried out in purely atomic samples have not provided any signatures of an avalanche effect near the atom-dimer resonance position. The presence or absence of such features depending on the particular species is an unresolved issue that deserves more attention in future experiments.

Acknowledgements

We thank P. S. Julienne and Y. Wang for discussions and for providing us with their model results, and J. D’Incao, L. Khaykovich, and E. Braaten for fruitful discussions. This work was supported by the Austrian Science Fund FWF within project P23106. A. Z. was supported within the Marie Curie Project LatTriCs 254987 of the European Commission.

Publication: Resonant five-body recombination in an ultracold gas of bosonic atoms[†]

New J. Phys. **15**, 043040 (2013)

Alessandro Zenesini,^{1, 3} Bo Huang,¹ Martin Berninger,¹ Stefan Besler,¹
Hanns-Christoph Nägerl,¹ Francesca Ferlaino,¹ and Rudolf Grimm^{1,2}

¹*Institut für Experimentalphysik und Zentrum für Quantenphysik,
Universität Innsbruck, 6020 Innsbruck, Austria*

²*Institut für Quantenoptik und Quanteninformation,
Österreichische Akademie der Wissenschaften, 6020 Innsbruck, Austria*

³*Institut für Quantenoptik, Leibniz Universität Hannover,
D-30167 Hannover, Germany*

Chris H. Greene^{4,5} and Javier von Stecher^{4,6}

⁴*Department of Physics and JILA, University of Colorado, Boulder, CO 80309, USA*

⁵*Department of Physics, Purdue University, West Lafayette, IN 47907, USA*

⁶*Tech-X Corporation, Boulder, CO 80303, USA*

We combine theory and experiment to investigate five-body recombination in an ultracold gas of atomic cesium at negative scattering length. A refined theoretical model, in combination with extensive laboratory tunability of the interatomic interactions, enables the five-body resonant recombination rate to be calculated and measured. The position of the new observed recombination feature agrees with a recent theoretical prediction and supports the prediction of a family of universal cluster states at negative a that are tied to an Efimov trimer.

[†] A.Z. and the author of the present thesis recorded and analyzed the data together. M.B. and S.B. contributed in maintaining and improving the setup. C.H.G and J.v.S. provided theoretical support.

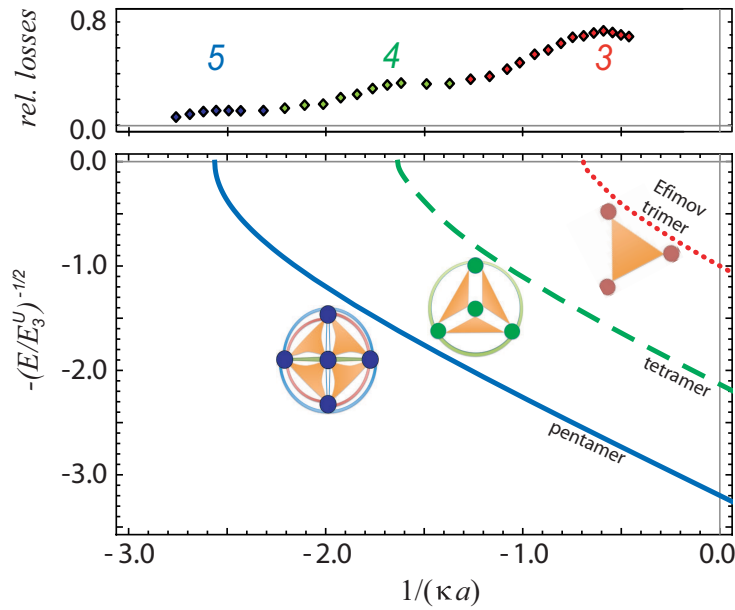


Figure 6.1: N -body scenario in the region of negative two-body scattering length a . The lower panel shows the N -body binding energies as functions of the inverse scattering length. $E_3^U = (\hbar\kappa)^2/m$ is the trimer binding energy for resonant interaction. The dotted, dashed and solid lines refer to the ground states of three-, four- and five-body cluster, respectively. Excited states are not drawn here. The pictorial representations of the three-, four-, and five-body bound state illustrate one of the possible spatial arrangements of atoms, given that an N -body cluster state has $N(N-1)(N-2)/6$ possible combinations of the three-body sub-clusters. The upper panel shows the relative losses from the atomic sample for a typical set of measurements, performed with a hold time of 100 ms for a sample of 10^5 atoms at 100 nK in a trap with mean trap frequency of about 30 Hz.

6.1 Introduction

Few-body physics with ultracold atoms has emerged as a new research field combining concepts from atomic, nuclear and condensed-matter physics. A growing number of experimental and theoretical studies have been focused on both the fundamentals of few-body phenomena [Bra06] and the connections with many-body systems [Fer10a, Gre10]. The cornerstone of recent experimental advances is the control of interactions in an ultracold atomic gas, offered by magnetically tuned Feshbach resonances [Chi10]. In particular, the tunable s -wave scattering length a allows to access the regime of resonant two-body interactions. Here, the system is governed by universal behavior, independent of the short-range details of the interaction potential. The paradigm of universality is Efimov's solution to the problem of three resonantly interacting particles [Efi70]. Once the intimate connection between Efimov states and three-body recombination has been established [Nie99, Esr99, Bra06], resonant loss features became the fingerprint of Efimov physics in experimental studies with ultracold atoms [Kra06, Ott08, Huc09, Kno09, Zac09, Bar09, Gro09, Nak10, Gro10, Lom10a, Nak11, Pol09, Fer11].

Advances in three-body physics led to intriguing questions on the generalization of Efimov's scenario to more particles and on the existence and observability of universal few-body

cluster states [Blu00, Blu02, Adh81, Nau87, Pla04, Han06]. N -body cluster states known as *Brunnian* states exist in a range of interaction where no $(N - 1)$ -body weakly bound subsystems are present [Ric94, Yam11]. The general connection, however, between cluster states and the three-body Efimov states has remained an open issue. It was soon realized that no “true” Efimov states¹ with $N > 3$ exist, because of the quite different scaling and threshold properties of the cluster states [Ama73]. However, other approaches to extend universal Efimov theory to larger systems have been pursued along different lines [Sør02, Yam06, Thø08a]. The development of accurate descriptions of four-boson systems [Ham07b, von09, Del10] demonstrates the existence of four-body states tied to each three-body Efimov state. In a major extension of Efimov physics, Ref. [von10] predicts the existence of a family of cluster states tied to an Efimov trimer.

According to Refs. [von09, Del10, von10, vS11], the binding energy of the cluster states follows universal scaling laws, which are directly connected to the Efimov effect. Figure 6.1 shows the calculated energy spectrum for the ground states of three-, four- and five-body clusters (lower panel). The corresponding experimental observables are loss peaks in the atom number (upper panel), which appear at values of the scattering length a_- , $a_{4,-}$, and $a_{5,-}$, where the three-, four- and five-body states cross the free atom threshold, respectively. The resonant values of the scattering length are predicted to be universally connected by the simple relations $a_{4,-} = 0.44(1) a_-$ and $a_{5,-} = 0.65(1) a_{4,-}$ [vS11]. A more recent study [Del12] has theoretically explored the four-boson resonance and has determined its position with greater accuracy. For four-body states, the universal relation has been confirmed in experiments [Zac09, Pol09, Fer09, Fer11] and the four-body recombination rate has been measured [Fer09] and calculated within the hyperspherical framework [von09]. A straightforward extension to five-body systems is not currently possible for experiment nor theory. The experimental challenge is to discriminate the five-body recombination signal against a strong background resulting from fewer-body processes. The numerical difficulty of the scattering few-body problem grows exponentially with the number of particles making the description of five and larger systems beyond current theoretical capabilities.

This article presents a combined theoretical and experimental study of universal few-body physics up to five-body states. We present strong evidence for the existence of an Efimov-related cluster state of five identical bosons and we provide quantitative results for the corresponding five-body recombination rate. Our results highlight a new level of understanding concerning few-body physics and its experimental manifestations in ultracold atomic quantum gases.

6.2 Theoretical approach

The theoretical analysis of N -body recombination processes requires the description of the N -body scattering continuum. The hyperspherical framework has been successfully applied to describe recombination processes for $N > 3$ [von09, Meh09]. In this framework, the Hamiltonian is diagonalized adiabatically as a function of the hyperradius R , which describes the

¹ The “true” Efimov effect refers to the appearance of an infinite number of N -body bound states, which have a discrete scale invariance and which exhibit well-defined thresholds given by the $(N - 1)$ -body subsystem.

overall size of the system, leading to a set of coupled one-dimensional Schrödinger equations. At ultralow temperatures and large scattering lengths, N -body recombination events are mainly controlled by scattering processes with incoming flux in the lowest N -body scattering channel and outgoing flux in deeper loss channels. The coupling to the deep channels is assumed to remain approximately unaffected as the scattering length and the collision energy are varied throughout our regime of interest. Thus, all the relevant information comes from the analysis of the lowest N -body potential curve corresponding to the incoming scattering channel.

However, the extraction of the hyperspherical potential curves and couplings becomes computationally unfeasible as the number of particles increases. Currently, the numerical technology allows for the calculation of potential curves of three and four-body systems but no tractable method has yet been implemented that can calculate both the potential curves and couplings for $N > 4$. However, the trapped energy eigenvalue spectrum of a five-body system can be accurately obtained with current technology. Thus, the present study extracts the relevant recombination information from an analysis of the trapped spectrum.

Our starting point is the hyperspherical description of the ultracold N -body recombination rate [Meh09],

$$L_N^{0+} = \left(\frac{4\pi}{k^2}\right)^{(3N-5)/2} \frac{\hbar N \Gamma(3N/2 - 3/2)}{\mu_N} (1 - |S_{00}^{0+}|^2), \quad (6.1)$$

where $\mu_N = m / \sqrt[N]{N}$ with m being the atomic mass, $k = (2\mu_N E / \hbar^2)^{1/2}$ is the incoming hyperradial scattering wavenumber and S_{00}^{0+} is the diagonal element of the S-matrix for the lowest channel (00) in the $J^{\Pi} = 0^+$ symmetry. For purely elastic scattering $|S_{00}^{0+}|^2 = 1$ and the recombination rate is zero. In the limit in which every N -body collision leads to losses, $|S_{00}^{0+}|^2 = 0$. Taking the thermal average in the full loss case at a temperature T , one obtains the unitary limit for N -body recombination at low energy:

$$\langle L_N \rangle_T = (2\pi)^{(3N-5)/2} N \frac{k_B T}{\hbar} \left(\frac{\hbar^2}{\mu_N k_B T}\right)^{3(N-1)/2}. \quad (6.2)$$

Based on potential curves computed for the three- and four-body cases, we expect that the five-body potential curve should have the topology depicted as a solid curve in Fig. 6.2, i.e., the lowest potential curve exhibits a barrier that separates the inner region (small R) from the asymptotic scattering region at large R . Note that the effective mock-centrifugal barrier [Fan76] in the lowest N -body continuum channel at large R is guaranteed to have the form (for finite a), $U(R) \rightarrow \hbar^2(3N-4)(3N-6)/2\mu_N R^2$. For this potential curve topology, an extension of the semiclassical (WKBJ) treatment of Berry [Ber66] to include the decay to the lowest channels yields [Meh09]:

$$(1 - |S_{00}|^2) = \frac{e^{-2\gamma}}{2} \frac{\sinh(2\eta_-)}{\cos^2 \phi_{\text{in}} + \sinh^2 \eta_-} A(\eta_-, \gamma, \phi_{\text{in}}), \quad (6.3)$$

where ϕ_{in} is the WKBJ phase for the inner allowed region, γ is the WKBJ tunneling integral in the barrier region, η_- describes the decay to deeper, non-universal, channels and is treated as a fitting parameter, and $A(\eta_-, \gamma, \phi_{\text{in}})$ ensures the proper normalization. Thus,

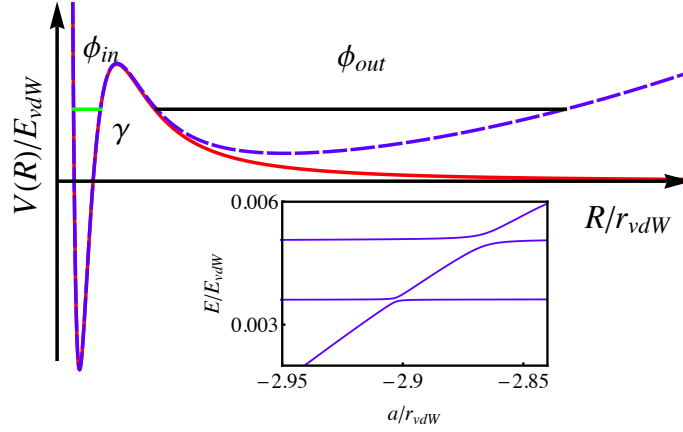


Figure 6.2: Schematic representation of lowest five-body hyperspherical potential curve. The solid curve represents the free-space hyperspherical potential while dashed curves represent hyperspherical potential curves in the presence of a harmonic potential. Solid lines represent the inner and outer WKB phases. Inset: Five-body trapped energy spectrum in the region where the bound five-body state crosses the lowest trapped states.

the determination of γ and ϕ_{in} for the relevant range of energy and scattering length gives an approximate description of five-body recombination.

The novelty of our approach is the determination of γ and ϕ_{in} from an analysis of the trapped spectrum. The five-body trapped energy spectrum is obtained using a correlated Gaussian basis set expansion [vS11]; for details see 6.5. In the region where the five-body resonance occurs, the spectrum exhibits a series of avoided crossings between the five-body states bound in the inner region and the outer trap region states (see Fig. 6.2). In the WKBJ approximation, the quantization condition for the trapped potential curve (dashed curve in Fig. 6.2) is $\frac{\Delta}{2} \tan(\phi_{in}) \tan(\phi_{out}) = 1$, where $\Delta = e^{-2\gamma}/2$. For collision energies below the barrier local maximum and away from the avoided crossings, the allowed energy eigenvalues occur when $\phi_{\alpha}(E, a) \approx \pi(i+1/2)$, where i is an integer and $\alpha = in, out$. The phase ϕ_{in} in the four-boson case near the resonance energy is known from our previous work [Meh09] to be well-described by $\phi_{in} \approx \phi_{in,0} + b(a/r_{vdW}) + caE/(r_{vdW}E_{vdW})$, where $\phi_{in,0}$, b and c are fitting parameters and r_{vdW} and E_{vdW} are the van der Waals radius and energy, respectively, as defined in [Chi10]. Using this simple form in the five-body case and imposing the eigenstate condition for bound states, the values of $\phi_{in,0}$, b and c for $N = 5$ are extracted.

Next, an analysis of the spectrum at the avoided crossings (see e.g. Fig. 6.2) determines γ , as explained in detail in 6.5. The relevant avoided crossings occur when $\phi_{in} \approx \phi_{out} \approx \pi(i+1/2)$. For narrow avoided crossings ($\Delta \ll 1$), the quantization condition reduces to $\delta\phi_{in} \delta\phi_{out} \approx \frac{\Delta}{2}$ where $\phi_{\alpha} = \pi(i+1/2) + \delta\phi_{\alpha}$. Right at the avoided crossing, the energy difference between the two states ($2\Delta E$) is related to Δ , namely as $\delta\phi_{\alpha} \approx (d\phi_{\alpha}/dE)\Delta E$. The quantization condition thus reduces to $\Delta \approx 2\Delta E^2(d\phi_{in}/dE)(d\phi_{out}/dE)$. Consequently knowledge of ϕ_{in} , ϕ_{out} and the energy avoided crossings allows the tunneling γ to be determined. At large R , interactions can be treated perturbatively leading to an hyperspherical potential curve valid at large R that determines ϕ_{out} .

By changing the trapping confinement we can change ϕ_{out} and by introducing short range three-body forces we can modify ϕ_{in} without affecting the barrier. This allow us to explore how γ depends on both E and a . Interestingly, at low energies our numerical results are nicely fitted by the formula: $e^{-2\gamma} \propto (E/E_{\text{vdW}})^5 |a/r_{\text{vdW}}|^{9.6}$, which is in good agreement with the predicted threshold behavior $(1 - |S_{00}^+|^2) \propto E^5 |a|^{10}$ [Meh09].

6.3 Experiment

We prepare an optically trapped sample of cesium atoms in the lowest sub-level of the electronic ground state under similar conditions as described in Ref. [Ber11b]. The final evaporation process, performed at a magnetic field of 894 G ($a = +285 a_0$, where a_0 is the Bohr radius), is stopped before the onset of Bose-Einstein condensation. The sample is then adiabatically recompressed to avoid further evaporation from the trap. At this point, the sample contains about 6×10^4 atoms at a temperature $T = 78(3)$ nK and the confining optical potential has a mean trap frequency $\bar{\omega} = 2\pi \times 36.2(2)$ Hz, which results in a peak number density of $4.2 \mu\text{m}^{-3}$ and a peak phase space density close to unity. The wide s -wave Feshbach resonance with its pole at 786 G offers ideal tuning properties [Ber11b, Ber13], superior to the low-field region investigated in our previous works [Kra06, Fer09].

We measured the decay of the atom number in the region of negative scattering length (from $-500 a_0$ at 863 G to $-200 a_0$ at 873 G), where the four- and five-body recombination resonances are expected. After the recompression stage, we tune the scattering length to its target value, and we measure the atom number after a variable hold time by absorption imaging. After 100 ms, the typical loss fraction is around 10% at $-300 a_0$ and almost 35% at $-450 a_0$.

The time evolution of the number \mathcal{N} of trapped atoms and temperature T are determined by the different N -body loss processes and can be expressed [Web03c] in terms of a system of coupled differential equations,

$$\dot{\mathcal{N}}/\mathcal{N} = - \sum_{N=1}^{+\infty} L_N \langle n^{N-1} \rangle, \quad (6.4)$$

$$\dot{T}/T = \sum_{N=1}^{+\infty} \epsilon_N L_N \langle n^{N-1} \rangle, \quad (6.5)$$

where L_N represents the N -body rate coefficients. The averaged atom densities are evaluated as $\langle n^{N-1} \rangle = \int n^N d^3\mathbf{r} = \mathcal{N}^{N-1} N^{-3/2} [(m\bar{\omega}^2)/(2\pi k_B T)]^{(3N-3)/2}$ from a thermal distribution of the harmonically trapped atoms. Equation (6.5) incorporates the anti-evaporation heating [Web03c] that results from the higher recombination rate in the densest part of the cloud ($2\epsilon_N \equiv 1 - 1/N$).

Under our experimental conditions, the first two terms of the sums can be omitted. One-body losses, resulting from collisions with the background gas, are negligible on our experimental time scale ($L_1 = 0$), and the use of atoms in their lowest sub-state assures that

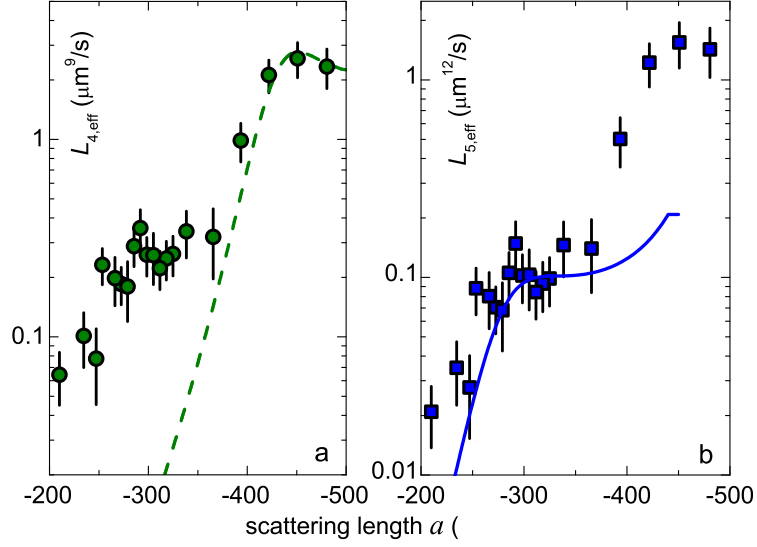


Figure 6.3: Effective four- (a) and five-body recombination rates (b). The green dashed curve and the blue solid line follow the theoretical model for L_4 and L_5 , respectively, with an additional scaling factor for L_5 ; see text. The error bars include the statistical uncertainties from the fitting routine, the temperature and the trap frequencies.

two-body losses vanish ($L_2 = 0$). Therefore, the three-body rate coefficient L_3 is the leading term contributing to the atom losses, and its resonant behavior is related to the Efimov trimers. This contribution is well understood and the coefficient L_3 can be described by the well-established result of effective field theory [Bra01]. The rates of recombination events involving more particles are generally smaller than the one related to three-body losses and the contributions are difficult to discriminate because of the very similar behavior. Since the rate of recombination events for typical gas densities decreases rapidly with N , contributions with $N > 5$ are considered negligible in the following.

A general fit to the experimental decay curves with L_3 , L_4 , and L_5 as free parameters in Eq. (6.4) and Eq. (6.5) turns out to be practically impossible. Therefore, we fix L_3 according to effective field theory, with parameters $a_- = -955 a_0$ and $\eta_- = 0.08$ as determined for three-body recombination ($N = 3$) in our previous experiment [Ber11b]. We can now interpret the additional losses in terms of four-body and five-body decay. In order to avoid any fitting ambiguities, we chose the simple approach to describe these losses either in terms of an effective four-body loss coefficient $L_{4,\text{eff}}$ (setting $L_5 = 0$) or an effective five-body loss coefficient $L_{5,\text{eff}}$ (setting $L_4 = 0$).

Figure 6.3(a) shows $L_{4,\text{eff}}$ as extracted from our experimental data in comparison with the theoretical predictions, obtained by numerically evaluating L_4 from Eqs. (6.1) and (6.3) for our experimental conditions. Here we have adjusted the decay parameter to $\eta_- = 0.33$, which as a non-universal parameter depends on N . The comparison shows that the losses observed around $-450 a_0$ can be fully attributed to the four-body recombination resonance. The four-body loss peak position $a_{4,-} = -440(10) a_0$ corresponds to $0.46(1) a_-$ and is in very good agreement with the theoretical value $0.44(1) a_-$ [von09] and previous observations

[Fer09, Fer11, Pol09, Zac09]. In contrast the enhancement of losses centered at about $-300 a_0$ cannot be interpreted in terms of the known universal four-body cluster states², suggesting that a different loss mechanism is present.

An alternative representation of the same data in terms of $L_{5,\text{eff}}$ is shown in Fig. 6.3(b), together with the results of our theoretical model for L_5 ; here we adjusted the relevant decay parameter to $\eta_- = 0.20$. The model nicely explains the loss rates in the region where three- and four-body losses cannot account for the experimental observations. Remarkably, the resonance position $a_{5,-} = 0.64(2) a_{4,-}$ is in agreement with the theoretical predictions $0.65(1) a_{4,-}$ [von10, vS11]. However, quantitatively, the experimental values for L_5 are about 15 times larger than the calculated ones. To account for this, we introduce a corresponding scaling factor. We find that this deviation might derive from non-universal effects that modify the value of the calculated WKB phase γ by about 10%, which remains within the realistic uncertainty range of our theory.

An experimental search for higher-order recombination resonances ($N > 5$) that would be expected at lower values of the scattering length did not show clear signatures. A general problem arises, namely that the phase-space density cannot be further increased without causing the collapse of a Bose-Einstein condensate at negative values of a . To induce faster losses, adiabatic compression can increase the density, but then the higher temperatures cause increasing problems with the unitarity limit for high N . By decreasing the temperature, constraints by the unitarity limit can be avoided, but then losses for high N get so small that they become practically unobservable.

Based on the above results and parameters, we model the general loss behavior in the region of interest. Figure 6.4 shows an example for three-, four- and five-body recombination by plotting the atom losses, under typical experimental conditions, for a fixed hold time and variable scattering length. The “family portrait” of N -body recombination highlights the different contributions and confirms how the different loss features dominate the losses at the resonant positions. The experimental data plotted in the inset show that the peak positions and the magnitude of losses are in very good agreement with the simulated losses. Note that the somewhat higher experimental losses can be attributed to an additional loss that occurs during the ramp to the target magnetic field strength.

6.4 Conclusion

By pushing the limits of ultracold few-body physics, we have explored a universal five-body recombination resonance both experimentally and theoretically. The observed series of recombination features, which we interpret in terms of three-, four- and five-body recombination resonances, provides crucial evidence for the existence of a family of universal N -body bound states tied to Efimov trimers. The infinite series of N -boson cluster states represents a paradigm for the general implications of Efimov physics for many-body systems. We speculate that similar scenarios also exist for other few-body systems of increasing size, containing

² We cannot rule out the possibility of a non-universal few-body state, which may be associated with higher partial waves. However, such an accidental coincidence appears to be rather unlikely.

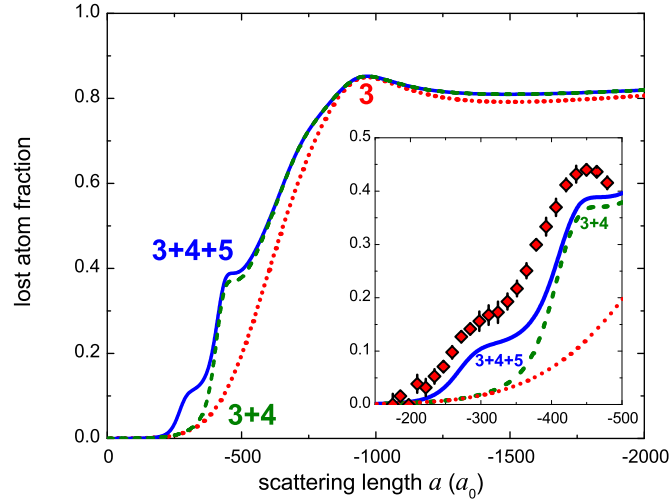


Figure 6.4: Calculated and measured fraction of loss atoms from an atomic sample of initially 5×10^4 atoms at a temperature of 80 nK after a hold time of 100 ms. The red dotted line corresponds to the losses predicted for three-body recombination only, while the dashed green line and the blue solid line include also contributions from four- and five body recombination, as quantified in this work. A cut-off to the maximum losses has been applied according to Eq. (6.2), as suggested in [Gre04]. The inset shows a close up of the region of dominant four- and five-body recombination and compares the theoretical results with the experimental observations.

fermionic constituents or particles of different masses, with important consequences for the interaction properties of the many-body system.

Acknowledgments

This work was supported by the Austrian Science Fund FWF within project P23106, and in part by the U.S. National Science Foundation. A. Z. was supported within the Marie Curie Project LatTriCs 254987 of the European Council.

6.5 Appendix

Extraction of the trapped five-body spectrum

A crucial ingredient of our recombination analysis is the accurate extraction of the five-body trapped spectrum. The trapped few-boson Hamiltonian is given by

$$\mathcal{H} = \sum_{i=1}^N \left(-\frac{\hbar^2 \nabla_i^2}{2m} + \frac{m\omega^2 r_i^2}{2} \right) + \sum_{i>j} V_{2b}(r_{ij}) + \sum_{i>j>k} V_{3b}(R_{ijk}) \quad (6.6)$$

where ω is the trapping frequency, $V_{2b}(r) = V_{2b0}e^{-r^2/(2r_0^2)}$ is the two-body potential and $V_{3b}(R) = V_{3b0}e^{-R^2/(2R_0^2)}$ is a three-body potential. Here, r_0 and R_0 are the ranges of the two and three-body potentials that are fixed during the calculation, and $R_{ijk} = \sqrt{(r_{ij}^2 + r_{ik}^2 + r_{jk}^2)}/3$. The two-body potential strength V_{2b0} is used to tune the two-body scattering length and V_{3b} is set to zero in most calculations (see discussion below). To relate the model potential with the experimental we rely on the universal character of the low energy few-boson physics and we relate r_0 with the van der Waals length r_{vdw} so that the three- and four-body recombination peaks coincide with those experimentally observed. In this transformation, we relate the energy scales so that they scale as inverse length squared.

To extract the recombination parameters, the five-body spectrum is analyzed as a function of the scattering length and the trapping confinement. The scattering length is changed in the region $-4r_0 < a < 0$ and the trapping frequency is changed so that the corresponding trapping length $a_{ho} = \sqrt{\hbar/(m\omega)}$ varies in the range $5r_0 < a_{ho} \leq 100r_0$. This region of scattering lengths and energies corresponds to the low energy region where the five-body resonance occurs.

The three-body interaction is used to shift the position of the five-body resonance and explore the dependence of the recombination on the scattering length. The range of the three-body potential is taken to be R_0 , which is smaller than the two-body r_0 so that it is mainly relevant at small hyperradii, i.e. so that its main contribution in our recombination formula is to change the inner phase. For the three-body interactions considered, the spectrum follows the linear dependence with the scattering length that is expected at small and negative scattering lengths. This linear dependence arises from only two-body physics which, in the hyperspherical framework, is described by the long-range behavior of the potential curves. Using the zero-range model of the two-body interaction, one can derive a first order correction of the hyperspherical potential curve. Here, we follow a similar procedure to that on Ref. [Boh98], but for a set of coordinates in which the center of mass has been removed. In this approximation, the lowest potential takes the form

$$V(R) = \frac{3(N-2)(3N-4)\hbar^2}{8\mu_N R^2} + \frac{\mu_N \omega^2 R^2}{2} + \frac{\hbar^2 a(N-1)N^{\frac{2N-1}{2N-2}} \Gamma(\frac{3}{2}N - \frac{3}{2})}{\sqrt{2\pi}\mu_N R^3 \Gamma(\frac{3}{2}N - 3)}. \quad (6.7)$$

The first two terms correspond, respectively, to the hyperangular or “mock-centrifugal” kinetic energy and the trapping potential; and the third term represents the interaction corrections. Equation 6.7 is *only* valid for small $|a|$ in the region where R is much larger than the interaction range. Using perturbation analysis, one derives the well-known corrected energy of the lowest state,

$$E \approx 3(N-1)\frac{\hbar\omega}{2} + \sqrt{\frac{2}{\pi}} \frac{a}{a_{ho}} \hbar\omega \frac{N(N-1)}{2}. \quad (6.8)$$

Our numerical calculations, with and without the three-body forces, show the linear behavior described in Eq. 6.8 in the region $|a| < |a_{5,-}|$. This suggests that the hyperradial potential in the $R \gg r_0$ is well described by Eq. 6.7 and that, in this region, the potential is independent of the three-body forces. Thus, it is consistent to interpret the main contribution of the three-body interaction as a modification of the short range physics that controls ϕ_{in} .

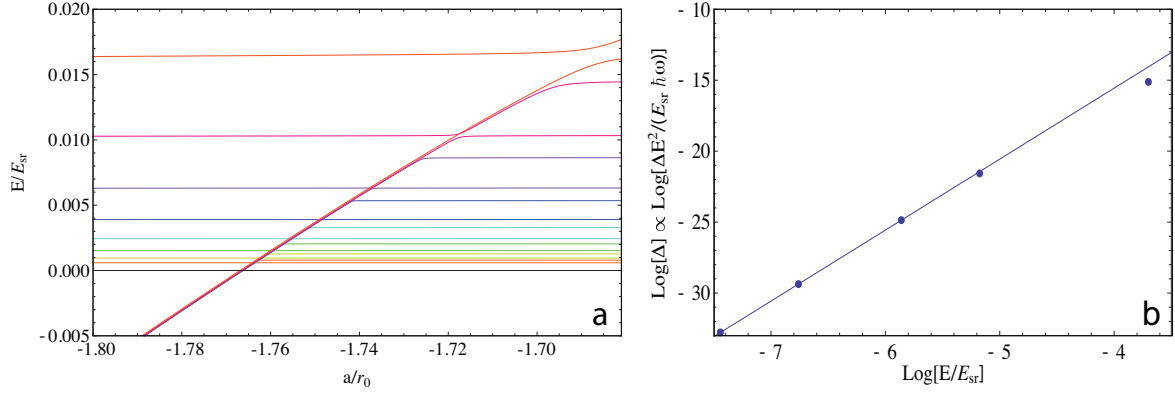


Figure 6.5: (a) The lowest two eigenenergies of a trapped five body system are shown as functions of the scattering length for different trapping frequencies. Different colors represent different trapping frequencies. The combination of these states essentially describes the energy of the five-body state in the inner region of the potential $E_{mol}(a)$ (the diagonal curve). Here $E_{sr} = \hbar^2/(mr_0^2)$ and r_0 is the characteristic range of the two-body model potential that can be tuned to obtain the five-body resonance (i.e. $r_0 \sim 1.7r_{vdw}$ where r_{vdw} is the van der Waals length). (b) The near-threshold behavior of Δ . The fitting of the lowest energy points leads that $\Delta \propto AE^b$. The lowest three points lead to $b \approx 5.004$ as expected from the known threshold behavior [Meh09].

The calculations are carried out using a correlated Gaussian basis set expansion limited to describe $L^P = 0^+$ trapped states since the energetically lowest scattering continuum corresponds to zero angular momentum and positive parity. In this computation, we are only interested in the lowest trapped states which, in the hyperspherical picture, are supported mainly by the lowest potential curve. Therefore, the basis set is designed to accurately describe those states. The calculations include thousands of basis functions which are optimized for different scattering lengths and trap lengths. To verify the convergence of the energies, we carry out several optimization steps. The typical spectrum obtained by this analysis is shown in Fig. 6.5(a).

Semiclassical analysis of the trapped spectrum

To extract the semiclassical recombination parameters, we repeat the same semiclassical analysis used to derive Eqs. (2,3) but for a hyperspherical potential with the trapping potential (see Fig. 6.2). This basically amounts to solve a double well problem using a semiclassical analysis. For this analysis, we follow closely the prescription in Ref. [Ber66] to determine the quantization condition

$$\beta = -\tan^{-1} \left(\frac{1}{4} e^{-2\gamma} \tan(\phi_{in}) \right) - \phi_{out} + \frac{\pi}{2} = n\pi \quad (6.9)$$

where ϕ_{in} is the phase in the inner region, γ is the barrier phase and ϕ_{out} is the phase in the external trapped region (see Fig. 6.2). The semiclassical phases are

$$\phi_{in} = \int_{\text{inner well}} q(R) dR, \quad (6.10)$$

$$\gamma(E, a) = \text{Im} \int_{\text{barrier}} q(R) dR, \quad (6.11)$$

$$\phi_{out} = \int_{\text{trap well}} q(R) dR, \quad (6.12)$$

where $q(R) = \sqrt{2\mu[E - V(R)]}$ and $V(R)$ is the hyperspherical curve with the Langer correction. Here, the different integration regions are bounded by the classical turning points, i.e. the R positions at which $q(R) = 0$. In our analysis, ϕ and γ are assumed to be unaffected by the trapping potential which is expected to be negligible at small hyperradii.

After some mathematical manipulation, the quantization condition can be written as

$$\frac{1}{\tan(\phi_{in}) \tan(\phi_{out})} = \frac{\Delta}{2} \quad (6.13)$$

where $\Delta = e^{-2\gamma}/2$. For tunneling energies well below the barrier height $\Delta \ll 1$ which implies that the quantization condition is fulfilled when either $\phi_{in} \approx \pi(i_{in} + 1/2)$ or $\phi_{out} \approx \pi(i_{out} + 1/2)$. These conditions ($\phi_{in} \approx \pi(i_{in} + 1/2)$ and $\phi_{out} \approx \pi(i_{out} + 1/2)$) can be interpreted as having a bound state either in the inner or outer region. We call $E_{in}(a)$ and $E_{out}(a)$ the energies at which $\phi_{in} = \pi(i_{in} + 1/2)$ and $\phi_{out} = \pi(i_{out} + 1/2)$, respectively. Here i_{α} are integers representing the number of bound states supported by the inner and outer well respectively. Thus, close to those energies, the inner and outer phases take the form $\phi_{\alpha} = \pi(i_{\alpha} + 1/2) + \phi'_{\alpha}(E - E_{\alpha}(a))$ where $\phi'_{\alpha} \equiv d\phi_{\alpha}/dE$. In the vicinity of the avoided crossings, the quantization condition can be approximated to

$$(E_{in}(a) - E)(E_{out}(a) - E) - \frac{\Delta}{2\phi'_{in}\phi'_{out}} \approx 0. \quad (6.14)$$

Equation 6.14 resembles a determinant of a 2×2 Hamiltonian matrix which lends itself to the following physical interpretation. The states supported by the inner and outer regions are coupled to each other and the coupling energy $V_{in,out}$ is related to the tunneling through the barrier by $V_{in,out}^2 = \frac{\Delta}{2\phi'_{in}\phi'_{out}}$. The eigenenergies of this double well problem (E_1 and E_2) reach their squared minimal difference at the avoided crossing, equal to:

$$(E_2 - E_1)^2 = 2\Delta/(\phi'_{in}\phi'_{out}). \quad (6.15)$$

To verify the validity of this equation, the energy dependence of Δ is explored by varying the strength of the trapping potential. According to the threshold laws [Meh09], for a five-boson problem, Δ increases with energy as $\Delta \propto E^5$. Figure 6.5(b) confirms that the scaling of Δ calculated through the avoided crossing analysis shows excellent agreement with the threshold law prediction.

Publication: Observation of the second triatomic resonance in Efimov's scenario[†]

Phys. Rev. Lett. **112**, 190401 (2014)

Bo Huang,¹ Leonid A. Sidorenkov,^{1,2} and Rudolf Grimm^{1,2}

¹*Institut für Experimentalphysik, Universität Innsbruck, 6020 Innsbruck, Austria*

²*Institut für Quantenoptik und Quanteninformation,
Österreichische Akademie der Wissenschaften, 6020 Innsbruck, Austria*

Jeremy M. Hutson

*Joint Quantum Centre (JQC) Durham/Newcastle, Department of Chemistry,
Durham University, South Road, Durham, DH1 3LE, United Kingdom*

We report the observation of a three-body recombination resonance in an ultracold gas of cesium atoms at a very large negative value of the s -wave scattering length. The resonance is identified as the second triatomic Efimov resonance, which corresponds to the situation where the first excited Efimov state appears at the threshold of three free atoms. This observation, together with a finite-temperature analysis and the known first resonance, allows the most accurate demonstration to date of the discrete scaling behavior at the heart of Efimov physics. For the system of three identical bosons, we obtain a scaling factor of 21.0(1.3), close to the ideal value of 22.7.

[†] The author of the present thesis maintained the experiment, designed and performed the measurements and analyzed the data with the finite-temperature model. R.G. provided the original concept of the experiment and guided the analysis and interpretation of the data. L.A.S. contributed in data processing and interpretation. J.M.H. provided improved error analysis for the magnetic field dependence of the scattering length.

7.1 Introduction

Efimov's prediction of weakly bound three-body states in a system of three resonantly interacting bosons [Efi70, Bra06] is widely known as the paradigm of universal few-body quantum physics. Its bizarre and counterintuitive properties have attracted a great deal of attention. Originally predicted in the context of nuclear systems, Efimov states are now challenging atomic and molecular physics and have strong links to quantum many-body physics [Jen11]. Experimentally the famous scenario remained elusive until experiments in an ultracold gas of Cs atoms revealed the first signatures of the exotic three-body states [Kra06]. A key requirement for the experiments is the precise control of two-body interactions enabled by magnetically tuned Feshbach resonances [Chi10]. With advances in various atomic systems [Zac09, Pol09, Gro09, Huc09, Ott08, Wil09, Gro10, Lom10a, Nak10, Bar09, Roy13, Wil12] and theoretical progress in understanding Efimov states and related states in real systems [Jen11, Wan13], the research field of few-body physics with ultracold atoms has emerged.

Three-body recombination resonances [Esr99] are the most prominent signatures of Efimov states [Bra06, Fer11]. They emerge when an Efimov state couples to the threshold of free atoms at distinct negative values of the s -wave scattering length a . The resonance positions $a_-^{(n)}$ are predicted to reflect the discrete scaling law at the heart of Efimov physics, and for the system of three identical bosons follow $a_-^{(n)} = 22.7^n a_-^{(0)}$. Here $n = 0$ refers to the Efimov ground state and $n = 1, 2, \dots$ refer to excited states. The starting point $a_-^{(0)}$ of the infinite series, i.e. the position of the ground-state resonance, is commonly referred to as the three-body parameter [Ber11b, Roy13, Wan12, Sør12, Sch12].

For an observation of the second Efimov resonance, the requirements are much more demanding than for the first one. Extremely large values of the scattering length near $a_-^{(1)}$ need to be controlled and the relevant energy scale is lower by a factor $22.7^2 \approx 500$, which requires temperatures in the range of a few nK. So far, experimental evidence for an excited-state Efimov resonance has been obtained only in a three-component Fermi gas of ${}^6\text{Li}$ [Wil09], but there the scenario is more complex because of the involvement of three different scattering lengths. Experiments on bosonic ${}^7\text{Li}$ have approached suitable conditions for a three-boson system [Pol09, Dyk13, Rem13] and suggest the possibility of observing the excited-state Efimov resonance [Rem13].

In this Letter, we report on the observation of the second triatomic resonance in Efimov's original three-boson scenario realized with cesium atoms. Our results confirm the existence of the first excited three-body state and allow the currently most accurate test of the Efimov period. Moreover, our results provide evidence for the existence of the predicted universal N -body states that are linked to the excited three-body state.

Two recent advances have prepared the ground for our present investigations. First, we have gained control of very large values of the scattering length (up to a few times $10^5 a_0$ with a_0 being Bohr's radius), which in ultracold Cs gases is achieved by exploiting a broad Feshbach resonance near 800 G [Lee07, Ber11b]. Precise values for the scattering length as a function of the magnetic field can be obtained from coupled-channel calculations based on the M2012 model potentials of Refs. [Ber11b, Ber13]. Second, Ref. [Rem13] has provided a model, based

on an S-matrix formalism [Efi79, Bra08], to describe quantitatively the finite-temperature effects on three-body recombination near Efimov resonances. While for the first Efimov resonance experimental conditions can be realized practically in the zero-temperature limit, finite-temperature limitations are unavoidable for the second resonance and therefore must be properly taken into account.

7.2 The observations

Our experimental procedure of preparing an ultracold sample of cesium atoms near quantum degeneracy is similar to the one reported in Refs. [Ber11a, Ber11b]. In an additional stage, introduced into our setup for the present work, we adiabatically expand the atomic cloud into a very weak trap. The latter is a hybrid with optical confinement by a single infrared laser beam and magnetic confinement provided by the curvature of the magnetic field (see supplemental material Sec. 7.4). The mean oscillation frequency $\bar{\omega}/2\pi$ of the nearly isotropic trap is about 2.6 Hz. This very low value corresponds to a harmonic oscillator length of $\sim 5 \mu\text{m}$, which is about a factor of five larger than the expected size of the second Efimov state. Our ultracold atomic sample consists of about $N = 3 \times 10^4$ Cs atoms at a temperature of 7 nK and a dimensionless phase-space density of about 0.2. We probe the atomic cloud by *in-situ* absorption imaging near the zero crossing of the scattering length at 882 G. We obtain the in-trap density profile and the temperature T assuming the gas is thermalized in a harmonic trap.

To study recombinative decay for different values of the scattering length a , we ramp the magnetic field from the final preparation field (~ 820 G) (see Sec. 7.4) down to a target value (between 818 G and 787 G)¹ within 10 ms. After a variable hold time t , between tens of milliseconds and several seconds, we image the remaining atoms. The maximum hold time is chosen to correspond to an atom number decay of about 50%. In addition to the resulting decay curves $N(t)$ we record the corresponding temperature evolution $T(t)$. Recombinative decay is known to be accompanied by heating [Web03c] (see Sec. 7.4), which needs to be taken into account when analyzing the results.

For extracting recombination rate coefficients from the observed decay curves, we apply a model that is based on the general differential equation for α -body loss in a harmonically trapped thermal gas,

$$\frac{\dot{N}}{N} = -L_\alpha \alpha^{-3/2} \left(\frac{N}{V} \right)^{\alpha-1}, \quad (7.1)$$

with the volume $V = (2\pi k_B T / m \bar{\omega}^2)^{3/2}$. The factor $\alpha^{-3/2}$ arises from the spatial integration of the density-dependent losses.

Since three-body recombination is expected to dominate the decay, we fix α to a value of 3, numerically integrate Eq. (7.1) over time and fit the measured atomic number evolution with L_3 and the initial atom number N_0 as free parameters. In cases where there are significant

¹ The magnetic field range between 787 and 818 G corresponds to a range of scattering lengths between -10^5 and $-2600a_0$.

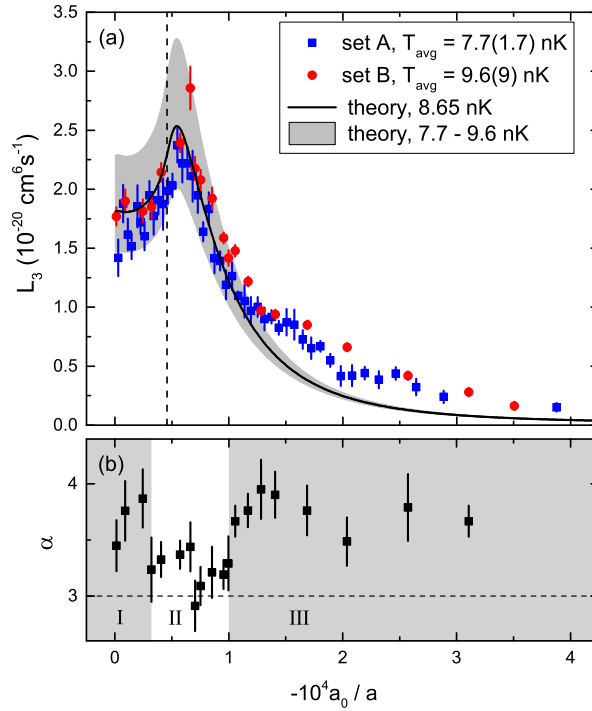


Figure 7.1: Observation of the second triatomic Efimov resonance. In (a), we show the effective three-body loss coefficient L_3 as a function of the inverse scattering length. Blue squares and red circles are two sets of measurements taken with slightly different trap settings. The error bars include statistical uncertainties from numerical fitting. The black solid line is the theoretical calculation of L_3 (based on the parameters of the first Efimov resonance) at 8.65 nK (average temperature of two sets) while the gray-shaded region corresponds to the temperature range between 7.7 and 9.6 nK (see text). The vertical dashed line indicates the position where the resonance would be expected in the zero-temperature limit based on the previously investigated first Efimov resonance [Ber11b] and Efimov’s scaling factor. In (b), the fitted loss index α shows a larger deviation from a value of 3 in the regions (gray-shaded) away from the second Efimov resonance (white region, where $\alpha < 3.5$), indicating contributions from higher-order recombination processes.

contributions from higher-order decay processes, e.g. four-body decay, the fitted L_3 can be interpreted as an ‘effective’ loss coefficient [von09] that includes all loss processes. Considering a typical temperature change of about 50% during the decay, a slight complication arises from the fact that L_3 itself generally depends on T , while our fit assumes constant L_3 . To a good approximation, however, we can refer a fit value for L_3 to a time-averaged temperature T_{avg} (see Sec. 7.4).

Figure 7.1(a) shows our main result, the recombination resonance caused by an excited Efimov state. Here we plot the fit values obtained for L_3 as a function of the inverse scattering length $1/a$. Our sets of measurements (A: blue squares and B: red circles) (see Sec. 7.4) were taken on different days with similar trap frequencies but slightly different average temperatures T_{avg} of 7.7(1.7) nK and 9.6(9) nK (see Sec. 7.4). Our results exhibit a loss peak near $a = -17000a_0$ (~ 797 G), which we interpret as a clear manifestation of the second Efimov resonance. Multiplying $a_-^{(0)} = -963a_0$ (see Sec. 7.4) by Efimov’s ideal scaling factor of 22.7 predicts that, in the zero-temperature limit, this feature would occur

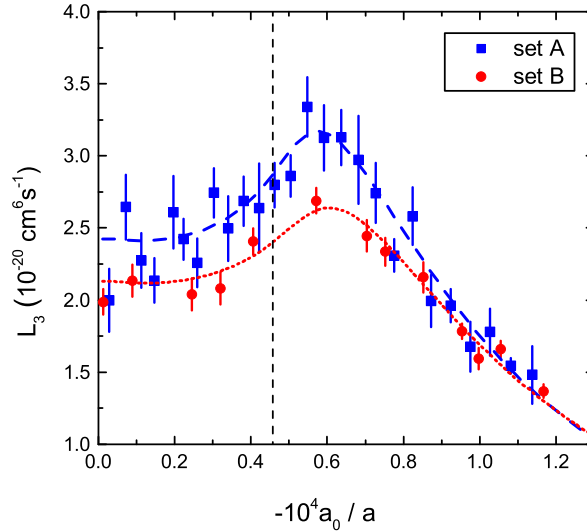


Figure 7.2: Fits to the second Efimov resonance. The two sets of points represent the same sets of results as in Fig. 7.1, but limited to the resonance region and with one clear outlier removed. In addition, the absolute scaling for L_3 is changed as we here use the fit values (see text) for the temperature, 8.7 nK for set A and 10.0 nK for set B, to calculate the volume V . The vertical dashed line is the same as in Fig. 7.1. The fits to sets A and B are plotted as blue dashed and red dotted lines, respectively.

at $-21900a_0$ (dashed vertical line in Fig. 7.1(a)). At finite temperatures, however, a downshift towards somewhat lower values of $|a|$ is expected [Kra06] and may to a large extent explain the observed position. The finite temperature in our experiment also explains why the resonance is not as pronounced as the first Efimov resonance observed previously [Ber11b].

In order to compare our results with theoretical predictions, we use the finite-temperature model of Ref. [Rem13] with the two resonance parameters, position $a_-^{(0)} = -963a_0$ and decay parameter $\eta_-^{(0)} = 0.10$ (see Sec. 7.4), independently derived from previous measurements on the first Efimov resonance. For the temperature we use $T_{\text{avg}} = 8.65$ nK, which is the mean value for the two sets. The agreement between our present results and the prediction (black solid line in Fig. 7.1(a)) is remarkable, and highlights the discrete scaling behavior of the Efimov scenario.

The measurements on the ‘shoulder’ of the resonance ($-10^4 a_0 / a > 1.2$ in Fig. 7.1(a)) show a broad increase of the effective L_3 as compared to the expectation from the three-body loss theory (black solid line in Fig. 7.1(a)). Since similar enhanced loss features were observed previously near the first Efimov resonance [Fer09, Zen13, Pol09, Dyk13, Fle13] and were explained by the presence of four- or five-body states associated with an Efimov state, we attribute this feature to higher-order decay processes. To check this, we fit set B with Eq. (7.1) as discussed above,² while now using α as an additional free parameter. The fit results for α are shown in Fig. 7.1(b). In the region close to the Efimov resonance (white

² We use only set B for this purpose, because it contains more data at different hold times and therefore the fit converges better when both L_α and α are free in the fitting procedure.

Set	T/nK	$a_-^{(1)}/a_0$	$\eta_-^{(1)}$	λ
A	8.7(2)	-20790(390)	0.15(2)	-
B	10.0(2)	-19740(430)	0.19(3)	-
A	7.7*	-20580(390)	0.17(3)	0.52(5)
B	9.6*	-19650(430)	0.19(3)	0.80(7)

Table 7.1: Fitted parameters for the second Efimov resonance. The upper part of the table shows the fitting results when temperature T is a free parameter, while the lower part corresponds to fixed-temperature fitting with λ as a free amplitude scaling factor. The uncertainties indicate 1σ errors from fitting. The symbol * indicates that the corresponding parameter is kept fixed.

region II), where we expect dominant three-body behavior, the value of α is relatively close to 3.³ On the ‘shoulder’ of the Efimov peak (gray-shaded region III), a significant increase of α , compared to the resonance region, confirms the existence of higher-order decay processes. It is interesting to note that the relatively broad shoulder that we observe for the higher-order features is in contrast to the narrow features observed in ^7Li [Pol09, Dyk13]. On the other side of the Efimov resonance (gray-shaded region I), we also observe an enhancement of α , which is likely to be caused by similar higher-order decay features associated with highly excited N -body cluster states.

The temperature uncertainty plays an important role in the interpretation of our results. The measured values of L_3 depend sensitively on the temperature, with a general scaling $\propto T^3$ according to the volume V in Eq. (7.1). The theoretical L_3 values also depend strongly on the temperature. The gray-shaded area in Fig. 1(a) demonstrates the variation between 7.7 nK and 9.6 nK, which correspond to T_{avg} for sets A and B, respectively. It may be seen that the temperature uncertainty results mainly in an amplitude error rather than an error in the peak position.

To analyze the observed resonance in more detail, and especially to study the possible small deviation of $a_-^{(1)}$ from a predicted value of $22.7a_-^{(0)}$, we now fit the results in the resonance region ($0 < -10^4 a_0/a < 1.2$ in Fig. 7.2) with the finite-temperature model to extract an experimental value for $a_-^{(1)}$. Here, because of the large effect of the temperature uncertainty, we use the temperature T as an additional parameter in the fits. The results (blue dashed and red dotted lines in Fig. 7.2 for sets A and B) are summarized in the upper part of Table 7.1 and yield a mean $a_-^{(1)}$ value of $-20270(680)a_0$.

The fitted results for the temperature, 8.7(2) nK for set A and 10.0(2) nK for set B, are somewhat larger than the independently determined temperatures T_{avg} , but they are consistent with T_{avg} within the error range. The higher temperatures also imply a rescaling of the measured L_3 values because of the temperature dependence of the volume V . With these corrections, Fig. 7.2 shows that the measurements of set A, taken at a lower temperature, now produce larger L_3 values than those of set B.

Uncertainties in L_3 might also arise from errors in the atom number calibration, resulting

³ The small deviation from $\alpha = 3$ in region II can be explained by the heating effect, which leads to somewhat faster decay in the initial stage and a somewhat slower decay at the end of the hold time. This mimics higher-order loss.

from imaging imperfections and errors in trap frequency measurements. To account for these effects, we follow an alternative fitting strategy and introduce an additional parameter λ as an amplitude scaling factor for L_3 into the finite-temperature model, while fixing the temperature at the measured T_{avg} . The resulting parameters for each set are given in the lower part of Table 7.1. Remarkably, this alternative approach gives a mean value of $-20120(630)a_0$ for $a_-^{(1)}$, which is consistent with the one extracted before. This shows the robustness of our result for $a_-^{(1)}$. From all the four fits listed in Table 7.1, we derive a mean value and a corresponding uncertainty of $-20190(660)a_0$.

A final significant contribution to our error budget for $a_-^{(1)}$ stems from uncertainty in the M2012 potential model [Ber11b, Ber13] that provides the mapping between the measured magnetic field B and the scattering length a . To quantify this, we have recalculated the derivatives of all the experimental quantities fitted in Ref. [Ber13] with respect to the potential parameters, and used them to obtain fully correlated uncertainties in the calculated scattering lengths at the magnetic fields $B = 852.90$ G and 795.56 G, corresponding to the two Efimov loss maxima, using the procedure of Ref. [Alb76]. The resulting scattering lengths and their 1σ uncertainties are $a_-^{(0)} = -963(6) a_0$ and $a_-^{(1)} = -20190(1000) a_0$. These values accord well with the uncertainty in the position of the Feshbach resonance pole, which was determined to be $786.8(6)$ G in Ref. [Ber13] with a 2σ uncertainty.

Taking all these uncertainties into account, we get $a_-^{(1)} = -20190(1200)a_0$ and $a_-^{(0)} = -963(11)a_0$, and we finally obtain $a_-^{(1)}/a_-^{(0)} = 21.0(1.3)$ for the Efimov period. This result is consistent with the ideal value of 22.7 within a 1.3σ uncertainty range. Theories that take the finite interaction range into account consistently predict corrections toward somewhat lower values than 22.7 [D'I09, Pla09, Thø08b]. Ref. [Sch12] predicts a value of 17.1 in the limit of strongly entrance-channel-dominated Feshbach resonances. This theoretical value differs by 3σ from our experimental result, but the precise value depends at a 10% level on a form factor that accounts for the range of the coupling between the open and closed channels. Universal van der Waals theory [Wan14] applied to our specific Feshbach resonance predicts a value that is smaller than the ideal Efimov factor by only 5-10%,⁴ which would match our observation.

Additional systematic uncertainties may slightly influence our experimental determination of the Efimov period. Model-dependence in the earlier fit to various interaction-dependent observables in Cs [Ber13] may somewhat affect the mapping $a(B)$ from magnetic field to scattering length. The finite-temperature model [Rem13] applied here, which employs the zero-range approximation, may be influenced by small finite-range corrections. Moreover, confinement-induced effects may play an additional role even in the very weak trap [Jon02, Lev14]. While an accurate characterization of these possible systematic effects will require further effort, we estimate that our error budget is dominated by the statistical uncertainties.

⁴ Y. Wang and P. S. Jullienne, private communication (2014).

7.3 Conclusion

Previous experiments aimed at determining the Efimov period in ^{39}K [Zac09] and ^7Li [Pol09, Dyk13] considered recombination minima for $a > 0$, from which values of 25(4) and 16.0(1.3) were extracted, respectively. There the lower recombination minima serving as lower reference points appear at quite small values of the scattering length (typically only at 3 to 4 times the van der Waals length R_{vdW} [Chi10]), so that substantial quantitative deviations from Efimov's scenario, which is strictly valid only in the zero-range limit $|a|/R_{\text{vdW}} \rightarrow \infty$, may be expected. In our case the lower reference point $a_-^{(0)}$ is at about $-9.5 R_{\text{vdW}}$ (with $R_{\text{vdW}} = 101a_0$ for Cs) [Ber11b, Wan12, Sør12, Sch12], which makes the situation more robust. Moreover, at negative scattering length possible effects related to a non-universal behavior of the weakly bound dimer state are avoided. Another difference between our work and previous determinations of the Efimov period is the character of the Feshbach resonance, which in our case is the most extreme case so far discovered of an entrance-channel-dominated resonance, where the whole interaction can be reduced to an effective single-channel model [Chi10]. The resonances exploited in ^{39}K and ^7Li have intermediate character, so that the interpretation is less straightforward.

In conclusion, our observation of the second triatomic recombination resonance in an ultracold gas of Cs atoms demonstrates the existence of an excited Efimov state. Together with a previous observation of the first resonance and an analysis based on finite-temperature theory, our results provide an accurate quantitative test of Efimov's scenario of three resonantly interacting bosons. The character of the extremely broad Feshbach resonance that we use for interaction tuning avoids complications from the two-channel nature of the problem and brings the situation in a real atomic system as close as possible to Efimov's original idea. The value of 21.0(1.3) that we extract for the Efimov period is very close to the ideal value of 22.7 and represents the most accurate demonstration so far of the discrete scaling behavior at the heart of Efimov physics. Our results challenge theory to describe accurately the small deviations that occur in real atomic systems.

New possibilities for Efimov physics beyond the original three-boson scenario are opened up by ultracold mixtures with large mass imbalance [D'I06]. The ^{133}Cs - ^6Li mixture, where the Efimov period is reduced to a value of 4.88, has been identified as a particularly interesting system [Rep13, Tun13]. Two very recent preprints [Tun14, Pir14] report the observation of consecutive Efimov resonances in this system.

Acknowledgments

We thank D. Petrov for stimulating discussions and for providing the source code for the finite-temperature model. We thank C. Salomon for important discussions and comments on the manuscript. We further thank B. Rem, Y. Wang, P. S. Julienne, J. Levinsen, R. Schmidt and W. Zwerger for fruitful discussions and M. Berninger, A. Zenesini, H.-C. Nägerl, and F. Ferlaino for their important contributions in an earlier stage of the experiments. We acknowledge support by the Austrian Science Fund FWF within project P23106 and by

EPSRC under grant no. EP/I012044/1.

7.4 Supplemental material

Sample Preparation

Here we discuss the main procedures to create an ultracold near-degenerate sample of Cs atoms as the starting point for our measurements. We first cool the sample by forced evaporation in a crossed optical-dipole trap at magnetic field near 907 G, where the scattering length a is approximately $+500a_0$ (green filled circle in Fig. 7.3), and stop slightly before reaching quantum degeneracy. We then adiabatically remove one of the trapping beams and decrease the intensity of the other one to open the trap, thus lowering the temperature of the thermal cloud by adiabatic expansion. This transfers the atoms into the resulting hybrid trap, which is formed by one horizontal infrared laser beam and magnetic confinement caused by the curvature of the Feshbach magnetic field. A magnetic gradient field is applied to levitate the atoms in the field of gravity.

For reaching the target magnetic field near 800 G, we have to decrease the magnetic field by about 100 G and cross a narrow Feshbach resonance near 820 G. A fast ramp of the magnetic field introduces a drastic change in scattering length and also affects the trapping field. As a result, we observe the excitation of collective oscillations and heating. In order to reduce these unwanted effects, we ramp the magnetic field linearly in 20 ms to the positive side of a zero crossing of the scattering length a at 819.4 G (green open circle in Fig. 7.3, $a \approx +500a_0$) and stay there for half a second as an intermediate stage of preparation. During this time, the sample thermalizes by collisions and its collective breathing modes damp out. We also adiabatically recompress the optical dipole trap by increasing its power by 50% to avoid further evaporation during the measurements. Afterwards, we ramp the magnetic field to the target value, which is less than 34 G away, without crossing any Feshbach resonance, thus encountering much weaker effects from heating and excitation of collective modes.

To describe the final trap, we choose a coordinate system as follows: The z -axis is collinear with the propagation direction of the laser beam, the y -axis is the vertical one, and the x -axis is the remaining horizontal one. Using collective sloshing excitations near 819.4 G, we obtain the trap frequencies as $\omega_z/2\pi = 1.34(3)$ Hz, $\omega_x/2\pi = 3.97(8)$ Hz and $\omega_y/2\pi = 3.36(2)$ Hz for measurement set A. The corresponding trap frequencies for set B, which was taken later after small adjustments of the setup, are slightly different: $\omega_z/2\pi = 1.35(4)$ Hz, $\omega_x/2\pi = 3.96(8)$ Hz and $\omega_y/2\pi = 3.33(7)$ Hz. We neglect the slight magnetic field dependence of the trap frequencies, because its effect is smaller than the experimental uncertainties in the magnetic-field range of interest.

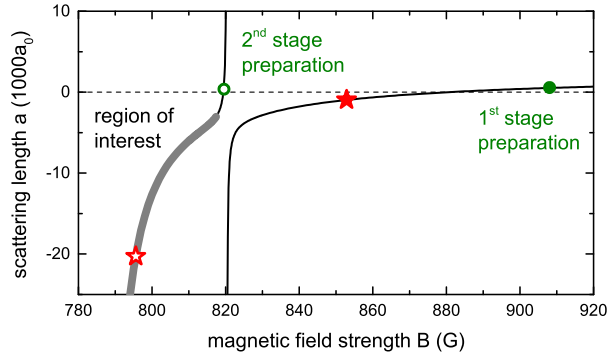


Figure 7.3: Illustration of the tunable region for Cs in the absolute atomic ground state $|F = 3, m_F = 3\rangle$ used in the present experiments. The green filled and open circles show the positions for the two stages of sample preparation (see text). The thick gray curve corresponds to the region of interest for observing the second Efimov resonance. The red filled star and the open star indicate the positions of the observed first and second Efimov resonances, respectively.

Density and Temperature Measurement

Knowledge of the cloud’s density profile is essential for obtaining accurate values for the three-body recombination rate coefficient, as well as for thermometry in our experiment. We probe the the Gaussian-shaped thermal atomic cloud by *in-situ* absorption imaging at 881.9 G near a zero crossing of the scattering length a . A very short ramp time (~ 20 ms) to this imaging field ensures that the cloud keeps its original spatial distribution. The optical axis of the imaging system lies in the horizontal plane, at an angle of $\theta = 60^\circ$ with respect to the z -axis. Therefore, the vertical cloud width obtained from the image is simply the cloud width w_y in the y -direction (half $1/e$ -width), while the measured horizontal width w_h is related to w_x and w_z , the widths in the x - and z -direction, via $w_h^2 = w_z^2 \sin^2 \theta + w_x^2 \cos^2 \theta$. We use w_y to calculate the width in the x -direction as $w_x = w_y \omega_y / \omega_x$ and then we extract w_z . Since the contribution to w_h^2 from the second term is only about 5%, the extracted w_z only weakly depends on w_y and is mostly defined by w_h .

The widths w_y and w_z are used to calculate the cloud temperatures $T_y = mw_y^2 \omega_y^2 / 2k_B$ and $T_z = mw_z^2 \omega_z^2 / 2k_B$. The value of T_y is typically found to be 10% higher than that of T_z , which may be caused by residual collective breathing excitations in the cloud and by the limited resolution of the imaging system. We finally take the mean value $T = (T_y + T_z) / 2$ with a corresponding error bar for the further analysis.

Fitting of Decay Curves

During the decay process, we observe a temperature increase, which results from antievaporation [Web03c], parametric heating in the trap, and heating caused by the damping of the residual collective excitations. In Fig. 7.4 we show typical data for an atom decay measurement near the second Efimov resonance, taken from measurement set B at 800.57 G. The substantial decay of the atom number, shown in Fig. 7.4(a), is accompanied by an increase of the cloud widths in horizontal (w_z) and vertical (w_y) directions; see Fig. 7.4(b). For mea-

surement sets A and B, the typical increase in width is about 20% and 30%, respectively, corresponding to an increase of 45% and 70% in temperature.

We numerically solve the differential equation $\dot{N}/N = -0.192 L_3(N/V)^2$, where the values for the time-dependent cloud volume V are obtained from the interpolation of measured $V = \pi^{3/2}w_xw_yw_z$ at different hold times. We extract L_3 by fitting the calculated $N(t)$ to the experimental data with L_3 and the initial atom number N_0 being free parameters.

In the fitting procedure, L_3 is assumed to be a constant during the decay process, while in reality it changes when the temperature increases. To compare the fitted L_3 with the theoretical expectations for a fixed temperature, we introduce for each atom decay measurement a time-averaged temperature $T_{\text{avg}} = [T(t_1) + 2 \sum_{i=2}^{n-1} T(t_i) + T(t_n)] / 2(n-1)$, where the sum is taken over the n different hold times of the individual decay curves. In principle, each L_3 measurement has its own T_{avg} , but within one set (A or B) the variations are small and mostly of statistical nature. Therefore, we characterize each measurement set by its mean value of T_{avg} .

Details on Measurement Sets A and B

Between the acquisitions of set A and B, we slightly adjusted the trap and carried out a routine optimization procedure of the imaging system. Moreover, for each point in set A, the maximum hold time is about 0.5 s and the maximum atom number loss is about 30% while for set B, the values are 2 s and 50%. Furthermore, in the case of data set A, atom number and cloud widths are measured at 3 different hold times and repeated for about 10 times. In the case of data set B, the maximum hold time is about 2 s and measurements are done at 11 different hold times and repeated for about 6 times.

The initial temperatures of set A and B are 6.1(1.5) nK and 7.2(5) nK and the time-averaged temperatures T_{avg} are 7.7(1.7) nK and 9.6(9) nK, respectively. The time-averaging of temperature also reduces possible temperature errors caused by residual breathing collective excitation when the data points at different hold times well sample a few oscillation periods. Compared to set A, set B has a similar sampling rate but a longer sampling time covering more oscillation periods. This makes the measured temperature of set B somewhat more reliable than that of set A.

Re-analyzing the First Efimov Resonance

The L_3 data on the first Efimov resonance presented in Ref. [Ber11b] (black squares in Fig 7.5) were previously fitted using a *zero-temperature* model with parameters $a_-^{(0)}$ and $\eta_-^{(0)}$ (same as for the model used in present work) and an additional parameter λ , which is an amplitude scaling factor for L_3 accounting for a possible systematic errors in the number density calibration. The result reported in Ref. [Ber11b] is $a_-^{(0)} = -955(28)a_0$, $\eta_-^{(0)} = 0.08(1)$ and $\lambda = 0.89(6)$ (black dashed line in Fig 7.5). In the present work, we fix the temperature

to the measured value of 15 nK and refit the data with the *finite-temperature* model [Rem13] and obtain more precise result as $a_-^{(0)} = -963(9)a_0$, $\eta_-^{(0)} = 0.10(1)$ and $\lambda = 1.24(6)$ (red line in Fig 7.5). Here the given errors do not account for uncertainties in the $a(B)$ mapping, as discussed in the main text. The difference in the most important parameter $a_-^{(0)}$ between two fitting approaches is, however, smaller than the 1σ uncertainty of the fitting. We conclude that finite-temperature effects have not significantly affected our previous determination of the three-body parameter.

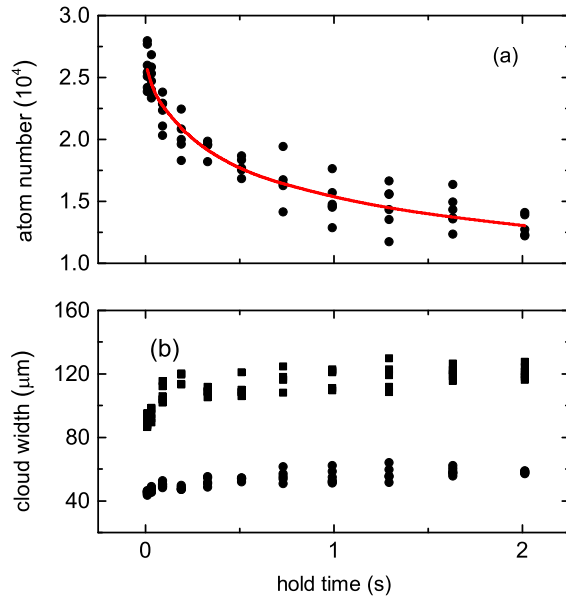


Figure 7.4: Typical data of an atom decay measurement (at 800.87 G or $a = -11800a_0$) near the second Efimov resonance, taken from set B. In (a), we plot measured atom number (black squares) against hold time. In (b), the cloud’s widths in horizontal and vertical directions are plotted as black squares and dots, respectively. The red solid curve in (a) is the result of numerical fitting used to extract L_3 .

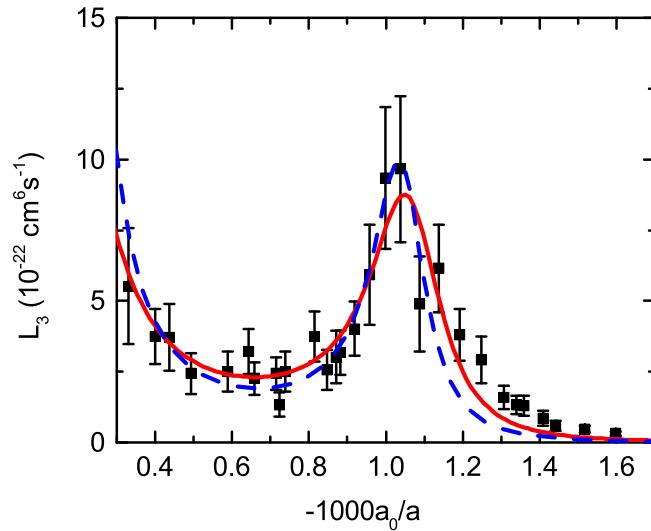


Figure 7.5: Re-fit of the first Efimov resonance. The data from Ref. [Ber11b] are plotted as black squares. The earlier zero-temperature fit and the new finite-temperature fit are represented by the blue dashed line and the red solid line, respectively.

Publication: The three-body parameter for Efimov states in lithium-6[†]

Phys. Rev. A **90**, 043636 (2014)

Bo Huang,¹ Ken M. O'Hara,^{2,3} and Rudolf Grimm^{1,3}

¹*Institut für Experimentalphysik, Universität Innsbruck, 6020 Innsbruck, Austria*

²*Department of Physics, Pennsylvania State University,
University Park, Pennsylvania 16802-6300, USA*

³*Institut für Quantenoptik und Quanteninformation,
Österreichische Akademie der Wissenschaften, 6020 Innsbruck, Austria*

Jeremy M. Hutson⁴

⁴*Joint Quantum Centre (JQC) Durham/Newcastle, Department of Chemistry,
Durham University, South Road, Durham, DH1 3LE, United Kingdom*

Dmitry S. Petrov^{5,6}

⁵*Université Paris-Sud, CNRS, LPTMS, UMR8626, Orsay F-91405, France*

⁶*Russian Research Center Kurchatov Institute, Kurchatov Square, 123182 Moscow, Russia*

We present a state-of-the-art reanalysis of experimental results on Efimov resonances in the three-fermion system of ${}^6\text{Li}$. We discuss different definitions of the 3-body parameter (3BP) for Efimov states, and adopt a definition that excludes effects due to deviations from universal scaling for low-lying states. We develop a finite-temperature model for the case of three distinguishable fermions and apply it to the excited-state Efimov resonance to obtain the most accurate determination to date of the 3BP in an atomic three-body system. Our analysis of ground-state Efimov resonances in the same system yields values for the three-body parameter that are consistent with the excited-state result. Recent work has suggested that the reduced 3BP for atomic systems is a near-universal quantity, almost independent of

[†] The author of the present thesis analyzed the data from K.M.O. with the finite-temperature model provided by D.S.P. and contributed to the interpretation of the results. R.G. guided the analysis of the data and the interpretation of the results. J.M.H. provided improved analysis of the scattering lengths.

the particular atom involved. However, the value of the 3BP obtained for ${}^6\text{Li}$ is significantly ($\sim 20\%$) different from that previously obtained from the excited-state resonance in Cs. The difference between these values poses a challenge for theory.

8.1 Introduction

Ultracold atomic gases with resonant interactions provide experimental model systems to explore the universal physics of few-body quantum states [Bra06, Fer10a]. Efimov states, which are weakly bound three-body quantum states in systems of resonantly interacting particles, are a paradigm of this field. Efimov [Efi70] showed that, when two bosons interact with an infinite scattering length, the corresponding three-particle system has an infinite number of three-body states just below threshold. For zero-range interactions, each successive Efimov state is larger than the previous one by a discrete length scaling factor, the ‘Efimov period’, which is 22.7 for a system of three identical bosons¹ but can be widely different for other systems [D’I06]. We refer to this universal scaling behavior as Efimov universality.

The interactions between pairs of ultracold atoms may be varied by tuning an applied magnetic field in the vicinity of a zero-energy Feshbach resonance [Chi10]. The scattering length has a pole at resonance, corresponding to a 2-body bound state exactly at threshold. Signatures of Efimov states were first observed in an ultracold gas of cesium atoms [Kra06], and have since been found in many other systems, including other bosonic gases [Zac09, Pol09, Gro09, Gro10, Wil12, Roy13], three-component fermionic spin mixtures [Ott08, Huc09, Wil09, Nak10], and mixtures of atomic species [Bar09, Blo13, Tun14, Pir14]. Moreover, extensions of the Efimov scenario to universal states of larger clusters [Ham07b, von09, von10] have been demonstrated in experiments [Fer09, Pol09, Zen13], highlighting the general nature of universal few-body physics.

In addition to their discrete scaling property, Efimov states are characterized by a *three-body parameter* (3BP), which determines the position of the entire ladder of states. In the realm of nuclear systems, the 3BP is a non-universal quantity [Bra06], determined by details of the short-range interaction. However, in atomic systems it has been found experimentally [Ber11b, Roy13] that the 3BP is nearly constant when expressed in terms of the van der Waals length r_{vdW} [Chi10], which quantifies the dispersion interaction between two neutral atoms. We refer to this feature of Efimov physics as van der Waals universality of the 3BP, and it has been the subject of a number of theoretical investigations [Chi11, Wan12, Sch12, Sør12, Nai14a, Wan14].

Three-body recombination resonances occur when Efimov states cross the three-atom threshold as a function of magnetic field (and hence of scattering length) [Esr99, Bra01, Fer11]. Recombination resonances due to Efimov ground states provide the most prominent observables in Efimov physics. Many experiments have focused on such features, including some that determined the 3BP [Ber11b, Wil12, Roy13]. In real atomic systems, however, finite-range corrections may significantly affect universal scaling, particularly for ratios involving

¹ The number 22.7 is rounded to three digits. The relative deviation from the exact value is only 0.025%, which is negligible for all practical purposes.

the Efimov ground state [Thø08a, Pla09, Nai11, Sch12]. However, such corrections decrease substantially for higher Efimov states and are already very small for the first excited state. Excited-state resonances are therefore particularly interesting for precise measurements of the 3BP.

Excited-state Efimov resonances occur at very large scattering lengths. They require extremely low temperatures for experimental observation, since the recombination peaks are less well defined when the de Broglie wavelengths are shorter than the scattering lengths [D'I04, Kra06, Rem13]. Excited-state resonances have therefore been observed in only a very few experiments, carried out with ${}^6\text{Li}$ [Wil09], with ${}^{133}\text{Cs}$ [Hua14b], and with mixtures of ${}^6\text{Li}$ and ${}^{133}\text{Cs}$ [Tun14, Pir14]. Quantitative understanding of these resonances requires both very precise knowledge of the two-body scattering properties and an accurate theoretical description of finite-temperature effects. Ref. [Hua14b] analyzed the excited-state Efimov resonance in cesium, using a highly accurate model of the two-body scattering [Ber13] and a theoretical finite-temperature approach recently developed in Ref. [Rem13]. This study provided the most precise measurement of the Efimov period so far.

In this Article, we re-analyze previous experimental results on the excited-state Efimov resonance in ${}^6\text{Li}$ observed in Ref. [Wil09] and on the ground-state Efimov resonances observed in Refs. [Ott08] and [Huc09]. In Sec. 8.2, we discuss different definitions of the 3BP and how they are affected by deviations from ideal Efimov behavior. We adopt a definition that excludes effects due to deviations from universal scaling for low-lying states. In Sec. 8.3, we summarize the main properties of the three-fermion system. In Sec. 8.4, we develop a new finite-temperature approach, which generalizes the theory introduced for the three-boson case in Ref. [Rem13] to the case of three distinguishable fermions. In Sec. 8.5, we present a refined analysis of the excited-state resonance observed in Ref. [Wil09]. This gives a high-precision value for the 3BP in ${}^6\text{Li}$, which deviates significantly from those found in other atomic systems. In Sec. 8.6, we re-analyze previous results on the ground-state Efimov resonance from Ref. [Ott08] and investigate the possible influence of finite-range effects. In Sec. 8.7, we discuss our findings in the context of other experiments in the field. The value of the 3BP found for ${}^6\text{Li}$ is not well explained by current theories and presents a challenge for future theoretical work.

8.2 Three-body parameter

For three identical bosons, ideal Efimov scaling leads to the simple relation

$$\kappa^{(n+1)} = \kappa^{(n)}/22.7 \quad (8.1)$$

between the wavenumbers $\kappa^{(n)}$ that characterize the energies $E_{\text{res}}^{(n)} = -(\hbar\kappa^{(n)})^2/m$ of successive Efimov states in the resonant limit $a \rightarrow \pm\infty$. Here m is the atomic mass and n is an integer quantum number. The corresponding relation between the scattering lengths at the positions of successive recombination resonances is

$$a_-^{(n+1)} = 22.7 \times a_-^{(n)}. \quad (8.2)$$

The universal relation

$$a_-^{(n)} = -1.508/\kappa^{(n)} \quad (8.3)$$

connects a resonance position with the corresponding bound-state wavenumber. In the ideal case, knowledge of any of the above quantities $\kappa^{(n)}$ or $a_-^{(n)}$ fixes the infinite series and thus provides a proper representation of the 3BP.

In a real system, where the interaction has a finite range, the Efimov spectrum is bounded from below. We refer to the lowest state as the Efimov ground state with $n = 0$ and to the corresponding resonance at $a_-^{(0)}$ as the ground-state Efimov resonance. Eqs. (8.1) and (8.2) then represent approximations, subject to finite-range effects.

One way to understand the Efimov effect is through a treatment in hyperspherical coordinates. Efimov states may be viewed as supported by an effective adiabatic potential that is a function of the hyperradius R . For a zero-range two-body potential with large scattering length a , this potential is attractive and proportional to R^{-2} for $R \lesssim |a|$ [Zhe86] and supports an infinite number of bound states as $a \rightarrow \pm\infty$. For potential curves with long-range van der Waals tails, however, Wang *et al.* [Wan12] have shown that the effective adiabatic potential reaches a minimum and then rises to a wall or barrier near $R = 2r_{\text{vdW}}$. The position of the minimum and wall depend to some extent on the details of the two-body potential and the number of bound states it supports, but become near-universal as the number of 2-body bound states increases. The presence of the minimum and wall have two principal effects on the physics. First, the deviation of the effective potential from R^{-2} behavior results in deviations from ideal Efimov scaling for the lowest-lying states. Secondly, the boundary condition provided by the wall defines the position of the entire ladder of Efimov states, and its nearly universal position is responsible for the near-universality of the 3BP. However, it should be noted that the wall itself is a product of physics around $2r_{\text{vdW}}$, so that variations in the physics in this region can produce deviations from universality of the 3BP even in the limit $a \rightarrow \pm\infty$.

Theoretical investigations [Tho08a, Pla09, Wan12, Sch12] have shown that the Efimov ground state may be subject to considerable modifications. For $n = 0$ this may change the factor 22.7 in Eqs. (8.2) - (8.3) by up to 25%. The relation (8.3) is subject to similar modifications [Sch12, Wan12]. The recent experiment on the excited-state resonance in Cs [Hua14b] and a related theoretical investigation [Wan14] also hint at deviations from the ideal scaling.

The deviations from universal scaling for low-lying Efimov states raise the question of the best representation of the 3BP. Definitions based on the limit $n \rightarrow \infty$ remove effects of this type from the 3BP. Accordingly, we adopt the definition [Bra06]

$$\kappa_* = \lim_{n \rightarrow \infty} \left(22.7^n \kappa^{(n)} \right), \quad (8.4)$$

and by analogy

$$a_-^* = \lim_{n \rightarrow \infty} \frac{a_-^{(n)}}{22.7^n}. \quad (8.5)$$

The position of the ground-state Efimov resonance, $a_-^{(0)}$, is commonly used as a 3BP. However, it gives a somewhat crude approximation to a_-^* , and in some cases may deviate from it

by as much as 25%. The quantities $a_-^{(1)}/22.7$ and $22.7\kappa^{(1)}$, obtained from the excited-state resonance, provide much better approximations to a_-^* and κ_* , with corrections of only about 1% due to deviations from universal scaling [Sch12]; these corrections are comparable to the other uncertainties in current experiments.

Efimov states are also characterized by a decay parameter η_* [Bra06], which describes their decay to lower-lying atom-dimer combinations. This parameter is usually considered to be a constant for a particular Efimov state, but may vary if the available product states change significantly. The resulting field dependence may be important when interpreting measurements that extend over wide ranges of field [Wen09].

8.3 Efimov states in a three-component Fermi gas

8.3.1 Three-fermion system

Efimov states in a three-component gas of fermions [Bra09b] exhibit the same discrete scaling behavior as in the three-boson case, provided that all three scattering lengths involved are large ($|a_{12}|, |a_{13}|, |a_{23}| \gg r_{\text{vdW}}$). In particular, if the masses of the three components are equal, the Efimov period is given by the same discrete scaling factor of 22.7. The special case of three equal scattering lengths ($a_{12} = a_{13} = a_{23}$) is formally equivalent to the situation for three identical bosons.

A gas of ${}^6\text{Li}$ atoms prepared in a mixture of the lowest three spin states allows a realization of large scattering lengths by Feshbach tuning [Chi10]. However, the applied magnetic field offers only one degree of freedom for tuning, thus limiting the experimentally accessible combinations of scattering lengths. Arbitrary combinations and, in particular, the situation of three equal scattering lengths thus remain hypothetical cases, but universal theory allows them to be linked to the combinations that exist in real systems.

In real experiments on a three-fermion system, Efimov resonances appear at certain combinations of large scattering lengths a_{12}, a_{13}, a_{23} , where typically $a_{12} \neq a_{13} \neq a_{23}$. A generalization of the Skorniakov–Ter-Martirosian (STM) equations [Bra09b] can be employed to determine the 3BP from these generally unequal values. In the wavenumber representation, κ_* then refers to the hypothetical case of three infinite scattering lengths, while a_-^* refers to a hypothetical system with three equal scattering lengths.

The STM approach is based on the zero-range approximation and therefore does not take account of finite-range corrections, which are significant at relatively small scattering lengths. It can thus be expected to provide an excellent approximation for excited Efimov states ($n \geq 1$), but it may be subject to significant corrections if applied to the Efimov ground state ($n = 0$).

8.3.2 Three-body recombination

In a three-component Fermi gas, the dominant contribution to three-body losses results from triples of three non-identical particles. All other combinations involve pairs of identical fermions, which leads to a strong Pauli suppression of losses at ultralow temperatures [Esr01].

Three-body losses can be modeled by the simple rate equation

$$\frac{d}{dt}n_i = -L_3n_1n_2n_3, \quad (8.6)$$

where the n_i represent the number densities of the three different spin states. After a spatial integration of losses over the density profile of the trapped cloud, the loss rate coefficient L_3 can be experimentally determined by fitting the time-dependent decay of the total atom numbers [Ott08, Huc09, Wil09]. Efimov states show up as distinct loss resonances [Fer11] when they couple to the three-atom threshold.

8.3.3 Lithium-6

The situation of a three-component Fermi gas of ${}^6\text{Li}$ is unique because of overlapping Feshbach resonances in all three combinations of the lowest three spin states together with large negative background scattering lengths. The two-body scattering properties are known to an extraordinarily high level of precision thanks to the characterization in Ref. [Zür13], which significantly improved the conversion from magnetic field to scattering lengths compared to previous work [Bar05].

In the resonance region between 832 and 900 G, all three scattering lengths are very large and negative, with absolute values of a few thousand times the Bohr radius a_0 that vastly exceed $r_{\text{vdW}} = 31.26 a_0$. In this extreme regime, an excited Efimov state exists [Wil09]. This trimer state crosses the three-atom threshold near 900 G and leads to a strong enhancement of three-body recombination. The corresponding Efimov ground state exists over a much wider range of magnetic fields, but it does not cross threshold at currently accessible magnetic fields and thus does not lead to an observable recombination resonance.

In the magnetic-field region below the zero crossings of the Feshbach resonances, the three scattering lengths are moderately large and negative, so that an Efimov ground state exists. This state crosses the three-atom threshold near 130 G and near 500 G [Ott08, Huc09], leading to two observable Efimov resonances. In this low-field region, the scattering lengths never reach large enough values for an excited Efimov state to exist.

8.3.4 The effective range

One way to quantify the finite (non-zero) range of an atomic interaction is through the effective range [Bet49, Hin71], which characterizes the leading term in the energy-dependence

of the scattering length. The effective range behaves very differently in the vicinity of Feshbach resonances of different types [Bla14]. For a resonance that is strongly entrance-channel-dominated [Chi10], the effective range takes a small and fairly constant value close to $2.8r_{\text{vdW}}$ at fields near the resonance pole [Gao98]. By contrast, for resonances that are closed-channel-dominated, the effective range is much larger and varies very fast with magnetic field [Bla14]. The Feshbach resonances used in the present work for ${}^6\text{Li}$ are all strongly entrance-channel-dominated [Chi10], so that deviations from Efimov scaling due to finite-range effects are expected to be relatively small in comparison to some of the other atomic systems that have been studied.

8.4 Finite-temperature theoretical approach

A convenient way of modeling three-body losses in Efimovian systems is provided by the S -matrix formalism based on Efimov's radial law [Ef79], which is elaborated in Refs. [Bra06, Bra08, Rem13] for the case of three identical bosons. Its generalization to three distinguishable atoms with different scattering lengths is straightforward and we will present only a brief derivation. This is a zero-range theory for which κ_* and η_* are external parameters.

First, one introduces three-atom scattering channels describing the motion of free atoms at large distances. By contrast, all atom-dimer channels are substituted by the single Efimov channel defined in the scaling region $r_{\text{vdW}} \ll R \ll \min\{1/k, |a_{12}|, |a_{23}|, |a_{13}|\}$, where $k = \sqrt{mE}/\hbar$, E is the energy in the center of mass reference frame, R is the hyperradius, and we consider the case of negative scattering lengths. The reason for this substitution is that when $r_{\text{vdW}} \ll \min\{1/k, |a_{12}|, |a_{23}|, |a_{13}|\}$ this channel becomes essentially the only one that can conduct three atoms from large distances to the recombination region of size $\sim r_{\text{vdW}}$.

One can think of this short-distance channel and the long-distance three-atom channels as being fused together at intermediate distances where the transmission, reflection, and mixing of the channels takes place. We can then introduce a unitary matrix s_{ij} , which defines the amplitude of the outgoing wave in channel j if the incoming wave is injected in channel i . The terms ‘‘incoming’’ and ‘‘outgoing’’ are defined with respect to the fusion region. In particular, the incoming Efimov wave R^{-2+is_0} actually propagates towards larger distances and R^{-2-is_0} describes the outgoing one. Here $s_0 \approx 1.00624$ is a constant and the ideal Efimov period of 22.7 is e^{π/s_0} .

The simple fact that the matrix s_{ij} is unitary turns out to be very useful in describing the scaling properties of Efimovian systems [Bra06]. We point out that s_{ij} does not depend on the 3BP κ_* or the decay parameter η_* . These quantities come into play when one fixes the relative phase and amplitude of the incoming and outgoing Efimov waves,

$$R^2\Psi \propto (R/R_0)^{is_0} - e^{2\eta_*} (R/R_0)^{-is_0}, \quad (8.7)$$

where R_0 is a three-body length related to κ_* by

$$(\kappa_* R_0/2)^{2is_0} = -\Gamma(is_0)/\Gamma(-is_0) \quad (8.8)$$

and Γ is the gamma function. One can imagine that Efimov waves are reflected at small hyperradii by a lossy mirror with reflection/loss properties given by Eq. (8.7). The three-body problem is then analogous to a Fabry-Perot interferometer with the other mirror quantified by the matrix s_{ij} . This picture gives a convenient way of understanding and describing three-body loss peaks as resonances of the Fabry-Perot cavity. In particular, if we denote the Efimov channel by subscript 1, the loss probability for a given incoming channel $i \neq 1$ is [Bra08]

$$P_i = \frac{(1 - e^{-4\eta_*})|s_{i1}|^2}{|1 + (kR_0)^{-2is_0} e^{-2\eta_*} s_{11}|^2}, \quad (8.9)$$

where the denominator accounts for multiple reflections “inside” the resonator. The total loss rate constant for three distinguishable fermions is obtained by using unitarity ($\sum_{i=1}^{\infty} |s_{1i}|^2 = 1$) and averaging over the Boltzmann distribution,

$$L_3 = \frac{24\sqrt{3}\pi^2\hbar(1 - e^{-4\eta_*})}{mk_{\text{th}}^6} \times \int_0^{\infty} \frac{(1 - |s_{11}|^2)e^{-k^2/k_{\text{th}}^2}}{|1 + (kR_0)^{-2is_0} e^{-2\eta_*} s_{11}|^2} k dk, \quad (8.10)$$

where $k_{\text{th}} = \sqrt{mk_{\text{B}}T}/\hbar$. Equation (8.10) differs from the bosonic result of Ref. [Rem13] only by the factor $1/3$, which is due to the bosonic bunching effect and different ways of counting triples in the two cases. A more profound change is hidden in the quantity s_{11} , which, in contrast to the case of identical bosons, now depends on three dimensionless numbers ka_{12} , ka_{23} , and ka_{13} .

In order to determine s_{11} we look for the three-body wave function that behaves as $A(kR)^{-2+is_0} + B(kR)^{-2-is_0}$ in the scaling region and contains only outgoing waves at large distances. By definition, $s_{11} = B/A$. We solve this problem by using the STM equations in a very close analogy to the bosonic case (see Supplemental Material of [Rem13]). For distinguishable atoms with generally different scattering lengths we end up with three coupled STM equations (see Ref. [Pet13] for details of the method).

In practice, we use the known dependence of a_{ij} on B [Zür13] and tabulate s_{11} as a function of k and B . This then allows fast integration of Eq. (8.10) for any desired values of T , κ_* , and η_* .

8.5 Excited-state Efimov resonance

In Ref. [Wil09], the excited-state Efimov resonance was observed in the high-field region of ${}^6\text{Li}$. In Figure 8.1 we show the experimental results for the three-body loss coefficient L_3 as a function of the magnetic field, measured for two different temperatures of about 30 nK (set A) and 180 nK (set B). In this section we reanalyze these results, taking account of finite-temperature effects using the theory described in Sec. 8.4, in order to obtain a refined estimate of the 3BP for ${}^6\text{Li}$.

The two free parameters in the temperature-dependent theory of Sec. 8.4 are the 3BP κ_* and the decay parameter η_* . In addition, experimental uncertainties in the number density

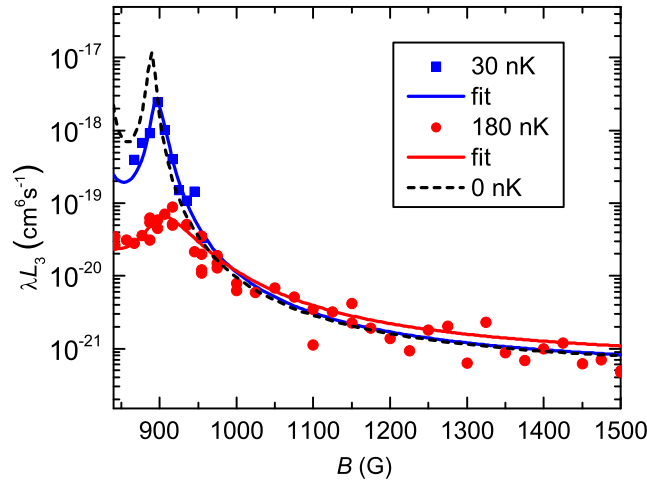


Figure 8.1: (Color online). Finite-temperature fits to the excited-state Efimov resonance. The experimental results obtained for L_3 in Ref. [Wil09] for two different temperatures are plotted as filled blue squares (set A, 30 nK) and filled red circles (set B, 180 nK). The amplitude scaling parameter λ is of order 1, see text. The corresponding solid lines are the fixed-temperature fits to both data sets, carried out on a linear scale (see first and fifth row in Table 8.1). The black dashed curve is calculated for the zero-temperature limit using the parameters from the fixed-temperature fit to the 30 nK set.

calibration may considerably affect the amplitude of the observed losses. Such uncertainties may result from the atom number calibration, from the limited knowledge of the trap frequencies, and from errors in the temperature measurements. It is therefore useful to introduce an additional scaling parameter λ for the amplitude of the observed losses [Hua14b]. Under realistic experimental conditions, variations of up to a factor of two from the ideal value $\lambda = 1$ are plausible.

To analyze the data we follow several different strategies, similar to those applied to the three-boson case of cesium [Hua14b]. First, we fix the temperature T to the measured values $T_{\text{meas}} = 30$ nK (set A) and 180 nK (set B), and we perform a fit with κ_* , η_* , and λ as the free parameters. Alternatively, we allow for a variable temperature T , and instead we fix $\lambda = (T/T_{\text{meas}})^{-3}$ to take account of the resulting change in the volume of the harmonically trapped gas.² Moreover, we fit the data sets A and B on either a linear or a logarithmic scale, which puts different weights on the different regions. In this way, we obtain four different fits for each data set. We note that the experimental results of Ref. [Wil09] indicated that the effect of heating during the decay of the trapped sample remained very small, so that this effect can safely be neglected in our fit analysis.

Table 8.1 summarizes the results of our fits for both data sets, and Fig. 8.2 shows the values obtained for the 3BP (from the third column of the Table). The comparison between the four different fits for each data set provides information on the robustness of the fits and possible systematic effects beyond simple statistical uncertainties. In our results from the low-temperature set A, the errors on κ_* from individual fits range between 0.5% (for

² Fits with both T and λ as free parameters are numerically unstable because the parameters are too strongly correlated.

Set	T (nK)	$\kappa_* a_0$	η_*	λ
A	30^a	0.006808(36)	0.032(5)	0.546(27)
A log	30^a	0.006744(91)	0.048(15)	0.498(107)
A	35(5)	0.006774(39)	0.029(5)	0.644^T
A log	36(2)	0.006689(97)	0.042(14)	0.593^T
B	180^a	0.006839(80)	0.088(15)	0.258(16)
B log	180^a	0.006665(130)	0.067(16)	0.270(49)
B	237(5)	0.006736(84)	0.072(15)	0.438^T
B log	218(10)	0.006624(118)	0.034(8)	0.562^T

Table 8.1: Results of fits for the excited-state Efimov resonance, obtained from the two sets of measurements presented in Fig. 8.1. The fits using a logarithmic L_3 scale are indicated with ‘log’ in the column ‘Set’. The superscript a means that corresponding parameter is kept fixed. The superscript T indicates that the corresponding parameter is calculated from the fitted values for T .

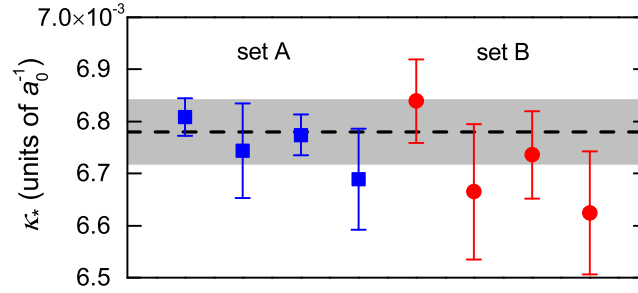


Figure 8.2: (Color online). Fitted values for κ_* corresponding to the third column in Table 8.1. The dashed line indicates the final result $\kappa_* = 0.00678(6) a_0^{-1}$, as obtained from a weighted average of the four data points of the low-temperature data set A (filled blue squares), and the gray-shaded region shows the corresponding uncertainty. The high-temperature data set B (filled red circles) is not used for deriving the final value, but within the uncertainties the values are fully consistent with the result from data set A.

linear fits) and 1.5% (for logarithmic fits). Within the error bars no significant systematic deviations appear between the central values obtained from the different fits, which shows that the errors are consistent with purely statistical uncertainties. From the low-temperature data set A, by calculating a weighted average over all four fitted values,³ we obtain the final value $\kappa_* = 0.00678(6) a_0^{-1}$, where the uncertainty includes both the weighted errors of the four individual fits and the standard deviation of the four slightly different values. The result for κ_* and the error are shown by the dashed horizontal line and the gray-shaded region in Fig. 8.2. Note that all the statistical uncertainties specified in this work correspond to one standard deviation.

The higher-temperature data set B yields similar results, but with somewhat larger uncertainties. Again, there are no systematic deviations between the four different fit strategies applied. Here the final result for the 3BP, $\kappa_* = 0.00674(13) a_0^{-1}$, is fully consistent with the

³ We use weights inversely proportional to the square of the errors of the individual fits. This strongly favors the results obtained from the linear fits (first and third data points in Fig. 8.2). This is reasonable because these fits are more sensitive to the resonance peaks than the logarithmic fits, which are more sensitive to the wings of the resonance

result obtained at lower temperatures, with an uncertainty about two times larger than for set A. This confirms that temperature-induced shifts of the resonance are properly taken into account in our theoretical approach.

The original data analysis in Ref. [Wil09] yielded $\kappa_* = 0.0069(2) a_0^{-1}$, remarkably close to the present result but with a quoted error about three times larger. However, the present work reveals two systematic shifts, which in the previous work partially canceled each other. The updated values of the scattering lengths [Zür13] shift the value of κ_* up by about 3%, while residual finite-temperature effects shift the value down by about 5%.⁴

A further contribution to our error budget comes from the uncertainty in the mapping from magnetic field to scattering length. The scattering lengths used here were obtained from the potential curves of Ref. [Zür13], which were fitted to highly precise measurements of binding energies of ${}^6\text{Li}_2$ in the resonant region, together with measurements of collision properties. The fits have recently been extended to include binding energies for ${}^7\text{Li}_2$, with an explicit mass-dependence of the potential curves [Jul14]. In order to establish the uncertainties in the scattering lengths at the magnetic field of the excited-state resonance, we have repeated the fits of Ref. [Zür13] and calculated explicit statistical uncertainties in the three scattering lengths a_{12} , a_{13} and a_{23} at 891 G, using the procedure of Ref. [LR98]. The resulting contribution to the uncertainty in κ_* is about 0.1%. We have also estimated the nonstatistical uncertainties in the scattering lengths by repeating the fits with the experimental binding energies set to the values at the upper and lower limits of their systematic errors, producing a further uncertainty of 0.07%. The uncertainty of 0.1 G in the magnetic-field calibration of Ref. [Wil09] corresponds to a further error of 0.07%. All these error sources are thus negligibly small compared to the fitting errors described above.

Based on the results of our fits for κ_* and η_* , we can calculate the recombination rate coefficient L_3 in the zero-temperature limit. The resulting curve is shown as a dashed line in Fig. 8.1. The peak occurs at 891 G, which marks the point where the Efimov state crosses the three-atom threshold. Here the three scattering lengths are $a_{12} = -8671(38) a_0$, $a_{13} = -2866(3) a_0$, and $a_{23} = -5728(16) a_0$.

8.6 Ground-state Efimov resonances

References [Ott08, Huc09] reported the observation of the two ground-state Efimov resonances in the low-field region of ${}^6\text{Li}$ near 130 G and near 500 G. The L_3 results of Ref. [Ott08] have been further analyzed in Refs. [Bra09b, Wen09, Nai11], using different models within the zero-temperature approximation. Ref. [Bra09b] treated the three different scattering lengths within the approach of the generalized STM equations, which is exact within the zero-range limit, while Ref. [Wen09] introduced the approximation of an ‘effective scattering length’. As an important improvement, Ref. [Wen09] introduced a magnetic-field dependence in the decay parameter η_* , determined by the binding energies of the different target

⁴ In the original analysis, a zero-temperature model was applied to fit only a subset of data in the wings of the resonance, where temperature limitations remain small. This eliminated a large contribution to the temperature-induced shift.

molecular states. The latter has proved very useful to describe the different widths of the narrower Efimov resonance near 130 G and the wider Efimov resonance near 500 G. Ref. [Nai11] considered the effects of finite-range corrections and of a two-channel model of the atom-atom scattering.

Our new analysis of the results of Ref. [Ott08] is based on the generalized STM approach in combination with the magnetic-field-dependent decay parameter η_* . We also use the updated scattering length values from Ref. [Zür13], instead of the ones from Ref. [Bar05], but this has negligible effect on the value resulting for the 3BP in the low-field region. All our fits assume a temperature of 215 nK [Ott08], but we find that including finite-temperature effects makes a negligible difference for the ground-state resonances, in contrast to the excited-state case.

Our theoretical model to calculate L_3 from the three different scattering lengths relies on the zero-range approximation, and is applicable only for $|a_{12}|, |a_{13}|, |a_{23}| \gg r_{\text{vdW}}$. However, at the resonance positions of 130 G and 500 G, the smallest of the three scattering lengths, $|a_{12}|$, exhibits rather small values of $\sim 4 r_{\text{vdW}}$ and $\sim 3 r_{\text{vdW}}$, respectively. This makes the analysis quite vulnerable to finite-range effects, and the extracted values for κ_* can be expected to provide only an approximation to the limiting case of Eq. (8.4). To deal with this nonideal situation, we introduce a lower cutoff scattering length a_{min} and restrict our fit to the region where $|a_{12}|, |a_{13}|, |a_{23}| > a_{\text{min}}$. The dependence of the resulting values for κ_* on a_{min} then gives an indication of the sensitivity to finite-range and model-dependent corrections.

Figure 8.3 shows three different fits to the same data points, differing in the cutoff scattering length, $a_{\text{min}}/r_{\text{vdW}} = 2, 4$, and 6. The fits are applied globally to both resonances, appearing near 130 G and near 500 G. The three free parameters of the fit are κ_* , the amplitude scaling factor λ (see Sec. 8.5), and the parameter A defined in Ref. [Wen09], from which the magnetic-field-dependent η_* can be calculated. The lines in Fig. 8.3 represent the behavior within the fit region (solid lines) and extrapolated beyond that region (dashed lines). We find that the fit with $a_{\text{min}}/r_{\text{vdW}} = 4$ captures both resonances and the overall behavior quite well. Here we obtain $\kappa_* = 0.00645(3) a_0^{-1}$ (linear scale) and $0.00641(3) a_0^{-1}$ (logarithmic scale). For the amplitude scaling factor the fits yield the plausible values $\lambda = 1.65(5)$ (linear) and $1.68(7)$ (logarithmic). From the corresponding values of A we obtain the values $\eta_* = 0.0814(3)$ (linear) and $0.0745(3)$ (logarithmic) for the decay parameter at the lower-field (sharper) resonance, which the fit locates at 132 G.

In contrast to the fit with $a_{\text{min}}/r_{\text{vdW}} = 4$, the two other fits in Fig. 8.3 are problematic. The fit for $a_{\text{min}}/r_{\text{vdW}} = 2$ puts some weight on regions where the applicability of zero-range theory is highly questionable, while the fit for $a_{\text{min}}/r_{\text{vdW}} = 6$ excludes the centers of the two resonances, which provide the most sensitive information on the Efimov resonance positions.

Figure 8.4 shows the values for κ_* resulting from fits with different cutoff scattering lengths a_{min} in the range between 2 and $6 r_{\text{vdW}}$. The filled blue squares represent the fit to the L_3 results on a linear scale. This fit puts most weight on the lower resonance, but as a_{min} increases it gives more weight to the region between the resonances, and the resulting value for κ_* decreases by almost 10%. The fits to the L_3 data on a logarithmic scale (filled red

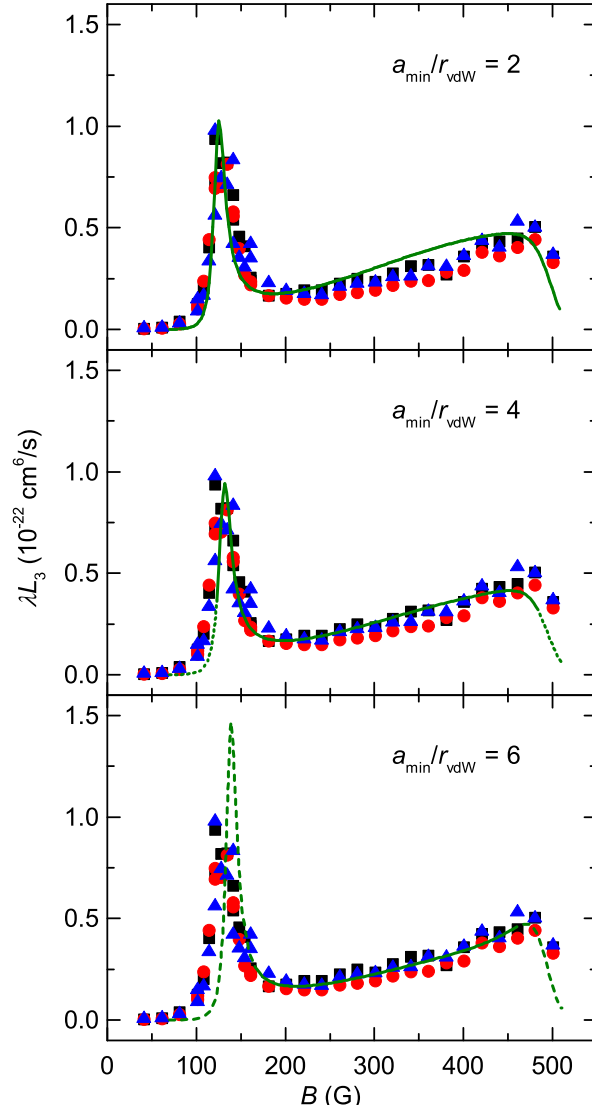


Figure 8.3: (Color online). Fits to the ground-state Efimov resonances. All three panels show the same experimental data on the loss rate coefficient L_3 from Ref. [Ott08], where the filled squares, filled circles, and filled triangles refer to losses measured in the lowest three spin states. The theoretical curves represent our fits to the data on a linear scale. The solid lines indicate the region used for the fit with all three scattering lengths being larger than the cutoff value a_{\min} . The dashed lines extrapolate the theory to regions not used for the fit.

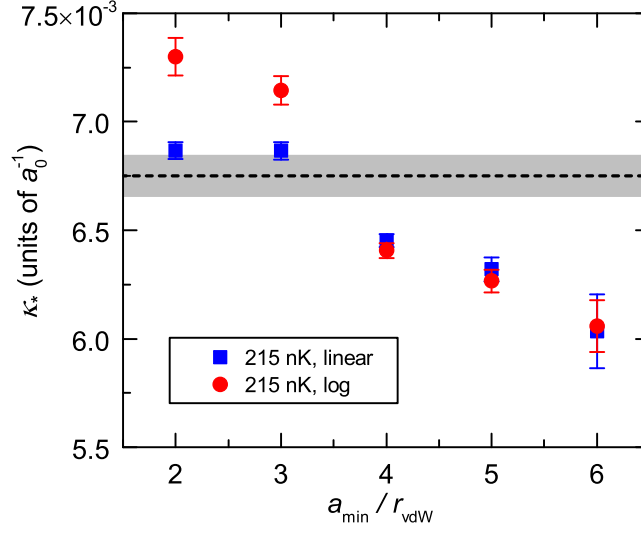


Figure 8.4: (Color online). Dependence of the fitted values for κ_* on the cutoff scattering length a_{\min} for the ground-state Efimov resonance. The blue filled squares and red filled circles refer to fits performed with a linear and logarithmic L_3 scale. The error bars represent the 1σ uncertainties from the individual fits. The horizontal dashed line marks the value of κ_* obtained from the excited-state Efimov resonance. The gray-shaded region marks the corresponding error range.

circles) show a similar behavior with a trend towards smaller values of κ_* at larger values of a_{\min} .

The fits for $a_{\min}/r_{\text{vdW}} \geq 5$ do not provide satisfactory results, mainly because of significant problems in reproducing the position of the resonance near 130 G. The fits for $a_{\min}/r_{\text{vdW}} \leq 4$ (central panel in Fig. 8.3) appear good, but for lower values of a_{\min} the result may be subject to significant finite-range effects. We therefore consider $a_{\min}/r_{\text{vdW}} = 4$ to be the best choice. It gives $\kappa_* = 0.00643(4) a_0^{-1}$, based on averaging the results of the linear and logarithmic fits. The error given here indicates only the statistical uncertainty, but the dependence of the results on a_{\min} suggests additional systematic errors on the order of 10%.

The dashed horizontal line and the gray-shaded region in Fig. 8.4 indicate the value of κ_* obtained from the excited-state resonance in Sec. 8.5, together with the corresponding error range. It may be seen that our results are consistent with discrete scaling as described by Eq. (8.1) within the relatively large uncertainties due to finite-range effects in the low-field region.

8.7 Conclusion

We have reanalyzed experimental results for the Efimov recombination resonances in ${}^6\text{Li}$ arising from the ground and excited Efimov states, using a very precise model of the two-body scattering [Zür13] and a new model of temperature-dependent effects in three-body recombination of three nonidentical fermions. From the excited-state Efimov resonance

[Wil09], we obtain the value for the 3BP in the wavenumber representation,

$$\kappa_* = 0.00678(6) a_0^{-1}.$$

This gives the reduced 3BP

$$\kappa_* r_{\text{vdW}} = 0.212(2).$$

According to Eq. (8.3) this corresponds to a reduced 3BP in the scattering length representation,

$$a_-^*/r_{\text{vdW}} = -7.11(6).$$

This latter representation of the 3BP facilitates a direct comparison with three-boson systems, which are characterized by a single scattering length.⁵

Our analysis of the ground-state Efimov resonances [Ott08, Huc09] yields values for the 3BP that are consistent with the above result within an estimated 10% uncertainty. Alternatively, they may be viewed as confirming that the lowest Efimov period in ${}^6\text{Li}$ is within 10% of the universal value of 22.7. The uncertainties, which follow from systematic shifts that depend on the choice of the lower cutoff applied to the scattering lengths in the data analysis, place an upper bound on the magnitude of possible finite-range corrections to the lowest Efimov period. The rapid decrease of such shifts with increasing order of the Efimov state [Thø08b, Sch12] gives us confidence that such corrections can be neglected for the 3BP if determined from the position of an excited-state resonance.

It is very interesting to compare the present result with the recent measurement for cesium in Ref. [Hua14b], which gave $a_-^{(1)} = -20190(1200) a_0$, implying a reduced 3BP $a_-^*/r_{\text{vdW}}^{\text{Cs}} = -8.8(4)$ with $r_{\text{vdW}}^{\text{Cs}} = 101.1 a_0$ [Ber13]. In both cases, the Feshbach resonances used for interaction tuning are strongly entrance-channel-dominated [Chi10]. The present result for the reduced 3BP in ${}^6\text{Li}$ differs from that measured for Cs by a factor 0.81(4). This clearly demonstrates that the van der Waals length is not the only relevant quantity in determining the 3BP. Even for strongly entrance-channel-dominated Feshbach resonances, van der Waals universality of the 3BP is only approximate, and is subject to further influences. It remains a challenge for theory to understand fully the role of finite-range effects [Nai11], of the physics of particular Feshbach resonances [Sch12, Wan14], of the role of genuine short-range three-body forces [Axi43, Sol03, D'I09], and of other species-dependent factors such as the number of bound states in the two-body potentials [Wan12]. It is also possible that light particles can tunnel through the barrier in the effective potential [Wan12] more effectively than heavy ones.

It would be highly desirable to investigate other systems at the precision of the present work, by detecting excited-state Efimov resonances and thus accurately measuring the 3BP. The bosonic gas of ${}^7\text{Li}$ [Gro09, Pol09, Rem13] is a prime candidate for such experiments, because it provides another example of a light system with exceptionally well characterized two-body scattering properties [Dyk13, Jul14]. Atoms such as ${}^{39}\text{K}$ [Zac09, Roy13, Fle13] and ${}^{85}\text{Rb}$ [Wil12] also provide very interesting systems for future precision experiments: ${}^{85}\text{Rb}$

⁵ The approximation of an effective scattering length from Ref. [Wen09] leads instead to $a_-^*/r_{\text{vdW}} = -8.15(7)$, which is not consistent with our result based on the generalized STM equations. This shows the limited usefulness of the effective scattering length at the precision level of the present work.

offers access to another entrance-channel-dominated case, while ${}^7\text{Li}$ and ${}^{39}\text{K}$ offer Feshbach resonances of intermediate character [Chi10].

Acknowledgements

We thank Selim Jochim for providing the experimental L_3 data for the ground-state Efimov resonances and Benno Rem for useful discussions. We acknowledge support by the Austrian Science Fund FWF within project P23106 and by EPSRC under grant no. EP/I012044/1. D.S.P. acknowledges support from the IFRAF Institute. The research leading to these results has received funding from the European Research Council (FR7/2007-2013 Grant Agreement no. 341197). K.M.O. acknowledges support from the NSF (Grant No. 1312430).

Finite-temperature effects on a triatomic Efimov resonance in ultracold cesium[†]

arXiv:1504.05360(2015)

Bo Huang,^{1,2} Leonid A. Sidorenkov,^{1,2} and Rudolf Grimm^{1,2}

¹*Institut für Experimentalphysik, Universität Innsbruck, 6020 Innsbruck, Austria*

²*Institut für Quantenoptik und Quanteninformation,
Österreichische Akademie der Wissenschaften, 6020 Innsbruck, Austria*

We report a thorough investigation of finite-temperature effects on three-body recombination near a triatomic Efimov resonance in an ultracold gas of cesium atoms. Our measurements cover a wide range from a near-ideal realization of the zero-temperature limit to a strongly temperature-dominated regime. The experimental results are analyzed within a recently introduced theoretical model based on a universal zero-range theory. The temperature-induced shift of the resonance reveals a contribution that points to an energy-dependence of the three-body parameter. We interpret this contribution in terms of the finite range of the van der Waals interaction in real atomic systems and we quantify it in an empirical way based on length scale arguments. A universal character of the corresponding resonance shift is suggested by observations related to other Efimov resonances and the comparison with a theoretical finite-temperature approach that explicitly takes the van der Waals interaction into account. Our findings are of importance for the precise determination of Efimov resonance positions from experiments at finite temperatures.

[†] The author of the present thesis maintained the experiment, designed and performed the measurements and analyzed the data. L.A.S. contributed in data processing. R.G. guided the analysis and interpretation of the results.

9.1 Introduction

Few-body quantum physics with ultracold atoms has emerged as a new research field, connecting basic concepts from nuclear, molecular, and atomic physics [Bra06, Fer10a, Wan13]. The paradigm of the field is Efimov's prediction of universal three-body states [Efi70]. Efimov showed that, when two bosons interact with an infinite scattering length, the corresponding three-particle system has an infinite number of three-body states just below threshold. Signatures of Efimov states were first observed in an ultracold gas of cesium atoms [Kra06], and have since been found in many other ultracold systems, including other bosonic gases [Zac09, Pol09, Gro09, Gro10, Wil12, Roy13], three-component fermionic spin mixtures [Ott08, Huc09, Wil09, Nak10], and mixtures of atomic species [Bar09, Blo13, Pir14, Tun14]. Very recently, the existence of an Efimov state has also been confirmed for helium atoms in a molecular beam [Kun15]. Moreover, extensions of the Efimov scenario to universal states of larger clusters [Ham07b, von09, von10] have been demonstrated in experiments [Fer09, Pol09, Zen13], highlighting the general nature of universal few-body physics.

The universal regime of few-body physics is realized when the s -wave scattering length a is well separated from all other length scales of the problem. This means that a has to be large compared with the relevant range of the two-body interaction potential, but small compared with the thermal de Broglie wavelength of the sample. Thus, the conceptually most simple case is the idealized scenario of a zero-range two-body interaction in a zero-temperature ensemble. This case, which has been widely discussed in the literature, is commonly referred to as the "universal limit" of few-body physics, where all observables are uniquely connected by fixed relations [Bra06, Wan13]. Many experiments have focused on tests of these universal relations, concerning the famous Efimov period [Zac09, Pol09, Dyk13, Hua14b], the relation between features at positive and negative scattering lengths [Kra06, Kno09, Zac09, Zen14], and the relation between three-body and N -body resonances [Fer09, Pol09, Zen13]. Some of the experiments [Kno09, Dyk13, Hua14b, Zen14] have revealed deviations from perfect universality, which challenge our understanding of the intricate connections between the idealized few-body scenario and systems that exist in the real world.

Efimov resonances in three-body loss [Fer11] represent the main observables in few-body physics with ultracold atoms. They mark the points where the three-atom states cross the dissociation threshold. The finite temperature of the ensemble shifts those resonances as the Efimov state then couples to the scattering continuum, and the feature turns into a triatomic continuum resonance [Bri04]. The limitations by unitarity [D'I04, Rem13, Fle13] lead to a saturation of the maximum resonance amplitude, and the resulting effect is a blurring with a loss of visibility [Jon06, Mas08, Wan14]. Nevertheless, even when an experimental observation is strongly influenced by the finite temperature, an appropriate theoretical model allows one to extract the zero-temperature position of an Efimov resonance. Knowledge of this position also determines the three-body parameter (3BP) [Bra06, Wan13], which fixes the ladder of Efimov states.

In our recent work on cesium [Hua14b], we have observed and analyzed an *excited-state* Efimov resonance. Such higher-order resonances are, under realistic experimental conditions, always strongly influenced by the temperature. We have employed the theoretical model of

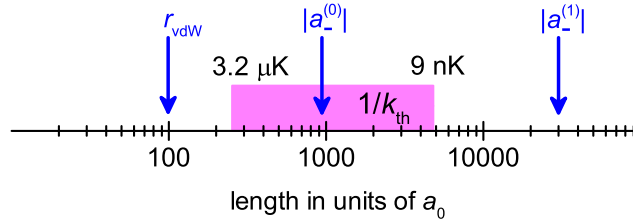


Figure 9.1: (Color online) Length scales involved in experiments on Efimov states in ultracold cesium gases. The parameters $a_-^{(0)}$ and $a_-^{(1)}$ denote the zero-temperature positions of the resonances associated with the Efimov ground state and the first excited state, respectively. The shortest length scale is the van der Waals length r_{vdW} . The temperature is described by the corresponding length $1/k_{\text{th}}$ (see text). The shaded region indicates the temperature range explored in our Cs experiments, which extends from 9 nK to 3.2 μK , corresponding to $1/k_{\text{th}}$ from $4800 a_0$ to $250 a_0$.

Ref. [Rem13] to extract the resonance position for the zero-temperature limit. The theoretical approach is based on an S -matrix formalism and provides a non-perturbative solution for any temperature under the basic assumption of a two-body interaction with a zero range. We thus refer to it as the universal zero-range (UZR) model. An extension of the theory has been applied in Ref. [Hua14a] to analyze observations of an excited-state Efimov resonance in the three-fermion system of ${}^6\text{Li}$ [Wil09]. A further extension has been presented in Ref. [Pet15] for mass-imbalanced three-body systems, which are in the focus of current experimental work [Pir14, Tun14, Ulm15].

In this Article, we investigate a *ground-state* Efimov resonance in cesium over a wide temperature range. Our measurements cover conditions from a near-ideal realization of the zero-temperature limit to a strongly temperature-dominated regime. The experimental results are analyzed within the framework of the UZR theory. This reveals a temperature-dependent resonance shift that corresponds to a variation of the 3BP with the collision energy. For a real atomic system, we introduce the length that is associated with the van der Waals attraction and characterize the shift in an empirical way based on length scale arguments. This improves the accuracy of the determination of the zero-temperature resonance position (and thus of the 3BP in the zero-energy limit) from experimental data. In Sec. 9.2, we discuss different finite-temperature regimes relevant for the experiments in Cs. In Sec. 9.3, we present our experimental results together with an analysis based on the UZR model. In Sec. 9.4, we discuss our findings in view of previous and future experiments in the field.

9.2 Finite-temperature regimes

Different regimes in experiments on Efimov states can be discussed in terms of length scales. Figure 9.1 illustrates the situation for the Cs atom. The shortest relevant length scale is the van der Waals length $r_{\text{vdW}} = \frac{1}{2}(mC_6/\hbar^2)^{1/4}$ [Chi10], where m is the atomic mass and C_6 is the van der Waals coefficient. This length quantifies the long-range part of the two-body interatomic potential, and for Cs $r_{\text{vdW}} = 101.1 a_0$ with a_0 denoting Bohr's radius. The Efimov ground-state is characterized by the parameter $a_-^{(0)}$, which specifies the scattering length at which an Efimov state crosses the dissociation threshold. This parameter, which

corresponds to the 3BP in the zero-energy limit, also characterizes the typical size of the Efimov ground state. Recent work has revealed a new kind of ‘3BP universality’ [Ber11b, Wan12, Sch12, Sør12, Nai14a, Wan14], which is specific to atomic systems and links this parameter to the van der Waals length by $a_-^{(0)} \approx -9.5 r_{\text{vdW}}$. The first excited Efimov state is characterized by the analogously defined resonance position $a_-^{(1)} \approx 22.7 a_-^{(0)}$.

To tune the scattering length in Cs, a broad Feshbach resonance near 800 G serves as an excellent tool [Ber11b, Ber13]. This resonance represents the most extreme case of an entrance-channel dominated resonance [Chi10] that is known for any species. Here the scattering problem can be described in terms of an effective single-channel model, neglecting the intrinsic two-channel nature of a Feshbach resonance. For this resonance, the length parameters $a_-^{(0)} = -963(11) a_0$ and $a_-^{(1)} = -20190(1200) a_0$ have been determined [Hua14b], corresponding to an Efimov period of $a_-^{(1)}/a_-^{(0)} = 21.0(1.3)$. The first observation of an Efimov resonance in Cs [Kra06] was made at low magnetic fields near 7.5 G, where a Feshbach resonance of similar character exists. Here $a_-^{(0)} = -872(22) a_0$ was found, which is very close to the observation on the high-field resonance.

We now introduce the thermal length scale $1/k_{\text{th}}$, where $k_{\text{th}} = \sqrt{2\pi m k_B T}/\hbar$ is the thermal de Broglie wavenumber. Experiments on Cs have been carried in a temperature range between 9 nK [Hua14b] and $3.2 \mu\text{K}$. For the lowest temperature, $T = 9 \text{ nK}$, the length $1/k_{\text{th}} = 4800 a_0$ is right between $|a_-^{(0)}|$ and $|a_-^{(1)}|$. This means that the ground-state Efimov resonance will show very little temperature effects since the dimensionless parameter $k_{\text{th}}|a_-^{(0)}| = 0.26$ is quite small, which indeed was the case in the experiments reported in Refs. [Kra06, Ber11b]. In contrast, the excited-state Efimov resonance will be strongly dominated by finite-temperature effects since $k_{\text{th}}|a_-^{(1)}| \approx 4$ is rather large, which was the case in the experiments of Ref. [Hua14b]. In an intermediate experimental temperature regime, with $T \approx 220 \text{ nK}$ one obtains $k_{\text{th}}|a_-^{(0)}| \approx 1$, which means that also the ground-state Efimov resonance will be subject to substantial temperature effects. This intermediate regime was already investigated in Ref. [Kra06].

At the highest experimental temperatures of $3.2 \mu\text{K}$ (this work) we realize $k_{\text{th}}|a_-^{(0)}| \approx 4$, so that strongly temperature-dominated behavior of the ground-state resonance can be expected, quite similar to the excited-state Efimov resonance at 9 nK. However, in this regime, an additional complication arises as even the smallest dimensionless parameter in the problem, $k_{\text{th}}r_{\text{vdW}}$, is no longer small. This suggests the appearance of a combined effect of finite temperature and finite range.

9.3 Experiments

In this Section, we present our experimental results for the temperature dependence of the ground-state Efimov resonance that appears in Cs near a magnetic field of 853 G [Ber11b]. For an accurate conversion of the magnetic field to the scattering length we employ the model of Ref. [Ber13]. In Sec. 9.3.1, we describe our experimental methods. In Sec. 9.3.2, we present

detailed measurements of the three-body loss rate coefficient L_3 , which are then compared and analyzed with the UZR model. In Sec. 9.3.3, we present an empirical description of a small temperature-dependent shift of the resonance position as determined within the UZR approach.

9.3.1 Experimental procedures

Our experimental setup and the procedures for preparing an ultracold cesium sample are similar to the ones reported in Refs. [Ber11b, Ber13]. Here we use a single laser beam instead of two crossed laser beams to form an optical dipole trap, which contains the atoms in the lowest hyperfine and Zeeman sublevel $|F = 3, m_F = 3\rangle$. The near-infrared trapping beam with a waist of $40 \mu\text{m}$ is provided by a fiber laser at a wavelength of 1064 nm . Along the axial direction the trapping potential is mainly provided by the curvature of the magnetic field. A magnetic levitation gradient of $\sim 31 \text{ G/cm}$ is applied to compensate the gravitational force. To prepare atoms at various temperatures, we vary the trap depth at which the evaporation is stopped. An increase in trap depth of typically 50% is applied adiabatically at the end of the evaporation to avoid unwanted evaporative losses during the hold time. By varying the final power of the trapping light between 1.2 and 260 mW , we can set the temperature in a range between about 30 nK and $3 \mu\text{K}$. For the shallowest trap, the trap frequencies are $2\pi \times [19.0(2), 20.8(7), 1.46(1)] \text{ Hz}$, where the last one is the axial frequency. For the deepest trap, the trap frequencies are $2\pi \times [296(1), 359(3), 2.21(2)] \text{ Hz}$. Correspondingly, the geometric mean frequency $\bar{\omega}/2\pi$ varies between $8.3(1) \text{ Hz}$ and $61.7(3) \text{ Hz}$. The typical atom numbers after the preparation procedure are about 5×10^4 for our lowest T and 1.5×10^6 for our highest T .

The three-body recombination rate coefficient L_3 is obtained from the decay curves of the atoms hold in the dipole trap. The maximum hold time is chosen to provide a typical loss of 30%, and thus varies between 1 and 7 s. Because of anti-evaporation [Web03c], the temperature T of the gas increases by about 10% during the decay process. The corresponding time evolution of T needs to be taken into account to extract accurate values for L_3 . We perform time-of-flight absorption imaging at the end of the hold period to obtain the remaining atom number N and the temperature T at each t . For each setting of the magnetic field, both N and T are recorded as functions of the variable hold time t .

To obtain the values for the loss-rate coefficient L_3 , we model the atomic number evolution by the differential equation $\dot{N}/N = -3^{-3/2}L_3(N/V)^2$, where $V = (2\pi k_B T/m\bar{\omega}^2)^{3/2}$ is the time-dependent effective volume. The differential equation is solved with the same method as used in Ref. [Hua14b]. We numerically integrate the equation and fit it to the observed atom number evolution while leaving L_3 and the initial atom number N_0 as free parameters. Since our model neglects the effect of the small temperature increase on L_3 , the results represent temperature-averaged values. We treat them as the L_3 values at the mean temperature. For the roughly 10% temperature increase the resulting errors are small and we consider them as part of the uncertainties of T .

9.3.2 Experimental results and fit analysis

An overview of all our experimental results on the temperature dependence of the ground-state Efimov resonance in the high-field region is presented in Fig. 9.2. The measured values of L_3 are shown as a function of the inverse scattering length $1/a$ for temperatures between 15 nK and 3.2 μ K. While panel (a) shows the results at our lowest temperature from Ref. [Ber11b], panel (b) shows five new sets of measurements at higher temperatures. Our measurements clearly show that, with increasing temperature, the amplitude of the resonance decreases and the loss maximum shifts towards smaller values of $|a|$.

We now compare our experimental results with the temperature dependence according to the UZR model. The model has two free parameters, the zero-temperature position a_- of the Efimov resonance and the dimensionless quantity η_* , which characterizes its width. For fitting the predictions of the model to the experimental data, we follow the strategies of our previous work [Ber11b, Hua14b], introducing an additional amplitude scaling factor λ to account for systematic errors in the determination of the atomic number density. To account for the uncertainties in our measurements of the temperature, i.e. deviations of the relevant temperature T from the observed temperature T_{obs} , we can alternatively use T as a free fit parameter [Hua14b]. In this case, the amplitude scaling factor is not a free parameter any more, but it is determined as $\lambda = (T_{\text{obs}}/T)^3$. A comparison between the results from the two fit methods provides information on model-dependent errors.

We follow two different strategies to compare the UZR model to our experimental data. In the first case, we fit the data set at our lowest temperature (15 nK), which is a near-ideal representation of the $T = 0$ limit, to extract the resonance position or 3BP a_- (for simplicity of our notation $a_- \equiv a_-^{(0)}$) and the two other parameters η_* and λ . In this fit we only take into account the experimental points for $|a| > 600a_0$ to avoid the influence of a four-body resonance [Fer09], the effect of which is clearly visible in Fig. 9.2(a). With these parameters, we then apply the UZR model to predict the corresponding L_3 curves for the five higher temperatures under the assumption that the 3BP is unchanged. These predictions, which are represented by the solid lines in Fig. 9.2(b), show a reasonable agreement with the experimental data. They reproduce the observed decrease of the resonant value of L_3 over more than three decades and they show a similar temperature shift of the maximum. A closer inspection, however, reveals significant deviations, in particular in the position of the loss maximum.

Our second strategy is to fit all curves independently and to extract the corresponding sets of three parameters for all different temperatures separately. For the resonance position extracted in this way we use the notation a_-^{UZR} to emphasize the difference between this fit parameter of the UZR model and the true zero-temperature resonance position a_- . Indeed, our results in Fig. 9.3(a) show a clear systematic change in a_-^{UZR} emerging with increasing temperature. The values obtained for η_* in (b) show relatively large uncertainties. While for lower temperatures up to about 300 nK we do not observe any significant trend, the data points at the highest two temperatures indicate a decrease of η_* with temperature. Finally, in (c) the amplitude scaling parameter λ also does not show any significant trend up to about 300 nK. For the highest two temperatures, however, a clear increase is observed. This

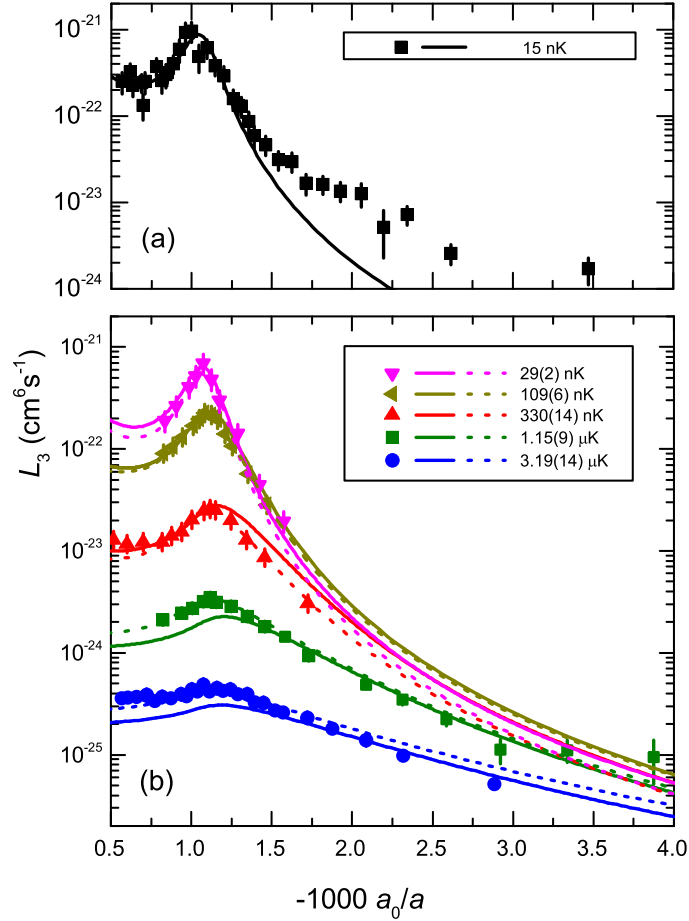


Figure 9.2: (Color online) Three-body recombination rate coefficient L_3 as a function of the inverse scattering length $1/a$ at finite temperatures, measured for the ground-state Efimov resonance. Panel (a) shows the measurements at 15 nK (filled black squares) from Ref. [Ber11b] and the updated fit (solid black line) from Ref. [Hua14b]. In panel (b), five new sets of measurements taken at different temperatures in a range between 29 nK and 3.2 μ K are presented. The solid lines show the corresponding predictions from the UZR model using the resonance position and width that results from the fit to the 15 nK data in (a). The dashed lines result from individual fits based on the UZR model. The error bars show the 1σ statistic fit uncertainties.

appears to be rather unphysical as it is too big to be explained by our uncertainties in the atom number calibration or the temperature.

9.3.3 Empirical characterization of the resonance shift

The observed temperature dependence of the fit parameter a_-^{uzr} can be discussed within the UZR approach as a dependence of the 3BP on the collision energy. From a different perspective, the effect may be interpreted as a consequence of the finite interaction range in real atomic systems. These two interpretations are naturally connected, since in our system the 3BP is essentially determined by the finite range of the van der Waals potential [Ber11b, Wan12, Sch12, Sør12, Nai14a, Wan14].

To characterize the effect we follow the length scale arguments outlined in Sec. 9.2 and introduce the dimensionless parameter $k_{\text{th}}r_{\text{vdW}}$. For the temperatures investigated, this quantity varies between 0.02 (at 15 nK) and 0.36 (at 3.2 μK). We now quantify the resonance shift in an empirical way using the linear expansion

$$a_-^{\text{uzr}}/a_- = 1 + c \times k_{\text{th}}r_{\text{vdW}}. \quad (9.1)$$

Figure 9.4 shows our results for a_-^{uzr} plotted as a function of $k_{\text{th}}r_{\text{vdW}}$. For the four lowest temperatures with $k_{\text{th}}r_{\text{vdW}} \lesssim 0.15$ ($T \lesssim 330$ nK) the data points are fully consistent with a linear behavior. Only for the largest two temperatures, we observe significant deviations from the linear behavior. For these two points also the two other fit parameters η_* and λ show substantial deviations from the behavior in the low-temperature limit, so that there is good reason to restrict our further analysis to the four lowest temperatures.

By fitting a straight line according to Eq. (9.1) to the data points for $k_{\text{th}}r_{\text{vdW}} < 0.15$ (solid line in Fig. 9.4), we extract the coefficient $c = 0.60(3)$ and the zero-temperature resonance position $a_- = -943(2)a_0$. This new value for a_- , obtained as an extrapolation to $T = 0$, slightly deviates from the value obtained previously [Hua14b] from analyzing only the set of measurements at 15 nK.

9.4 Discussion

The question remains to what extent we can consider the resonance shift according to Eq. (9.1) as universal. On the experimental side, this can in principle be tested by comparing it with observations on different Feshbach resonances in the same system or with other systems. On the theoretical side, the UZR model can be compared with other finite-temperature approaches that do not rely on the zero-range approximation. Here we analyze the additional pieces of information that are available on resonances in Cs and ${}^6\text{Li}$ and discuss the consequences of our work in view of previous and future experiments on Efimov resonances.

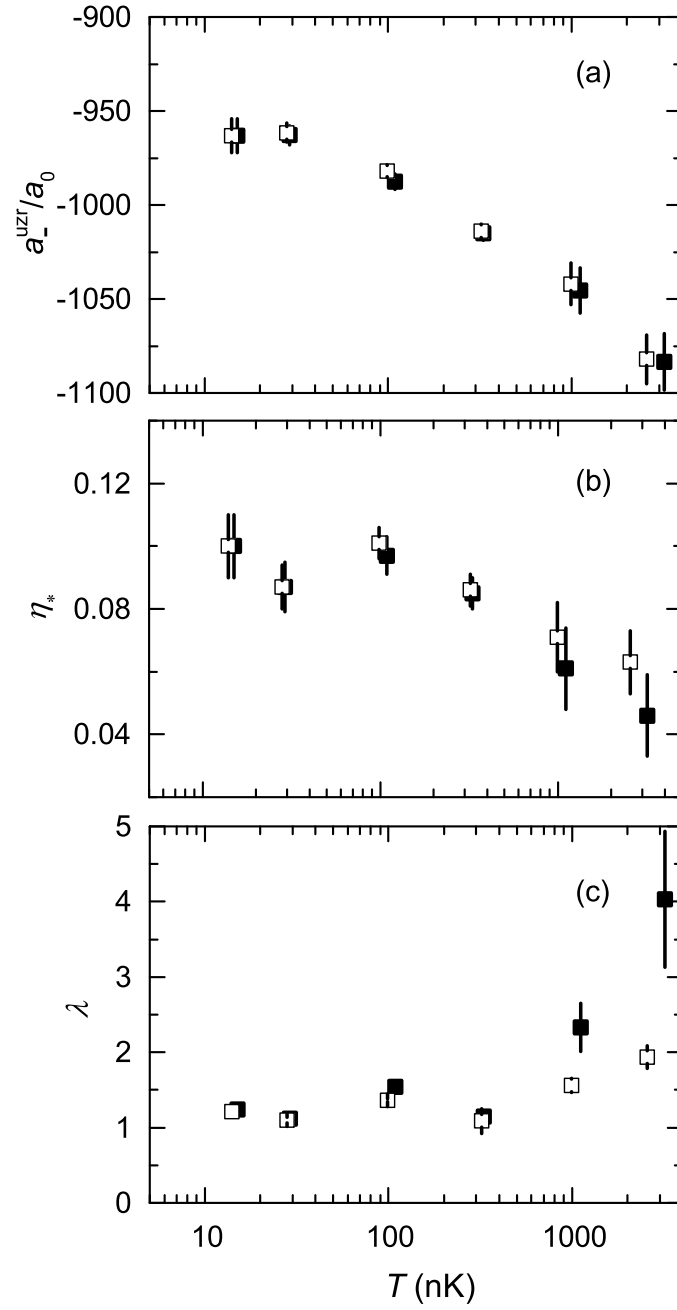


Figure 9.3: Fit results for the UZR model applied to the experimental data of Fig. 9.2. Panels (a), (b), and (c) show a_{-}^{uzr} , η_* , and λ for the six different experimentally realized temperatures. The filled (open) squares refer to the fitting method with T being fixed (free); see text. The error bars represent the 1σ statistic fit uncertainties.

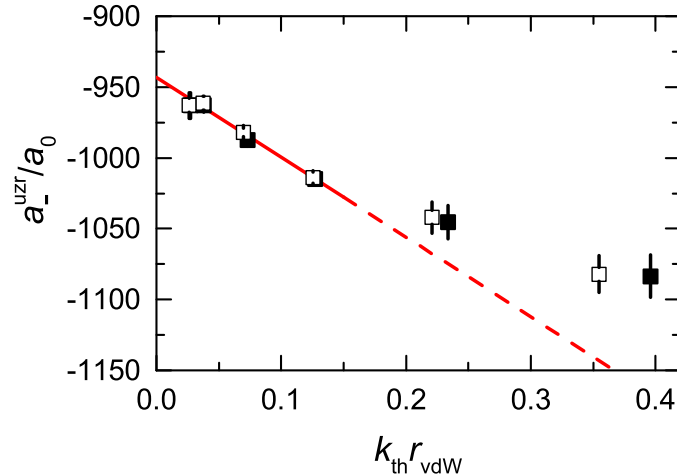


Figure 9.4: (Color online) The resonance position parameter a_{-}^{uzr} from the UZR model fit as a function of the dimensionless quantity $k_{th}r_{vdW}$. The experimental data points are identical to the black squares in the panel (a) of Fig. 9.3. For the four lowest temperatures the data points are fitted by a straight line (solid red). The dashed line is an extrapolation to higher temperatures. The error bars show the 1σ statistic errors from fits.

9.4.1 Ground-state Efimov resonance of Cs in the low-field region

In our early experiments on Efimov physics [Kra06], we investigated Cs in the region of low magnetic fields, where a Feshbach resonance with very similar character as in the high-field case is available. This resonance is also strongly entrance-channel dominated, but less extremely than the high-field resonance. The main set of measurements in Ref. [Kra06] was taken at a temperature of 10 nK, and two further sets were recorded at 200 nK and 250 nK. For the present purpose we have analyzed the original L_3 data in the same way as described above. The results for the resonance position parameter a_{-}^{uzr} are shown by the triangles in Fig. 9.5. Only a few data points are available with relatively large uncertainties, but they nevertheless show a clear temperature shift. We can extract a corresponding coefficient $c = 0.48(15)$, consistent with our findings for the high-field resonance. However, the few data points do not permit a test of the linearity with respect to k_{th} .

Wang and Julienne [Wan14] have analyzed the situation at the low-field Feshbach resonance with a theoretical model that takes into account the van der Waals interaction and the parameters of the Feshbach resonance. The predictions of the model were found in excellent agreement with the experimental results of Ref. [Kra06]. We have analyzed six sets of theoretical predictions produced with this model¹ for the L_3 coefficient in the same way as we did for the experiments. The results for a_{-}^{uzr} are shown by the round symbols in Fig. 9.5. The comparison of these theoretical results with the experimental results shown in Fig. 9.4 reveals a striking similarity. We find an essentially linear behavior in the range $k_{th}r_{vdW} < 0.15$ and by fitting a straight line (solid line) we obtain a coefficient $c = 0.55(6)$, which is fully consistent with the experimental result for the Efimov resonance in the high-field region.

¹ Y. Wang and P. S. Julienne, private communication (2014).

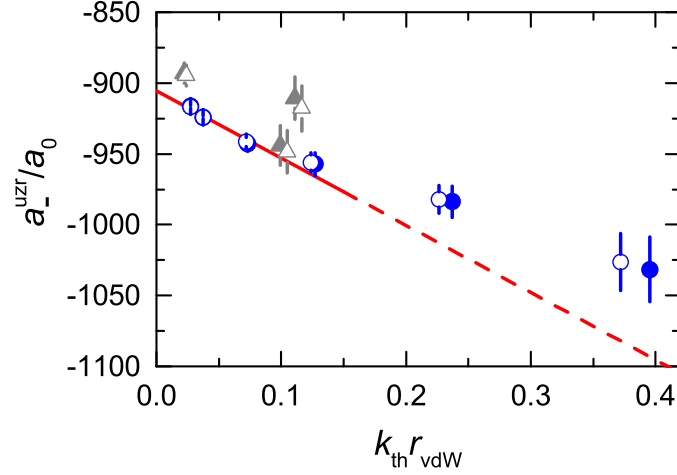


Figure 9.5: (Color online) Analysis of the ground-state Efimov resonance in Cs at low magnetic field. The parameter a_{-}^{uzr} resulting from the UZR fit is shown as a function of the dimensionless quantity $k_{\text{th}}r_{\text{vdW}}$. The triangles refer to the experimental results of Ref. [Kra06]. The circles represent the data from the numerical model of Ref. [Wan14], and the straight line corresponds to a linear fit for $k_{\text{th}}r_{\text{vdW}} < 0.15$. The filled (open) symbols refer to fits with fixed T (free T) and the error bars show the 1σ fit uncertainties. Note the striking similarity with Fig. 9.4.

This comparison suggests that the Efimov resonance in the low-field region behaves in essentially the same way as in the high-field region. The resonance shift seems to be universal, at least for different Feshbach resonances of the same character in the same atomic system.

9.4.2 Excited-state Efimov resonance in ${}^6\text{Li}$

Another interesting case for which temperature-dependent experimental data are available is the excited-state Efimov resonance in ${}^6\text{Li}$. The observation [Wil09] was made in a three-component spin mixture in a scenario of three overlapping Feshbach resonances, all of them with strongly entrance-channel dominated character. The results were reanalyzed in Ref. [Hua14a] based on the UZR theory. For the very large length scale of an excited Efimov state, finite-range corrections can be expected to be very small. Indeed, the measurements at two different temperatures ($T = 30$ nK corresponding to $k_{\text{th}}r_{\text{vdW}} = 0.0025$ and $T = 180$ nK corresponding to $k_{\text{th}}r_{\text{vdW}} = 0.0062$) do not reveal any significant difference.

A straightforward ansatz to generalize Eq. (9.1) to higher-order Efimov resonances reads

$$a_{-}^{(n); \text{uzr}}/a_{-}^{(n)} = 1 + c^{(n)} \times k_{\text{th}}r_{\text{vdW}}, \quad (9.2)$$

where $a_{-}^{(n); \text{uzr}}$ denotes the resonance position obtained by the UZR fit for finite temperatures. Our analysis of the excited-state resonance in ${}^6\text{Li}$ yields a coefficient $c^{(1)} = 1.6(5.8)$, which within a large uncertainty is consistent with zero. The most simple assumption would be a constant coefficient $c^{(n)} = c$, independent of the resonance order. Within this assumption, the ${}^6\text{Li}$ result would be consistent with $c = 0.60(3)$ as we have obtained for the Cs ground-state resonance case. In general $c^{(n)}$ can be a function of the dimensionless parameter

$r_{\text{vdW}}/a^{(n)}$, but because of the very large uncertainty our analysis does not provide any further information on that.

The results on the ${}^6\text{Li}$ excited-state resonance are nevertheless very instructive as they provide a test of an alternative explanation for the observed deviations. Let us assume that there is a systematic problem with the UZR theory and the temperature-dependent shift is unrelated to the finite interaction range. In this case r_{vdW} would not be a relevant quantity and the problem would perfectly follow the discrete scale invariance of the Efimov problem. Then the only way to express the relative shift would be

$$a_{-}^{(n); \text{uzr}}/a_{-}^{(n)} = 1 + \tilde{c} \times k_{\text{th}}|a^{(n)}|. \quad (9.3)$$

Here the relative shift of ground-state and excited-state Efimov resonances would be the same if $k_{\text{th}}|a^{(n)}|$ is kept constant. Following this ansatz to analyze the data, we obtain $\tilde{c} = 0.063(3)$ for the Cs ground-state Efimov resonance and $\tilde{c} = 0.010(35)$ for the ${}^6\text{Li}$ excited-state resonance. These two results are inconsistent with 90% confidence, which supports our hypothesis of a finite-range effect instead of a systematic problem in the UZR theory.

9.4.3 Efimov period in Cs revisited

A main result of Ref. [Hua14b] is the determination of the Efimov period as the ratio $a_{-}^{(1)}/a_{-}^{(0)} = 21.0(1.3)$, where we applied the UZR theory to both the ground-state and the excited-state Efimov resonance. The present result suggests small corrections to the positions of both resonances. From the zero-temperature extrapolation of Sec. 9.3.3 we obtain the updated value $a_{-}^{(0)} = -943(2) a_0$, and Eq. (9.2) with the assumption $c^{(1)} = c = 0.6$ yields the slightly corrected value $a_{-}^{(1)} = -19930(1200) a_0$. In this case, the updated result for the Efimov period would be $a_{-}^{(1)}/a_{-}^{(0)} = 21.1(1.3)$. If we take the updated value for $a_{-}^{(0)}$, but assume there is no correction to $a_{-}^{(1)}$, we obtain an Efimov period of 21.4(1.3). The differences to the previous result are well within the error bar, so that the conclusions of Ref. [Hua14b] remain unchanged.

9.4.4 Open questions

The considerations in Secs. 9.4.1 and 9.4.2 provide some support for a universal character of the temperature-dependent shift of the resonance position, when the UZR theory is applied to real atomic systems with a small, but finite interaction range. The generalization from the ground-state Efimov resonance to excited-state resonances according to Eq. (9.2) raises the question on the connection between the coefficients $c^{(n)}$ for Efimov resonances of different order. Another open problem is the situation of closed-channel dominated Feshbach resonances [Roy13], where the two-channel nature implies an additional length scale [Pet04] larger than the van der Waals length. Also the role of finite-range effects related to Efimov states near Feshbach resonances of intermediate character [Zac09, Dyk13, Gro09] needs further investigations. Finally we note that in the high-temperature regime where $k_{\text{th}}r_{\text{vdW}}$ is

no longer a small quantity, higher partial waves may substantially contribute to three-body recombination [Wer06, D'I09] and lead to non-universal behavior.

9.5 Conclusion

We have investigated the temperature dependence of three-body recombination near a ground-state triatomic Efimov resonance in cesium. Our measurements of the recombination rate coefficient extend from conditions near the zero-temperature limit to a strongly temperature-dominated regime, thus characterizing the temperature-induced resonance shift in a wide range. The two-body interactions are controlled via a broad Feshbach resonance, the character of which is strongly entrance-channel dominated.

To determine the precise zero-temperature Efimov resonance position from the finite-temperature experimental data, we have employed the universal zero-range finite-temperature theory of Refs. [Rem13, Pet15], following our earlier investigations in Refs. [Hua14b, Hua14a]. The present results reveal a small shift, which increases linearly with the thermal wavenumber, i.e. proportionally to the square root of the temperature. We attribute this effect to the finite range of the two-body interaction, which in our case is determined by the van der Waals attraction.

A comparison with other available experimental results and a theoretical approach that explicitly takes into account the van der Waals interaction [Wan14] suggests a universal character of the shift, at least for entrance-channel dominated Feshbach resonances. More work is required to understand the physics of the shift, its effect on excited-state Efimov resonances, and its implications for the precise determination of Efimov resonance positions in other systems.

Acknowledgments

We thank Dmitry Petrov for stimulating discussions, for critical remarks on the manuscript, and for providing the source code for the UZR model. We are indebted to Yujun Wang and Paul Julienne for providing temperature-dependent predictions based on their theoretical model. We furthermore thank Martin Berninger, Alessandro Zenesini and Jesper Levinsen for fruitful discussions. We acknowledge support by the Austrian Science Fund FWF within project P23106.

Bibliography

- [Adh81] S. K. Adhikari and A. C. Fonseca, *Four-body Efimov effect in a Born-Oppenheimer model*, Phys. Rev. D **24**, 416 (1981).
- [Aki91] H. Akima, *A method of univariate interpolation that has the accuracy of a third-degree polynomial*, ACM Trans. Math. Softw. **17**, 341 (1991).
- [Alb76] D. L. Albritton, A. L. Schmeltekopf, and R. Zare, *An introduction to the least-squares fitting of spectroscopic data*, Molecular Spectroscopy: Modern Research, Vol. II (K. N. Rao, ed.), Academic Press, 1976.
- [Ale84] M. H. Alexander, *Hybrid quantum scattering algorithms for long-range potentials*, J. Chem. Phys. **81**, 4510 (1984).
- [Ale87] M. H. Alexander and D. E. Manolopoulos, *A stable linear reference potential algorithm for solution of the quantum close-coupled equations in molecular scattering theory*, J. Comput. Phys. **86**, 2044 (1987).
- [Ama73] R. D. Amado and F. C. Greenwood, *There is no Efimov effect for four or more particles*, Phys. Rev. D **7**, 2517 (1973).
- [And04] J. O. Andersen, *Theory of the weakly interacting Bose gas*, Rev. Mod. Phys. **76**, 599 (2004).
- [Arl98] J. Arlt, P. Bance, S. Hopkins, J. Martin, S. Webster, A. Wilson, K. Zetie, and C. J. Foot, *Suppression of collisional loss from a magnetic trap*, J. Phys. B **31**, L321 (1998).
- [Axi43] B. M. Axilrod and E. Teller, *Interaction of the van der Waals type between three atoms*, J. Chem. Phys. **11**, 299 (1943).
- [Bar05] M. Bartenstein, A. Altmeyer, S. Riedl, R. Geursen, S. Jochim, C. Chin, J. Hecker Denschlag, R. Grimm, A. Simoni, E. Tiesinga, C. J. Williams, and P. S. Julienne, *Precise determination of ^6Li cold collision parameters by radio-frequency spectroscopy on weakly bound molecules*, Phys. Rev. Lett. **94**, 103201 (2005).
- [Bar09] G. Barontini, C. Weber, F. Rabatti, J. Catani, G. Thalhammer, M. Inguscio, and F. Minardi, *Observation of heteronuclear atomic Efimov resonances*, Phys. Rev. Lett. **103**, 043201 (2009).

- [Bea10] Q. Beaufils, A. Crubellier, T. Zanon, B. Laburthe-Tolra, É. Maréchal, L. Vernac, and O. Gorceix, *Radio-frequency association of molecules: an assisted Feshbach resonance*, Eur. Phys. J. D **56**, 99 (2010).
- [Bed99] P. Bedaque, H.-W. Hammer, and U. van Kolck, *Renormalization of the three-body system with short-range interactions*, Phys. Rev. Lett. **82**, 463 (1999).
- [Bed00] P. F. Bedaque, E. Braaten, and H.-W. Hammer, *Three-body recombination in Bose gases with large scattering length*, Phys. Rev. Lett. **85**, 908 (2000).
- [Ber66] M. V. Berry, *Semi-classical scattering phase shifts in the presence of metastable states*, Proceedings of the Physical Society **88**, 285 (1966).
- [Ber11a] M. Berninger, *Universal three- and four-body phenomena in an ultracold gas of cesium atoms*, Ph.D. thesis, University of Innsbruck (2011).
- [Ber11b] M. Berninger, A. Zenesini, B. Huang, W. Harm, H.-C. Nägerl, F. Ferlaino, R. Grimm, P. S. Julienne, and J. M. Hutson, *Universality of the three-body parameter for Efimov states in ultracold cesium*, Phys. Rev. Lett. **107**, 120401 (2011).
- [Ber13] M. Berninger, A. Zenesini, B. Huang, W. Harm, H.-C. Nägerl, F. Ferlaino, R. Grimm, P. S. Julienne, and J. M. Hutson, *Feshbach resonances, weakly bound molecular states, and coupled-channel potentials for cesium at high magnetic fields*, Phys. Rev. A **87**, 032517 (2013).
- [Bet35a] H. Bethe and R. Peierls, *Quantum theory of the dipion*, Proc. Roy. Soc. A **148**, 146 (1935).
- [Bet35b] H. Bethe and R. Peierls, *The scattering of neutrons by protons*, Proc. Roy. Soc. A **149**, 176 (1935).
- [Bet49] H. A. Bethe, *Theory of the effective range in nuclear scattering*, Phys. Rev. **76**, 38 (1949).
- [Bla14] C. L. Blackley, P. S. Julienne, and J. M. Hutson, *Effective-range approximations for resonant scattering of cold atoms*, Phys. Rev. A **89**, 042701 (2014).
- [Blo13] R. S. Bloom, M.-G. Hu, T. D. Cumby, and D. S. Jin, *Tests of universal three-body physics in an ultracold Bose-Fermi mixture*, Phys. Rev. Lett. **111**, 105301 (2013).
- [Blu00] D. Blume and C. H. Greene, *Monte Carlo hyperspherical description of helium cluster excited states*, J. Chem. Phys. **112**, 8053 (2000).
- [Blu02] D. Blume, B. D. Esry, C. H. Greene, N. N. Klausen, and G. J. Hanna, *Formation of atomic tritium clusters and Bose-Einstein condensates*, Phys. Rev. Lett. **89**, 163402 (2002).

- [Boh98] J. L. Bohn, B. D. Esry, and C. H. Greene, *Effective potentials for dilute Bose-Einstein condensates*, Phys. Rev. A **58**, 584 (1998).
- [Bra01] E. Braaten and H.-W. Hammer, *Three-body recombination into deep bound states in a Bose gas with large scattering length*, Phys. Rev. Lett. **87**, 160407 (2001).
- [Bra06] E. Braaten and H.-W. Hammer, *Universality in few-body systems with large scattering length*, Phys. Rep. **428**, 259 (2006).
- [Bra07] E. Braaten and H.-W. Hammer, *Resonant dimer relaxation in cold atoms with a large scattering length*, Phys. Rev. A **75**, 052710 (2007).
- [Bra08] E. Braaten, H.-W. Hammer, D. Kang, and L. Platter, *Three-body recombination of identical bosons with a large positive scattering length at nonzero temperature*, Phys. Rev. A **78**, 043605 (2008).
- [Bra09a] E. Braaten and H.-W. Hammer, *Erratum: Resonant dimer relaxation in cold atoms with a large scattering length [phys. rev. a 75, 052710 (2007)]*, Phys. Rev. A **79**, 039905(E) (2009).
- [Bra09b] E. Braaten, H.-W. Hammer, D. Kang, and L. Platter, *Three-body recombination of ${}^6\text{Li}$ atoms with large negative scattering lengths*, Phys. Rev. Lett. **103**, 073202 (2009).
- [Bre31] G. Breit and I. I. Rabi, *Measurement of nuclear spin*, Phys. Rev. **38**, 2082 (1931).
- [Bri04] F. Bringas, M. T. Yamashita, and T. Frederico, *Triatomic continuum resonances for large negative scattering lengths*, Phys. Rev. A **69**, 040702 (2004).
- [Brü05] R. Brühl, A. Kalinin, O. Kornilov, J. P. Toennies, G. C. Hegerfeldt, and M. Stoll, *Matter wave diffraction from an inclined transmission grating: Searching for the elusive ${}^4\text{He}$ trimer Efimov state*, Phys. Rev. Lett. **95**, 063002 (2005).
- [Cav99] R. M. Cavalcanti, *Exact Green's functions for delta-function potentials and renormalization in quantum mechanics*, Rev. Bras. Ens. Fis. **21**, 336 (1999).
- [Chi00] C. Chin, V. Vuletić, A. J. Kerman, and S. Chu, *High resolution Feshbach spectroscopy of cesium*, Phys. Rev. Lett. **85**, 2717 (2000).
- [Chi03] C. Chin, A. J. Kerman, V. Vuletić, and S. Chu, *Sensitive detection of cold cesium molecules formed on Feshbach resonances*, Phys. Rev. Lett. **90**, 033201 (2003).
- [Chi04] C. Chin, V. Vuletić, A. J. Kerman, S. Chu, E. Tiesinga, P. J. Leo, and C. J. Williams, *Precision Feshbach spectroscopy of ultracold Cs_2* , Phys. Rev. A **70**, 032701 (2004).

- [Chi05] C. Chin, T. Kraemer, M. Mark, J. Herbig, P. Waldburger, H.-C. Nägerl, and R. Grimm, *Observation of Feshbach-like resonances in collisions between ultracold molecules*, Phys. Rev. Lett. **94**, 123201 (2005).
- [Chi10] C. Chin, R. Grimm, P. S. Julienne, and E. Tiesinga, *Feshbach resonances in ultracold gases*, Rev. Mod. Phys. **82**, 1225 (2010).
- [Chi11] C. Chin, *Universal scaling of Efimov resonance positions in cold atom systems*, arXiv:1111.1484.
- [Dan61] G. S. Danilov, *On the three-body problem with short-range forces*, Sov. Phys. JETP **40**, 498 (1961).
- [Dan08] J. G. Danzl, E. Haller, M. Gustavsson, M. J. Mark, R. Hart, N. Bouloufa, O. Dulieu, H. Ritsch, and H.-C. Nägerl, *Quantum gas of deeply bound ground state molecules*, Science **321**, 1062 (2008).
- [Dan10] J. G. Danzl, M. J. Mark, E. Haller, M. Gustavsson, R. Hart, J. Aldegunde, J. M. Hutson, and H.-C. Nägerl, *An ultracold high-density sample of rovibronic ground-state molecules in an optical lattice*, Nat. Phys. **6**, 265 (2010).
- [Del10] A. Deltuva, *Efimov physics in bosonic atom-trimer scattering*, Phys. Rev. A **82**, 040701 (2010).
- [Del12] A. Deltuva, *Momentum-space calculation of four-boson recombination*, Phys. Rev. A **85**, 012708 (2012).
- [D'I04] J. P. D'Incao, H. Suno, and B. D. Esry, *Limits on universality in ultracold three-boson recombination*, Phys. Rev. Lett. **93**, 123201 (2004).
- [D'I06] J. P. D'Incao and B. D. Esry, *Enhancing the observability of the Efimov effect in ultracold atomic gas mixtures*, Phys. Rev. A **73**, 030703(R) (2006).
- [D'I09] J. P. D'Incao, C. H. Greene, and B. D. Esry, *The short-range three-body phase and other issues impacting the observation of Efimov physics in ultracold quantum gases*, J. Phys. B **42**, 044016 (2009).
- [Dyk13] P. Dyke, S. E. Pollack, and R. G. Hulet, *Finite-range corrections near a Feshbach resonance and their role in the Efimov effect*, Phys. Rev. A **88**, 023625 (2013).
- [Efi70] V. Efimov, *Energy levels arising from resonant two-body forces in a three-body system*, Phys. Lett. B **33**, 563 (1970).
- [Efi79] V. Efimov, *Low-energy properties of three resonantly interacting particles*, Sov. J. Nuc. Phys. **29**, 546 (1979).

- [Esr99] B. D. Esry, C. H. Greene, and J. P. Burke, *Recombination of three atoms in the ultracold limit*, Phys. Rev. Lett. **83**, 1751 (1999).
- [Esr01] B. D. Esry, C. H. Greene, and H. Suno, *Threshold laws for three-body recombination*, Phys. Rev. A **65**, 010705 (2001).
- [Fad60] L. D. Faddeev, *Scattering theory for a three-particle system*, Sov. Phys. JETP **39**, 1459 (1960).
- [Fan61] U. Fano, *Effects of configuration interaction on intensities and phase shifts*, Phys. Rev. **124**, 1866 (1961).
- [Fan76] U. Fano, *Dynamics of electron excitation*, Physics Today **29**, 32 (1976).
- [Fed93] D. V. Fedorov and A. S. Jensen, *Efimov effect in coordinate space Faddeev equations*, Phys. Rev. Lett. **71**, 4103 (1993).
- [Fed96] P. O. Fedichev, M. W. Reynolds, and G. V. Shlyapnikov, *Three-body recombination of ultracold atoms to a weakly bound s level*, Phys. Rev. Lett. **77**, 2921 (1996).
- [Fer08] F. Ferlaino, S. Knoop, M. Mark, M. Berninger, H. Schöbel, H.-C. Nägerl, and R. Grimm, *Collisions between tunable halo dimers: Exploring an elementary four-body process with identical bosons*, Phys. Rev. Lett. **101**, 023201 (2008).
- [Fer09] F. Ferlaino, S. Knoop, M. Berninger, W. Harm, J. P. D’Incao, H.-C. Nägerl, and R. Grimm, *Evidence for universal four-body states tied to an Efimov trimer*, Phys. Rev. Lett. **102**, 140401 (2009).
- [Fer10a] F. Ferlaino and R. Grimm, *Forty years of Efimov physics: How a bizarre prediction turned into a hot topic*, Physics **3**, 9 (2010).
- [Fer10b] F. Ferlaino, S. Knoop, M. Berninger, M. Mark, H.-C. Nägerl, and R. Grimm, *Collisions of ultracold trapped cesium Feshbach molecules*, Laser Phys. **20**, 23 (2010).
- [Fer11] F. Ferlaino, A. Zenesini, M. Berninger, B. Huang, H.-C. Nägerl, and R. Grimm, *Efimov resonances in ultracold quantum gases*, Few-Body Syst. **51**, 113 (2011).
- [Fes58] H. Feshbach, *United theory of nuclear reactions*, Ann. Phys. **5**, 357 (1958).
- [Fes62] H. Feshbach, *United theory of nuclear reactions II*, Ann. Phys. **19**, 287 (1962).
- [Fle13] R. J. Fletcher, A. L. Gaunt, N. Navon, R. P. Smith, and Z. Hadzibabic, *Stability of a unitary Bose gas*, Phys. Rev. Lett. **111**, 125303 (2013).
- [Gao98] B. Gao, *Quantum-defect theory of atomic collisions and molecular vibration spectra*, Phys. Rev. A **58**, 4222 (1998).

- [GM07] M. L. González-Martínez and J. M. Hutson, *Ultracold atom-molecule collisions and bound states in magnetic fields: zero-energy Feshbach resonances in He-NH ($^3\Sigma^-$)*, Phys. Rev. A **75**, 022702 (2007).
- [GO98a] D. Guéry-Odelin, J. Söding, P. Desbiolles, and J. Dalibard, *Is Bose-Einstein condensation of atomic cesium possible?*, Europhys. Lett. **44**, 25 (1998).
- [GO98b] D. Guéry-Odelin, J. Söding, P. Desbiolles, and J. Dalibard, *Strong evaporative cooling of a trapped cesium gas*, Opt. Exp. **2**, 323 (1998).
- [Gog08] A. O. Gogolin, C. Mora, and R. Egger, *Analytical solution of the bosonic three-body problem*, Phys. Rev. Lett. **100**, 140404 (2008).
- [Gre04] C. H. Greene, B. D. Esry, and H. Suno, *A revised formula for 3-body recombination that cannot exceed the unitarity limit*, Nucl. Phys. A **737**, 119 (2004).
- [Gre10] C. H. Greene, *Universal insights from few-body land*, Phys. Today **63(3)**, 40 (2010).
- [Gri93] G. F. Gribakin and V. V. Flambaum, *Calculation of the scattering length in atomic collisions using the semiclassical approximation*, Phys. Rev. A **48**, 546 (1993).
- [Gri00] R. Grimm, M. Weidemüller, and Y. B. Ovchinnikov, *Optical dipole traps for neutral atoms*, Adv. At. Mol. Opt. Phys. **42**, 95 (2000).
- [Gro09] N. Gross, Z. Shotan, S. Kokkelmans, and L. Khaykovich, *Observation of universality in ultracold ^7Li three-body recombination*, Phys. Rev. Lett. **103**, 163202 (2009).
- [Gro10] N. Gross, Z. Shotan, S. Kokkelmans, and L. Khaykovich, *Nuclear-spin-independent short-range three-body physics in ultracold atoms*, Phys. Rev. Lett. **105**, 103203 (2010).
- [Gus08a] M. Gustavsson, E. Haller, M. J. Mark, J. G. Danzl, G. Rojas-Kopeinig, and H.-C. Nägerl, *Control of interaction-induced dephasing of Bloch oscillations*, Phys. Rev. Lett. **100**, 080404 (2008).
- [Gus08b] M. Gustavsson, *A quantum gas with tunable interactions in an optical lattice*, Ph.D. thesis, University of Innsbruck (2008).
- [Ham07a] H.-W. Hammer, T. A. Lähde, and L. Platter, *Effective-range corrections to three-body recombination for atoms with large scattering length*, Phys. Rev. A **75**, 032715 (2007).
- [Ham07b] H.-W. Hammer and L. Platter, *Universal properties of the four-body system with large scattering length*, Eur. Phys. J. A **32**, 113 (2007).

- [Han06] G. J. Hanna and D. Blume, *Energetics and structural properties of three-dimensional bosonic clusters near threshold*, Phys. Rev. A **74**, 063604 (2006).
- [Heg00] G. C. Hegerfeldt and T. Köhler, *How to study the elusive Efimov state of the $^4\text{He}_3$ molecule through a new atom-optical state-selection technique*, Phys. Rev. Lett. **84**, 3215 (2000).
- [Her03] J. Herbig, T. Kraemer, M. Mark, T. Weber, C. Chin, H.-C. Nägerl, and R. Grimm, *Preparation of a pure molecular quantum gas*, Science **301**, 1510 (2003).
- [Hin71] O. Hinckelmann and L. Spruch, *Low-energy scattering by long-range potentials*, Phys. Rev. A **3**, 642 (1971).
- [Hop00] S. A. Hopkins, S. Webster, J. Arlt, P. Bance, S. Cornish, O. Maragò, and C. J. Foot, *Measurement of elastic cross section for cold cesium collisions*, Phys. Rev. A **61**, 032707 (2000).
- [Hu14] M.-G. Hu, R. S. Bloom, D. S. Jin, and J. M. Goldwin, *Avalanche-mechanism loss at an atom-molecule Efimov resonance*, Phys. Rev. A **90**, 013619 (2014).
- [Hua14a] B. Huang, K. M. O'Hara, R. Grimm, J. M. Hutson, and D. S. Petrov, *Three-body parameter for Efimov states in ^6Li* , Phys. Rev. A **90**, 043636 (2014).
- [Hua14b] B. Huang, L. A. Sidorenkov, R. Grimm, and J. M. Hutson, *Observation of the second triatomic resonance in Efimov's scenario*, Phys. Rev. Lett. **112**, 190401 (2014).
- [Huc09] J. H. Huckans, J. R. Williams, E. L. Hazlett, R. W. Stites, and K. M. O'Hara, *Three-body recombination in a three-state Fermi gas with widely tunable interactions*, Phys. Rev. Lett. **102**, 165302 (2009).
- [Hut93] J. M. Hutson, *BOUND computer program, version 5*, distributed by Collaborative Computational Project No. 6 of the UK Engineering and Physical Sciences Research Council.
- [Hut94a] J. M. Hutson, *Coupled-channel methods for solving the bound-state Schrödinger equation*, Comput. Phys. Commun. **84**, 1 (1994).
- [Hut94b] J. M. Hutson and S. Green, *MOLSCAT computer program, version 14*, distributed by Collaborative Computational Project No. 6 of the UK Engineering and Physical Sciences Research Council.
- [Hut07] J. M. Hutson, *Feshbach resonances in the presence of inelastic scattering: threshold behavior and suppression of poles in scattering lengths*, New J. Phys. **9**, 152 (2007).
- [Hut08] J. M. Hutson, E. Tiesinga, and P. S. Julienne, *Avoided crossings between bound states of ultracold cesium dimers*, Phys. Rev. A **78**, 052703 (2008).

- [Jen04] A. S. Jensen, K. Riisager, D. V. Fedorov, and E. Garrido, *Structure and reactions of quantum halos*, Rev. Mod. Phys. **76**, 215 (2004).
- [Jen11] A. S. Jensen (editor), *Special issue on Efimov physics*, Few-Body Syst. **51**, 77-269 (2011).
- [JL10] M. Jona-Lasinio and L. Pricoupenko, *Three resonant ultracold bosons: Off-resonance effects*, Phys. Rev. Lett. **104**, 023201 (2010).
- [Joh73] B. R. Johnson, *Multichannel log-derivative method for scattering calculations*, J. Comput. Phys. **13**, 445 (1973).
- [Jon02] S. Jonsell, H. Heiselberg, and C. J. Pethick, *Universal behavior of the energy of trapped few-boson systems with large scattering length*, Phys. Rev. Lett. **89**, 250401 (2002).
- [Jon06] S. Jonsell, *Efimov states for systems with negative scattering lengths*, Europhys. Lett. **76**, 8 (2006).
- [Jul04] P. S. Julienne, E. Tiesinga, and T. Köhler, *Making cold molecules by time-dependent Feshbach resonances*, J. Mod. Opt. **51**, 1787 (2004).
- [Jul06] P. S. Julienne and B. Gao, *Simple theoretical models for resonant cold atom interactions*, Atomic Physics 20 (C. Roos, H. Häffner, and R. Blatt, eds.), AIP Conf. Proc. No. 869, 2006, pp. 261–268.
- [Jul14] P. S. Julienne and J. M. Hutson, *Contrasting the wide Feshbach resonances in ${}^6\text{Li}$ and ${}^7\text{Li}$* , Phys. Rev. A **89**, 052715 (2014).
- [Ker00] A. J. Kerman, V. Vuletić, C. Chin, and S. Chu, *Beyond optical molasses: 3D Raman sideband cooling of atomic cesium to high phase-space density*, Phys. Rev. Lett. **84**, 439 (2000).
- [Kno08] S. Knoop, M. Mark, F. Ferlaino, J. G. Danzl, T. Kraemer, H.-C. Nägerl, and R. Grimm, *Metastable Feshbach molecules in high rotational states*, Phys. Rev. Lett. **100**, 083002 (2008).
- [Kno09] S. Knoop, F. Ferlaino, M. Mark, M. Berninger, H. Schöbel, H.-C. Nägerl, and R. Grimm, *Observation of an Efimov-like trimer resonance in ultracold atom-dimer scattering*, Nat. Phys. **5**, 227 (2009).
- [Kot00] S. Kotochigova, E. Tiesinga, and P. S. Julienne, *Relativistic ab initio treatment of the second-order spin-orbit splitting of the $a^3\sigma_u^+$ potential of rubidium and cesium dimers*, Phys. Rev. A **63**, 012517 (2000).
- [Kra90] M. Krauss and W. J. Stevens, *Effective core potentials and accurate energy curves for Cs_2 and other alkali diatomics*, J. Chem. Phys. **93**, 4236 (1990).

- [Kra04] T. Kraemer, J. Herbig, M. Mark, T. Weber, C. Chin, H.-C. Nägerl, and R. Grimm, *Optimized production of a cesium Bose-Einstein condensate*, Appl. Phys. B **79**, 1013 (2004).
- [Kra06] T. Kraemer, M. Mark, P. Waldburger, J. G. Danzl, C. Chin, B. Engeser, A. D. Lange, K. Pilch, A. Jaakkola, H.-C. Nägerl, and R. Grimm, *Evidence for Efimov quantum states in an ultracold gas of caesium atoms*, Nature (London) **440**, 315 (2006).
- [Kun15] M. Kunitski, S. Zeller, J. Voigtsberger, A. Kalinin, L. P. H. Schmidt, M. Schöffler, A. Czasch, W. Schöllkopf, R. E. Grisenti, T. Jahnke, D. Blume, and R. Dörner, *Observation of the Efimov state of the helium trimer*, Science **348**, 551 (2015).
- [Lan32] L. Landau, *On the theory of transfer of energy at collisions II*, Phys. Z. Sowjetunion **2**, 46 (1932).
- [Lan65] L. D. Landau and E. M. Lifshitz, *Quantum mechanics (course of theoretical physics)*, Pergamon Press, Oxford, 1965.
- [Lan09] A. D. Lange, K. Pilch, A. Prantner, F. Ferlaino, B. Engeser, H.-C. Nägerl, R. Grimm, and C. Chin, *Determination of atomic scattering lengths from measurements of molecular binding energies near Feshbach resonances*, Phys. Rev. A **79**, 013622 (2009).
- [Lan12] C. Langmack, D. H. Smith, and E. Braaten, *Avalanche mechanism for atom loss near an atom-dimer Efimov resonance*, Phys. Rev. A **86**, 022718 (2012).
- [Lan13] C. Langmack, D. H. Smith, and E. Braaten, *Atom loss resonances in a Bose-Einstein condensate*, Phys. Rev. Lett. **111**, 023003 (2013).
- [Law97] M. M. Law and J. M. Hutson, *I-NoLLS computer program, version 1*, Comput. Phys. Commun. **102**, 252 (1997).
- [Lee57] T. D. Lee, K. Huang, and C. N. Yang, *Eigenvalues and eigenfunctions of a Bose system of hard spheres and its low-temperature properties*, Phys. Rev. **106**, 1135 (1957).
- [Lee07] M. D. Lee, T. Köhler, and P. S. Julienne, *Excited thomas-Efimov levels in ultracold gases*, Phys. Rev. A **76**, 012720 (2007).
- [Leo00] P. J. Leo, C. J. Williams, and P. S. Julienne, *Collision properties of ultracold ^{133}Cs atoms*, Phys. Rev. Lett. **85**, 2721 (2000).
- [Leo01] P. J. Leo, P. S. Julienne, F. H. Mies, and C. J. Williams, *Collisional frequency shifts in ^{133}Cs fountain clocks*, Phys. Rev. Lett. **86**, 3743 (2001).

- [Lev14] J. Levinsen, P. Massignan, and M. M. Parish, *Efimov trimers under strong confinement*, Phys. Rev. X **4**, 031020 (2014).
- [Lim77] T. K. Lim, S. K. Duffy, and W. C. Damer, *Efimov state in the ^4He trimer*, Phys. Rev. Lett. **38**, 341 (1977).
- [Lom10a] T. Lompe, T. B. Ottenstein, F. Serwane, K. Viering, A. N. Wenz, G. Zürn, and S. Jochim, *Atom-dimer scattering in a three-component Fermi gas*, Phys. Rev. Lett. **105**, 103201 (2010).
- [Lom10b] T. Lompe, T. B. Ottenstein, F. Serwane, A. N. Wenz, G. Zürn, and S. Jochim, *Radio-frequency association of Efimov trimers*, Science **330**, 940 (2010).
- [LR98] R. J. Le Roy, *Uncertainty, sensitivity, convergence, and rounding in performing and reporting least-squares fits*, J. Mol. Spectrosc. **191**, 223 (1998).
- [Mac68] J. Macek, *Properties of autoionizing states of He*, J. Phys. B **1**, 831 (1968).
- [Mac05] J. H. Macek, S. Ovchinnikov, and G. Gasaneo, *Solution for boson-diboson elastic scattering at zero energy in the shape-independent model*, Phys. Rev. A **72**, 032709 (2005).
- [Mac12] O. Machtey, D. A. Kessler, and L. Khaykovich, *Universal dimer in a collisionally opaque medium: Experimental observables and Efimov resonances*, Phys. Rev. Lett. **108**, 130403 (2012).
- [Man86] D. E. Manolopoulos, *An improved log-derivative method for inelastic scattering*, J. Chem. Phys. **85**, 6425 (1986).
- [Mar91] B. Markovski, A. Suzko, and S. Vinitzky, *New adiabatic representation for three-body scattering problem* (1991).
- [Mar94] M. Marinescu, J. F. Babb, and A. Dalgarno, *Long-range potentials, including retardation, for the interaction of two alkali-metal atoms*, Phys. Rev. A **50**, 3096 (1994).
- [Mar07] M. Mark, F. Ferlaino, S. Knoop, J. G. Danzl, T. Kraemer, C. Chin, H.-C. Nägerl, and R. Grimm, *Spectroscopy of ultracold trapped cesium Feshbach molecules*, Phys. Rev. A **76**, 042514 (2007).
- [Mas08] P. Massignan and H. T. C. Stoof, *Efimov states near a Feshbach resonance*, Phys. Rev. A **78**, 030701 (2008).
- [Maz06] I. Mazumdar, A. R. P. Rau, and V. Bhasin, *Efimov states and their Fano resonances in a neutron-rich nucleus*, Phys. Rev. Lett. **97**, 062503 (2006).

- [Meh09] N. P. Mehta, S. T. Rittenhouse, J. P. D’Incao, J. von Stecher, and C. H. Greene, *General theoretical description of N -body recombination*, Phys. Rev. Lett. **103**, 153201 (2009).
- [Mie96] F. H. Mies, C. J. Williams, P. S. Julienne, and M. Krauss, *Estimating bounds on collisional relaxation rates of spin-polarized ^{87}Rb atoms at ultracold temperatures*, J. Res. Natl. Inst. Stand. Technol **101**, 521 (1996).
- [Min61] R. A. Minlos and L. D. Faddeev, *Comment on the problem of three particles with point interactions*, Sov. Phys. JETP **41**, 1850 (1961).
- [Moe95] A. J. Moerdijk, B. J. Verhaar, and A. Axelsson, *Resonances in ultracold collisions of ^6Li , ^7Li , and ^{23}Na* , Phys. Rev. A **51**, 4852 (1995).
- [Nai11] P. Naidon and M. Ueda, *The Efimov effect in lithium 6*, C. R. Phys. **12**, 13 (2011).
- [Nai14a] P. Naidon, S. Endo, and M. Ueda, *Microscopic origin and universality classes of the Efimov three-body parameter*, Phys. Rev. Lett. **112**, 105301 (2014).
- [Nai14b] P. Naidon, S. Endo, and M. Ueda, *Physical origin of the universal three-body parameter in atomic Efimov physics*, Phys. Rev. A **90**, 022106 (2014).
- [Nak10] S. Nakajima, M. Horikoshi, T. Mukaiyama, P. Naidon, and M. Ueda, *Nonuniversal Efimov atom-dimer resonances in a three-component mixture of ^6Li* , Phys. Rev. Lett **105**, 023201 (2010).
- [Nak11] S. Nakajima, M. Horikoshi, T. M. P. Naidon, and M. Ueda, *Measurement of an Efimov trimer binding energy in a three-component mixture of ^6Li* , Phys. Rev. Lett. **106**, 143201 (2011).
- [Nap94] R. Napolitano, J. Weiner, C. J. Williams, and P. S. Julienne, *Line shapes of high resolution photoassociation spectra of optically cooled atoms*, Phys. Rev. Lett. **73**, 1352 (1994).
- [Nau87] H. W. L. Naus and J. A. Tjon, *The Efimov effect in a four-body system*, Few-Body Syst. **2**, 121 (1987).
- [Nie99] E. Nielsen and J. H. Macek, *Low-energy recombination of identical bosons by three-body collisions*, Phys. Rev. Lett. **83**, 1751 (1999).
- [Nie01] E. Nielsen, D. Fedorov, A. Jensen, and E. Garrido, *The three-body problem with short-range interactions*, Physics Reports **347**, 373 (2001).
- [Ott08] T. B. Ottenstein, T. Lompe, M. Kohnen, A. N. Wenz, and S. Jochim, *Collisional stability of a three-component degenerate Fermi gas*, Phys. Rev. Lett. **101**, 203202 (2008).

- [Pas10] B. Pasquiou, G. Bismut, Q. Beaufils, A. Crubellier, E. Maréchal, P. Pedri, L. Vernac, O. Gorceix, and B. Laburthe-Tolra, *Control of dipolar relaxation in external fields*, Phys. Rev. A **81**, 042716 (2010).
- [Pet04] D. S. Petrov, *Three-boson problem near a narrow Feshbach resonance*, Phys. Rev. Lett. **93**, 143201 (2004).
- [Pet13] D. S. Petrov, *The few-atom problem*, Proceedings of the Les Houches Summer Schools, Session 94 (C. Salomon, G. V. Shlyapnikov, and L. F. Cugliandolo, eds.), Oxford University Press, Oxford, England, 2013, p. 109.
- [Pet15] D. S. Petrov and F. Werner, *Three-body recombination in heteronuclear mixtures at finite temperature*, arXiv:1502.04092.
- [Pir14] R. Pires, J. Ulmanis, S. Häfner, M. Repp, A. Arias, E. D. Kuhnle, and M. Weidemüller, *Observation of Efimov resonances in a mixture with extreme mass imbalance*, Phys. Rev. Lett. **112**, 250404 (2014).
- [Pla04] L. Platter, H.-W. Hammer, and U.-G. Meißner, *Four-boson system with short-range interactions*, Phys. Rev. A **70**, 052101 (2004).
- [Pla09] L. Platter, C. Ji, and D. R. Phillips, *Range corrections to three-body observables near a Feshbach resonance*, Phys. Rev. A **79**, 022702 (2009).
- [Pol09] S. E. Pollack, D. Dries, and R. G. Hulet, *Universality in three- and four-body bound states of ultracold atoms*, Science **326**, 1683 (2009).
- [Rem13] B. S. Rem, A. T. Grier, I. Ferrier-Barbut, U. Eismann, T. Langen, N. Navon, L. Khaykovich, F. Werner, D. S. Petrov, F. Chevy, and C. Salomon, *Lifetime of the Bose gas with resonant interactions*, Phys. Rev. Lett. **110**, 163202 (2013).
- [Rep13] M. Repp, R. Pires, J. Ulmanis, R. Heck, E. D. Kuhnle, M. Weidemüller, and E. Tiemann, *Observation of interspecies ${}^6\text{Li}$ - ${}^{133}\text{Cs}$ Feshbach resonances*, Phys. Rev. A **87**, 010701 (2013).
- [Ric94] J.-M. Richard and S. Fleck, *Limits on the domain of coupling constants for binding N -body systems with no bound subsystems*, Phys. Rev. Lett. **73**, 1464 (1994).
- [Roy13] S. Roy, M. Landini, A. Trenkwalder, G. Semeghini, G. Spagnolli, A. Simoni, M. Fattori, M. Inguscio, and G. Modugno, *Test of the universality of the three-body Efimov parameter at narrow Feshbach resonances*, Phys. Rev. Lett. **111**, 053202 (2013).
- [Sch94] W. Schöllkopf and J. P. Toennies, *Nondestructive mass selection of small van der Waals clusters*, Science **266**, 1345 (1994).

- [Sch12] R. Schmidt, S. Rath, and W. Zwerger, *Efimov physics beyond universality*, Eur. Phys. J. B **85**, 1 (2012).
- [Sko57] G. V. Skorniakov and K. A. Ter-Martirosian, *Three body problem for short range forces. I. scattering of low energy neutrons by deuterons.*, Sov. Phys. JETP **4**, 648 (1957).
- [Smi65] B. M. Smirnov and M. S. Chibisov, *Electron exchange and changes in the hyperfine state of colliding alkaline metal atoms*, Sov. Phys. JETP **21**, 624 (1965).
- [Söd98] J. Söding, D. Guéry-Odelin, P. Desbiolles, G. Ferrari, and J. Dalibard, *Giant spin relaxation of an ultracold cesium gas*, Phys. Rev. Lett. **80**, 1869 (1998).
- [Sol03] P. Soldán, M. T. Cvitaš, and J. M. Hutson, *Three-body nonadditive forces between spin-polarized alkali-metal atoms*, Phys. Rev. A **67**, 054702 (2003).
- [Sør02] O. Sørensen, D. V. Fedorov, and A. S. Jensen, *Correlated trapped bosons and the many-body Efimov effect*, Phys. Rev. Lett. **89**, 173002 (2002).
- [Sør12] P. K. Sørensen, D. V. Fedorov, A. S. Jensen, and N. T. Zinner, *Efimov physics and the three-body parameter within a two-channel framework*, Phys. Rev. A **86**, 052516 (2012).
- [Sto88] H. T. C. Stoof, J. M. V. A. Koelman, and B. J. Verhaar, *Spin-exchange and dipole relaxation rates in atomic hydrogen: rigorous and simplified calculations*, Phys. Rev. B **38**, 4688 (1988).
- [Sun02] H. Suno, B. D. Esry, C. H. Greene, and J. J. P. Burke, *Three-body recombination of cold helium atoms*, Phys. Rev. A **65**, 042725 (2002).
- [Tak12] T. Takekoshi, M. Debatin, R. Rameshan, F. Ferlaino, R. Grimm, H.-C. Nägerl, C. R. L. Sauer, J. M. Hutson, P. S. Julienne, S. Kotochigova, and E. Tiemann, *Towards the production of ultracold ground-state RbCs molecules: Feshbach resonances, weakly bound states, and the coupled-channel model*, Phys. Rev. A **85**, 032506 (2012).
- [Tan08] S. Tan, *Energetics of a strongly correlated Fermi gas*, Ann. Phys. **323**, 2952 (2008).
- [Tha09] G. Thalhammer, G. Barontini, J. Catani, F. Rabatti, C. Weber, A. Simoni, F. Minardi, and M. Inguscio, *Collisional and molecular spectroscopy in an ultracold Bose-Bose mixture*, New J. Phys. **11**, 055044 (2009).
- [Tho35] L. H. Thomas, *The interaction between a neutron and a proton and the structure of H^3* , Phys. Rev. **47**, 903 (1935).
- [Tho05] S. T. Thompson, E. Hodby, and C. E. Wieman, *Ultracold molecule production via a resonant oscillating magnetic field*, Phys. Rev. Lett. **95**, 190404 (2005).

- [Thø08a] M. Thøgersen, D. V. Fedorov, and A. S. Jensen, *N-body Efimov states of trapped bosons*, Europhys. Lett. **83**, 30012 (2008).
- [Thø08b] M. Thøgersen, D. V. Fedorov, and A. S. Jensen, *Universal properties of Efimov physics beyond the scattering length approximation*, Phys. Rev. A **78**, 020501(R) (2008).
- [Tim99] E. Timmermans, P. Tommasini, M. Hussein, and A. Kerman, *Feshbach resonances in atomic Bose-Einstein condensates*, Physics Reports **315**, 199 (1999).
- [Tre01] P. Treutlein, K. Y. Chung, and S. Chu, *High-brightness atom source for atomic fountains*, Phys. Rev. A **63**, 051401(R) (2001).
- [Tun13] S.-K. Tung, C. Parker, J. Johansen, C. Chin, Y. Wang, and P. S. Julienne, *Ultracold mixtures of atomic ^6Li and ^{133}Cs with tunable interactions*, Phys. Rev. A **87**, 010702 (2013).
- [Tun14] S.-K. Tung, K. Jiménez-García, J. Johansen, C. V. Parker, and C. Chin, *Geometric scaling of Efimov states in a ^6Li - ^{133}Cs mixture*, Phys. Rev. Lett. **113**, 240402 (2014).
- [Ulm15] J. Ulmanis, S. Häfner, R. Pires, E. D. Kuhnle, M. Weidemüller, and E. Tiemann, *Universality of weakly bound dimers and Efimov trimers close to Li-Cs Feshbach resonances*, arXiv:1501.04799.
- [Van04] N. Vanhaecke, C. Lisdat, B. T’Jampens, D. Comparat, A. Crubellier, and P. Pillet, *Accurate asymptotic ground state potential curves of Cs_2 from two-colour photoassociation*, Eur. Phys. J. D **28**, 351 (2004).
- [von09] J. von Stecher, J. P. D’Incao, and C. H. Greene, *Signatures of universal four-body phenomena and their relation to the Efimov effect*, Nat. Phys. **5**, 417 (2009).
- [von10] J. von Stecher, *Weakly bound cluster states of Efimov character*, J. Phys. B **43**, 101002 (2010).
- [vS11] J. von Stecher, *Five- and six-body resonances tied to an Efimov trimer*, Phys. Rev. Lett. **107**, 200402 (2011).
- [Vul99] V. Vuletić, A. J. Kerman, C. Chin, and S. Chu, *Observation of low-field Feshbach resonances in collisions of cesium atoms*, Phys. Rev. Lett. **82**, 1406 (1999).
- [Wan11] Y. Wang, J. P. D’Incao, and B. D. Esry, *Ultracold three-body collisions near narrow Feshbach resonances*, Phys. Rev. A **83**, 042710 (2011).
- [Wan12] J. Wang, J. P. D’Incao, B. D. Esry, and C. H. Greene, *Origin of the three-body parameter universality in Efimov physics*, Phys. Rev. Lett. **108**, 263001 (2012).

- [Wan13] Y. Wang, J. P. D’Incao, and B. D. Esry, *Ultracold few-body systems*, Adv. At. Mol. Opt. Phys. **62** (2013).
- [Wan14] Y. Wang and P. S. Julienne, *Universal van der Waals physics for three cold atoms near Feshbach resonances*, Nat. Phys. **10**, 768 (2014).
- [Web03a] T. Weber, J. Herbig, M. Mark, H.-C. Nägerl, and R. Grimm, *Bose-Einstein condensation of cesium*, Science **299**, 232 (2003).
- [Web03b] T. Weber, *Bose-Einstein condensation of optically trapped cesium*, Ph.D. thesis, University of Innsbruck (2003).
- [Web03c] T. Weber, J. Herbig, M. Mark, H.-C. Nägerl, and R. Grimm, *Three-body recombination at large scattering lengths in an ultracold atomic gas*, Phys. Rev. Lett. **91**, 123201 (2003).
- [Web08] C. Weber, G. Barontini, J. Catani, G. Thalhammer, M. Inguscio, and F. Minardi, *Association of ultracold double-species bosonic molecules*, Phys. Rev. A **78**, 061601(R) (2008).
- [Wen09] A. N. Wenz, T. Lompe, T. B. Ottenstein, F. Serwane, G. Zürn, and S. Jochim, *Universal trimer in a three-component Fermi gas*, Phys. Rev. A **80**, 040702(R) (2009).
- [Wer06] F. Werner and Y. Castin, *Unitary quantum three-body in a harmonic trap*, Phys. Rev. Lett. **97**, 150401 (2006).
- [Wig33] E. Wigner, *Über die streuung von neutronen an protonen*, Zeitschrift für Physik **83**, 253 (1933) (German).
- [Wig48] E. P. Wigner, *On the behavior of cross sections near thresholds*, Phys. Rev. **73**, 1002 (1948).
- [Wil09] J. R. Williams, E. L. Hazlett, J. H. Huckans, R. W. Stites, Y. Zhang, and K. M. O’Hara, *Evidence for an excited-state Efimov trimer in a three-component Fermi gas*, Phys. Rev. Lett. **103**, 130404 (2009).
- [Wil12] R. J. Wild, P. Makotyn, J. M. Pino, E. A. Cornell, and D. S. Jin, *Measurements of Tan’s contact in an atomic Bose-Einstein condensate*, Phys. Rev. Lett. **108**, 145305 (2012).
- [Yam06] M. T. Yamashita, L. Tomio, A. Delfino, and T. Frederico, *Four-boson scale near a Feshbach resonance*, Europhys. Lett. **75**, 555 (2006).
- [Yam08] M. Yamashita, T. Frederico, and L. Tomio, *Neutron-¹⁹c scattering near an Efimov state*, Phys. Lett. B **670**, 49 (2008).

- [Yam11] M. Yamashita, D. Fedorov, and A. Jensen, *Brunnian and Efimov N -body states*, *Few-Body Syst.* **51**, 135 (2011).
- [Zac09] M. Zaccanti, B. Deissler, C. D’Errico, M. Fattori, M. Jona-Lasinio, S. Müller, G. Roati, M. Inguscio, and G. Modugno, *Observation of an Efimov spectrum in an atomic system*, *Nat. Phys.* **5**, 586 (2009).
- [Zei78] E. Zeiger, *Quantum-mechanical few-body scattering equations with half-on-shell energy-independent subsystem input*, May 1978.
- [Zen32] C. Zener, *Non-adiabatic crossing of energy levels*, *Proc. R. Soc. London, Ser. A* **137**, 696 (1932).
- [Zen12] A. Zenesini, B. Huang, M. Berninger, S. Besler, H.-C. Nägerl, F. Ferlaino, and R. Grimm, *Creation of Bose-Einstein condensates of cesium at high magnetic fields*, (2012), in preparation.
- [Zen13] A. Zenesini, B. Huang, M. Berninger, S. Besler, H.-C. Nägerl, F. Ferlaino, R. Grimm, C. H. Greene, and J. von Stecher, *Resonant five-body recombination in an ultracold gas of bosonic atoms*, *New J. Phys.* **15**, 043040 (2013).
- [Zen14] A. Zenesini, B. Huang, M. Berninger, H.-C. Nägerl, F. Ferlaino, and R. Grimm, *Resonant atom-dimer collisions in cesium: Testing universality at positive scattering lengths*, *Phys. Rev. A* **90**, 022704 (2014).
- [Zhe86] Z. Zhen and J. Macek, *Loosely bound states of three particles*, *Z. Phys. D* **3**, 31 (1986).
- [Zür13] G. Zürn, T. Lompe, A. N. Wenz, S. Jochim, P. S. Julienne, and J. M. Hutson, *Precise characterization of ^6Li Feshbach resonances using trap-sideband-resolved rf spectroscopy of weakly bound molecules*, *Phys. Rev. Lett.* **110**, 135301 (2013).

Acknowledgments

*The dark night gave me black eyes,
I use them nonetheless seeking for the
light.*

— Gu Cheng, *A Generation*

It has been more than seven years since my first arrival in Innsbruck for the interview of a master position. I will never regret that I came to Innsbruck for science and spent my seven years of youth here. I would like to express my gratitude to all the people who made my accomplishments here possible.

First of all, I would like to thank my supervisor Rudi Grimm who provided me with the opportunity to work with a group of brilliant and friendly colleagues. Rudi leads the group with plenty of patience and freedom and influence us with his earnestness in science. Under Rudi's guidance, I benefit greatly from his profound and intuitive thoughts in physics. He also support me warmly in case of non-scientific issues and I can not forget the dawn when he helped me at the Innsbruck airport during my first visit. Without Rudi, I would not be in Innsbruck and all the works presented in this thesis would be impossible.

I can never thank my lab-colleagues Martin Berninger and Alessandro Zenesini enough. For years, we worked together like comrades in a battle field. I must also thank the bright master students, like Stefan Besler and Walter Harm, in our lab. They contributed significantly to the experiments. Especially, I learned a lot of programming techniques from Stefan. I worked happily with my former roommate Leonid Sidorenkov for several months when he has finished his PhD work, and we also enjoyed hiking and skiing together. Moreover, I want to thank Francesca Ferlaino, Hanns-Christoph Nägerl and Michael Mark, who are the older generation used to work with this experiment. They keep providing valuable suggestions all the time.

My colleagues in the institute provided me with a lot of knowledge and help, and I sincerely appreciate our friendships. Especially, Mengkhon Tey was as kind as an elder brother of mine. Albert Frisch, Manfred Mark and Gerhard Hendl always suggest elegant solutions for the urgent problems of the setup. It has been also delightful to discuss with my master-thesis supervisor Florian Schreck, my office-mate Lukas Reichsöllner and many other colleagues. Beyond the lab, I must thank my colleague and ski teacher Slava Tzanova who was very

patient and calm when I rolled down a snow mountain for more than three kilometers. I also want to thank Katharina Lauber who provided a lot of valuable suggestions and helps when my wife and I were overwhelmed by our arriving baby.

I must say a big thank you to the secretaries of the institute, especially Christine Götsch-Obmascher, Nicole Jorda and Elisabeth Huck. Thanks to their friendly and careful help, I have been saved from bureaucratic problems.

During the time I wrote my thesis, I received a lot of helps. I would like to thank Dmitry Petrov and Pascal Naidon for stimulating discussions. I am very grateful to Jesper Levinsen, Alessandro Zenesini, Mengkhon Tey and Tadas Pyragius for their detailed and valuable comments on my manuscript.

Finally, I would like to thank my family, thank you for your love and trust. I thank my parents for their endless and selfless support and encouragement. My lovely wife Wei-Er gave me a lot of support when I was writing the thesis during her pregnancy. She brightens up my life with wisdom, love and hope.